



Dynamic Nanostructured Scaffolds as Advanced Biomaterials

A thesis submitted in fulfilment of the requirements for the degree of Doctor of Philosophy

Mitchell Duncan Boyd-Moss

Bachelor of Engineering (Biomedical Engineering) (Honours), RMIT

School of Engineering

College of Science, Engineering and Health

RMIT University

July 2019

DECLARATION

I certify that except where due acknowledgement has been made, the work is that of the author alone; the work has not been submitted previously, in whole or in part, to qualify for any other academic award; the content of the thesis is the result of work which has been carried out since the official commencement date of the approved research program; any editorial work, paid or unpaid, carried out by a third party is acknowledged; and, ethics procedures and guidelines have been followed.

I acknowledge the support I have received for my research through the provision of an Australian Government Research Training Program Scholarship.

Mitchell Boyd-Moss

01/07/2019

ACKNOWLEDGEMENTS

I would like to show my greatest appreciation to the people and institutions who have inspired me and assisted me during this project.

During my PhD, I have been fortunate enough to have access to various outstanding laboratories and facilities. I would firstly, like to thank RMIT for funding received during my project. I would also like to thank RMIT for access to world-class laboratories and would like to express my gratitude to staff at the RMIT Microscopy and Microanalysis Facility (RMMF) and MicroNano Research Facility (MNRF). I would also like to extend my gratitude to funding partners and staff at the St. Vincent's BioFab3D centre and would like to acknowledge grant funding received for beamtime at the Australian Synchrotron (ANSTO, AUS). Use of all these laboratories, and the well-maintained equipment within was of substantial benefit to the project.

I would like to show my utmost appreciation to my principle supervisor Dr. Richard Williams, for his invaluable supervision and genuine interest in the project. I would particularly like to thank Richard for his eagerness to broaden my skillsets, for inspiring me, and for pushing me to do beyond what I thought capable. I have learnt a substantial amount during this project, however, perhaps the greatest lessons were those demonstrated during conferences.

In a similar fashion, I would like to extend this gratitude to my other supervisors, Dr. Dodie Pouniotis and Prof. David Nisbet. Thank you, Dodie, for your willingness to help, and advice given through the course of this project, your expertise is always appreciated. Thank you, David, for your advice and contribution in various aspects of the project. I would particularly like to thank David for his willingness to impart wisdom during conferences and professionalism in every circumstance.

I am deeply grateful of all those who I had the privilege to work with during this project. In particular, I would like to emphasise my appreciation to Dr. Anita Quigley for the substantial time she placed into my project, particularly in the culturing of cells, or in advice given during project development. Thank you, Anita, for your patience in teaching me cell techniques, and for your constant willingness to help,

whether it be in the lab or regarding biological aspects of experimental design. I would also like to extend my heartfelt appreciation to Dr. Chaitali Dekiwadia who taught me various electron microscopy techniques, including sample preparation, TEM and CryoSEM techniques. Thank you Chaitali for your genuine interest in my work and eagerness to teach. I appreciate all the time placed into my research and all advice given spanning from improvements in technique to potential postdoctoral direction.

I would like to thank Dr. Benjamin Long for assistance in SAXS data acquisition and modelling, your ability to teach me the fundamental techniques was of substantial benefit to my project. Likewise, I want to thank Dr. Cathal O'Connell, who managed BioFab3D during the course of my project. Your advice concerning material analysis, and training in rheology and bioprinting was of considerable value to my project. Thank you, Cathal, for inspiring me to be a better researcher and for your willingness to set aside time to teach and discuss ideas. Your help in analysing structure-function relationships and genuine interest in scientific advance is greatly appreciated. I would also like to thank Prof. Robert Kapsa for his constant support and interest in my project. Thank you, Rob, for challenging me to be a better researcher and for the lessons you've given during the completion of this project. I am also extremely grateful to A.Prof. Elena Pirogova for supervising me during my honours year and for constantly being interested in the progression of my Doctoral project. Thank you, Elena, for your sincere interest in scientific development and for the substantial amount of time you place into your students.

I would like to express my gratitude to all my collaborators, with particular thanks to Dr. Rui Li, whom was the primary investigator for work presented in chapters 4 and 6, and who trained me in the foundations of cell culture during my first year of PhD. Similarly, I would like to thank Dr. Kiara Bruggeman for the time spent training me at ANU during my first week of PhD, somehow, you made peptide synthesis exciting. I would also like to extend my gratitude to Kate Firipis who was a key collaborator during my PhD, I appreciate the assistance you offered in the lab, during experimental design, and during result analysis/experimental write-up. I would also like to show my heartfelt appreciation for Noora Al Balushi who was the lead researcher for much of the data presented in Chapter 5 and alongside whom I have performed various experiments. I would like to thank Dr. Catherine Ngan,

for challenging me professionally and for the kindness and friendliness shown during my candidature, I truly appreciate our discussions.

Finally, I would like to thank my friends and family. To my peers and friends from RMIT and BioFab3D, thank you for providing a platform to discuss concepts in a non-formal yet intellectual way. To my friends outside of my studies, thank you for providing a social environment separate from my project. Lastly, to my family, I am deeply grateful for your understanding and encouragement during my studies. Particularly, I would like to thank my parents for their support during my candidature and for showing the value of hard work, my brother for inspiring me academically, and my uncle for mentoring me during my honours. You have all helped shaped me into the person I am today.

LIST OF AWARDS AND PUBLICATIONS

Awards

1. Awarded ANSTO (AUS) Grant as Primary Investigator (*value \$32,784.00 (AUD)*), Australian Synchrotron, Clayton, 2019.
2. 1st Prize - “Under the Coverslip”, Melbourne University, 2018.
3. Finalist - Australian-French Entrepreneurship Challenge, 2017

Publications:

a. Refereed Journal Articles

1. Duc, D., Stoddart, P. R., McArthur, S. L., Kapsa, R. M., Quigley, A. F., **Boyd-Moss, M.**, & Moulton, S. E. (2019). Fabrication of a Biocompatible Liquid Crystal Graphene Oxide–Gold Nanorods Electro-and Photoactive Interface for Cell Stimulation. *Advanced healthcare materials*, 1801321.
2. Ngan, C., D O'Connell, C., Blanchard, R., **Boyd-Moss, M.**, Williams, R., Bourke, J. L., ... & Choong, P. F. (2019). Optimising the biocompatibility of 3D printed photopolymer constructs in vitro and in vivo. *Biomedical Materials*.
3. Aye, S. S., Li, R., **Boyd-Moss, M.**, Long, B., Pavuluri, S., Bruggeman, K., ... & Williams, R. (2018). Scaffolds formed via the non-equilibrium supramolecular assembly of the synergistic ECM peptides RGD and PHSRN demonstrate improved cell attachment in 3D. *Polymers*, 10(7), 690.
4. Li, R., McRae, N. L., McCulloch, D. R., **Boyd-Moss, M.**, Barrow, C. J., Nisbet, D. R., ... & Williams, R. J. (2018). Large and small assembly: Combining functional macromolecules with small peptides to control the morphology of skeletal muscle progenitor cells. *Biomacromolecules*, 19(3), 825-837.
5. Li, R., **Boyd-Moss, M.**, Long, B., Martel, A., Parnell, A., Dennison, A. J., ... & Williams, R. J. (2017). Facile Control over the Supramolecular Ordering of Self-assembled Peptide Scaffolds by Simultaneous Assembly with a Polysaccharide. *Scientific reports*, 7(1), 4797.

6. **Boyd-Moss, M.**, Baratchi, S., Di Venere, M., & Khoshmanesh, K. (2016). Self-contained microfluidic systems: a review. *Lab on a Chip*, 16(17), 3177-3192.
- b. Articles under Review and in Preparation
1. Ngan, CGY., Quigley, A., Bourke, J., Blanchard, R., O'Connell, CD., Duchi, S., Onofrillo, C., **Boyd-Moss, M.**, Williams, R.J., Dekiwadia, C., Wallace, GG., Choong, PFM., Kapsa, RMI. (2019) *Bioprinting skeletal muscle fibres in gelatin methacryloyl (GelMA) with advanced maturation and functionality. Manuscript in preparation.*
 2. Al Balushi, N., **Boyd-Moss, M.**, Firipis, K., Darby, I., Nisbet, D., Pouniotis, D., Williams, R., (2019) '*Bioactive Peptide Microenvironments as functional lung tumour models.*' **Manuscript in preparation.**
 3. **Boyd-Moss, M.**, N., Firipis, K., Quigley, A., Dekiwadia, C., Long, B., Cichocki, A., Kapsa, RMI., Nisbet, D., Williams, R. (2019) '*SAP Inspired Hybrid Bioinks for Neural Tissue Engineering Applications.*' **Manuscript in preparation.**
 4. **Boyd-Moss, M.**, Firipis, K., Quigley, A., Cichocki, A., Dekiwadia, C., Long, B., Ngan, C., Witty, S., Nisbet, D., Kapsa, RMI., Williams, R (2019) '*Bioink Development using fmoc-SAP/Gelatin Methacrylate Blends.*' **Manuscript in preparation.**
 5. **Boyd-Moss, M.**, Firipis, K., O'Connell CD., Long, B., Nisbet, D., Williams, R (2019) '*SAXS investigation into Gelatin Methacryloyl Structure-function Relationships.*' **Manuscript in preparation.**
- c. Scholarly Book Chapter
1. **Boyd-Moss, M.**, Fox, K., Brandt, M., Nisbet, D., & Williams, R. (2017). Bioprinting and Biofabrication with Peptide and Protein Biomaterials. In *Peptides and Peptide-based Biomaterials and their Biomedical Applications* (pp. 95-129). Springer, Cham.
- d. Conference Presentations
1. 3rd – 6th April, 2019. **Society For Biomaterials 2019 Annual Meeting and Exposition: Exploring the Nexus of Research and Application**, Seattle, Washington, USA.
 2. 6th August, 2018. **2018 ACMD Research Week**, St Vincent's Hospital, Melbourne, Victoria.

3. 31st May, 2018. **ARC Training Centre for innovative Biotechnology Launch**, Sydney, NSW, Australia.
4. 3rd – 5th April, 2018. **26th Annual Australasian Society for Biomaterials and Tissue Engineering Conference (ASBTE)**, Fremantle, WA, Australia.
5. 30th October, 2017. **Graeme Clark Biomedical Innovation Showcase**, Melbourne, VIC, Australia.
6. 24th – 25th May, 2017. **AusMedTech Conference (ICMMB)**, Melbourne, VIC, Australia.
7. 18th-20th April, 2017. **25th Annual Australasian Society for Biomaterials and Tissue Engineering Conference (ASBTE)**, Canberra, ACT, Australia.
8. 15th July, 2016. **The 1st Annual Additive Manufacturing, Innovative Manufacturing or light structures (AIL) Symposium**. RMIT, Melbourne, Vic, Australia.
9. 27th-29th June, 2016. **The 7th International Nanomedicine Conference**. Sydney, NSW, Australia.

TABLE OF CONTENTS

DECLARATION	I
ACKNOWLEDGEMENTS	II
LIST OF AWARDS AND PUBLICATIONS	V
TABLE OF CONTENTS	VIII
LIST OF FIGURES	XII
LIST OF TABLES	XIII
LIST OF ABBREVIATIONS	XIV
ABSTRACT	XIX
1. INTRODUCTION	1
1.1 Problem Statement	1
1.2 Background	1
1.3 Project Significance	3
1.4 Project Aims	4
1.5 Thesis Outline	5
2. LITERATURE REVIEW: BIOPRINTING AND BIOFABRICATION WITH PEPTIDE AND PROTEIN BIOMATERIALS	6
2.1 Preview	6
2.2 Introduction:	7
2.3 Cell-Therapy-based Techniques	11
2.3.1 Artificial Three-Dimensional Microenvironments as Native Extracellular Matrix Mimics	11
2.4 Techniques	26
2.4.1 Casting	26
2.4.2 Microinjection	26
2.4.3 Electrospinning	27
2.4.4 Bioprinting	29
2.5 Peptide-based Bioinks	34
2.5.1 Biomaterials for Bioink Development	34
2.5.2 Peptide and Protein-Based Hydrogels	35
2.6 <i>In Vitro</i> and <i>In Vivo</i> Applications of Peptide-Based Inks	47
2.6.1 Non-Organ Tissue Regeneration	49
2.6.2 Organ Regeneration	63
2.7 Conclusion and Future Perspectives	71

3.	MATERIALS AND METHODS	73
3.1	Preview	73
3.2	Fmoc-SAP Characterisation.....	74
3.2.1	Fmoc-SAP hydrogel Preparation	74
3.2.2	1% Agarose Preparation.....	76
3.2.3	Bioink Preparation	76
3.2.4	Circular Dichroism.....	78
3.2.5	Fourier Transform Infrared Spectroscopy.....	78
3.2.6	Fluorescence Spectroscopy	79
3.2.7	Atomic Force Microscopy	79
3.2.8	Transmission Electron Microscopy.....	80
3.2.9	Cryo-Scanning Electron Microscopy	80
3.2.10	Small-Angle X-ray Scattering.....	81
3.2.11	Small-Angle Neutron Scattering	82
3.2.12	Oscillatory Rheology	82
3.2.13	Printability Tests	84
3.2.14	Bioprinting	86
3.3	<i>In Vitro</i> Cell Culture	87
3.3.1	Cell Lines and Culture Conditions.....	87
3.3.2	Preparation of Versican and Empty Vector Conditioned Media.....	88
3.3.3	Western Blotting of Versican Enriched Conditioned Media	88
3.3.4	Immunofluorescence to Confirm Media Incorporation to Scaffolds	89
3.3.5	Live/Dead Cell Staining.....	89
3.3.6	Cell Proliferation and Metabolic Activity.....	90
3.3.7	Flow Cytometry	91
3.3.8	Nucleus (DAPI) and Actin (Phalloidin) Staining.....	92
3.3.9	Immunofluorescence Staining for DAPI, Vinculin and F-actin.....	94
3.3.10	Cell Migration Tracking.....	94
3.3.11	SEM Observation of Cell Interaction with Bioinks	95
3.4	Statistical Analysis.....	96
4.	TUNING THE BIOMECHANICAL AND BIOCHEMICAL PROPERTIES OF SCAFFOLDS VIA COASSEMBLY.....	97
4.1	Preview	97
4.2	Introduction.....	99
4.3	Results and Discussion	101
4.3.1	Development of Multi-Sequence Self-Assembled Peptide Hydrogels	101

4.3.2	Investigation into Network Topology of Engineered SAP Hydrogels.....	103
4.3.3	Investigation of Self-Assembly Mechanisms.....	106
4.3.4	Biological Effect of Synergistic Scaffolds.....	110
4.4	Enabling Mechanical Tunability Through Macromolecule Addition.....	112
4.4.1	Formation of Hydrogels.....	112
4.4.2	Investigation into Network Topology of Macromolecule Functionalised SAPs	114
4.4.3	Investigation of Self-Assembly Mechanisms and Impact on Mechanical Properties .	119
4.5	Conclusion	122
5.	INVESTIGATION OF MULTISEQUENCE MATERIAL AS AN ADVANCED TUMOUR MICROENVIRONMENT	124
5.1	Preview	124
5.2	Introduction.....	126
5.3	Results and Discussion	128
5.3.1	Formation of Spheroids and Artificial Microenvironments.....	128
5.3.2	Mechanical Characterisation of Formulated Materials	130
5.3.3	Comparisons of 2D, 3D and Encapsulated 3D Cultured Conditions	135
5.3.4	Effect of Microenvironment.....	142
5.4	Conclusion	144
6.	FUNCTIONALISING SCAFFOLDS VIA INCORPORATION OF MACROMOLECULES..	145
6.1	Preview	145
6.2	Introduction.....	147
6.3	Results and Discussion	151
6.3.1	Formation of Hydrogels	151
6.3.2	Confirmation of Macromolecule Presentation	153
6.3.3	Investigation of Hydrogel Architecture.	155
6.3.4	Characterisation of Coassembled Structure, Mechanisms, and Mechanical Properties....	157
6.3.5	Effect of Macromolecule Functionalisation on Cell Viability and Protein Production. ...	159
6.3.6	Effect of Macromolecule Functionalisation on Cell-Size and Spreading	161
6.3.7	Effect of Macromolecule Functionalisation on Formation of Multinucleated Syncytia...	164
6.4	Conclusion	166
7.	CHARACTERISATION OF GELATIN METHACRYLOYL MACROMOLECULES AS A HYDROGEL FOR BIOENGINEERING.....	168
7.1	Preview	168
7.2	Introduction.....	171

7.3	Results and Discussion	174
7.3.1	Non-crosslinked GelMA Trends	175
7.3.2	Crosslinked GelMA Trends	182
7.4	Conclusion	188
8.	MUSCLE BIOINK	190
8.1	Preview	190
8.2	Introduction.....	193
8.3	Results and Discussion	195
8.3.1	Formation of Bioinks	195
8.3.2	Visualisation of Assembled Structures and Network Architecture.....	197
8.3.3	Investigation of Assembled Structures and Mechanical Properties	200
	<i>Determination of Mass Fractal Dimension</i>	201
8.3.4	Mechanical Characteristics	204
8.3.5	Investigation of Bioink Printability.....	206
8.3.6	Investigation of Cytocompatibility	208
8.4	Conclusion	212
9.	NEURAL BIOINK	213
9.1	Preview	213
9.2	Introduction.....	216
9.3	Results and Discussion	219
9.3.1	Formation of Bioinks	219
9.3.2	Investigation of bioink Micro-/nano-architecture	221
9.3.3	Material Printability and Thermoresponsive Viscoelasticity	226
9.3.4	<i>In Vitro</i> Analysis of Developed Bioinks using Rat Cortical Neurospheres	231
9.3.5	<i>In Vitro</i> Analysis of Printed Constructs.	233
9.4	Conclusion	238
10.	CONCLUSIONS.....	239
11.	FUTURE DIRECTIONS	243
	REFERENCES	246
	APPENDIX.....	266

LIST OF FIGURES

Figure 2-1 – Artistic depiction of native extracellular matrix showing fibrous proteins and proteoglycans.....	8
Figure 2-2 – Considerations for ideal biomaterial design	10
Figure 2-3 – Microstructure of tissue and common biomaterials as observed under SEM.....	18
Figure 2-4 – Structure of Synthetic Biomaterials.....	22
Figure 2-5 – Peptide self-assembly mechanisms.....	25
Figure 2-6 – Tubular Electrospun chitosan nanofibrous scaffolds for nerve regeneration	28
Figure 2-7 – Schematic showing working principles, bioprinting systems, and outcomes.....	30
Figure 2-8 – Bioprinted Gelatin-based (GelMA Physical Gels, GPG) constructs showing printed macroscopic shape (4% GPG gels) (A-H), microscale organisation observed via SEM (I-K), and cell spreading (L-N)	41
Figure 2-9 – <i>In vivo</i> bioprinted osteochondral regeneration approach.....	52
Figure 2-10 - Bioprinting approach for multicomponent tissue fabrication	58
Figure 2-11 – Bioprinted non-organ tissue constructs.....	61
Figure 2-12 – Bioprinted organ tissue constructs.....	66
Figure 4-1 – Structure of three Fmoc-based self-assembling peptides.....	102
Figure 4-2 – Hydrogel Nano/Microtopology observations in response to assembly mechanism.	104
Figure 4-3 – Investigation of material nanostructure via SAXS.....	105
Figure 4-4 – Spectroscopic characterisation of the peptide hydrogels.....	107
Figure 4-5 – Spectroscopic and rheological characterisation of the peptide hydrogels.....	109
Figure 4-6 – Cytocompatibility of HMFCs on Fmoc-SAP hydrogels.....	111
Figure 4-7 – Peptide self-organisation in the presence of fucoidan	113
Figure 4-8 –Hydrogel Nano/Microtopology changes upon macromolecule addition	115
Figure 4-9 – Characterisation of nanostructured changes as observed through SANS.	116
Figure 4-10 – Spectroscopic and rheological analysis of peptide assembly with increasing fucoidan concentration	121
Figure 5-1 – Schematic of spheroid and hydrogel formation.....	129
Figure 5-2 – Material characterisation.	134
Figure 5-3 – Biological activity of spheroids in response to hydrogel microenvironment.....	136
Figure 5-4 – Cytoskeleton in A) 2D cultures, B) non-encapsulated spheroids and C) 3D+ECM spheroids.....	139
Figure 5-5 – Analysis of α -SMA expression.....	141
Figure 5-6 – Investigation of cell motility.	143
Figure 6-1 – Schematic of peptide self-assembly, macromolecule co-assembly and resultant hydrogel formation.	152
Figure 6-2 – Verification of versican production by HEK-293T cells and visualisation of versican incorporation in Fmoc-FRGDF scaffolds	154
Figure 6-3 – Hydrogel Nano/Micromorphological changes in response to macromolecule incorporation.....	156
Figure 6-4 – Hydrogel assembly and mechanical properties	158
Figure 6-5 – Analysis of material cytocompatibility.	160
Figure 6-6 –Determination of cell morphology and spreading.....	163
Figure 6-7 – Observation of cell morphological characteristics as determined through DAPI/actin staining and determination of multinucleation as an indication of cell maturity	165
Figure 7-1 – Schematic showing Nanostructured properties as determined by SAXS.....	174

Figure 7-2 – Nanostructured and Viscoelastic properties of Non-crosslinked Gelma.....	178
Figure 7-3 – Nanostructured and Viscoelastic properties of crosslinked GelMA	184
Figure 8-1 – Schematic showing hydrogel assembly	196
Figure 8-2 – Network Morphology	198
Figure 8-3 – Analysis of material nanostructure.....	200
Figure 8-4 – Analysis of material viscoelastic properties.	205
Figure 8-5 – Investigation into material printability	207
Figure 8-6 – Representative-images of Live/Dead stain	209
Figure 8-7 – Representative confocal images of 3D printed samples after 14 days of differentiation	210
Figure 8-8 – SEM analysis of myotube formation.....	211
Figure 9-1 – Schematic of hydrogel assembly	220
Figure 9-2 – Observation of hydrogel network morphology.....	222
Figure 9-3 – Investigation of hydrogel nanostructure and viscoelastic properties	224
Figure 9-4 – Investigation into material printability	228
Figure 9-5 – Images of Print Geometries	229
Figure 9-6 – Analysis of GelMA regions within DIKVAV-Hybrid bioink.....	230
Figure 9-7 – Preliminary hydrogel cytotoxicity tests.	232
Figure 9-8 – Biological response to scaffolds	234
Figure 9-9 – SEM analysis of cells	235
Figure 9-10 – Analysis of cell morphology, migration and spreading following 14 days differentiation in LM-GelMA (Top) and DIKVAV-Hybrid (Bottom)	237

LIST OF TABLES

Table 2-1 - Bioprinting processes showing working principle, materials, advantages and disadvantages.....	32
Table 2-2 - Peptide-based bioink classification, formulation, and application.....	36
Table 2-3 - Application specific peptide-based bioprinting examples classified into non-organ and organ tissue regeneration.	48

LIST OF ABBREVIATIONS

2D	Two-dimensional
3D	Three-dimensional
ADSC	Adipose-derived stromal cells
AFA-LIFT	Absorbing film-assisted laser-induced forward transfer
AFM	Atomic force microscopy
BMSC	Bone marrow stem cells
BSA	Bovine serum albumin
CaCl ₂	Calcium chloride
CAD	Computer aided design
CAF	Cancer-associated fibroblast
CB[6]-HA	Cucurbit[6]uril – Hyaluronic Acid
CD	Circular dichroism
CNS	Central nervous system
CPC	Cardiac progenitor cell
CryoSEM	Cryo-scanning electron microscopy
D ₂ O	Deuterium oxide (heavy water)
DAH	2,6-diaminohexane
DAPI	4',6-diamidino-2-phenylindole
DCP	Dicumyl peroxide
dECM	Decellularised extracellular matrix
DIKVAV-Hybrid	Fmoc-DIKVAV-gelatin methacryloyl blend
DMEM	Dulbecco's modified eagle medium
DNA	Deoxyribonucleic acid
DoF	Degree of functionalisation
DPBS	Dulbecco's phosphate-buffered saline

ECM	Extracellular matrix
EDTA	Ethylenediaminetetraacetic acid
EMT	Epithelial to mesenchymal transition
FACs	Fluorescence-activated cell sorting
F-actin	Filamentous-actin
FBS	Fetal bovine serum
FF	Di-phenylalanine
FITC	Fluorescein isothiocyanate
Fmoc	Fluorenylmethyloxycarbonyl
Fmoc-SAP	Fluorenylmethyloxycarbonyl-self-assembling peptide
FPG-Hybrid	Fmoc-FRGDF/Fmoc-PHSRN/Gelatin methacryloyl blend
FT-IR	Fourier transform infrared spectroscopy
G'	Storage (elastic) modulus
G''	Loss (viscous) modulus
G6PD	Glucose-6-phosphatedehydrogenase
GAG	Glycosaminoglycan
GelMA	Gelatin methacryloyl
Gel-PEO	Gelatin-poly(ethylene oxide)
GG	Gellan gum
GPG	GelMA physical gels
HA	Hyaluronic acid (Hyaluronan)
HAMA	Hyaluronic acid methacryloyl
Hap	Hydroxyapatite
hASCs	Human adipose-derived stem cells
HAVIC	Human aortic valvular interstitial cells
HCl	Hydrogen chloride/Hydrochloric acid
hdECM	Heart-derived decellularised extracellular matrix

HEK-293	Human embryonic kidney cells
hFB	Human fibroblast cells
hMFC	Human mammary fibroblast cells
hMSC	Human mesenchymal stem cells
HMVEC	Human microvascular Endothelial Cells
HNDF	Human neonatal dermal fibroblasts
HSPG	Heparin sulphate proteoglycan
hTMSC	Human turbinate mesenchymal stromal cells
HUVEC	Human umbilical vein endothelial cells
IFT	Indirect fourier transform
LAP	Lithium phenyl-2,4,6-trimethylbenzoylphosphinate
LLC	Lewis lung carcinoma cell
LM-GelMA	Low methacryloyl gelatin methacryloyl
MAPLE-DW	Matrix-assisted pulsed laser evaporation direct writing
mdECM	Muscle-derived decellularised extracellular matrix
MSC	Mesenchymal stem cells
mTgase	Microbial transglutaminase
NaCl	Sodium chloride
NaOH	Sodium hydroxide
PA	Peptide amphiphiles
PBS	Phosphate-buffered saline
PCL	Poly(caprolactone)
PDMS	Polydimethylsiloxane
PECAM-1	Platelet endothelial cell adhesion molecule
PEG	Poly(ethylene glycol)
PEGDA	Poly(ethylene glycol) diacrylate
PEGDMA	Poly(ethylene glycol) dimethacrylate

PEGTA	Poly(ethylene glycol)-tetra-acrylate
PGA	Poly(glycolic acid)
PLA	Poly(lactic acid)
PLGA	Poly(lactide-co-glycolide)
PPF	Poly(propylene fumarate)
PVA	Poly(vinyl alcohol)
PVDF	Polyvinylidene difluoride
qPCR	Quantitative polymerase chain reaction
RT-qPCR	Reverse transcription quantitative polymerase chain reaction
Ru/SPS	Ruthenium/sodium persulfate
SANS	Small-angle neutron scattering
SAP	Self-assembling peptide
SAXS	Small-angle X-ray scattering
SF-G	Silk fibroin-Gelatin
SLA	Stereolithography apparatus
SMC	Smooth muscle cells
SPPS	Solid-phase-peptide-synthesis
TAIC	Triallyl isocyanurate
TBST	Tris-buffered saline with tween
TCA	Tricarboxylic acid
TEM	Transmission electron microscopy
TGF- β	Transforming growth factor beta
TME	Tumour microenvironment
TRITC	Tetramethylrhodamine isothiocyanate
UV	Ultraviolet
VIC	Aortic valve leaflet interstitial cells
α -SMA	Alpha smooth muscle actin

Amino Acid	Abbreviation	Single-Letter Code
Alanine	Ala	A
Arginine	Arg	R
Asparagine	Asn	N
Aspartic Acid	Asp	D
Cysteine	Cys	C
Glutamic Acid	Glu	E
Glutamine	Gln	Q
Glycine	Gly	G
Histidine	His	H
Isoleucine	Ile	I
Leucine	Leu	L
Lysine	Lys	K
Methionine	Met	M
Phenylalanine	Phe	F
Proline	Pro	P
Serine	Ser	S
Threonine	Thr	T
Tryptophan	Trp	W
Tyrosine	Tyr	Y
Valine	Val	V

ABSTRACT

Growing replacement tissues and organs in the laboratory will revolutionise healthcare; however, the maturation of cells into functional tissue constructs requires the controlled presentation of biochemical factors within a mechanically suitable scaffold. In nature, the presentation of such signals is provided through factors and structures existent within the nanoarchitecture of the extracellular matrix (ECM); therefore, in tissue engineering there is significant need to develop dynamic advanced artificial tissue constructs capable of mimicking the complexities of the native ECM. The requirement for bioactive, innervated constructs that contain biologically relevant signals delivered through tuneable mechanisms has yet to be achieved.

One approach to address this key-challenge is offered through bioprinting, which allows for the controlled spatial distribution of bioinks containing cells, structures and signals within a single printed construct. However, currently bioprinting applications are severely limited by bioink function – with the majority of bioinks either lacking sufficient mechanical properties or biochemical signalling. Therefore, there is a key need to develop bioinks which adequately mimic the native ECM on a nanostructured, chemical level – particularly in establishing effective control over cell fate and tissue innervation.

Tissue composition and extracellular signalling varies substantially between tissue-types, and therefore, advanced approaches that allow for ease of mechanical and biological tuneability through modular mechanisms would provide a practical avenue for bioink development. Self-assembling peptides (SAPs) are a unique class of biomaterials capable of spontaneously forming simple biomimetic structures which entangle to form highly hydrated, bioactive networks with favourable conditions for cell maturation. These biomaterials are easily tuned through modification of amino acid sequence, enabling tailored control over biochemical signalling between cells and scaffold. This provides the ability to artificially replicate natural signalling in a controlled manner – bringing about desired cell behaviour. Using these peptides, a variety of synergistic ECM-protein analogues have been developed, including Fmoc-FRGDF containing fibronectin's attachment motif RGD, and Fmoc-DIKAV,

containing laminin's attachment motif IKVAV. Fmoc-SAPs possess the ability to be further functionalised through macromolecule addition, allowing for the presentation of charged, developmentally or structurally-important macromolecules on the surface of peptide fibrils. These macromolecules can integrate with the peptide networks, facilitating additional signalling and allowing for mechanical tunability.

Here, we take advantage of these properties to develop an advanced and dynamic bioink for bioprinting applications. Initially, material enhancement is investigated through development of multi-sequence scaffolds. Specifically, Fmoc-FRGDF is combined with a synergistic cell attachment motif PHSRN, either through sequence engineering (Fmoc-FRGDFPHSRN) or through control over assembly properties (Fmoc-FRGDF/Fmoc-PHSRN coassembly). Here, the coassembled (Fmoc-FRGDF/Fmoc-PHSRN) system forms a synergistic network which promotes the attachment, proliferation and migration of muscle cells *in vitro*. The potential of Fmoc-SAP multi-sequence scaffolds is further investigated through the development of an artificial tumour microenvironment for cancer-cell studies. Here, Fmoc-FRGDF is combined with Fmoc-DIKVAV and used as a spheroid (LLC, NOR-10, LLC + NOR-10) micro-environment. The coassembled Fmoc-FRGDF/Fmoc-DIKVAV microenvironment enhances cancer-cell growth and progression compared to 2D cultures, non-encapsulate spheroids, and spheroids encapsulated in agarose. Agarose was selected as a control owing to the similar physical properties yet lack of biofunctionalisation. Results from this study reinforce the potential of Fmoc-SAPs as advanced microenvironments, and further support the ease of biological functionalisation inherent with this material.

Further scaffold functionalisation is investigated through macromolecule addition. Here, one of two macromolecules are coassembled into a Fmoc-FRGDF network. The first macromolecule is fucoidan, a seaweed-derived polysaccharide with known anti-inflammatory properties, while the second is versican, a developmentally important proteoglycan which plays a variety of roles in muscle development. Versican was selected owing to its charge similarity to fucoidan, yet vastly different biological function. Fucoidan addition was found to increase fibre bundling and alter hydrogel mechanical properties, while versican addition had no substantial effect on hydrogel mechanics when

compared to an Fmoc-FRGDF empty-vector control. Cell morphology was substantially altered by macromolecule addition, with fucoidan samples resulting in smaller, rounder cells with fewer multinucleated syncytia compared to an Fmoc-FRGDF control, while versican hydrogels showed an initial decrease in cell-size and multinucleation after 24h and a comparable cell-size and multinucleation following 72h. Here, it is possible that macromolecule addition perturbs cells attachment, and therefore, macromolecule selection is a key consideration. Interestingly, the regain of cell morphological characteristics in versican-containing hydrogels following 72h indicates the ability of cells to break-down versican, while the maintenance of small, round cells in the fucoidan hydrogels shows an inability for cells to break down fucoidan.

The ability of Fmoc-SAPs to form components in bioinks is investigated through assembly with gelatin methacryloyl (GelMA) macromolecules. Initially, GelMA nanostructure and mechanical properties are investigated in response to increased degree of methacrylation or increased control. Here, structure-function relationships are drawn, and 18% methacryloyl Gelma (LM-GelMA) is selected for further bioink development owing to favourable thermoresponsive viscoelastic properties and improved strain tolerance. LM-GelMA assembly with coassembled Fmoc-FRGDF/Fmoc-PHSRN is investigated as a potential avenue to develop biologically and mechanically tuneable hydrogels. The incorporation of Fmoc-SAPs allows for control over sequence selection, while control over mechanical properties is offered through GelMA inclusion. LM-GelMA/Fmoc-FRGDF/Fmoc-PHSRN (FPG-Hybrid) bioinks demonstrate enhanced printability and are shown to support primary myoblast differentiation. The potential of Fmoc-SAP/GelMA bioinks to act as a modular bioink toolkit is further investigated through Fmoc-FRGDF/Fmoc-PHSRN substitution with Fmoc-DIKVAV, to develop a neural-suitable bioink (DIKVAV-Hybrid). This DIKVAV-Hybrid bioink demonstrated unique mechanical morphological properties and is shown to support rat cortical neurosphere viability.

Throughout this project, the networks have been vigorously characterised through various analytical techniques, including micro/nanoimaging (Transmission electron microscopy, Atomic force microscopy, Cryo-scanning electron microscopy), Small-angle X-ray scattering, Small-angle neutron scattering, rheology, and spectroscopy; while the overall effectiveness of these systems have been

analysed through *in vitro* muscle and neural cultures. Work detailed through this thesis aims to vigorously characterise Fmoc-SAP hydrogels and bioinks, providing the foundations for further biological studies and material optimisation.

Chapter One:

INTRODUCTION

1.1 Problem Statement

Natural and synthetic biomaterials have long been investigated in their potential to recapitulate the native extracellular matrix (ECM) accurately and subsequently promote healthy tissue development. The ability of these materials to provide artificial cellular microenvironments to transplanted cells provides significant promise for regenerative medicine and tissue engineering applications. However, material development remains a key challenge, with few materials adequately mimicking the complexities of the native cellular microenvironment.

1.2 Background

The ECM is a protein-rich microenvironment which supports cells and provides signals controlling cellular behaviour. These signals may be mechanical or biochemical, both of which are crucial for adequately differentiating cells down the desired lineage and toward healthy tissue development.¹ Furthermore, the natural architectures existent in the ECM play a key role in regulating nutrient/oxygen diffusion and cell fate.²⁻³ As such, biomaterials are required to demonstrate high biomimicry in regard to mechanical, biochemical, and morphological characteristics, all while being consistent (between batches), biodegradable, biocompatible (with non-cytotoxic degradation products), and immunogenic.⁴⁻⁶

Hydrogels are biomaterials characteristic in their high hydration and similarity to the natural ECM. Self-assembling peptides (SAPs) are a unique class of hydrogels formed through the spontaneous immobilisation of surrounding fluid through the formation of larger structures from short peptide building blocks.⁷ These materials are highly advantageous for tissue engineering applications owing to their simple synthesis (through routine peptide synthesis practices), high mechanical tuneability, and ability to incorporate bioactive amino acid motifs.⁷ Furthermore, these materials are inherently biocompatible as they are formed from amino acids, making them readily degradable *in vivo*.⁷ Fluorenylmethoxycarbonyl (Fmoc)-SAPs have grown substantial interest of late owing to their ability to take advantage of π - β assembly and subsequently facilitate self-organisation through π - π stacking between Fmoc-groups and antiparallel β -sheet formation between short peptide sequences.⁸ This allows for self-assembly of peptide sequences which are significantly shorter than other SAP types and therefore enables relatively simple control over mechanical properties and biological functionality.⁹ Furthermore, the short nature of these peptides allow for ease of synthesis, ultimately resulting in a highly versatile, low-cost material.⁹

Controlling extracellular architecture is another important consideration which can influence cell fate. The mechanisms of self-assembly in nature are similar to those experienced by SAPs; consequently, the resultant nano/microarchitectures of the fabricated artificial matrix are highly reminiscent of the native ECM.¹⁰ Control of scaffold micro/macrostructure is another critical consideration. Advances in additive manufacturing techniques have enabled the bioprinting of cell-laden constructs capable of providing a spatiotemporal presentation of biological and physical cues to cells in a multicomponent structure.¹¹ Despite this, material development for bioprinting applications remains a key challenge.

1.3 Project Significance

Preclinical trials using cell replacement therapy has shown substantial promise for the treatment of many conditions.¹²⁻¹⁴ The range of applications for these therapies include cartilage repair,¹⁵ skeletal muscle regeneration,¹⁶ myocardial infarction,¹⁷ lung disease,¹⁸ burn treatment,¹⁹ and neuronal repair.²⁰ This technology is rich in potential for improving patient quality of life, with studies demonstrating that if therapeutic cells transplanted into the damaged tissue manage to survive, they integrate within the host tissue and provide symptomatic relief. However, one of the major limitations has been the restricted availability of appropriately specified cells suitable for transplantation and unacceptably high rates of cell death following transplantation.

Current tissue engineering approaches fail to adequately model the complexities of cell-ECM interactions required for effective cell proliferation and differentiation; furthermore, the lack of an advanced matrix which can easily be co-implanted to foster the transfer and integration of cells in an inflammatory environment severely limits the utility of this approach.²¹

Inspired by this challenge, this thesis investigates the development of an advanced, biomimetic SAP-based scaffold, through tailored control of bioactivity, mechanical properties, and deposition technique. We seek to develop design protocols for increasing Fmoc-SAP bioactivity; while enhancing material suitability for emerging deposition technologies through the development of Fmoc-inspired bioink toolkits that can be used for multiple tissue types and demonstrate ease of mechanical and biological customisation. We show that bioactivity of Fmoc-hydrogels may be increased through the inclusion of multiple bioactive sequences and developmentally important biomacromolecules, resulting in a more comprehensive model of the ECM. Furthermore, we show enhanced structural properties enabled through the inclusion of structurally advantageous macromolecules, resulting in the development of hybrid, Fmoc-inspired bioinks which facilitate cell viability, attachment, migration, and proliferation. Moreover, the multi-component nature of these hybrid materials allows extensive tuning of bioactive properties through sequence selection and ease of mechanical customisation through macromolecule modification.

1.4 Project Aims

Research Aim: To control the supramolecular assembly of peptides, proteins and polysaccharides to create a bioinspired, multicomponent, nanostructured biomaterial that can present multiple signals to mimic the structure/function relationship of living systems to advance *in vitro* cell culture technologies.

Breaking this aim down further provides the following deliverables:

Deliverable 1: Engineer SAPs that form nanostructured scaffolds to present multiple bioactive sequences to mimic the ECM more effectively

Deliverable 2: Use supramolecular interactions to incorporate structurally and developmentally important macromolecules to the matrix, improving its mechanical and chemical properties.

Deliverable 3: Develop SAP-inspired bioinks demonstrating enhanced printability and suitable long-term shape fidelity.

Deliverable 4: Implement bioprinting technologies to fabricate complex three-dimensional (3D) constructs conducive to cellular survival, proliferation, and differentiation.

1.5 Thesis Outline

This thesis focuses on the use of Fmoc-based SAPs as versatile tissue-engineering biomaterials, with a particular focus on improving scaffold bioactivity and mechanical tunability through the introduction of multiple cell-recognised motifs and biomacromolecules. Furthermore, this thesis aims to build on understandings of macromolecule interactions and subsequently develop bioink toolkits through the development of SAP-based hybrid hydrogels.

The thesis begins with a literature review in **Chapter 2** to highlight current research in biomaterial development, Fmoc-SAPs design, bioink development, and deposition techniques (including bioprinting). **Chapter 3** provides a comprehensive account of the materials and methods used throughout the thesis. **Chapter 4** details the development of multi-sequence bioactive scaffolds, and in particular the development of Fmoc-SAP hydrogels containing synergistic epitopes, RGD, and PHSRN. **Chapter 5** investigates the use of a coassembled Fmoc-FRGDF/Fmoc-DIKVAV hydrogel as a 3D cancer model. **Chapter 6** focuses on further functionalising SAP hydrogels through the introduction of structurally and developmentally essential macromolecules. **Chapter 7** investigates gelatin modification through functionalisation with methacryloyl groups, analysing structure-function relationships in response to peptide concentration and degree of functionalisation (DoF); then, **Chapter 8** builds on these findings to develop novel SAP-based bioinks which demonstrate optimised printability. **Chapter 9** investigates the ability of these bioinks to be used in neural tissue engineering applications, demonstrating the efficacy of this approach for use as a modular bioink toolkit. Finally, **Chapter 10** acts as a concise review of the thesis, summarising the project before **Chapter 11** discusses future direction. The **Appendix** provides supplementary information not detailed elsewhere.

Chapter Two:

LITERATURE REVIEW: BIOPRINTING AND BIOFABRICATION WITH PEPTIDE AND PROTEIN BIOMATERIALS

2.1 Preview

We introduce cell-therapy based techniques and subsequently discuss biomaterial source with emphasis on peptide and protein-based biomaterials for 3D tissue engineering applications. Methods for controlling scaffold deposition are highlighted, including hydrogel casting, electrospinning, and bioprinting. Biomaterials intended for bioprinting applications are discussed thereafter; following which we review frontier application-specific bioprinting approaches; highlighting printing technique and material design. Finally, we summarise essential findings and expected future direction.

Publications Relevant to chapter:

Boyd-Moss, M., Fox, K., Brandt, M., Nisbet, D., & Williams, R. (2017). Bioprinting and Biofabrication with Peptide and Protein Biomaterials. In *Peptides and Peptide-based Biomaterials and their Biomedical Applications* (pp. 95-129). Springer, Cham.¹¹

Abstract The ability to fabricate biomimetic artificial tissue constructs through the controlled organisation of cells, structures and signals within a 3D scaffold offers significant promise to the fields of regenerative medicine, drug delivery and tissue engineering. Advances in additive manufacturing technologies have facilitated the printing of spatially defined cell-laden artificial tissue constructs

capable of providing a biomimetic spatiotemporal presentation of biological and physical cues to cells in a designed multicomponent structure. Despite significant progress in the field of bioprinting, a key challenge remains in developing and utilising materials that can adequately recapitulate the complexities of the native ECM on a nanostructured, chemical level during the printing process. This necessitates materials capable of establishing effective control over cell fate and innervation; with recent investments focusing on the development of candidate materials from protein and peptide-derived biomaterials. The ability of these materials to form highly printable hydrogels which are reminiscent of the native ECM has seen significant use in a variety of regenerative applications, including organ bioprinting and non-organ bioprinting. Here, we discuss current and emerging technologies for tissue engineering applications, with a particular focus on bioprinting and the development of peptide-based bioinks. Furthermore, this work highlights application specific, peptide-based bioprinting approaches and provides insight into current limitations and future perspectives of peptide-based bioprinting techniques.

2.2 Introduction:

Regenerative medicine and tissue engineering are rapidly advancing fields which aim to replace functional tissue which may have been lost to disease, trauma or congenital anomalies.²² A key challenge for researchers is the requirement to develop an advanced tissue engineered scaffold capable of adequately mimicking the complexities of the native ECM; providing the necessary behaviour cues to cells while promoting angiogenesis to enable the delivery of nutrients to developing tissue while facilitating waste removal.²³⁻²⁵ To achieve this, multidisciplinary techniques and insight from engineering, chemistry, material science, nanotechnology and biology are required to enable the tailored design of biomimetic scaffolds. These highly structured materials must reproduce aspects of the natural tissue environment; for instance, having the capacity to simultaneously provide both physical support and biologically relevant molecules to cells. Effective materials are required to mimic the native ECM, resulting in active promotion and regulation of regenerative cell behaviours, including survival, migration, proliferation, and differentiation down appropriate lineages.²⁶

The native ECM is a protein-rich, 3D microenvironment responsible for providing much of the structure and signalling of tissue while maintaining hydration and homeostatic balance.²⁷ This non-cellular constituent of tissue and comprises two main components; the fibrous network and the interstitial fluid. The relative proportion of fibrous ECM proteins to interstitial fluid differs between tissue types; as does the proportions of each different fibrous protein type, and is dependent on the functional and physical requirements of the tissue, with many tissue microenvironments having a very low proportion of solid material ²⁸.

The ECM fibrous network is formed from macromolecules secreted from epithelial and stromal cells and includes collagen, elastin, laminin, fibronectin, and proteoglycans (**Figure 2-1**); providing tissue with structural architecture, physical signalling and stress resistance. Collagens are the most abundant fibrous protein in the ECM¹. Secreted by fibroblasts; collagen gives the bulk physical structure and tensile resistance of the ECM, while providing physical signals through cryptic bioactive motifs ²⁹. Furthermore, collagen forms binding partners with many of the ECM proteins, strengthening the ECM.³⁰ The physical and bioactive signalling of collagen provides cues relating to cellular migration and adhesion; both of which are essential for viable tissue growth and development.

Another major structural protein existent within the ECM is elastin, which provides tissue with recoil and elasticity. Multiple crosslinked tropoelastin subunits form mature elastin fibres; which are secreted by endothelial cells, chondroblasts and fibroblasts ^{31, 32}. To avoid overstretch and maintain integrity, glycoproteins (predominantly fibrillins) coat elastin fibres, while collagen fibrils form binding partners with elastin and limit stretch under severe stress ^{30, 33}. Laminins are another structural protein existent within the ECM; these proteins provide

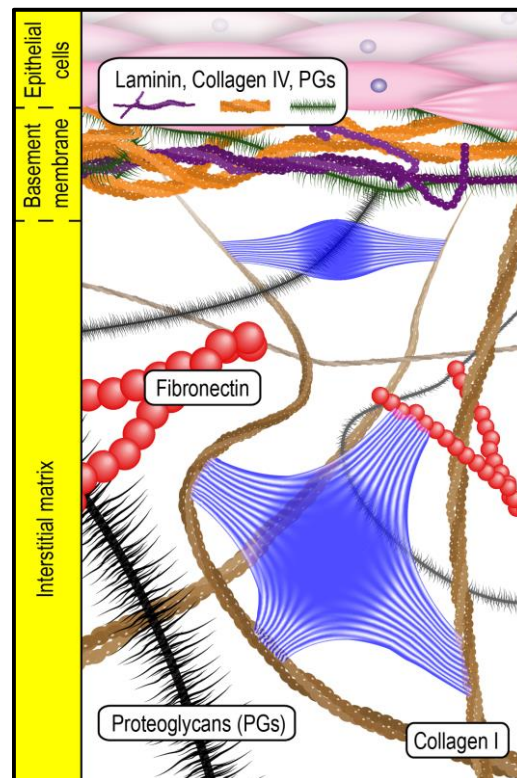


Figure 2-1 – Artistic depiction of native extracellular matrix showing fibrous proteins and proteoglycans.

signalling to cells while aiding in tensile stress resistance.³⁴ Three laminin subunits (α , β and γ) form laminin, which when constructed, form a cross-like pattern; this structure allows the laminins to bind to other laminins and ECM proteins.³⁵ Within laminin lies the cell signalling motif, IKVAV, which facilitates cell communication through integrin-mediated pathways; providing environmental cues to cells – particularly neural cells.³⁶ Laminins are a major component in basement membranes, which allow cell anchorage.^{30, 33} Heparin sulphate proteoglycans (HSPGs) are proteoglycans found within the ECM with multiple heparan sulphate side chains. HSPGs can bind to various structural proteins through protein-protein interactions, heparin sulphate-protein (HS-protein) interactions or interactions with heparin sulphate chains. Furthermore, HSPGs also bind to growth factors, where they are later presented or ‘cleaved and released’ to receptors³⁰. Fibronectin is another essential glycoprotein secreted by fibroblasts. This fibrous macromolecule binds to numerous ECM proteins and integrins, and plays a key role in intercellular signalling thorough bioactive sequence presentation - including synergistic cell attachment sequences Arg-Gly-Asp (RGD) and Pro-His-Ser-Arg-Asn (PHSRN).^{30, 37}

The interstitial fluid component of the ECM primarily consists of glycosaminoglycans (GAGs), growth factors, water and electrolytes.³⁸ One particular GAG, hyaluronic acid (HA), is a non-proteoglycan polysaccharide, which acts to hydrate cells and proteins existent within the ECM microenvironment. HA provides tissues with resistance against compressive stresses through the absorption of water resulting in swelling.³⁹ Proteoglycans are also involved with the uptake of water and binding of growth factors, all contributing to the interstitial fluid component of the ECM.⁴⁰ The non-fibrous portion of the ECM acts as a buffer and a growth factor reservoir, while resisting compressive stresses applied to tissues and organs. The combination of the interstitial fluid component with the fibrous protein network results in a complex stress resistant system ideal for healthy cell growth.

The biological and mechanical characteristics of the native ECM differs significantly between tissue types, suggesting there is no ‘one size fits all’ solution, therefore, careful consideration of biological and mechanical properties is required when engineering biomaterials for tissue engineering applications. There are three key aspects which dictate the effectiveness of a tissue engineering

approach; these being: 1) Cell selection, 2) Material design, and 3) Deposition technique. Cell selection is an obvious yet essential consideration; not only must cell type be carefully considered, but so too cell seeding density, as cell-cell interactions are vital for successful control of cell behaviour.⁴¹⁻⁴³ Material design must consider biological and physical signalling, including motif presentation, material stiffness, and material nano/microarchitecture.⁴⁴⁻⁴⁵ Moreover, the material source is an important consideration, with various materials available from natural, synthetic, and semi-synthetic sources – all of which have respective advantages and disadvantages.¹¹ Deposition technique allows for control over biomaterial spatial deposition; here, a key focus is bioprinting technique, owing to the high spatial temporal control inherent with these systems. Ultimately, an advanced biomaterial must protect cells during the deposition technique (e.g. bioprinting), while providing suitable biological and mechanical signals to promote desired cell-fate within a cytocompatible environment.

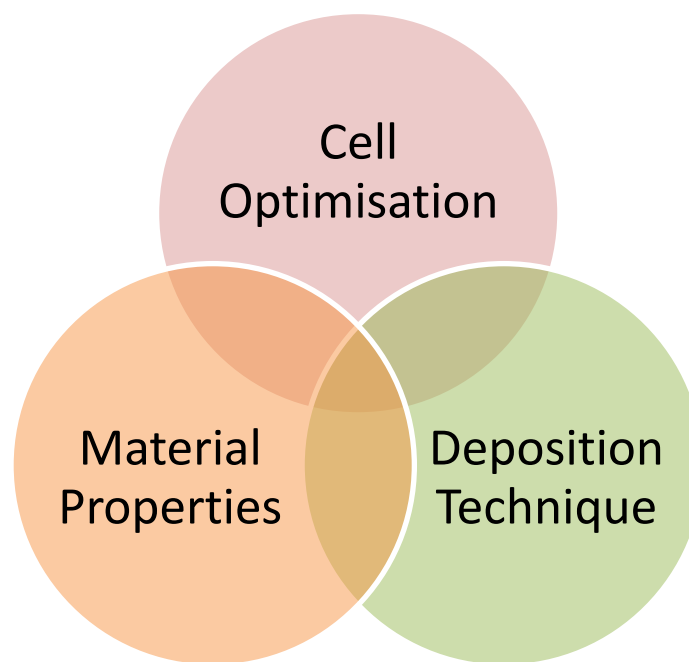


Figure 2-2 – Considerations for ideal biomaterial design.

2.3 Cell-Therapy-based Techniques

Despite efforts of self-repair, the human body is limited in its potential to replace tissue lost to damage or disease. In most cases where cell function is disrupted, the innate ability of self-repair in mature tissue is insufficient.⁴⁶ Regenerative medicine aims to remedy these shortcomings resulting in sufficient and desirable tissue repair; one promising avenue is offered through cell therapy.

Cell therapy aims to repair, replace or enhance tissue which has been damaged or lost to disease or trauma.⁴⁷ Here, isolated and well-characterised cells are transplanted into damaged sites, where cells ideally integrate with host tissue achieving improved tissue repair. However, for cell therapy to be successful, careful consideration must be placed into cell type and seeding density.^{43, 48} The success of cell therapy is dependent on effective integration of multiple fields, including biology, immunology, tissue-engineering, molecular biology, material science, and transplantational biology, and requires clinical expertise relating to the disease being treated.⁴⁶ Therefore, a comprehensive tissue engineering approach not only focuses on cell isolation, characterisation, and transplantation; but also on artificial environment design, deposition, and engineering.

2.3.1 Artificial Three-Dimensional Microenvironments as Native Extracellular Matrix Mimics

Two-dimensional (2D) cell culture practices have been traditionally used for *in vitro* cell and drug research, however, the efficiency of such practices have been called into question as the environment is quite far removed from tissues native, *in vivo* state.⁴⁹ Therefore, 3D culturing techniques have become increasingly popular as of late owing to a greater ability to mimic the native ECM. Similarly, complex cell therapy approaches require more than just isolated cell transplantation; as such, the enhancement of biomaterials to better mimic the native ECM is a growing area of frontier research. These ECM mimics can be broadly placed into three classes: natural, synthetic, or semisynthetic.

2.3.1.1 Natural

The native ECM contains a variety of fibrous proteins and polysaccharides which provide both structure and biochemical support to tissue.²⁷ Natural peptide/protein-based hydrogels are extensively used in tissue engineering and regenerative medicine due to their high bioactivity which provides suitable

chemical, physical, and biological signals essential for supporting cell responses including survival, adhesion, differentiation and proliferation.⁵⁰ These materials also provide favourable degradation properties and are capable of producing hydrogels with high biocompatibility and biodegradability;⁵⁰ yet present a risk of pathogen transfer, immunogenic reaction and batch-to-batch variance.^{51 52}

In tissue engineering and regenerative medicine, the central aim of scaffold development is to recapitulate the ECM. As such, many studies use physical, chemical and enzymatic processes to remove cellular content from tissue and yield a decellularised extracellular matrix (dECM).⁵³⁻⁵⁴ Other common protein-based biomaterials including collagen, gelatin, fibrin, and fibroin/fibrinogen are discussed further below.

Animal Sourced Decellularised ECM

To address the shortcomings of conventional tissue and organ transplantations, current research focuses on developing scaffolds of greater biocompatibility, resulting in reduced immunological rejection. As such, the use of dECM materials in tissue engineering applications has gained significant momentum due to their inherent ability to mimic the complexities of the native ECM; providing signals and structure to developing tissue. Currently, there is no gold standard decellularisation process, rather a variety of processes exist which may be categorised as chemical, physical, or biological.⁵⁵ Chemical decellularisation processes make use of chemical agents, including acids and bases, hypotonic and hypertonic solutions, detergents, alcohols, and other solvents; physical processes take advantage of temperature, force and pressure, and non-thermal irreversible electroporation; whilst biological processes may employ enzymatic agents or non-enzymatic agents, including chelating agents, toxins, serum and serine protease inhibitors.⁵⁶ The effectiveness of decellularisation is dependent on tissue source, density, organisation, composition, and finally, the desired final use of the tissue or organ.⁵⁵⁻⁵⁶

An alternative approach focuses on the development of highly hydrated networks using lyophilised dECM tissue which is ground into a powder before subsequent dissolve in solution. These hydrated networks - or hydrogels - have become increasingly popular in soft tissue engineering applications due to their innate ability to maintain cell hydration and homeostatic balance. The ability

of hydrogels to absorb incredibly large amounts of water arises from hydrophilic functional groups attached to the polymeric backbone, while their resistance to dissolution arises from crosslinks between network chains.⁵⁷ Hydrogels developed from dECM do not retain the 3D ultrastructure of the native tissue, but still maintain *in vitro* and *in vivo* biologic activity, and thus, still retain much of the functional complexities of their tissue origin.⁵⁸⁻⁵⁹

The use of dECM tissue provides significant promise to tissue engineering applications; either as whole decellularised tissue constructs or as hydrogels. The use of whole decellularised constructs which retain the ultrastructure of tissues may be highly beneficial when considering full organ replacement; while dECM hydrogels may be of greater benefit when gels need to conform to specific shapes or fill voids. Despite the potential promise of this class of material, there are still significant issues relating to batch-batch variability and dECM composition.

Collagen and Gelatin-based Biomaterials

Similar to dECM-based hydrogels, collagen and gelatin-based hydrogels have been extensively investigated in tissue engineering applications due to their inherent biocompatibility, adhesive qualities, high porosity, high tensile strength and biodegradability; however their lack of rigidity, batch-to-batch variability and immunogenicity concerns limit their applicability in tissue engineering applications.⁶⁰⁻⁶¹ There are at least 19 different types of collagens existent in the native ECM; however, collagen type I is most extensively used in tissue engineering applications owing to its abundance and biocompatibility.^{4, 62} Collagen has a unique structure in which three individual polypeptide chains twist to form a 3-stranded rope-like structure.⁶³ Partial hydrolysis of collagen breaks down this structure into single-stranded, gelatin molecules.⁵⁰ Despite being denatured, gelatin can retain relevant moieties, including important cell attachment motifs such as Arg-Gly-Asp (RGD) sequences.⁶⁴ Crosslinking of collagen and gelatin hydrogels is enabled through the use of glutaraldehyde, genipin, or water-soluble carbodiimides; or non-covalently through the entanglement of fibres.^{4, 50} Collagen is enzymatically degraded through collagenase and serine protease, allowing for local degradation controlled by cells present in the ECM.⁴

Gelatin may be further chemically modified through the addition of methacryloyl (methacrylamide and methacrylate groups) side groups, resulting in biofunctional materials of high mechanical tuneability which is reminiscent of a collagen-rich native ECM.⁶⁵ The resulting material, gelatin methacryloyl (GelMA), facilitates covalent crosslinking – typically through (photo)radical-initiating systems and enzymatic crosslinking.⁶⁵ In contrast to enzymatic crosslinking, photo-crosslinking offers high spatial and temporal control over the crosslinking process.⁶⁶ GelMA has demonstrated incredible promise for regenerative engineering applications, including bone,⁶⁷ cartilage,⁶⁸ muscle,⁶⁹ and vascular tissue engineering.⁷⁰

Hyaluronic Acid

Hyaluronic acid (HA) (also known as hyaluronan) is an anionic, non-sulphated linear GAG composed of repeating disaccharide units of D-glucuronic acid and N-acetylglucosamine⁶¹. The abundant negative charges allow HA to absorb a substantial quantity of water, enabling expansion up to 1000 times its solid volume and consequently, the formation of a loose hydrated network with limited stability⁷¹. This viscoelastic ECM protein is readily modified to permit the tuning of physical and biological properties, including solubility, degradation rate, viscosity and amphiphilicity.⁷² HA modification is performed through photopolymerization, enzyme-catalysed crosslinking, and Michael addition to form hydrogel structures.⁶¹ HA naturally interacts with several cell surface receptors (hyaladherins) which are involved in regulation of growth factor signalling and metabolism; however, HA is unable to bind with adhesion receptors such as integrins and therefore offers poor adhesion properties. HA is slowly degraded by hyaluronidase and can be modified with various chemical groups and polymers to incorporate cell-adhesion ligands, protease-sensitive sequences, and signalling molecules for protein retention, increasing the adhesion and altering the degradation properties of the biopolymer^{61, 73}. Hydrogels developed from this protein are an attractive option for tissue engineering applications owing to their non-immunogenicity, biocompatibility, biodegradability, ease of chemical modification, cost-effectiveness, targeting properties and high availability.⁷²⁻⁷³ Moreover, HA is highly versatile and as such has been widely used in a diverse range of applications, from surgery to tissue engineering.^{61, 72}

Fibrin/Fibrinogen

Fibrinogen is a soluble plasma protein which is converted to insoluble polymeric fibrin in response to vascular system damage, initiating clotting at the wound site.⁷⁴ The conversion of fibrinogen to fibrin is initiated by the serine protease thrombin (factor IIa) which plays a crucial role in haemostasis, inflammation and wound healing.⁷⁵ Fibrin is a significant component of the provisional ECM formed during tissue repair following injury, and enables cell infiltration and anchoring at the wound site.⁷⁶ Fibrin clots allow platelet, leukocyte and fibroblast infiltration and adherence in wound sites enabling natural wound repair; this, combined with the ease of fibrinogen purification from blood has resulted in fibrin development for a number of applications⁷⁶ - including tissue engineering,⁷⁷ drug delivery⁷⁸ and clinically as a tissue sealant.⁷⁹ The provisional fibrin matrix also provides a physically supportive network to the wound site before eventually being replaced by natural ECM proteins, including collagen and fibronectin to form new tissue.⁸⁰

Fibroin

Fibroin is a natural fibrous protein existent in silk spun by silk-producing arthropods, including silkworms and spiders.⁸¹ Fibroin is one of two main proteins of silk. The other protein, sericin, is usually processed out of the natural material through alkali- or enzyme-based degumming processes. The composition of silk fibroin is dependent on its source. Silk fibroin sourced from *B. mori* is composed of a heavy (H) and a light (L) chain linked together by a disulphide bond, and another glycoprotein (P25) is also non-covalently linked to these chains;⁸² these fibroin proteins can form anti-parallel β -sheets.⁸¹ Alternatively, silk produced by non-mulberry Saturniidae do not contain L chain or P25; instead, they contain H-chain homodimers;⁸³ forming β -sheets due to the higher Ala/Gly ratio and poly-alanine blocks.^{81, 83} Silk fibroin offers numerous advantages for use as a biomaterial including its excellent inherent mechanical properties, good biocompatibility, biodegradability, ease of processing and ease of modification.⁸¹ As such, these materials have been used for the regeneration of a variety of tissues, including bone,⁸⁴⁻⁸⁵ tendon,⁸⁶⁻⁸⁷ and cartilage.⁸⁸⁻⁹⁰

Chitosan

Chitosan is a linear polysaccharide derived from natural chitin – an abundant protein found in the exoskeletons of many crustaceans.⁹¹ Chitosan is non-toxic, stable, biodegradable and sterilisable; making it exceedingly versatile for an extensive range of applications. The insolubility of unmodified chitosan at neutral pH necessitates further modification for use in hydrogel synthesis. Modification of chitosan involves the formation of carboxylate salts, such as formate, acetate, lactate, malate, citrate, glyoxylate, pyruvate, glycolate, and ascorbate.^{50, 92} The deployment of unique crosslinking mechanisms enables chitosan gels to have tailored porosities, mechanical strengths and dimensions; allowing for a highly engineered natural scaffold. Finally, chitosan elicits no immunogenic response; making it extremely desirable for tissue engineering applications.⁹²

Plant-Sourced

Agarose

Agarose is a natural, seaweed-sourced polysaccharide polymer which demonstrates unique characteristics beneficial to tissue engineering applications. Hydrogels developed from this natural carbohydrate polymer have resemblances to the natural ECM, are highly hydrated, show excellent biocompatibility, and demonstrate unique thermo-reversible gelation properties.⁹³ Furthermore, the controllable permeation of oxygen and nutrients through agarose scaffolds, combined with its inherently inert structure, has seen significant use in tissue engineering applications – as both an artificial scaffold and drug delivery vehicle.⁹³⁻⁹⁴ However, the lack of bioactivity in agarose hydrogels have also restricted its use in tissue engineering applications, resulting in poor cell-material interactions; therefore, agarose hydrogels are often combined with other natural or synthetic hydrogels to develop biomaterial blends.⁹³

Alginate

Alginate is an abundant protein isolated primarily from brown seaweed. Alginate is a highly biocompatible, non-immunogenic, hydrophilic unbranched polysaccharide which gels gently through ionic binding between divalent or trivalent cations and guluronic-acid rich blocks.⁵⁰ This mild gelation method makes gels highly suitable for encapsulation of cells, proteins and peptides, minimizing trauma while allowing the controlled release of growth factors and signalling molecules.

Unfortunately, alginate is not naturally biodegradable in mammals; this leads to a poorly regulated degradation pathway.⁹⁵⁻⁹⁶ Moreover, cells have no specific receptors for binding to alginate, and as such unmodified alginate offers poor cellular adhesion properties.⁹⁶ Mechanical properties of the hydrogel can be controlled through alteration of physical factors including crosslinking density, crosslinker type, molecular weight distribution, gelation temperature and chemical modification of the polymer. Degradation may be improved through gamma-irradiation of alginate, ‘mismatching’, and partial oxidation; all of which work through the weakening of bonds within the polymer yielding enhanced degradation.⁹⁶ To encourage cell adhesion to the scaffold, alginate can be functionalised through coupling of ECM proteins including laminin, collagen and fibronectin. However, the coupling of whole proteins to alginate is difficult to control and can lead to non-specific interactions.⁹⁶⁻⁹⁷ Therefore, as an alternative, the bioactive epitope, RGD, may be bound to alginate through carbodiimide chemistry to offer a specific means to control cell adhesion while maintaining high specificity.⁹⁶ The addition of the RGD motif has been shown to encourage myoblasts adherence, proliferation, and diffusion through a modified RGD-alginate scaffold; while a further study by the same author demonstrates control over myoblast phenotype through alteration of RGD motif concentration.^{97,98} Alginate hydrogels are soft and have been shown to have shear shielding effects on cells which they encompass during extrusion;⁹⁹ making them a highly sought after natural hydrogel material.

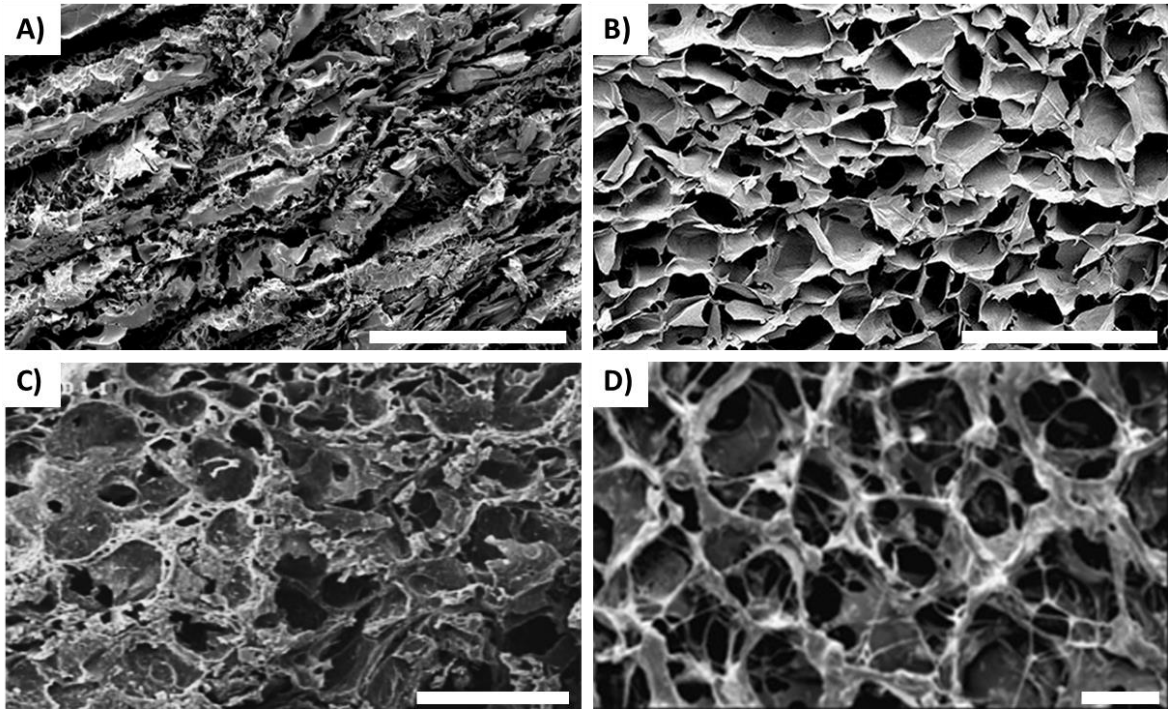


Figure 2-3 – Microstructure of tissue and common biomaterials as observed under SEM. A) Sectioned skeletal muscle (Scalebar = 500 μm), B) Porcine muscle-derived decellularised ECM (dECM) (Scalebar = 500 μm), C) Collagen/Gelatin Blend (Scalebar = 600 μm), and D) Alginate (Scalebar = 100 μm). Reproduced with permission from^{100,101} and ¹⁰²

2.3.1.2 *Synthetic*

Compared to natural hydrogels, synthetic hydrogels demonstrate higher water absorption capabilities and have more controlled structures.^{51, 57} These materials are also consistent between batches and demonstrate high chemical and physical tuneability.^{4, 103} Conversely, synthetic hydrogels are less biocompatible and less bioactive compared to natural hydrogels.¹⁰³ Commonly used synthetic biomaterials include poly(caprolactone), poly(ethylene glycol), poly(lactic acid), poly(propylene fumarate) and poly(vinyl alcohol).

Poly(caprolactone)

Poly(caprolactone) (PCL) is a synthetic polyester of semi-crystalline structure which has been granted FDA approval for use in medical devices and drug delivery applications.¹⁰³ PCL demonstrates excellent biocompatibility and is extensively used in bone-tissue engineering applications;¹⁰⁴⁻¹⁰⁵ and may be degraded under physiological conditions through microorganism, hydrolytic, enzymatic, or intercellular mechanisms.⁵¹ However, use of PCL in tissue engineering applications has been limited owing to its considerably slow degradation time.¹⁰³

Poly(ethylene glycol)

Modification and copolymerization of the widely used synthetic polyether compound, poly(ethylene glycol) (PEG), results in the development of a variety of different hydrogels. Through specific modifications, favourable mechanical properties may be introduced into the hydrogel; specifically, photo-crosslinked and temperature-responsive PEG hydrogels may be synthesised through the modification of PEG with known degradable polymers, such as acrylates or methacrylates and poly(lactic acid) (PLA) or poly(lactide-co-glycolide) (PLGA) respectively.⁵⁰ PEG hydrogels have also been synthesised through the grafting of enzyme sensitive molecules such as tyramine, to enable enzyme-mediated crosslinking.⁵⁰ Crosslinked PEG hydrogels have been used in tissue engineering scaffolds wherein cells or signalling molecules and factors are encapsulated; as such, PEG has successfully been used for the encapsulation of islet cells, chondrocytes, fibroblasts and stem cells.¹⁰⁶ Recently, the use of a degradable PEG scaffold (PEG-PLA) has seen successful encapsulation of HA;

through degradation of the scaffold, HA is released to bovine chondrocyte cells, resulting in significantly higher cell numbers than the HA-free control following four weeks culture.¹⁰⁷

Poly(lactic acid) and Poly(lactic-co-glycolic acid)

PLA and PLGA are thermoplastic aliphatic polyesters which have been approved for certain human clinical applications by the FDA.¹⁰³ These materials have been extensively studied and have shown significant promise in health and tissue engineering applications, owing to their suitable mechanical strength and favourable biodegradability.¹⁰³ Furthermore, their extended release rates spanning from days to months provides substantial application for biotherapeutic delivery.¹⁰⁸ Degradation rates and products can be tuned via alteration of composition, structure and molecular weight of polymers, with degradation usually a result of hydrolysis of ester groups in their backbones.⁵¹ These materials can form biocompatible scaffolds which are frequently used in cartilage and bone engineering applications.¹⁰³

Poly(vinyl alcohol)

Similar to PEG, Poly(vinyl alcohol) (PVA) is a hydrophilic synthetic polymer which has been widely explored for various tissue engineering and regenerative medicine applications. The formation of hydrogels from PVA involves crosslinking through either physical, chemical or radiation methods.¹⁰⁹ Physical crosslinking employs a freeze-thaw process, where repeated freeze-thawing cycles of the aqueous polymer leads to crosslinking and subsequently hydrogel formation. Chemical crosslinking may be performed through the addition of organic aldehydes to produce a hydrogel structure; while crosslinking through radiation may be done via γ -ray and electron-beam irradiation.⁵⁰ Due to the possible toxicity of hydrogels produced through chemical or radiation methods, many authors prefer physical and photo-polymerisation crosslinking.¹⁰⁹⁻¹¹¹ Effective crosslinking yields a biocompatible hydrogel which is mechanically tuneable, tough, and elastic, while maintaining a high water content.^{109, 111-113} Furthermore, PVA hydrogels are easily fabricated and sterilized, have the ability to attach to a variety of molecules, and through correct tailoring of mechanical properties, may be able to mimic the physical architectures of a variety of soft tissues.^{109-110, 112} However, PVA demonstrates poor cell adhesion and resists protein absorption, and therefore cells seeded onto the unmodified hydrogel display

low proliferation rates.^{112, 114} Nevertheless, PVA has a high abundance of hydroxyl pendant groups on its backbone which, through modification, provides sites available for the attachment of bioactive molecules including growth factors, adhesion proteins, and other molecules of biological importance.^{52, 113-114} The covalent linkage of biological factors or amino-acid motifs to create a functionalised scaffold adequately promotes cell attachment, proliferation and migration, and provides a method to mediate biospecific cell attachment.^{109, 111-112, 114}

Poly(propylene fumarate)

Poly(propylene fumarate) (PPF) is a linear, unsaturated, hydrophobic polyester which undergoes degradation through hydrolysis of the ester linkage to form propylene glycol and fumaric acid by-products.¹¹⁵ Fumaric acid is a naturally occurring product of the tricarboxylic acid (TCA) cycle, and as such is biocompatible; while propylene, also known as 1,2-Propanediol is metabolised by the body and is commonly used as a drug diluent in pharmaceutical applications.¹¹⁶ Hydrogel formation of PPF can occur when synthesised as a block copolymer with PEG and crosslinked either chemically¹¹⁷⁻¹¹⁸ or through photo-crosslinking.¹¹⁹⁻¹²¹ Alginate-PPF hydrogels have also been developed to create a hybrid biosynthetic tissue engineering scaffold material.¹²²

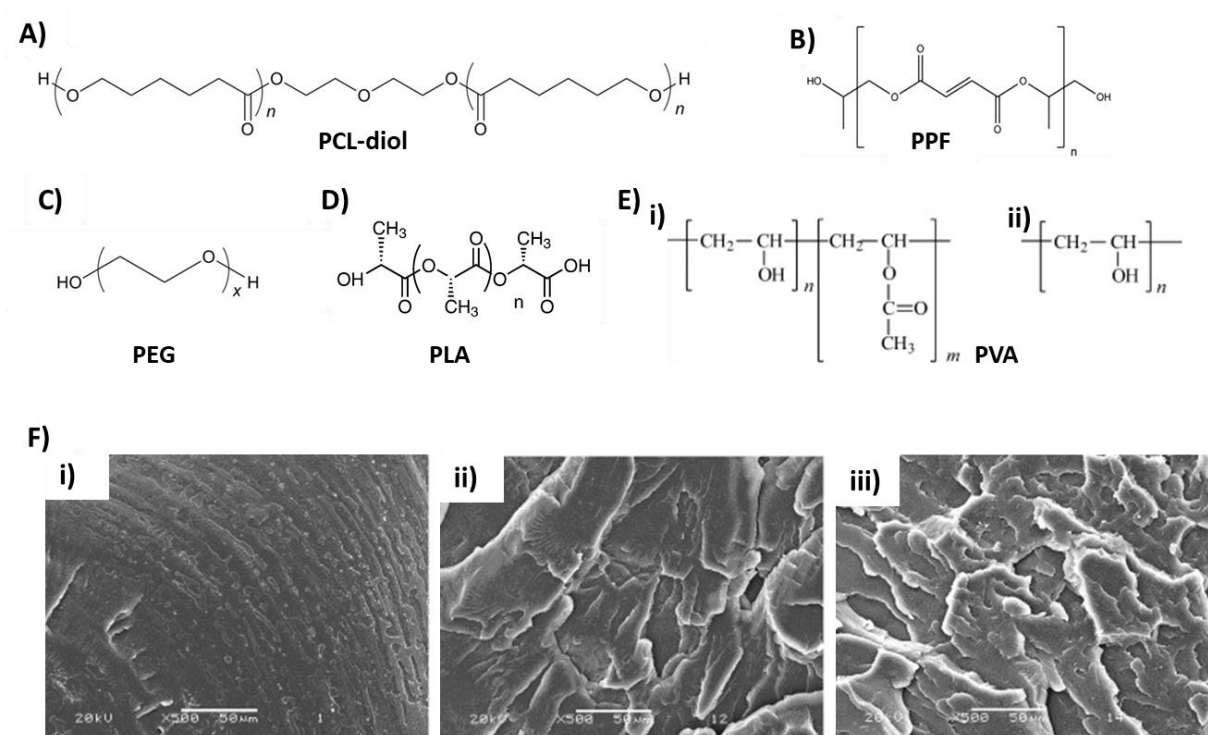


Figure 2-4 – Structure of Synthetic Biomaterials. (A-E) Chemical Structure of A)PCL-diol, B) PPF, C)PEG, D)PLA, and E) PVA in i) partially hydrolysed and ii) fully hydrolysed form. F) SEM observation of Poly(lactic-acid) hydrogel microstructure with different triallyl isocyanurate (TAIC) and dicumyl peroxide (DCP) crosslinker concentrations. i) PLA alone, ii) PLA + 1.0% wt. TAIC and 1.0% wt. DCP, and iii) PLA + 3.0% wt. TAIC and 1.0% wt. DCP. Reproduced with permission from ^{123-126 127}

2.3.1.3 *Semi-synthetic*

Semi-synthetic materials include synthetically sourced natural peptide-based materials and synthetic protein analogues. The primary focus of this section will be on novel self-assembling peptides.

Self-assembling Peptides

In nature, biological molecules self-organise into larger hierarchical structures to fulfil and perform a specific purpose, similarly SAPs are a class of bioinspired materials capable of forming complex biomimetic structures through the spontaneous self-assembly of low-molecular-weight peptide sequences.²⁶ The ability of SAPs to spontaneously form hydrogels containing intricate nanofibrous networks, combined with their ability to be synthesised through standard peptide synthesis approaches has resulted in success in tissue engineering applications.¹²⁸ As these peptides are synthesised from amino acids, they are inherently biocompatible and demonstrate good biodegradability.⁷ Mechanically, SAPs offer high tuneability; while biological functionalisation may be incorporated through the addition of well-known bioactive motifs.¹²⁸ One particular advantage of these materials is their ability to undergo reversible shear thinning, making them highly suited to minimally invasive tissue engineering and drug delivery applications, particularly when loaded with cells.^{24,129} Semi-synthetic SAPs include peptide amphiphiles (PAs), lipid-like peptides, and aromatically-capped peptide derivatives.

Peptide Amphiphiles

PAs are unique bioinspired molecules consisting of two distinct regions: 1) hydrophobic aliphatic tail of variable length (usually between 12-16 carbon alkyl subunits in length), and 2) a hydrophilic biofunctional head-group attached to the tail via an amide bond.⁷ Under aqueous conditions, aliphatic tails aggregate driving assembly and resulting in high-presentation of peptide portions displayed on the surface of the structure.¹³⁰ Depending on the sequence employed, self-assembly can be triggered via manipulation of pH or ionic concentration enabling supramolecular ordering into a variety of architectures including nanotapes,¹³¹ ribbons,¹³¹⁻¹³² fibrils,¹³¹ fibres,^{131, 133} and helical ribbons.^{7, 134}

PAs tail organisation leads to the self-assembly of nanofibrous architectures similar to cylindrical micelles where the hydrophobic tails pack in the core of the fibre while hydrophilic peptide

portions are expressed in high affinity on the surface of the structure.¹³⁰ These compounds presented on the surface can be cell targeting through extracellular targeting ligands, receptor-specific peptides, or antibodies; enabling control of cell fate.¹³⁵ PAs can be further functionalised through electrostatic interactions with macromolecules or other oppositely charged PAs – yielding hierarchically ordered networks.¹³⁶ The nature of PA systems allows for use in both tissue engineering and drug delivery, wherein a high concentration of peptide may be delivered to the target (60-90% introduced concentration).¹³⁵

Unfortunately, many PAs still lack control over thickness, composition, and structure, as well as the functional dynamic nature and structural complexity found in the biological systems which limit many biological applications.¹³⁶ Furthermore, PAs are synthetically complex which yields high costs for synthesis – ultimately limiting the potential for large scale production.⁷

Aromatically-capped Peptide Derivatives

Aromatically-capped peptide derivatives are a class of SAPs containing short peptide sequences paired to aromatic side-chains. These materials take advantage of π -interactions to drive self-assembly, resulting in the formation of biomimetic structures.⁸ Research in recent years has focused on protecting peptides with N-fluorenylmethoxycarbonyl (Fmoc) groups. One system which has been illustrated is that of Fmoc- di-phenylalanine (Fmoc-FF) which forms a hydrogel under physiological conditions.^{8, 137} Di-phenylalanine (FF) without Fmoc-protection has been shown to form elongated tubular structures in the presence of an organic solvent,¹³⁸ however FF is unable to form supramolecular structures under biological conditions without the addition of an inorganic solvent.⁷ The addition of a Fmoc-group to the N-terminal has been shown to enable spontaneous self-assembly using a pH switch method under physiological conditions.^{7-8, 137} This self-assembly is driven by a combination of π - π stacking between aromatic side-chains and β -sheet formation between short peptide sequences.¹³⁹ The combination of several of these interactions results in the formation of elongated nanofibrils. These nanofibrils then interact with each other, forming larger, branched fibrous bundles through supramolecular ordering; which further entangle to highly hydrated networks.⁷ The true novelty of these hydrogels, however, is their ability to present amino acid sequences in high density, facilitating biochemical signalling and

enabling biofunctionality through interaction with cell-surface receptors.^{26, 140-141} Recently, the resultant self-assembled structure of this peptide is also found to be influenced by charge, allowing for charge induced α -helix transition, potentially providing advance in the therapy of neurological diseases through the inhibition of β -sheet aggregation.¹⁴² Research performed by Modepalli and coworkers focused on introducing the fibronectin-derived cell-attachment motif RGD to the extensively studied peptide Fmoc-FF, resulting in the development of Fmoc-FRGDF. The addition of the cell-attachment motif was found to promote fibroblast attachment and enhance cell viability when compared to a scrambled sequence Fmoc-FDGRF, highlighting the ability to functionalise these peptides with bioactive motifs.¹⁴³

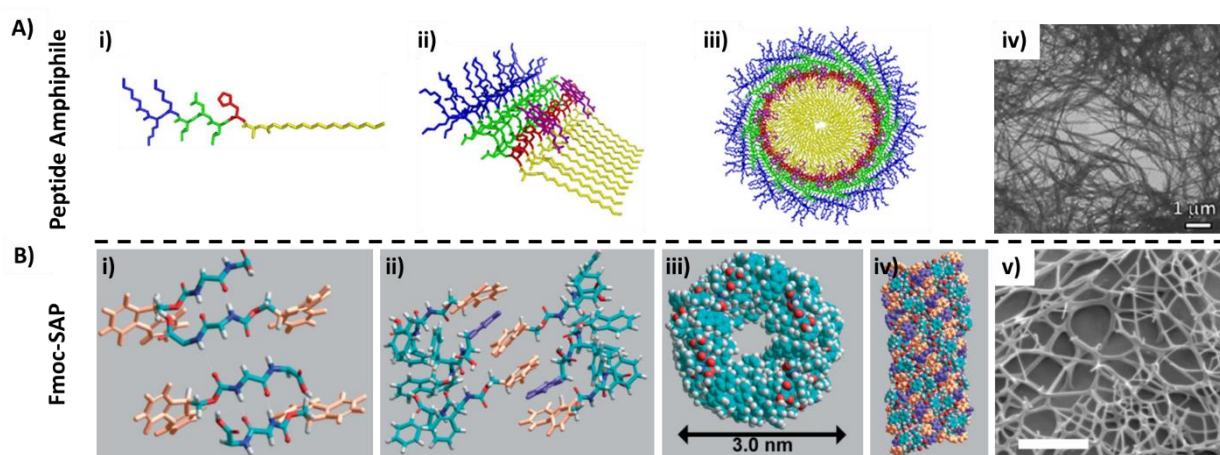


Figure 2-5 – Peptide self-assembly mechanisms of A) Peptide amphiphiles (c16-AHL₃K₃-CO₂H) showing i) peptide monomer showing lysine (blue), leucine (green), histidine (red), alanine and c16 (yellow), ii) β -sheet organisation ((PPIX)Zn in purple, showing ability to incorporate functional molecules) iii) Schematic of formed fibril cross-section showing hierarchical organisation, iv) TEM showing resultant fibrillar network formation. (scalebar 1 μ m) B) Fmoc-SAP (Fmoc-FF) showing i) anti-parallel β -sheet organisation, ii) π - π stacking of fmoc-groups, iii – iv) formation of nanofibrils and v) CryoSEM showing network formed (scalebar 10 μ m). Reproduced with permission ^{8, 144}

2.4 Techniques.

Further to material design, material deposition technique is of crucial consideration, with various deposition techniques available each with their respective benefits and shortcomings. Through control of deposition techniques, the macro- and microstructure of tissue engineered scaffolds can be tuned. Common material deposition techniques including casting, microinjection, electrospinning, and bioprinting are discussed further below.

2.4.1 Casting

Hydrogel casting is the most straightforward material deposition technique which forms the basis for preliminary biomaterial testing. Here, the material is deposited within a mould or culture plate and cells are either seeded on top or are encapsulated within the material. Casting provides a simplistic way of culturing tissue *in vitro* and allows for material testing regarding bioactivity and cytotoxicity. Despite the simplicity of this approach, material properties including porosity, material stiffness, signalling availability, and nutrient diffusion profile need to be well understood. Using casting approaches, bioactive properties of a range of materials has been tested, including materials intended for muscle¹⁴⁵ and cartilage regeneration.¹⁴⁶

2.4.2 Microinjection

Microinjection allows for minimally invasive material deposition *in vivo*. Microinjection is a simple technique where the material is passed through a needle and delivered to the site of interest. Materials intended for microinjection must be both biologically suitable (incorporating similar properties to cast materials), and must allow for adequate shear-thinning and recovery of structure post-injection.¹⁴⁷ Furthermore, these materials are required to protect encapsulated cells during the injection process. Microinjection techniques also need to consider needle diameter and flow-rate, as increased shear-stress is known to result in decreased cell-viability.¹⁴⁸ Microinjection is a fundamental technique from which various other material deposition techniques build on – including various bioprinting and electrospinning approaches.

2.4.3 Electrospinning

Electrospinning is a unique deposition technique which takes advantage of electrostatic forces to drive material extrusion. A typical electrospinning setup consists of several basic components, these being: a spinneret, a high-voltage power supply, a syringe pump, and a grounded collector.¹⁴⁹ During electrospinning, a high voltage difference is placed between the spinneret and a collector plate. Next, the syringe pump pushes material to the outlet of the spinneret; here it forms a small droplet (Taylor cone) which is influenced by the electric field created as a result of the high voltage difference.¹⁴⁹⁻¹⁵⁰ The electric field induces a charge on the spinning solution, resulting in a charge repulsion force which is directly opposite to the droplets surface tension force.¹⁵⁰ Upon raising the electric fields' intensity past a critical value, the repulsive force overcomes material surface tension forces, resulting in material expulsion from the spinneret toward the collector.¹⁵⁰ This jet of material undergoes a change in material state (usually from solution to gel or solid) resulting in the formation of a fibrous network on the collector plate. Nanofibre morphology can be altered through modification of electrospinning process properties (electric potential, flow-rate, needle to collector distance and, collector shape and composition), materials parameters (viscosity, conductivity, surface tension, molecular weight, and concentration of material), and/or ambient parameters (humidity, temperature).¹⁵¹ Spinneret design also influences fibre morphology which has driven the development of various spinneret types, including single-nozzle, double-/multi-nozzle, co-/multi-axial, multi-channel, flat, cylinder, and disk spinnerets.¹⁴⁹ Using these spinnerets, a range of fibres have been created, including core-shell, triaxial, multichannel, and Janus fibres.¹⁴⁹ Collector selection allows for control over network architectures, with a variety of collector types available, including traditional grounding plate, 3D columnar, helical spring-shaped, parallel electrodes, patterned, rotating drum, and rotating disk collector.¹⁴⁹ Using these collectors, networks can be designed with random orientation or aligned nanofibers. Electrospun scaffolds have similar architectures to the native ECM, and can be modified to include bioactive signalling; and as such have found success in a range of tissue engineering applications, including bone,¹⁵² cartilage,¹⁵³⁻¹⁵⁴ muscle,¹⁵⁵ cardiac¹⁵⁶ and nerve regeneration.^{151, 157-158} Electrospun scaffolds

have also found use in drug-delivery applications – particularly as a means of controlling drug release profiles.¹⁵⁹

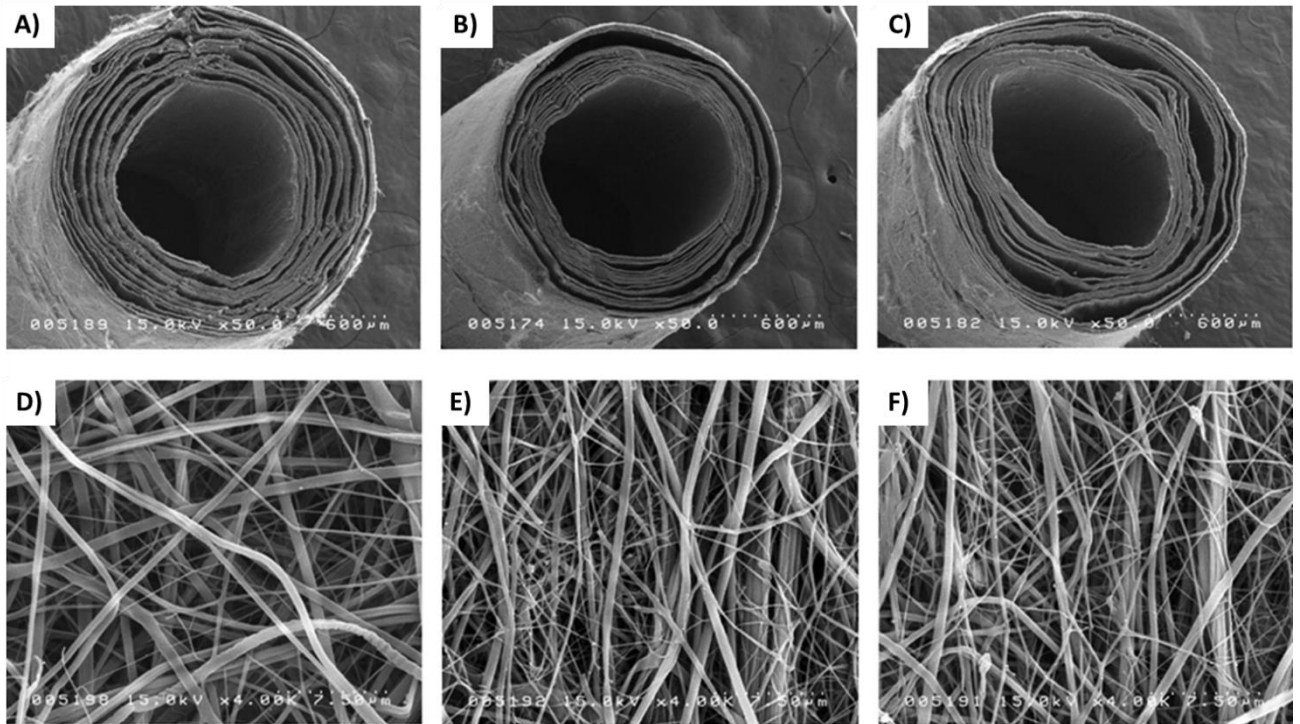


Figure 2-6 – Tubular Electrospun chitosan nanofibrous scaffolds for nerve regeneration. Top: Tubular structures formed from A) Non-orientated chitosan fibres, B) orientated chitosan fibres, C) Bi-layer chitosan scaffold with orientated fibres on the inside and non-orientated on the circumference. Bottom: Magnified inner tubular surface showing D) non-orientated construct network morphology, E) orientated network morphology F) Bi-layer construct with orientated inner surface. Reproduced with permission from ¹⁵⁸

2.4.4 Bioprinting

The recent advancements of additive manufacturing technologies, material science, and cell biology have brought forth the ability to print complex artificial tissue-engineered scaffolds through bioprinting.¹⁶⁰ This technology enables the precise placement of structural and biologically suitable materials containing living cells, biochemicals, and biologically relevant molecules within a well-defined geometry.¹⁶⁰ The ability of these printed tissue scaffolds to have spatially defined regions of different material enables previously unachievable fabrication of tissue constructs capable of providing the necessary behavioural cues to cells, while also facilitating vascular network generation.¹⁶¹ Currently several bioprinting techniques are being employed for the printing of tissue constructs based on commercially available or modified printers, including inkjet bioprinting, extrusion bioprinting, laser-assisted bioprinting, and stereolithography-based bioprinting. **Figure 2-7** (A) shows an idealised cartoon of the ability to present multiple cell types in a defined fashion with excellent fidelity.

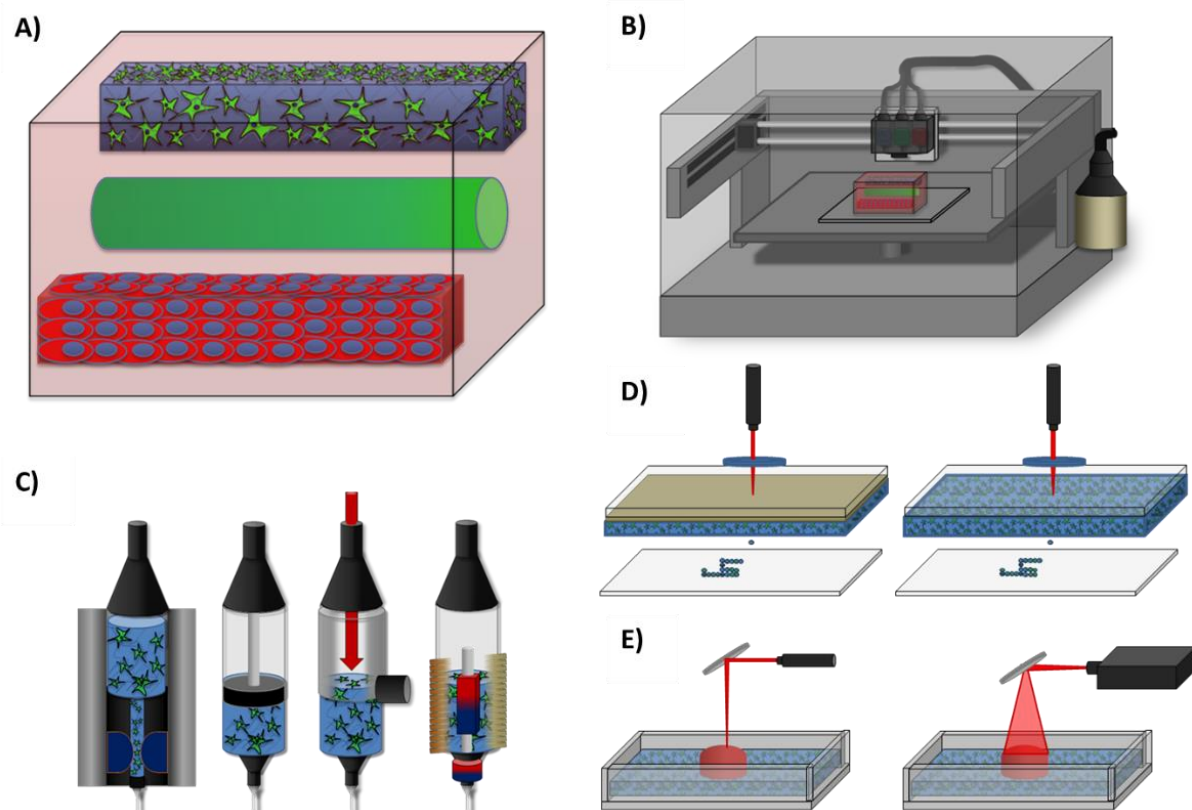


Figure 2-7 – Schematic showing working principles, bioprinting systems, and outcomes. A) Cartoon of multi-component tissue construct showing different cellular and structural regions; top neural cells, middle rigid component, bottom blood vessel. B) Basic bioprinter; C) Inkjet printhead workings showing actuator in dark blue, Mechanical printhead showing plunger configuration, Pneumatic-driven printhead showing compressed air input with valve, and solenoid printhead showing solenoid valve (left to right); D) AFA-LIFT laser-assisted bioprinter (left), MAPLE-DW laser-assisted printer (right); and E) Beam-scanning SLA (left), Mask-image projection SLA (right). Reproduced with permission from ¹¹

Developments in nanotechnology and microfabrication have led to advances in additive manufacturing, enabling the ability to fabricate micrometre scale scaffolds and control the spatial distribution of cells more accurately than before.¹⁶² Among these developments lies the advanced biofabrication technique of bioprinting, which enables the printing of cell-laden inks, distinguishing this method from traditional additive manufacturing techniques in which the processing parameters were typically too harsh to support cell viability.^{160, 162} The ability to print 3D, cell-embedded artificial tissue construct allows for highly intricate scaffold development, opening the possibilities for successful and complex tissue engineering approaches that were previously unavailable. Ultimately, bioprinting has the potential to (1) Create fully functional replacements for damaged or missing tissues in patients, and (2) Rapidly fabricate small-sized tissue models or organoids, for diagnostics, pathology modelling, and drug delivery.¹⁶³

Figure 2-7(B-E) shows schematic versions of each of these approaches. In bioprinting, the spatially controlled, layer-by-layer deposition of biological materials, biochemicals, and living cells yields 3D tissue constructs.¹⁶⁰ There are four necessary steps to this process: (1) a computerised 3D solid model is developed and converted to a suitable file format; (2) the file is then sent to the bioprinter for manipulation to control part orientation and scaling; (3) the structure is printed through layer-by-layer deposition, and finally; (4) maturation, where the materials undergo tissue culture conditions either *in vivo* or in a bioreactor^{160, 164} Different printing techniques depend on vastly different material dispersion mechanisms.¹⁶⁵ The four predominant bioprinting techniques currently being used for tissue engineering applications are inkjet bioprinting, extrusion bioprinting, laser-assisted bioprinting, and stereolithography-based bioprinting.¹⁶³ **Table 2-1** provides an overview of these techniques with references for further reading.

Table 2-1 - Bioprinting processes showing working principle, materials, advantages and disadvantages.

Bioprinting Process	Technique	Working Principle	Materials	Advantages	Disadvantages	References
Inkjet-based	Thermal-based	Thermally-vaporised bubble-induced pressure.	Low viscosity hydrogels and bioinks (relatively volatile)	High-speed printing, Cost-effective, Widely available	Require relatively volatile materials Thermal and mechanical stresses, Low droplet directionality, Nonuniform droplet size, Prone to clogging, Unreliable cell encapsulation	166-160
	Acoustic-based	Acoustically induced force (piezoelectric through actuator volume change, ultrasound through ultrasound field)	Low viscosity hydrogels and bioinks	Controlled droplet size and direction, No thermal stress	High Frequency induced cell damage and possible lysis	160
	Electrostatic-based	Actuator volume change through electrostatically induced pressure plate movement	Low viscosity hydrogels and bioinks	No thermal stress Stable over a variety of materials	Difficulty controlling droplet size	167-168
Microextrusion-based	Pneumatic-driven	Air-pressure driven extrusion (valve-free and valve-based)	Low viscosity hydrogels and bioinks	Very high precision and accuracy Simple mechanisms Force limited only by pressure capabilities of the system	Possible delay due to compressed gas movement Compressed gas/air must be sterile Increased system cost as accuracy increases	160, 169
	Mechanical-driven	Mechanical-induced pressure-driven flow (screw and piston)	High viscosity hydrogels and bioinks	Direct control over bioink flow Able to facilitate high viscosity hydrogels Affordable, portable, easy to program, great special control	Careful gear selection for screw-based approaches due to increased pressure and pressure drops along the nozzle Lower force capabilities	160, 169
	Solenoid-based	Pressure-driven flow controlled by a solenoid valve	Low viscosity hydrogels and bioinks	High accuracy (>1 μ L drops) Advantageous for low viscosity inks particularly with ionic or UV-irradiation based crosslinking mechanisms	Time delays between actuation and opening/sealing. Vulnerable to factors affecting accuracy and reproducibility. Particularly affected by change in material temperature yielding a change in viscosity.	169-170

Laser-based	Laser-guided Direct flow	Laser-controlled optical-trapping enabling biological molecule positioning	Limited materials with low-reflective index.'	Simple mechanism	Requires high actuation pressure to force material through open valve Low cell viability Low throughput Low-range of fabrication potential Movement efficiency greatly affected by material refractive index	171-174
	Matrix-assisted pulsed laser evaporation direct-writing (MAPLE-DW)	Localised laser-induced pressure change resulting in hydrogel and cell deposition from 'ribbon' (hydrogel-coated) onto substrate	Non-transparent bioinks/hydrogels with cell coating.	Low-powered lasers	Potential for UV induced cell damage. Ineffective with optically transparent inks	160, 174-176
	Absorbing film-assisted laser-induced forward transfer (AFA-LIFT)	Localised laser-induced pressure change resulting in bioink deposition from 'ribbon' (film-coated) onto substrate	Moderate range of bioinks.	Offers UV protection to bioinks Can print transparent bioinks	Potential film-derived contamination.	160, 174-176
Stereolithography-based (SLA-based)	Beam-scanning	Photopolymerisation of bioinks through spatial control of scanning laser beam resulting in photosensitive ink irradiation and subsequent layer-by-layer deposition on build platform.	Photosensitive bioinks	Very High accuracy	Defocusing issues Risk of damage to cells (UV and chemical from photoinitiator) High costs	164, 166, 177
	Mask-image-projection	Photopolymerisation of bioinks through mask-controlled light irradiation, resulting in a layer-by-layer deposition on build platform.	Photosensitive bioinks	High accuracy prints Rapid printing (Whole layers at once)	Mask-associated challenges (accuracy, costs) Risk of damage to cells (UV and chemical from photoinitiator) High costs	164, 166, 177

2.5 Peptide-based Bioinks

2.5.1 Biomaterials for Bioink Development

Bioprinting allows the controlled deposition of biomaterial print-blends containing living cells in a liquid or hydrogel suspension, which are termed ‘bioinks’.¹⁷⁸ Ideally, bioinks should form tuneable, biocompatible scaffolds with desired mechanical strength, rigidity, and shape fidelity; should resemble the native ECM; and should facilitate large scale synthesis with minimal batch-to-batch variation.¹⁷⁹ Furthermore, bioinks are required to protect cells from shear stresses while maintaining printability and nutrient transport post-printing.¹⁸⁰ Understanding the biological, chemical, and mechanical requirements of cells is crucial for successful tissue growth while understanding the material properties of bioinks is essential for ensuring printability, biocompatibility, and suitable biodegradability.¹⁸¹

The study of bioink material science is of particular interest for biological and engineering fields, including drug delivery, tissue engineering, and regenerative medicine.¹⁸² Peptide and protein-based biomaterials, in particular, have been extensively researched for use in tissue engineering applications, due to their highly favourable inherent biological properties.⁵

Natural hydrogels are used extensively in tissue engineering applications due to their inherent biological properties; however challenges exist relating to batch-to-batch variation, risk of immune response and pathogen transfer.^{51-52, 128} Synthetic hydrogels provide good mechanical properties, high tuneability, and present no immunological concerns;^{51, 183} however generally demonstrate poor biodegradation and limited bioactivity unless modified.¹⁸⁴⁻¹⁸⁵ Semi-synthetic SAPs are engineered from versatile molecular building blocks which under appropriate conditions, spontaneously organise to form an entangled nanoscale scaffold. These are easily synthesised through standard peptide synthesis approaches such as solid-phase peptide synthesis (SPPS).⁷ The inherent biocompatibility and biodegradability of these molecules, combined with their batch-to-batch consistency and ease of synthesis have resulted in this material showing promise for biomedical applications.⁷

2.5.2 Peptide and Protein-Based Hydrogels

Peptide and protein hydrogels are formed through the entanglement of typically nanofibrous structures which immobilise their surrounding solvent to form highly hydrated networks. These biomaterials are promising candidates for bioink formulation, due to their highly hydrated state (99% w/w water of their dry weight), ability to mimic the native tissue ECM, and propensity to undergo shear thinning before returning to their original shape.^{6, 186-187} This combined with their ability to shield cells from stress during printing makes these materials highly sought after for tissue bioprinting applications.¹⁸⁸ Peptide and protein-based biomaterials may be natural (collagen, gelatin, fibrin)⁶¹, semi-synthetic (SAPs),^{141, 189-191} or may form part of a biosynthetic blend (Collagen-PEG, PEG-Fibrinogen).¹⁹²⁻¹⁹³

Table 2-2 gives an overview of these classes of materials and their uses.

Table 2-2 - Peptide-based bioink classification, formulation, and application.

	Base-Material	Bioink	Application	References
Natural	Decellularised ECM	3% Cartilage dECM, hASCs and hTMSCs	Cartilage regeneration	53
		3% Adipose dECM, hASCs and hTMSCs	Fat (adipose) tissue regeneration	53
		3% Heart dECM, Rat myoblast cells (L6)	Cardiac Muscle regeneration	53
	Collagen/gelatin	10% wt. GelMA, 0.6% wt. collagen type I, Ru/SPS (0.2 mM /2 mM), MCF-7	Various tissues, (successful tests using HACs and HSCs	194
		2wt% collagen, 4% wt. alginate, MC3T3-E1	Osteogenic regeneration	195
		2wt% collagen, 4% wt. alginate, hASCs	Various tissues	195
		5% collagen, crosslinked with 1 mM genpin (1h), MG63s, hASCs	Hard-tissue regeneration	196
		5% (w/v) gelatin, HEK-293s, 3U mL ⁻¹ mTgase	Angiogenesis/vasculogenesis	197
	Fibrin and fibrinogen	50 unit mL ⁻¹ thrombin, 80 mM Ca ²⁺ , HMVEC, (Thrombin printed onto fibrinogen biopaper to form fibrin gel)	Angiogenesis/microvascular fabrication	198
	Fibroin	8 wt% Silk Fibroin, 15wt% gelatin, hTMSCs, 500units tyrosine.	Osteogenesis, chondrogenesis.	199
Semi-SyntheticSAPs		10 mg mL ⁻¹ Ac-ILVAGK-NH ₂ , H1ESCs, hMSCs.	Gastrointestinal and skin regeneration	179
		2.24% (w/v) Gelatin + 0.75% (w/v) PA (CH ₃ (CH ₂) ₁₅ VVAAEEIKVAV, or CH ₃ (CH ₂) ₁₅ VVAAEE) + SV40SM Cells	Bile duct formation	200
	HA-Gel-PEG	4 parts 2% Heprasil, 4 parts 2% Gelin-S, 1 part 8% PEGDA, 1 part 8% 8-Arm PEG Alkyne	Liver regeneration (toolkit shows various other tissues)	201
	Gel-PEO	3% gelatin, 2% PEO, HUVECS, HEK-293s, 3U mL ⁻¹ mTgase	angiogenesis/vasculogenesis/various tissue	197

2.5.2.1 Natural

Decellularised Extracellular Matrix

In bioprinting applications, dECM constructs are often lyophilised before being ground into a powder and subsequently used to form a hydrogel.⁵³⁻⁵⁴ Pati et al. have developed application-specific dECM bioinks from decellularised adipose, cartilage and heart tissues.⁵³ Decellularisation of the ECM material is completed through a combination of physical, chemical and enzymatic processes to yield decellularised tissue with a ~98% reduction in cellular contents and only 39 ± 15 , 11 ± 1 and 6.7 ± 1.2 ng of deoxyribonucleic acid (DNA) mg^{-1} of fat, cartilage and heart dECM, respectively. The required amount of ground dECM powder was weighed and solubilised in a solution of 0.5 M acetic acid with 10 mg of pepsin for 100 mg dECM – such that the final concentration of dECM was 3%. Dropwise addition of 10 M cold sodium hydroxide (NaOH) neutralised the pH of the solution to physiological level (7.4). Human adipose-derived stem cells (hASCs) and human turbinate mesenchymal stromal cells (hTMSCs) were used to assess the effectiveness of adipose and cartilage dECM bioinks on adipogenic and chondrogenic differentiation respectively. Rat myoblast cells (L6) were used to verify the functional enhancement of myoblasts in heart-derived decellularised matrix (hdECM) bioinks. Concentrated culture media ($10\times$) was added to the cell-free bioink at 1/10th volume before cultured cells are mixed into the bioinks. Constructs were printed, and cell viability tested following 24h, 7 days, and 14 days of culture. All constructs demonstrated high cell viability (>95%) following 24h culture, and cell viability was maintained above 90% following 7 days and 14 days in culture, with active cell proliferation evident. Analysis of gene expression finds increased expression in chondrogenic (SOX9 and COL2A1), cardiogenic (Myh6 and Actn1) and adipogenic (PPAR γ and LPL) constructs when compared to that of a control collagen bioink. The authors further expand this work through the development of a photo-crosslinkable dECM hydrogel facilitated through addition of a vitamin B2 photoinitiator; resulting in a hydrogel which was approximately 33 times stiffer than the aforementioned dECM bioink.⁵⁴

Collagen and Gelatin

A gelatin-based photo-crosslinkable bioink composing 10% wt. GelMA and 0.6% wt. collagen type I was described by Lim et al.¹⁹⁴ wherein two bioinks are engineered with different photoinitiators; the first contains the photoinitiator Irgacure 2959 (0.05% wt.), while the second contains ruthenium/sodium persulfate (Ru/SPS, 0.2 mM /2 mM). The Irgacure 2959 containing bioink undergoes ultraviolet (UV) light (300-400 nm) enabled crosslinking while the second was crosslinked under visible light (400-450 nm). Using these bioinks, complex, multilayered constructs (dome and human nose) were printed. Breast adenocarcinoma cells (MCF-7) encapsulated within the hydrogels show the visible light system to be superior for bioprinting applications. When light source intensity is held constant (3 mW cm^{-2}), MCD-7 cells demonstrate >80% cell viability in the visual light system after day 1 at the highest photoinitiator concentration (2 mM/20 mM, 15-minute irradiation, 3 mW cm^{-2}) compared to ~45% at day 1 for the highest concentration of Irgacure 2959 (0.5%, 15-minute irradiation, 3 mW cm^{-2}). Similarly, when photoinitiator concentration was held constant at minimal concentration (0.05% for Irgacure 2959 and 0.2 mM/2 mM for Ru/SPS), the visual light maintained a high cell viability of ~90% even under the highest intensity (100 mW cm^{-2}) compared to ~45% for cells placed in the high intensity (100 mW cm^{-2}) UV environment. However, cell viability was sufficiently maintained when extremes were avoided in the UV crosslinked system. Recent research has extensively characterised GelMA - Irgacure 2959 UV crosslinking systems, enabling high cell viability (~91%) through careful control over UV intensity and photoinitiator concentration.²⁰²

Two collagen-based bioinks are developed by Lee et al.¹⁹⁵ The first bioink (CA-1) consists of collagen which has been cultured with preosteoblast cells for 1 day to allow for initial ECM deposition within the collagen bioink; while the second (CA-3) consists of collagen which has been cultured with preosteoblast cells for 3 days to allow for increased ECM deposition. Both inks were formulated as follows: 2% wt. collagen was gelled in an incubator for 30 minutes before preosteoblast cells were cultured on the gelled collagen for various periods (1 day and 3 days). Mixtures were then combined with 4% alginate and cells in equal volumes. Other culture periods were also investigated however culture periods of 1 day and 3 days were found to present the best balance between printability and

bioactivity. A pure alginate bioink was used as the control. An ionic crosslinking method was employed through aerosol dispersion of calcium chloride (CaCl_2) onto printed constructs, facilitating alginate crosslinking. The compressive moduli of the printed inks were found to be 68 ± 15 kPa, 67 ± 13 kPa, and 69 ± 8 kPa for CA-1, CA-3, and alginate respectively. Unfortunately, these moduli were considered too low and therefore had to be reinforced with PCL struts. Initial cell viability was sufficiently high with ~88% viability at day 1. Cell proliferation rates were significantly higher on scaffolds fabricated from CA-3 compared to those fabricated from either CA-1 or alginate. From this study, the collagen/ECM/alginate bioink was found to be effective in simultaneously presenting physical and biological cues required for tissue regeneration. Mechanically, the CA-3 bioink was able to protect cells from processing conditions, while biologically the ECM components of the ink provide a highly active cell-platform when compared to the alginate bioink.

Similarly, Kim et al. develop a collagen-based bioink which uses Genipin as a crosslinking agent.¹⁹⁶ Type-I collagen was mixed at 3, 5, and 7% wt. with cells (MG63s and hASCs) to yield a bioink that was biocompatible and mechanically stable. Printed constructs were crosslinked through structure incubation in 0.1, 0.5, 1, 3 and 5 mM genipin solutions over different periods (1, 6, 24, 48 hours). Of these conditions, 5% collagen crosslinked with genipin at a concentration of 1 mM for 1 hour was found to produce the best results. Using this ink, a cellblock was printed with a cell viability of >95%. *In vitro* testing of the printed construct shows increased viability, cell proliferation, and osteogenic activity compared to constructs printed using a control alginate-based bioink.

A gelatin-based bioink developed by Irvine et al. takes advantage of enzymatic crosslinking through microbial transglutaminase (mTgase).¹⁹⁷ Three gelatin concentrations (3%, 5%, 7%) were investigated. Human umbilical vein endothelial cells (HUVECS) and human embryonic kidney cells (HEK293s) were encapsulated within the hydrogels. Lower concentrations of gelatin showed increased cellular spreading resulting in pseudopodia; while cells in the higher concentration (7%) gelatin bioinks maintained a round shape. Constructs fabricated from bioinks with lower gelatin concentrations lacked sufficient mechanical strength, resulting in the inability to retain the printed structure; subsequently, a 5% gelatin concentration was used for all subsequent printing applications. Using this bioink,

substantial proliferation was achieved, however difficulty remained in controlling shear induced apoptosis immediately following printing.

Finally, Liu et al. reduce GelMA concentration thresholds in bioinks by controlling hydrogel temperature prior to printing. Physical crosslinking was initiated through bioink cooling to 4° C for 20 minutes, enabling the development of GelMA physical gels (GPGs). Using this technique, the authors print stable constructs using substantially lower (3-5% w/v) concentrations compared to previously reported concentration thresholds (7% (w/v)) (**Figure 2-8 A-H**). Following printing, GPGs were covalently crosslinked through subjection to UV light in the presence of a photoinitiator. Printing of GPG bioinks allowed for the formation of hydrogel networks with significantly larger average pore-size as assessed through SEM (**Figure 2-8 I-K**). HUVECs printed within the scaffolds demonstrated enhanced cell spreading compared to high concentration hydrogels with a smaller average pore-size (**Figure 2-8 L-N**).

Together, these studies suggest that gelatin and collagen hydrogels have substantial promise for bioprinting applications owing to their favourable bioactivity and inherent ECM nanoarchitecture, however, care needs to be taken to avoid cell damage during printing and subsequent crosslinking. Specifically, careful consideration needs to be placed into bioprinting conditions (temperature, pressure, shear stress) and crosslinking parameters (photoinitiator, wavelength, concentration, temperature and time). Furthermore, as these materials are animal derived, there is an inherent risk of batch-to-batch variation, and therefore, advanced material approaches should work toward developing synthetic analogues.

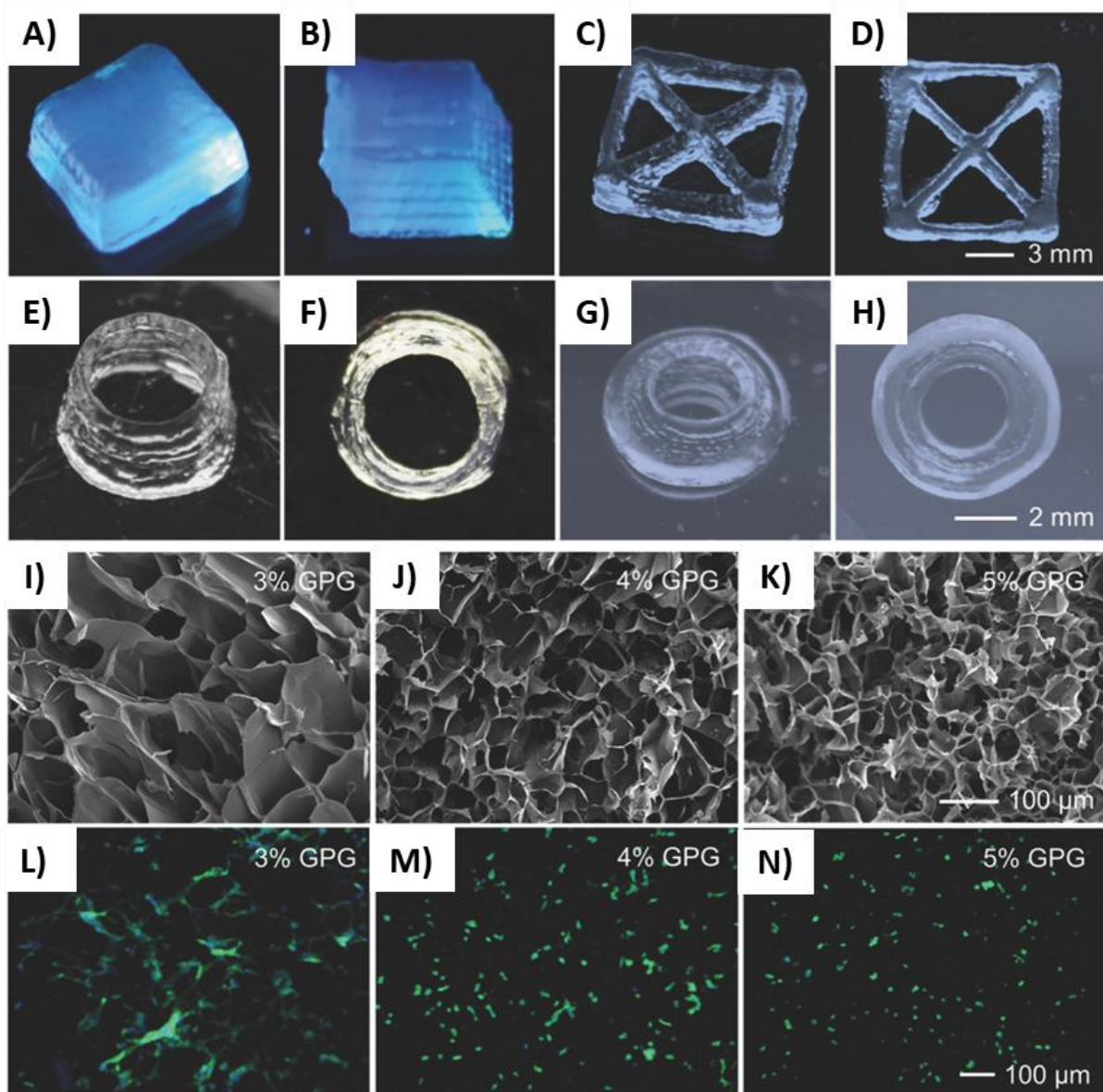


Figure 2-8 – Bioprinted Gelatin-based (GelMA Physical Gels, GPG) constructs showing printed macroscopic shape (4% GPG gels) (A-H), microscale organisation observed via SEM (I-K), and cell spreading (L-N). Printed construct macroscopic shape includes A) cube B) rhombus, C,D) diagonal square (scalebar 3 mm), E,F) a thin-walled tube, and G,H) a cone-shaped tube (scalebar 2 mm). SEM images show nanostructure organisation of I) 3% GPG, J) 4% GPG, and K) 5% GPG (scalebar 100 μ m). Cell-spreading on 3% GPG, 4% GPG, and 5% GPG hydrogels (scalebar 100 μ m). Reproduced with permission from ²⁰³

Fibrin and Fibrinogen

Fibrin-forming hydrogels have recently been investigated for use as bioinks in bioprinting applications, enabling highly effective tissue regeneration owing to fibrins inherent wound healing properties. Xu et al. investigate the effectiveness of fibrin in bioprinting applications through modification of a thermal-based inject printer to allow the layer-by-layer printing of neural (NT2) cells and fibrin gels, enabling the development of 3D cellular structures for use in neural tissue engineering applications..²⁰⁴ Two inks were developed, firstly, a NT2-containing cell ink was formulated through the re-suspension of cultured NT2 neuronal precursor cell pellets in Dulbecco's phosphate-buffered saline solution (DPBS), before secondly, a fibrin gel was formulated by printing bovine thrombin (dissolved in CaCl_2 to yield a final concentration of 20 IU mL^{-1}) onto a thin fibrinogen substrate. Bioinks were deposited in an alternating fashion starting with the fibrin ink. Once printed, this fibrin gel was allowed 3-5 minutes to facilitate fibrin formation before a new cartridge containing NT2 neurons was loaded into the printer and neurons printed on top of the fibrin layer. Another thin layer of fibrinogen was then placed over the printed structure, and the process was repeated. Results showed that this printing method allowed the controlled deposition of patterns and structures of primary hippocampal and cortical neurons while maintaining neuronal phenotypes and basic electrophysiological function.

The group further build on this work formulating a thrombin bioink containing human microvascular endothelial cells (HMVEC) which was printed onto a fibrinogen substrate to form cell-laden fibrin channels suitable for microvascular formulation.¹⁹⁸ Various concentrations of fibrinogen, thrombin and Ca^{2+} were investigated, and an optimal formulation was selected such that the final bioink contains: 1-8 million HMVEC mL^{-1} , 50 unit mL^{-1} thrombin, and 80 mM Ca^{2+} in $1\times$ DPBS. This bioink was able to be effectively printed onto a 'biopaper' containing 60 mg mL^{-1} fibrinogen solution, enabling the simultaneous deposition of cells within a fibrin support gel. The cells were found to align within the channel during gel formation and effectively proliferate to form confluent lining along with the fibrin scaffold after 21 days. During proliferation, endothelial cells within the scaffold were shown to form tubular structures which show angiogenesis functionality. Furthermore, the fibrin-based bioinks demonstrate desirable biodegradability and mechanical properties highlighting their potential use in

microvascular regeneration. Fibrin provides a novel natural biomaterial for use in bioprinting applications owing to its propensity to form a stable hydrogel upon thrombin and fibrinogen interaction. This enables the gentle encapsulation of cells within the printed scaffold and subsequently has attracted the interest of recent studies.

Fibroin

Fibroin-based bioinks were developed by Das et al. in which hTSMCs were encapsulated in a silk-fibroin-gelatin (SF-G) blend.¹⁹⁹ The SF-G blend was prepared by adding 15% wt. of sterilised gelatin powder to 8% (w/v) SF solution; next, hTSMCs were encapsulated within the SF-G solution to formulate the bioink. Two crosslinking mechanisms (enzymatic and physical) were investigated; the first incorporated tyrosinase (500 units) to enable enzymatic crosslinking; while the second was physically crosslinked through sonication at 50% amplitude for 10 seconds. When compared to an alginate control, both SF-G bioinks demonstrate superior mechanical properties regarding stiffness and stability, with the enzymatic crosslinking mechanism resulting in the best stability over 21 days. However, cellular responses of hTSMCs show cell proliferation to be highest in the enzyme crosslinked bioink. The enzyme-crosslinked ink also facilitates better cellular differentiation down chondrogenic and adipogenic lineages, while osteogenic differentiation favoured the physically crosslinked hydrogel. Cellular viability of the enzymatically crosslinked bioink was maintained for over a month when cultured under *in vitro* conditions. From this study, it is clear that the SF-G bioinks support better cell proliferation, differentiation and viability than the control bioink, likely due to the increased bioactivity facilitated through gelatin combined with the favourable mechanical properties of the silk fibroin.

2.5.2.2 Semi-Synthetic

Semi-synthetic materials include natural materials synthesised through artificial means, including SAPs. SAPs are a unique class of biomaterials able capable of spontaneously self-organising into larger, more useful structures. This process is similar to those that drive self-assembly in nature, and therefore, the developed fibrous architectures are biomimetic and highly reminiscent of the native ECM.²⁰⁵ Moreover, the high degree of control over biological sequence presentation offered by SAPs enables the development of novel ECM-inspired signalling, ultimately leading toward the development of novel

synthetic protein analogues.¹⁴⁰ However, despite SAPs being ideal candidates for bioprinting applications, few bioprinting studies have taken advantage of these semi-synthetic hydrogels.

Raphael and coworkers demonstrate the potential of SAPs to be used in bioprinting applications through the use of two SAP-based peptides: “PGD-Alpha1” and “PGD-AlphaProB”. The authors find both materials demonstrate enhanced printability and cell viability – with encapsulated mammary epithelial cells remaining viable over 7 days. Similarly, Loo et al. detail a novel SAP bioink formulated from lysine-containing hexapeptides which self-assemble into stable nanofibrous hydrogels.¹⁷⁹ Two hexapeptides (Ac-ILVAGK-NH₂ and Ac-LIVAGK-NH₂) were investigated and found to outperform various other SAPs regarding gelation behaviour – requiring both lower peptide concentration and gelation time. Optimised formulations of the Ac-ILVAGK-NH₂ and Ac-LIVAGK-NH₂ hydrogels resulted in the development of bioink suitable formulation, capable of gelating within 5 and 30 seconds respectively. Furthermore, both gels were shown to possess highly desirable mechanical properties with a stiffness of 40 kPa being achieved in Ac-ILVAGK-NH₂ gels. Human mesenchymal stem cells (hMSCs) encapsulated within Ac-ILVAGK-NH₂ gels were able to be successfully cultured and demonstrate uniform suspension within dispensed droplets. Using this bioink approach, multicellular constructs were fabricated by sequential deposition of different cell types localised to specific domains as demonstrated through the deposition of a multi-domain construct which could serve as an *in vitro* model for skin. Furthermore, through the culturing of intestinal epithelial cells on the SAP hydrogel, the native phenotype of the cultured cells was maintained – even outperforming that of the gold standard Corning transwell membranes. Finally, the peptide scaffolds were also shown to be inherently biocompatible and stable, with subcutaneous implantations of hydrogel discs into healthy mice persisting for at least two months with minimal immune response and no capsule formation evident. This study highlights the potential for SAPs in bioprinting applications; however more significant developments are still required to improve the gelation speed and mechanical properties of these materials.

Hedegaard et al. investigate the feasibility of PA-based bioinks for bioprinting applications.¹⁸⁹ Bioinks are developed from novel short peptide sequences which are coassembled with naturally

occurring biomacromolecules and proteins; including fibronectin, collagen, keratin, elastin-like proteins and HA. Through the coassembly of these materials, the authors can generate hierarchical constructs with tuneable molecular composition and structural control. Inkjet printing of these biomaterials allows for the formation of complex structures facilitating control of construct presentation in the micro-/macro-scale. The ability of these materials to encapsulate NIH-3T3 and adipose-derived stem cells enable printing in high cell density with high cell viability (>88%). Tuning of printing parameters allows for a high degree of control over print size, shape, surface topology and network orientation; with various print droplet shapes achievable – including hollow-toroid, open sac, and biconcave. Such systems provide significant promise for tissue engineering *in vitro* models and network orientation.

2.5.2.3 Biosynthetic

Although synthetic scaffolds offer the ability to precisely control the mechanical properties of a material, they often provide inadequate biological information for effective cell culture; alternatively, biologically derived scaffolds offer an array of biological signals to regulate cell activity which can make it difficult to precisely regulate specific cellular events.²⁰⁶ Thus, combining the two material types can yield a biosynthetic scaffold which simultaneously provides the structural characteristics of synthetic materials while presenting the inherent biofunctionality of natural materials.²⁰⁶ Despite this, few biosynthetic peptide-based bioinks have been developed to date.

Skardal et al. have developed a comprehensive hyaluronic acid-gelatin (HA-Gel) bioink toolkit comprised of a two-stage polymerisation technique.²⁰¹ A combination of PEG-based crosslinkers facilitates the development of a highly modular toolkit suitable for a variety of tissue types. Bioinks are formulated through the addition of tissue-derived dECM-based solutions containing combinations of growth factors, collagens, GAGs, and elastin, enabling the targeting of specific tissues for regeneration. Using this model, primary liver spheroids were encapsulated and printed within a liver-specific bioink to create *in vitro* liver-like constructs which demonstrate high cell viability and tissue functionality through measurable albumin and urea output. The biosynthetic bioink toolbox provides both

biochemical and physical properties required in tissue engineering applications and as such have a vast potential to make a significant impact in a variety of applications.

A biosynthetic gelatin-poly(ethylene oxide) (Gel-PEO) bioink was developed by Irvine et al. for 2D printing applications.¹⁹⁷ The bioink was formulated from 3% Type-A gelatin, 2% poly(ethylene oxide), 3 U mL⁻¹ mTgase, HUVECs, and HEK-293s. 3 U mL⁻¹ mTgase was chosen to enable rapid gelation (3 minutes for Gel-PEO bioink). The bioink showed consistent, even print lines with little ink bleeding, producing a well-defined grid pattern. Cellular fluorescence imaging showed increased cell proliferation and a high degree of spreading throughout the bioink.

Biosynthetic peptide-based materials show potential in bioprinting applications due to their ability to demonstrate a versatile range of mechanical properties while maintaining bioactivity; however, more research is required to increase the ease of synthesis and application-specific modification of these materials.

2.6 *In Vitro* and *In Vivo* Applications of Peptide-Based Inks

Bioprinting of artificial tissue constructs is set to revolutionise tissue engineering approaches allowing for rapid yet controlled deposition of cells, biomimetic structures and signals within a spatially-defined advanced tissue scaffold.²⁰⁷ The potential capability of these approaches to provide immediate perfuseable structures, facilitating a greater depth of nutrient transport, allows for fabrication of tissue with greater thickness.¹⁴⁵ Furthermore, the use of cell-laden bioinks provides superior-distribution of biological components within a scaffold,²⁰⁸ while the spatial delivery of different bioinks using multi-head bioprinting technologies allows for the printing of gradient transition tissue constructs.²⁰⁹ Bioprinting using peptide-based bioinks has been extensively investigated and have found use in both organ-engineering and non-organ tissue engineering applications. Non-organ tissue engineering includes the printing of bone,²¹⁰⁻²¹² osteochondral,^{208, 213} cartilage,^{209, 214-215}, vascular,^{70, 198, 216-217} muscular,²¹⁸ and neural tissue constructs,²¹⁹ while organ regeneration includes the printing of cardiac,^{53, 220-221} cardiac valve,²²²⁻²²³ liver,²²⁴⁻²²⁵ and skin constructs,²²⁶ as well as organoid regeneration for use in drug screening applications.²²⁴⁻²²⁵ **Table 2-3** highlights various applications where peptide-based bioinks have been used and details printing process and bioink selection.

Table 2-3 - Application specific peptide-based bioprinting examples classified into non-organ and organ tissue regeneration.

Application	Bioprinter Classification	Technique/configuration	Ink formulation	References
Tissue Regeneration				
Bone Regeneration	Extrusion	Mechanical-based	hMSC laden hydroxyapatite/alginate/gelatin bioinks	210
	Extrusion	Mechanical-based	MSC laden PLA/collagen microcarriers within GelMA-Gellan Gum hydrogel. (microcarrier containing bioink)	211
Osteochondral regeneration	Inkjet	-	hMSC laden agarose/collagen bioinks	212
	Extrusion	Pneumatic and Mechanical	hTMSMC laden Atelocollagen bioink, hTMSMC laden CB[6]-HA bioink, DAH-HA, PCL support ink	213
	Inkjet	Thermal	hMSC laden PEG-GelMA bioink	208
Cartilage Regeneration	Inkjet	Thermal	hMSC laden Acrylated peptide (GRDS and GCRDGPQGIWGQDRCG) /PEG hydrogel	208
	Extrusion	Mechanical-based	Chondrocytes laden Collagen type II	209
	Extrusion	Mechanical-based	BMSC laden Alginate, Agarose, PEGMA and GelMA bioinks, PCL support ink	214
	Extrusion	Pneumatic	hMSC laden GelMA bioink	215
Vascular Regeneration	Extrusion	Pneumatic-based	PDMS support-ink, Pluronic F127 fugitive ink, GelMA (cell free) ink, 10T1/2 laden GelMA bioink, hNDF laden GelMA bioink	70
	Extrusion	Mechanical-based	HUVEC and MSC laden GelMA/Alginate/PEGTA	216
	Inkjet	Thermal	HMVEC laden thrombin bioink (forms fibrin bioink)	198
	Laser-assisted	AFA-LIFT	Eahy926 endothelial cell or B16 carcinoma cell-laden thrombin/CaCl ₂ bioink printed onto Fibrinogen substrate.	217
Muscle Regeneration	Extrusion	Pneumatic	C2C12 Myoblast laden mdECM bioink	218
Neural Regeneration	Extrusion	Pneumatic	Schwann cell-laden fibrinogen/factor XIII/HA/PVA bioink	219
Organ Regeneration				
Cardiac Regeneration	Extrusion	Pneumatic- and Mechanical-driven	L6 laden hdECM bioinks	53
	Extrusion	Pneumatic- and Mechanical-driven	CPC and/or MSC laden hdECM,	220
	Extrusion	Mechanical-driven	HUVEC laden Alginate/GelMA	221
Cardiac Valve Regeneration	Extrusion	Mechanical-driven	SMC laden Gelatin/Alginate, VIC laden Gelatin/Alginate,	222
	Extrusion	Mechanical-driven	HAVIC laden HAMA/GelMA	223
Liver Regeneration	Extrusion	Mechanical-driven	ADSC laden gelatin/alginate/fibrinogen and Hepatocyte laden gelatin/alginate/chitosan	224
	Extrusion	Mechanical-driven	HepG2/C3A spheroid laden GelMA	225
Skin Regeneration	Extrusion	Mechanical-driven	hFB laden Fibrin gel	226

2.6.1 Non-Organ Tissue Regeneration

2.6.1.1 Bone-Tissue Regeneration

Bone is a bioceramic composite which is made up of organic collagen, inorganic hydroxyapatite (HAp), and water.²²⁷ The hierarchical organisation of these materials results in the development of various bone types through formation of mineralised collagen fibrils. The organisation of these fibrils is responsible for the determination of mechanical properties of bones, and therefore enables the formation of different bone types.²²⁸ Bone tissue engineering is of particular interest when considering the regeneration of large orthopaedic defects or the requirement to develop orthopaedic implants that are mechanically more suitable to their biological environments.²²⁹

Wüst et al. develop a bioink designed specifically for bone-tissue regeneration applications.²¹⁰ The bioink is composed of encapsulated hMSCs within an alginate and gelatin hydrogel prepared with differing amounts of HAp, and demonstrates good printability with an extrusion-based bioprinter. A two-step gelation method is employed which implements both reversible thermal- and irreversible chemical-crosslinking, enabling rapid gelation during printing and long-term stability post-printing. To facilitate thermal gelation, the bioink solution was liquefied through heating to 40°C before printing. After extrusion, the bioink was cooled through contact with a cold substrate (~10°C) leading to a temporary increase in ink rigidity. Scaffolds were soaked in a cold CaCl₂ solution following printing to enable chemical crosslinking of alginate within the ink; resulting in irreversible crosslinking yielding a scaffold which demonstrates long-term stability. Three different bioink formulations were investigated: 8% HAp/2% Alginate/10% Gelatin, 4% HAp/2% Alginate/10% Gelatin, and 2% Alginate/10% Gelatin. The bioinks all demonstrate good cell viability (84-85%) 3 days following printing; however, the inclusion of HAp was found to increase bioink viscosity that leads to more difficult handling during printing. Interestingly, the addition of HAp was not found to significantly alter the stiffness of crosslinked bioink constructs, and hydrogels were shown to be ineffective in resembling the mechanical properties of bone tissue.

An alternative approach for the development of bioprinted bone regeneration was investigated by Levato et al. wherein mesenchymal stem cell (MSC) laden poly(lactic acid) microcarriers were

distributed within a GelMA-Gellan Gum (GelMA-GG) hydrogel.²¹¹ Using a 'green solvent-based' method, PLA microcarriers of average diameter 120 μm were fabricated and later functionalised with human recombinant collagen type-I to improve cell responsiveness. The hydrogel component of the bioink was formulated through GelMA incorporated with 0.1% (w/v) Irgacure 2959 to facilitate photocrosslinking; and 1% (w/v) GG to improve printability. Microcarriers were either preseeded with rat derived MSCs and then supplemented at 30 mg mL^{-1} into hydrogel solutions (GelMA-GG MC-MSCs) or were supplemented alongside MSCs into the hydrogels (GelMA-GG, MC's, and MSCs); creating two separate bioinks. A cell viability of 60% was observed after 1 day of culture in GelMA-GG MC-MSCs, and 90% after 3 days of culture. The addition of PLA microcarriers was also shown to increase the compressive modulus of GelMA-GG. Alizarin red staining intensely marked diffused areas around MC-MSCs complexes, indicating strongly mineralised areas; furthermore, on a molecular level MC-MSCs gels showed the most osteocalcin secretion and demonstrated matrix calcification suggesting the ability to form mature bone-like tissues. Despite the bioink not reaching sufficient compressive strengths for initial load-bearing applications, clinically relevant sized constructs were able to be printed with large cell numbers and high shape fidelity; furthermore, the bioinks demonstrated good printability and showed homogeneous cell distribution throughout the printed scaffold.

Duarte Campos et al. utilise inkjet bioprinting for the fabrication of bone-tissue engineering scaffolds.²¹² In combining agarose hydrogels with collagen type-I, a thermoresponsive bioink can be developed which demonstrates superior printability than pure collagen hydrogels. The agarose/collagen bioinks (containing MSCs) demonstrated high cell viability (>98%) 21 days post-printing. Softer hydrogels with lower agarose concentrations and higher collagen concentrations were shown to demonstrate the highest degree of spreading with the longest elongation, as seen in ITGB3 staining; furthermore, through quantitative polymerase chain reaction (qPCR) it was evident that genes COL1 and RUNX2 were expressed significantly more in low stiffness hydrogels (AG0.5-COL0.21) compared to other hydrogels. The increased cell spreading in softer hydrogels also resulted in increased differentiation to osteoblast cells; leading the group to conclude osteogenic differentiation was improved in the softer agarose-collagen hydrogels due to less restricted cell spreading and branching.

The study shows the challenges between balancing printability (high agarose bioinks) and oestrogenic differentiation (high collagen gels).

2.6.1.2 Osteochondral Regeneration

Osteochondral defects affect both articular cartilage and underlying bone tissues; therefore, regenerative engineering approaches need to adequately address this interface transition while supporting both bone and cartilage regeneration within their respective regions. As such, several strategies have been employed for osteochondral repair, including single-phase, layered and graded approaches.²³⁰ In these approaches, both structure and signalling can be modified to enable cell differentiation and tissue regeneration.

A comprehensive 3D bioprinting process was presented by Shim et al. in which a multilayered 3D construct containing human mesenchymal stromal cells was developed for osteochondral-tissue regeneration (**Figure 2-9**).²¹³ Shim et al. made use of several hydrogels to provide support and conducive cellular microenvironments for tissue regeneration. The developed bioinks were based on atelocollagen and supramolecular HA, both of which are types of native ECM proteins. Atelocollagen containing hTMSCs and bone morphogenic protein-2 was used as the bone-forming bioink, whilst cucurbit[6]uril-Hyaluronic acid (CB[6]-HA) containing hTMSCs and transforming growth factor- β (TGF- β) formed guest-host interactions with another hydrogel, 1,6-diaminohexane (DAH)-conjugated HA (DAH-HA), to form the chondral layer. Pores are made available in the bone-forming portion of the 3D printed scaffold to allow for infiltration of vascularisation, while in the chondral section, the PCL framework was fully interconnected to inhibit vascular invasion. High cell viability is evident in both printed bioinks; demonstrating 93% and 86% for atelocollagen and CB[6]/DAH-HA bioinks respectively. *In vitro* tests showed hTMSCs in the atelocollagen hydrogel exhibited a stretched morphology typical of the osteogenic phenotype at day 10, while hTMSCs within the CB[6]/DAH-HA bioink demonstrate spherical morphologies, characteristic of the chondrogenic phenotype. Additionally, atelocollagen bioink layers demonstrated an increase in ALP, COL-I, and OSX genes compared to those in the CB[6]/DAH-HA bioink layer, while the CB[6]/DAH-HA layers showed increases in ACAN, COL-II, and SOX9 compared to the atelocollagen layer at day 14. Cells within

atelocollagen constructs showed high levels of RUNX2 (a master transcription factor in osteoblasts), whereas cells cultured within CB[6]/DAH-HA hydrogels demonstrated high levels of COL-II (the major collagen in cartilage); RUNX2 was not detected in CB[6]/DAH-HA gels, nor was COL-II detected in atelocollagen hydrogels. These results demonstrated that the materials used were cytocompatible and capable of directing desired cell differentiation. *In vivo* tests on rabbit knee, osteochondral defects reinforced these observations, with the printed scaffold yielding outstanding regenerative ability in both gross morphological and histological evaluations after eight-weeks implantation.

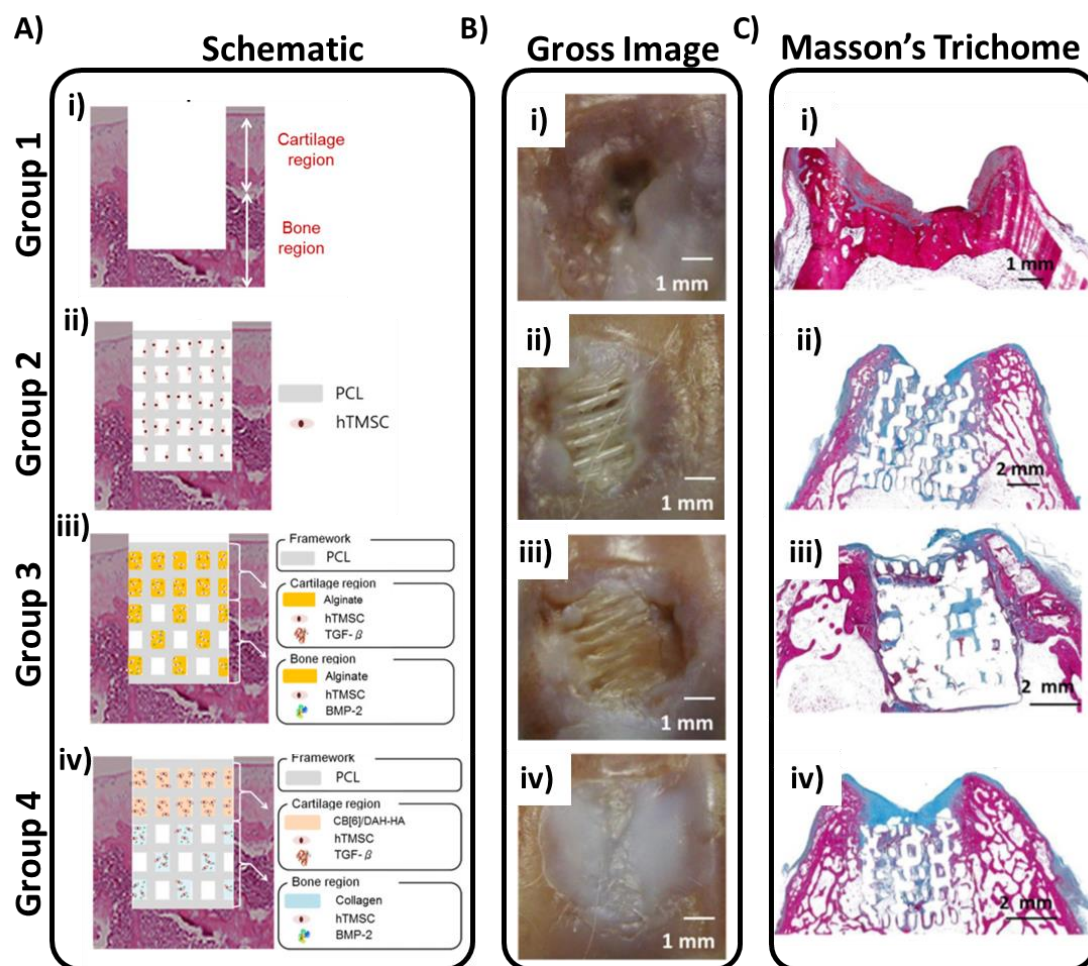


Figure 2-9 – *In vivo* bioprinted osteochondral regeneration approach. A) Schematic showing experimental groups including i) Group 1- the osteochondral defect without treatment as a negative control; ii) Group 2- defect filled with 3D-printed PCL scaffold seeded with hTMSCs; iii) Group 3 – defect filled with bioprinted PCL scaffold with alginate hydrogel encapsulating hTMSCs, and iv) Group 4 – defect filled with bioprinted PCL scaffold with CB[6]/DAH-HA and collagen hydrogels encapsulating hTMSCs. B) Gross images showing repair following 8 weeks implantation for i) group 1, ii) group 2, iii) group 3, and iv) group 4 (scalebar 1 mm). C) Histological analysis of tissue regeneration in the four groups with Massons Trichome staining at 8 weeks showing i) group 1, ii) group 2, iii) group 3, and iv) group 4. Reproduced with permission ²¹³

An alternative osteochondral bioprinting method was presented by Gao et al. in which thermal-based inkjet printing was employed to print acrylated-peptide/PEG bioinks.²⁰⁸ The bioinks were prepared at formulation 10% (w/v) poly(ethylene glycol) dimethacrylate (PEGDMA), 1 mM acrylated GRGDS, 1 mM acrylated MMP-sensitive (GCRDGPQGIWGQDRCG) peptides, 0.05% (w/v) Irgacure, and 6×10^6 hMSCs mL⁻¹. Using this bioink, cylindrical artificial bone and cartilage tissue constructs were printed with 4 mm internal diameter. Printed constructs were placed in a 24 well plate containing either 1 mL osteogenesis medium or 1 mL chondrogenesis medium with 10 ng mL⁻¹ TGF- β and cultured for 21 days. Bioinks were compared to regular, PEG, PEG-GelMA and GelMA inks regarding printability with results showing the peptide-PEG bioinks demonstrate excellent printability with viscosities highly similar to that of regular ink. Alternatively, PEG inks with the addition of GelMA demonstrated poor printability due to the significant increase in viscosity resulting in frequent printhead clogging. The pure GelMA bioink was found to be unprintable using this inkjet bioprinting setup. PEG/peptide bioinks demonstrated improved cell viability after 24 hours when compared to pure PEG hydrogels, with a ~90% cell viability in PEG/peptide hydrogels compared to ~83% in PEG hydrogels. The PEG-peptide scaffold demonstrated a lower compressive modulus than the PEG scaffold immediately following printing, however after osteogenic and chondrogenic differentiation, PEG/peptide scaffolds demonstrated a significant increase in compressive moduli with an increase of 100% and 82% respectively from day 7 to 21. Alternatively, PEG hydrogels only showed a 44% and 38% increase from day 7 to 21 for osteogenesis and chondrogenesis samples respectively. A complex analysis of gene expression found the printed scaffolds placed in the osteogenic media expressed very high levels of COL10A1 and MMP13 genes, suggesting that the PEG-peptide scaffold strongly stimulates endochondral bone formation; alternatively, scaffolds placed within the chondrogenic media demonstrates high chondrogenic differentiation factors, highlighting the ability for use in cartilage regeneration applications. Ultimately, the PEG/peptide bioink combined with the thermal inkjet bioprinting technique was found to promote homogeneous bone and cartilage regeneration, and thus, shows potential use in osteochondral regeneration applications.

A subsequent study by the same group investigated the use of an inkjet printable PEG/GelMA bioink for bone and cartilage tissue applications.²⁰⁸ Briefly, 10% (w/v) PEGDMA and 1.5% GelMA were mixed together with Irgacure 2959 (0.05% w/v) and subsequently seeded with hMSCs. The concentration of GelMA used in the bioink was determined as the highest concentration which maintained effective printability. Once again, through comprehensive cell viability testing, mechanical testing, gene expression, and histological analysis, the PEG/GelMA bioink developed was found to encourage stem cell differentiation down desired lineages.

2.6.1.3 Cartilage Regeneration

Cartilage is a dense connective tissue with a highly ordered matrix consisting predominantly of collagens and proteoglycans.²¹⁴ Depending on the composition of the matrix, cartilage is classified into three categories: elastic, hyaline, and fibrocartilage.²³¹ Elastic cartilage is surrounded by perichondrium and characterized by the presence of chondrocytes immersed in an ECM;²³² in humans this tissue is found in the external ear, auditory tube, and epiglottis.²³¹ Hyaline cartilage also contains primarily collagen type II; but rather is found in many load-bearing applications – particularly covering synovial joints as articular cartilage.²¹⁴ Fibrocartilage contains both type I and II collagens and is found extensively in tendons, vertebral disks and menisci.^{214, 231} Due to the limited regenerative capabilities of cartilage and potential for chondral defects to induce early arthritis, cartilage regeneration is of significant interest to current tissue engineering approaches.²³³

Ren et al. developed a gradient bioprinting method for the printing of zonal tissue constructs for cartilage engineering.²⁰⁹ Three collagen type-II based bioink groups were formulated, each with different cell densities (2×10^7 , 1×10^7 , and 0.5×10^7 cells mL^{-1}); for each bioink, two different types of constructs were prepared, one with a biomimetic gradient chondrocyte density and the other with a homogenous density. For gradient scaffolds, the gradient concentrations were designed such that the total cell concentration through the whole construct equalled that of the homogenous scaffold. The biomimetic approach aims to mimic the native cell densities in zonal articular cartilage tissues; therefore, a construct was fabricated with areas of 10% superficial layer (high cell density), 10% middle layer (medium cell density), and 80% deep layer (low cell density). Constructs were cultured over 3

weeks and investigated regarding cell viability, reverse-transcription quantitative polymerase chain reaction (RT-qPCR), biochemical assays, and histological analysis. Cell viability was found to be extremely high after 1 day, with an average live cell percentage of $93 \pm 3\%$ evident in all groups. A slight loss in cell numbers was evident over the 3 weeks; however, this was not statistically significant. Analysis of gene expression showed low expression of COL1A1 over the 3 weeks, while expression levels of COL2A1 and ACAN showed a significant increase over the same period. Average single-cell GAG production was found to be highest in group B (1×10^7 cells mL^{-1} total concentration) after 3 weeks; while Alcian blue staining and immunohistochemical analysis of chondrocytes in different gradient constructs showed high positive staining for collagen type-II. This study demonstrates the potential for gradient-based bioprinting in zonal articular cartilage regenerations, with results highlighting desired ECM deposition.

The use of bioprinting for fibrocartilage and hyaline cartilage regeneration was investigated by Daly et al. in which four commonly used hydrogel bioinks (agarose, alginate, GelMA and PEGMA) were compared regarding printing properties, and potential to support either hyaline cartilage or fibrocartilage development.²¹⁴ Each hydrogel was seeded with porcine bone-marrow-derived mesenchymal stem cells (BMSC), before being used to print cylindrical artificial tissue constructs. Histological, immunohistological and biochemical analysis of constructs showed that over the 4-week culture period, alginate supported the highest GAG synthesis, while GelMA demonstrated the lowest GAG synthesis. Furthermore, alginate and agarose hydrogels showed strong staining for collagen type-II; whilst GelMA and PEGMA stained weakly for collagen type-II and strongly for collagen type-I. These results suggest that the alginate and agarose bioinks support greater development of hyaline cartilage-like phenotypes, while fibrocartilage-like phenotypes were supported to a greater extent by GelMA and PEGMA-based bioinks. In printability investigations, GelMA (10% (w/v) combined with 0.05% (w/v) Irgacure 2959) demonstrated the greatest printability, while the PEGMA-based bioinks demonstrated poor printability. Alginate and agarose hydrogels presented moderate printability with higher filament spreading and variability compared to GelMA. Post-printing cell-viability was demonstrated to be sufficiently high ($>80\%$) for all bioinks. The addition of a PCL support was found

to reduce cell viability slightly; however, the viability of all groups remained sufficiently high (>70%). The addition of PCL microfiber reinforcement in printed constructs was shown to significantly increase compressive stiffness of the scaffolds, yielding a printed scaffold which was within the range of native hyaline tissue. Although this was higher than required for fibrocartilage tissue, modifications to fibre diameter and fibre spacing could result in a mechanically suitable construct. Ultimately, alginate and agarose-based bioinks were shown to support the development of hyaline-like cartilage tissues while demonstrating sufficient printability; alternatively, GelMA and PEGMA-based bioinks supported fibrocartilage development, with GelMA exhibiting good printability properties. Through these studies, the use of peptide-based bioinks paired with suitable printing techniques is shown to be effective for cartilage engineering applications, enabling printing of anatomically mimetic tissue constructs which encourage healthy tissue regeneration.

2.6.1.4 Vasculature Repair

Due to the relation between narrowing blood vessels and heart disease, there is a significant need to develop vascular-tissue engineering approaches.²³⁴ Vascular tissue is comprised of three histologically distinct layers. The innermost layer (tunica interna) consists of a single layer of endothelial cells mounted on a basil lamina; below this lies the sub-endothelial fibro-elastic connective tissue layer and an organised internal elastic lamina.²³⁵ The middle layer (tunica media) consists of predominantly smooth muscle cells and elastin fibres, and a layer of external elastic lamina; while the outermost layer (tunica adventitia) is composed of fibro-elastic connective tissue.²³⁵ Considering the multicomponent nature of these constructs, there is substantial difficulty in adequately recapitulating these vessels.

A novel 3D bioprinting method for the fabrication of tissue-engineered structures is described by Kolesky et al. wherein cells, vasculature, and ECM mimic were all able to be printed to form a multicomponent artificial tissue construct.⁷⁰ The study took advantage of a multi-head, extrusion-based bioprinting technique to print four different inks: the first ink a ‘fugitive’ pluronic ink was designed to be gently removed (at <4°C) post-printing. This fugitive-ink acts to provide a temporary structure, which upon removal creates an open channel facilitating later seeding with HUVECs to form the preliminary vascular network. The pluronic ink was made at a 40% (w/v) (Pluronic F127) concentration dissolved within deionised, ultrafiltrated water. A cell-free GelMA ink was prepared by dissolving 15% (w/v) GelMA powder in media. A photoinitiator (Irgacure 2959) was added to the solution at 0.3% (w/v); enabling photo-crosslinking under UV light. The second ink formulated was a GelMA based bioink; this ink was prepared with 15 % (w/v) GelMA dissolved in media and subsequently mixed with human neonatal dermal fibroblasts (hNDF). A third bioink was prepared with the same formulation as the GelMA-hNDFs bioink, except hDMFs were replaced with mouse embryo fibroblast (10T1/2) cells. Using these inks, a diverse range of biological structures were printed within a single tissue construct. A polydimethylsiloxane (PDMS) support-ink was also used to set a well-defined border for the whole tissue construct. Initially, ‘1D’, ‘2D’ and ‘3D’ structures were printed using the fugitive-ink surrounded and encapsulated by the GelMA cell-free bioink. Removal of the fugitive-ink was found to be effective and could be done quickly at high fidelity even in the 3D vascular constructs. Following removal, the

open channels of the 2D printed system were seeded with HUVECs through injection before being cultured in media 48 hours. After incubation, cells demonstrated good cell viability (>95%) as assessed through confocal analysis of live/dead stained structures. To further investigate the effectiveness of this printing technique, a 3D construct containing both vasculature (fugitive-ink) and cell-laden constructs (hNDF containing GelMA bioink) was printed surrounded by the cell-free GelMA bioink. The fugitive-ink was again removed, and endothelial cells were seeded as before; the scaffold shows good cell viability for both inks in confocal live staining images, with each cell-type being clearly distinguishable within its designated printed zone. Finally, multiple cell-types were printed into a single tissue construct, and endothelial cells were seeded into the fugitive-ink removed channels. Confocal observations show good cell viability (81% for hNDFs and 82% for 10T1/2 cells) after 7 days. Again, distinct regions were evident, correlating to the sections of different printed bioinks (**Figure 2-10**).

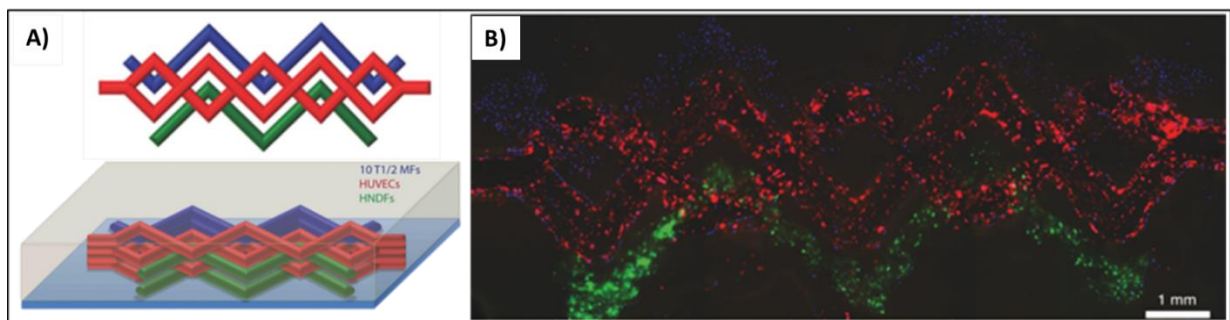


Figure 2-10 - Bioprinting approach for multicomponent tissue fabrication: A) Schematic view of printed 3D construct, and B) composite fluorescent image showing 10T1/2 fibroblasts (blue), hNDFs (green) and HUVECs (red). Reproduced with permission ⁷⁰.

An extrusion-based bioprinting method was employed by Jia et al. for the fabrication of perusable vascular constructs in tissue engineering applications.²¹⁶ Briefly, a bioink was developed from alginate (2 or 3% w/v), GelMA (5 or 7% w/v) and poly(ethylene glycol)-tetra-acrylate (PEGTA, 2 or 3% w/v); additionally, a photoinitiator was included at 0.25% (w/v) to enable GelMA photo-crosslinking. Using a coaxial nozzle, the bioink was printed from the outer sheath; and the inner sheath pumps a CaCl_2 solution to enable alginate crosslinking (ionic) inside the hollow vessel, while a spray of CaCl_2 solution was used to crosslink the external surface of the vessels. The alginate crosslinking provides immediate temporary structure stability to the hollow tubes. Next, covalent crosslinking occurs through GelMA photo-crosslinking, facilitating the development of a mechanically stable vessel. The vessel was then washed in mixture medium 3 times to remove excess CaCl_2 and photoinitiator, before being immersed in a Ca^{2+} -ethylenediaminetetraacetic acid (EDTA) chelating agent for 5 minutes to dissolve alginate. The PEGTA acts to combat the reduced mechanical strength post alginate removal, stabilising the crosslinked matrix. Printability investigations of the bioinks found the optimal ink formulation as follows: 7% (w/v) GelMA, 3% (w/v) Alginate, 2% (w/v) PEGTA; this ink was used for subsequent experimental observations. Cell viability (HUVECs and hMSCs) was shown to be sufficiently high when UV exposure does not exceed 30 seconds, demonstrating viability percentages above 80% after 1, 3, and 7 days. Cell metabolic activity was also found to increase as a function of culture time, confirming the cytocompatibility of the approach. The vascular constructs also demonstrated high expression levels of alpha-smooth muscle actin (α -SMA) and platelet endothelial cell adhesion molecule (PECAM-1), both of which were crucial for vessel formation and stabilisation. The perfusability of vessels was proven through confocal microscopy; and further extension of this work resulted in the use of a tri-layered nozzle which enables variance in vessel diameter through the controlled alternation of bioink delivery from the middle sheath to the external sheath, providing a comprehensive approach to tissue engineered vascularisation.

Using a laser-assisted bioprinting approach Guillotin et al. investigate the biofabrication of microvascular tissue constructs through various bioink formulations.²¹⁷ In this study, bioinks were formulated from alginate (containing glycerol), Matrigel, or a solution of thrombin; however due to the

scope of this study, only the thrombin solution will be focused on. The thrombin solution was formulated containing cell-laden (Eahy926 or B16) thrombin (250 UI) and CaCl_2 (40 mM) which was printed onto a fibrinogen substrate. Using this approach, a stable construct was printed with microscale resolution comparable to microvascular dimensions. Cell-viability testing of Eahy926 cells demonstrates the presence of viable cells and good cell distribution. These studies highlight the potential for peptide-based bioprinting applications in vasculature regeneration, providing a fundamental advance in addressing the requirement to develop healthy vasculature within constructs.

2.6.1.5 Muscle Regeneration

Skeletal muscle is the most abundant muscle type and is responsible for various mechanisms, including voluntary and controlled body movement, facial expression and viscera protection.²³⁶ Skeletal muscle is a hierarchical tissue composed of tightly bound muscular fascicles within an epimysium sheath. Each fascicle contains numerous tightly bound muscle fibres; each of which is a single, multinucleated cell.²³⁶ Within these muscle cells lie myofibrils, formed from actin and myosin filaments.²³⁷ Skeletal-muscle regeneration offers promise to clinical treatments for tissue lost through trauma or altered through disease.

Choi et al. employ pneumatic-driven extrusion for the bioprinting of functional skeletal muscle constructs.²¹⁸ The bioink was formulated from decellularised skeletal muscle ECM seeded with C2C12 myoblasts and compared to a collagen bioink regarding mechanical properties, cell viability, myotube formation, and myogenic differentiation. Characterisation of muscle-derived decellularised extracellular matrix (mdECM) verified that the cellular contents were removed while ECM components, including GAGs, collagen and laminin, were retained. The bioink was found to possess excellent printability due to its thermally controlled gelation properties (owing to collagen content) and ability to undergo shear thinning; from this ink, a number of 3D cell-encapsulated muscle constructs with varying shape, pores and architectures were able to be printed with uniform cell distribution and good cell viability (**Figure 2-11A**). High cell viability (>90%) was evident after 24 hours of printing and maintained over 14 days; furthermore, cells were found to begin longitudinally aligning over the culture period. Cell alignment was shown to be a function of line width and culture time; thinner printed

lines (500 μm diameter) demonstrated the highest degree of cell alignment after induced differentiation, with $76 \pm 2\%$ alignment evident at day 7 compared to an initial value of $64 \pm 9\%$ at day 1. Mechanical testing of the mdECM bioink shows improved stiffness, tensile strength, and storage moduli (G') compared to the control collagen hydrogel both at day 7 and day 14 of culturing. Furthermore, the mechanical properties of both collagen and mdECM were found to improve greatly between days 7 and 14. Cell proliferation assays of printed constructs showed significantly increased levels of cell proliferation in mdECM-bioink printed structures compared to collagen bioink printed structures; furthermore, both collagen and mdECM-bioinks demonstrate improved cell-proliferation following 7 days in culture. Investigation of gene expression showed significantly higher myogenic gene expression of Myf5, MyoG, MyoD, and MHC in the mdECM bioink compared to the collagen control; indicating a higher degree of cell stimulation toward myogenic maturation. A high level of myotube formation was evident in the mdECM printed constructs compared to the collagen control; with myotubes of greater length, width, area, and fusion index being evident in the mdECM bioink printed constructs. Finally, agrin preservation in mdECM was evident, providing the potential for increased acetylcholine receptor cluster formation in 3D printed constructs. The bioprinting approach investigated in this study highlights the potential for mdECM bioink use in functional skeletal muscle regeneration, enabling the customised formation of muscle substrates for the treatment of muscular injuries.

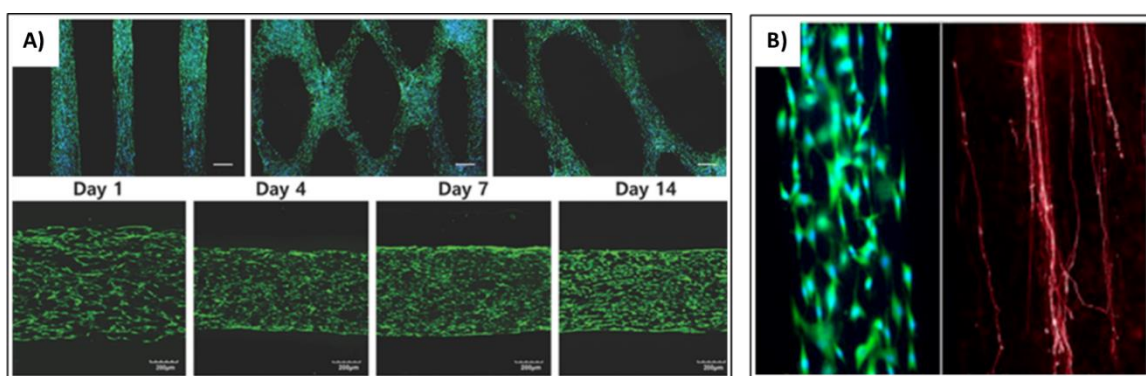


Figure 2-11 – Bioprinted non-organ tissue constructs A) Skeletal muscle constructs containing C2C12 myoblasts, [top] Fluorescence imaging showing high control over architecture, and [bottom] live dead staining of constructs at days 1, 4, 7, and 14; B) Bioprinted fibrin nerve construct: showing [left] encapsulated Schwann cell alignment, [right] neurite elongation and alignment. Reproduced with permission from ²¹⁸ and ²¹⁹ respectively.

2.6.1.6 Neural Regeneration

A nerve consists of a cell body (soma) and its extensions (axons and dendrites), the soma receives signals through its dendrites, before sending the signal down onward through the axon.²³⁸ Nerves are groups of axons, and may form part of the central nervous system or peripheral nervous system.²³⁸ In the peripheral nervous system, small injuries can be regenerated naturally; while more substantial injuries require surgical treatments.²³⁹ The central nervous system is more complicated, however, in that the body inhibits regeneration, and as such, there has been little success in spinal cord repair.²³⁹

Peptide-based bioprinting was investigated by England et al. in which a pneumatic-driven extrusion printer was employed to print a fibrin-forming bioink containing fibrinogen, factor XII and HA.²¹⁹ To enable nerve regeneration, Schwann cells were encapsulated within the hydrogel. The bioink was printed into a sodium chloride (NaCl), CaCl₂, PVA and thrombin ‘crosslinking’ solution enabling fibrin formation while supporting the fabrication of multilayered fibrin-HA scaffolds. PVA concentration was found to be a crucial factor which affects material spreading and regulates strand uniformity, furthermore, PVA inclusion was found to compensate strand buoyancy; allowing for the formation of complex shapes. However, high levels of PVA results in poor adjacent layer attachment, subsequently resulting in lateral displacement of layers relative to each other. Fibrin fibres were found to orientate parallel to strand direction, with 97% of fibres orientated within $\pm 10^\circ$, and 45% of fibres orientated within $\pm 1^\circ$ relative to the strand. Cell viability of Schwann cells within bioinks assessed immediately post-printing showed high cell viability (~98%), which was maintained over 7 days; high cell proliferation was also evident during the same period. Cell alignment was evident within printed constructs, with strands adopting elongated morphologies (**Figure 2-11B**); alternatively, no significant cell alignment was evident on control (plated) cultures of Schwann cells. Culturing of dorsal root ganglia on printed strands showed directional neurite growth compared to the control laminin-coated surface; furthermore, the dorsal root ganglia cultured on the fibrin-based strands demonstrated a greater average length of the longest dorsal root ganglia neurite. The findings of this study demonstrate the ability of naturally derived peptide bioink use in neural regeneration applications, enabling for printing of highly ordered autologous scaffolds.

2.6.2 Organ Regeneration

2.6.2.1 Cardiac Regeneration

Heart-failure is the primary cause of death in industrialised countries; therefore, there is a significant need to develop successful and practical cardiac regeneration approaches.²⁴⁰ Cardiac tissue engineering approaches are sophisticated as they are required to facilitate heart function while promoting cardiac tissue regeneration; thus, constructs should be (1) contractile, (2) electrophysiologic stable, (3) mechanically robust yet flexible, (4) vascularised, and (5) autologous.²⁴⁰

Using a multi-head, extrusion deposition system, Pati et al. bioprint heart, cartilage and adipose tissue constructs for *in vitro* culture through formulation of a dECM bioink as previously discussed (see Section 2.5.2.1).⁵³ In addition, a synthetic PCL hydrogel is used to provide structure and support to cartilage and adipose dECM constructs. A PCL framework was created, and the dECM bioink was printed in alternating gaps between PCL lines creating a porous structure. Alternatively, printed heart tissue constructs were printed containing no PCL supports. dECM bioinks were then used to encapsulate hASCs, hTMSCs, and L6 cells, and approach effectiveness was determined through observation of adipogenic, chondrogenic, and myogenic differentiation. Cell viability was found to be sufficiently maintained after printing, showing greater than 95% cell viability following 24h culture and remaining above 90% following day 7 and 14 analysis with active cell proliferation evident. Gene expression is also enhanced in chondrogenic (SOX9 and COL2A1), cardiogenic (Myh6 and Actn1) and adipogenic (PPAR γ and LPL) constructs when compared to that of the collagen bioink control.

Extending this work, the group develop a cardiac-specific approach wherein bioinks were formulated from hdECM bioinks.²²⁰ Three bioinks were formulated as follows: I) 20 mg mL⁻¹ hdECM and 0.02% (w/v) vitamin B2 laden with human cardiac progenitor cells (hCPCs); II) 20 mg mL⁻¹ hdECM, 0.02% (w/v) Vitamin B2, and 10 μ g mL⁻¹ vascular endothelial growth factor (VEGF) laden with hMSCs; and III) 20 mg mL⁻¹ hdECM, 0.02% (w/v) Vitamin B2, and 10 μ g mL⁻¹ VEGF laden with hCPCs and hMSCs. Bioinks I and II were used to make prevascularised patches; here, two PCL layers were extruded as support followed by sequential deposition of bioink I and II allowing for muscular and vascular regeneration, respectively. Meanwhile, bioink III was used to print a homogenous patch.

After printing, bioinks were irradiated with UV for 30-60 seconds, allowing for vitamin B2 initiated crosslinking. Cell viability 24 hours after printing demonstrates high cell survival (~95%) for the printed patch containing both bioinks printed alternately; and shows enhanced structural maturation of cells. MSCs supplemented with VEGF were shown to promote vascularisation after 5 days in culture, and *in vivo* tests demonstrated an improvement of cardiac function and decreased negative left ventricle modelling when compared to the negative control, bioink I or bioink III separately. These results highlight the potential of multi-bioink, hdECM bioink approaches for cardiac regeneration applications.

An alternative method for cardiac regeneration was investigated by Zhang et al. in which vasculature was printed prior to seeding with cardiomyocytes, resulting in highly vascularised tissue.²²¹ Briefly, vasculature was printed through a HUVEC seeded alginate/GelMA bioink containing Irgacure 2959. A two-step crosslinking method was employed wherein ionic crosslinking of alginate was first induced through CaCl_2 interaction, before photoinduced crosslinking of GelMA. The constructs were then washed in a phosphate-buffered saline solution (PBS) to remove excess CaCl_2 . Constructs were cultured for up to 33 days with endothelium formation evident following 15 days. Neonatal rat chondrocytes were seeded onto the scaffolds with spontaneous beating of cardiac tissues observed following 48 hours in culture. The method described was found to produce cardiac organoids with cardiomyocyte maturation, alignment, and contraction, and provides potential for use in both cardiac-tissue engineering applications and drug screening applications.

2.6.2.2 Cardiac-Valve Regeneration

Heart-valve disease is a substantial problem which can often result in valve dysfunction leading to further, potentially fatal cardiac or systemic complications.²⁴⁰ These structures ensure unidirectional flow enabled through a unique arrangement of leaflets within a circular root; however, as these valves do not self-repair, there is a significant need to develop tissue engineering approaches which adequately regenerate healthy living tissues for surgical valve replacement.^{222, 240}

An alginate/gelatin bioink was developed by Duan et al. for use in cardiac-valve regeneration applications (**Figure 2-12**).²²² The ink was initially investigated using a grid-like structure to assess its

printability - with results showing prints of high accuracy ($84.3 \pm 10.9\%$), high viability (VICs, $84.6 \pm 3.1\%$ after 7 days) and good shape fidelity. The grid-like scaffolds were found to maintain geometry and mechanical integrity post-printing, with an even distribution of cells existing through the structure. Mechanical properties of cell-free printed constructs were found to be comparable to that of non-calcified human aortic heart valve cusps following printing; however, stiffness decreased with increasing culture time. Alternatively, aortic valve leaflet interstitial cell (VIC)-laden constructs demonstrated a lower initial stiffness at day 0; however, remained constant over 7 days, after which sample stiffness was statistically equivalent to cell-free samples. To print the aortic-valve constructs, two bioinks were developed: the first contains smooth muscle cells (SMCs) and was used to print the root region; while the second contains VIC and was used to fabricate the leaflet region of the valve. Cells were able to be printed at high density (1×10^7 cells/mL) and were homogenously distributed within the printed tissue constructs; furthermore, the printed scaffold exhibits geometry comparable to the original scanned valve, with key anatomical features visible in the print. Cell viability was found to be sufficiently high, with an ~81% cell viability evident within the printed root (SMCs) component and a ~83% cell viability in the leaflets (VICs). Finally, the encapsulated VIC and SMCs were shown to demonstrate good spreading and phenotype expression in culture.

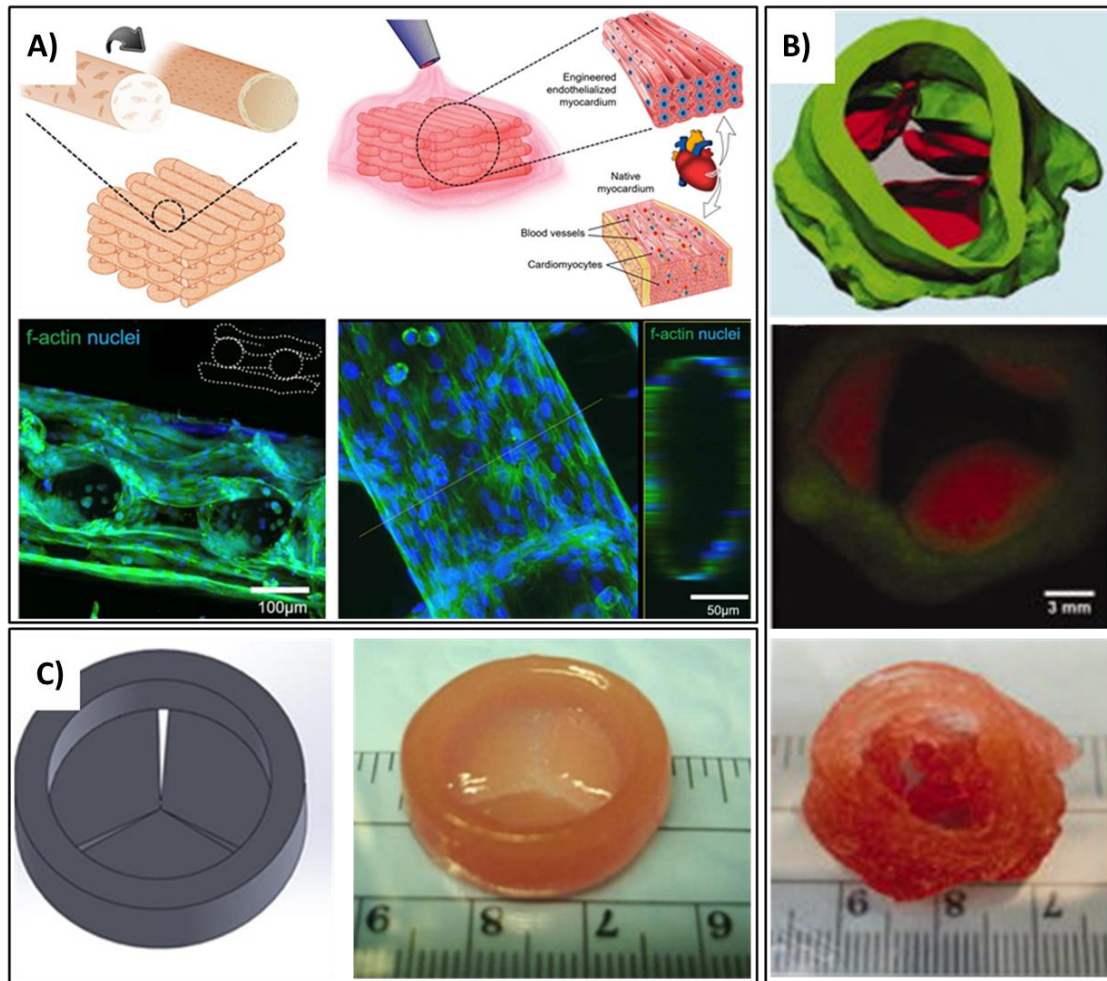


Figure 2-12 – Bioprinted organ tissue constructs. A) Endothelialised myocardium: [top] Schematic process showing formation of endothelialised vascular bed (left) and cardiomyocyte seeding resulting in endothelialised myocardium formation (right), [bottom] Confocal fluorescence image showing cross-sectional area of three-layer scaffold at day 14 (left), high-resolution fluorescence imaging showing HUVEC distribution within a single microfiber at day 14 and 3D rendering of tubular structure at microfiber cross-section through dotted line (right); B) Bioprinting of aortic valve conduit: [left] Aortic valve model reconstructed from micro-CT images (Green indicates valve root and red indicates valve leaflets), [middle] Fluorescent image of initial two bioprinted layers showing SMCs (labelled green) and VICs (labelled red), [right] printed aortic valve construct; C) Bioprinting of heart valve conduit with encapsulation of HAVICs within leaflets: [left] Solidworks® designed heart valve model, [right] printed valve construct; Reproduced with permission from ²²¹, ²²² and ²²³ respectively.

The group further extend this work using an alternate hydrogel formulation, laden with human aortic vascular interstitial cells (HAVICs).²²³ A variety of hydrogels were investigated, all based on formulations of methacrylated hyaluronic acid (HAMA) and GelMA with differing concentrations (2%, 4%, or 6% and 6%, 10%, or 12% respectively). Irgacure 2959 (0.05% w/v) was also added to GelMA solutions enabling photo-crosslinking. Mechanical testing of acellular hydrogels found the compressive moduli decreased with increasing GelMA concentration; while an increased HAMA concentration resulted in a stiffer hydrogel. The viscosity of hydrogels was found to be dependent on HAMA concentration, with viscosity too low for extrusion printing applications in 2% HAMA with 6-10% GelMA hydrogels; while viscosity was too high in gels with 6% HAMA with 10-12% GelMA, resulting in poor printability. For this reason, only gels containing 4% HAMA and 6%, 10% and 12% GelMA were used for subsequent cell encapsulation investigations. Cell viability testing demonstrated >90% viability for all tested hydrogels (4% HAMA/6% GelMA, 4% HAMA/10% GelMA, 4% HAMA/12% GelMA) on day 3 and day 7. Cells encapsulated within the 4% HAMA/12% GelMA bioink demonstrated the greatest degree of cell spreading compared to the other two gels (which demonstrated a more spherical shape) at day 7, likely due to favourable mechanical properties. Furthermore, all cells demonstrated a significant increase in cell metabolic activity over the 7-day period, corresponding with an increase in cell proliferation; however, no significant increase was seen between hydrogel formulations. GAG content within the scaffolds was also found to increase between days 3 and 7 for all hydrogel formulations; once again there was no significant difference between each hydrogel formulation tested. Analysis of gene expression showed significant α -SMA up-regulation in 4% HAMA/6% GelMA hydrogels; while all hydrogels demonstrated a significant increase in periostin and collagen I expression between day 3 and 7. Printability tests found the 4% HAMA/10% GelMA hydrogel to demonstrate the best accuracy at $111.3 \pm 7.2\%$ (the printed construct slightly increased in area) while maintaining sufficiently high cell viability (>90%). For this reason, this ink was selected to print the aortic heart valves. A printed construct was successfully fabricated showing high similarity to the original computer aided design (CAD) model. The heart-valve was constituted of two inks; the first was an acellular ink used to print the root, while the leaflets were printed using a HAVIC-laden bioink; both inks were formulated from a 4% HAMA/10% GelMA hydrogel base. The printed heart valve was shown

to demonstrate good viability, GAG increase, collagen deposition, and expression of both α -SMA and VIM after 7 days in culture; indicating the potential for peptide-based bioinks in heart-valve regeneration applications.

2.6.2.3 Liver Regeneration

The liver is a complex organ which plays an essential role in metabolic activities. Primarily, the liver is composed of two branched vascular networks and numerous hepatic lobules.²²⁴ Blood supply plays a crucial role in transporting nutrients into the liver while removing waste;²²⁴ therefore, there is a critical need for liver constructs to present a high degree of vascularisation.

Bioprinting for liver regeneration applications was investigated by Li et al. wherein an artificial liver-like construct was printed using two different inks.²²⁴ The first ink was designed for printing of vascular structures within the construct and therefore contains adipose-derived stromal cells (ADSCs) encapsulated within a gelatin/alginate/fibrinogen hydrogel (30%, 5%, and 10% w/w, respectively); while the second ink comprises the hepatic tissue and was formulated from hepatocytes encapsulated within a gelatin/alginate/chitosan (30%/5%/2% w/w) hydrogel. After assembly, the scaffold was crosslinked in a thrombin/ CaCl_2 / $\text{Na}_5\text{P}_3\text{O}_{10}$ solution. Using these bioinks, a preliminary analogue of a functional liver construct was printed. Scanning electron microscopy images of the printed acellular hydrogels show physical architectures unlike that of either alginate or gelatin. After two-weeks of culturing hepatocytes demonstrate an elliptical or round structure with ~23% containing double nuclei; suggesting hepatocytes were alive and proliferating. Immunofluorescence staining was positive for both nuclei and the mature hepatocyte biomarker ALB; confirming cell-life and secretion ability. ADSCs were stained positive for the mature endothelial cell biomarker PECAM-1; indicating endothelial cell differentiation in vascular printed constructs. However, few ADSCs demonstrated spindle morphologies - a key characteristic of endothelial cells; this may be due to insufficient culture time. To investigate functionality of the construct, the rate of increase in ALB, urea, and ALT secreta in media was analysed. ALB content was found to increase steadily over 14 culture days, while ALT secretion

was shown to increase during early stages before subsequently decreasing (after day 6). The steady increase in ALB confirms metabolic function. Alternatively, ALT secretion indicates acute liver damage; therefore, it was suggested that the initial increase was due to hepatocyte isolation yielding an early inflammatory reaction, while the decrease may be a result the inflammatory reaction subsiding upon hepatocyte adaption to the new environment. The urea content was found to increase before a slight decrease at day 14. Using this method, a liver-like construct is developed which upon culturing demonstrates preliminary functionality. The approach has potential application in tissue regeneration, physiological simulation, and drug screening systems.

A liver-on-a-chip platform containing bioprinted hepatic spheroids was presented by Bhise et al. wherein a GelMA bioink containing HepG2/C3A spheroids was bioprinted within a bioreactor platform.²²⁵ To ensure functional sustainability over long culture periods, the printed spheroids were cultured under continuous perfusion ($200\ \mu\text{L h}^{-1}$) for 30 days, with findings demonstrating sufficient biomarker (albumin, transferrin, A1AT, and ceruloplasmin) secretion over cultured days; indicating metabolic activity and function. Drug toxicity tests were facilitated through spheroid exposure to acetaminophen within the bioreactor. Analysis of cellular activity shows that the acute hepatotoxic dose results in apoptosis of HEPG2 cells within spheroids, resulting in decreased biomarker secretion levels over time. The liver-on-a-chip platformed detailed was shown to respond to acute toxic drug doses; and therefore, demonstrates the potential for bioprinting in organ engineering and drug-screening applications.

2.6.2.4 Skin Regeneration

Skin is the largest organ in the human body and serves as a protective barrier between the internal structures and the surrounding environment. This unique organ has three layers, the epidermis, dermis, and hypodermis. The epidermis is a thin layer attached to the basal membrane and primarily consists of keratinocytes and melanocytes.²⁴¹ The dermis is a vascularised layer which is rich in collagen and other ECM proteins excreted by fibroblasts; within this layer there are various other functional structures, including hair shafts and sweat glands.²⁴¹⁻²⁴² Alternatively, the hypodermis consists of mainly fat tissue which acts to insulate the body and provides an energy source.²⁴¹

Bioprinting-enabled skin regeneration was investigated by Cubo et al. wherein human bilayered skin constructs were printed using a fibrin-based bioink, containing fibroblasts and later seeded with keratinocytes.²²⁶ The bottom layer (dermal) of the construct was formed using a human fibroblast (hFB) laden fibrin bioink, whilst the upper layer (epidermal) was formed through seeding of human keratinocyte cells on top of the initial dermal equivalent. *In vitro* tests showed well-spread hFBs within the dermal layer after 17 days; with immunofluorescence analysis confirming proper growth and spreading of hFBs through human VIM expression. Keratin K10 expression was detected in suprabasal cells; indicating normal skin synthesis. *In vivo* tests completed through grafting skin substrates on immunodeficient athymic mice resulted in the development of grafted skin which was visually very similar to native human skin. Histological analysis found the regenerated skin presented a structure very similar to that of normal human skin, with all strata characteristic of normal skin easily identified. Immunofluorescence analysis of skin markers showed basal proliferation through K5 staining; while staining against human collagen VII shows high fluorescence at the dermo-epidermal junction demonstrating the presence of anchoring fibrils that bind together the epidermis and dermis. Analysis of K10 shows high expression which was characteristic of normal skin; while staining of filaggrin (a late differentiation marker) shows its presence in the granular layer. The presence of rete ridges suggests the developed skin was mature human skin rather than mouse skin, as mouse skin does not demonstrate the phenomenon. Immunostaining against human vimentin shows hFBs exclusively in the dermal region. This study highlights the potential of peptide-based bioprinting approaches in multicomponent tissue engineering applications.

2.7 Conclusion and Future Perspectives

The development of advanced artificial tissue-engineered constructs capable of effectively mimicking the intricacies of the native ECM would be of significant advance to the fields of tissue engineering, drug delivery and regenerative medicine. Currently, the requirement for vascularised, spatially defined constructs capable of simultaneously presenting biological and physical signals to cells is yet to be fully attained. Additive manufacturing offers promising resolve due to the inherent ability to spatially distribute cells, structures, and signals within an artificial biomimetic construct, enabling the development of a variety of tissues types.

Despite significant development of these systems, biomaterial selection remains a challenge; with few bioinks adequately recapitulating the complexities of the native ECM. Novel application-specific materials are required to truly mimic the properties of the native ECM. The materials must provide suitable biodegradability, biocompatibility and mechanical properties to the scaffold while enabling cell encapsulation and protection during printing processes. Furthermore, post-print crosslinking of these materials needs to be designed in such a way to minimise cell damage.

Peptide-based biomaterials are extensively researched and possess excellent biological properties including high biocompatibility and biodegradability. The ability of these materials to form hydrogels capable of encapsulating cells and biological factors while shielding cells from stresses encountered during bioprinting makes them highly suitable for in bioink development. Natural-peptide based biomaterials have been widely researched for bioprinting applications owing to their high bioactivity and resemblance to the native ECM. However, due to batch-to-batch variance and animal source, frontier applications would benefit from the development of synthetic peptide-based analogues. Semi-synthetic peptides have seen very little use in bioprinting applications, despite these inks demonstrating highly desirable properties for bioprinting applications.

The development of effective bioinks using functionalised SAPs would be a practical way to increase bioink bioactivity while maintaining desirable properties associated with synthetic materials. The propensity of these peptides to spontaneously self-assemble into nanoarchitectures which mimic

that of the ECM would not only provide a gentle cell-encapsulation mechanism but would also provide printed tissue constructs with favourable nanoarchitectures for tissue growth. However, to achieve advanced SAP-based bioinks, research needs to be placed into increasing SAP stability through triggered covalent crosslinking and improving the rate of material recovery post-printing.

The ability to print structures of controlled porosity as enabled through bioprinting applications would circumvent the immediate need to introduce vascularisation, enabling custom-controlled perfusability to printed constructs and allowing later infiltration of host-vascular tissues. Further improvements in material selection, bioink design, and printing technologies are essential to enable successful and effective tissue regeneration. The complex nature of organs necessitates elevated control over the spatial distribution of cells, structures and biological factors, and as such these need to be precisely controlled if functional tissue regeneration is to occur. Successful organ regeneration would greatly alleviate the current demand for donor organs and subsequently enable faster and more effective treatment methods; however, as of yet, organ engineering has seen limited success, with most current progress arising in simple tissue regeneration. The development of peptide and protein bioinks along with current advancements in printing technology will help to unlock the promise of 3D bioprinting to transform the field of regenerative medicine, and potentially, lead to the eventual regeneration of functional and effective organ tissues.

Chapter Three:

MATERIALS AND METHODS

3.1 Preview

This chapter gives a detailed account of all materials and experimental methods used throughout this research. All Fmoc-peptides were custom synthesised by Pepmic, Suzhou, Jiangsu, China. Peptides were tested for purity (>95%) using HPLC by Pepmic, Suzhou, Jiangsu, China upon purchase. Gelatin Methacryloyl (GelMA, 18% and 80% DoF) was purchased from the University of Wollongong, Wollongong, Australia. GelMA (46% and 61% DoF) was purchased from Sigma Aldrich, Australia. Transmission Electron Microscopy (TEM), Atomic Force Microscopy (AFM), and rheology shown in **Chapters 4 and 6** were performed at the labs of Institute for Frontier Materials (IFM), Deakin University, Waurn Ponds, Australia. TEM and Cryo-Scanning Electron Microscopy (CryoSEM) used through **Chapters 5, 8, and 9** were completed at RMIT Microscopy and Microanalysis Facility (RMMF), Melbourne, Australia. Small-angle X-ray scattering (SAXS) was completed at the Australian Synchrotron, Clayton, Australia. Small-angle neutron scattering (SANS) was completed at the ILL, Grenoble, France. Spectroscopic analysis performed as part of **Chapter 4 and 6** was performed at the Centre of Chemistry and Biochemistry, Deakin University, Waurn Ponds, Australia. Circular Dichroism (CD) performed through **Chapters 5, 8, and 9** were completed using the labs of the School of Science, RMIT, Bundoora, Australia. Fluorescence Spectroscopy and Fourier-Transform Infrared Spectroscopy (FT-IR) used in **Chapters 5, 8, and 9** were performed through the School of Engineering and Health, RMIT, Melbourne. Rheology presented in **Chapters 5, 7, 8, and 9**; and all bioprinting and printability

testing was performed at the Biofabrication 3D Centre (BioFab3D), St Vincent's Hospital, Melbourne, Australia.

All *in vitro* cell culture work completed in **Chapters 4 and 6** was performed in the labs of School of Medicine, Deakin University, Waurn Ponds, Australia. All *in vitro* cell culture detailed in **Chapter 5** was completed at labs in the School of Health and Biomedical Science, RMIT, Bundoora, Australia. *In vitro* cell culture work completed through **Chapters 8 and 9**, were completed in the labs of Biofabrication 3D Centre (BioFab3D), St Vincent's Hospital, Melbourne, Australia.

3.2 Fmoc-SAP Characterisation

3.2.1 Fmoc-SAP hydrogel Preparation

All solutions used to make peptides for *in vitro* cell culture were sterilise filtered using 0.22 µm PES Express® syringe filters (Merck Millipore Ltd. Cork, Ireland). Peptides were dissolved, and assembly was triggered under aseptic conditions.

3.2.1.1 Fmoc-SAP Hydrogels

The required amount (5 mg/mL or 10 mg/mL) of Fmoc-SAP was suspended into 400 µL MilliQ water (Direct-Q® 8 UV, Merck Millipore Ltd. Pty., Australia). 0.5 M NaOH was added via dropwise addition to the suspended peptide solution under constant, gentle vortex (BR-2000 Vortexer, Bio-Rad Laboratories Inc., NSW, Australia) until fully dissolved. Once dissolved, the peptide solution was charge neutralised via dropwise addition of 0.1 M Hydrochloric acid (HCl), such that a final pH of 7.4 was achieved. Finally, 0.1 M PBS (pH 7.4) solution, or Gibco® Dulbecco's Modified Eagle Medium (DMEM), (Life Technologies, Melbourne, Australia) containing 10% fetal bovine serum (FBS) was added such that the final, diluted concentration of peptide was either 5 mg/mL (for **Chapters 8, 9**) or 10 mg/mL (for **Chapters 4, 5 and 6**). The pH of the peptide hydrogel was measured using a microprobe pH meter (Oakton™ pH 700, Thermo Fisher Scientific). Fmoc-FRGDF and Fmoc-DIKVAV hydrogels were allowed to gel overnight in 37°C, while Fmoc-FRGDF, Fmoc-PHSRN and Fmoc-FRGDFPHSRN used through **Chapter 5** were allowed to gel over 10 days.

3.2.1.2 Coassembled Fmoc-SAP Hydrogels

The coassembled Fmoc-SAP hydrogels for **Chapters 4, 5 and 8** were prepared similarly to the Fmoc-SAP hydrogels mentioned above (**Section 3.2.1.1**); however, the single peptide was substituted for a 1:1 mix of peptide powder. Specifically, coassembled hydrogels used in **Chapter 4** contained 10 mg/mL of the peptide at a 1:1 mix (mass) of Fmoc-FRGDF and Fmoc-PHSRN. The coassembled hydrogel in **Chapter 5** contained 10 mg/mL of a 1:1 mix of Fmoc-FRGDF and Fmoc-DIKVAV. Finally, the coassembled Fmoc-FRGDF/Fmoc-PHSRN hydrogel used as a control in **Chapter 8** contained 5 mg/mL of Fmoc-FRGDF and Fmoc-PHSRN at a 1:1 weight ratio. Hydrogel formation was achieved as detailed above (**Section 3.2.1.2**).

Fmoc-FRGDF/Fmoc-DIKVAV hydrogels were allowed to form a gel over 24h, while PHSRN containing coassembly were allowed to gel over 72h.

3.2.1.3 Fmoc-SAPs containing Fucoidan or Versican Macromolecules

Fucoidan-Containing Hydrogel (Coassembled)

Fmoc-FRGDF was prepared as above (*section 3.2.1.1*), however prior to assembly the required amount of fucoidan (0.5 mg mL^{-1} , 2 mg mL^{-1} , 5 mg mL^{-1} , or 10 mg mL^{-1}) was added as a powder.

Fucoidan-Containing Hydrogel (Post-assembled)

Fmoc-FRGDF was prepared as above (*section 3.2.1.1*), however following assembly the required amount of fucoidan was added in solution such that a final concentration of 10 mg mL^{-1} is achieved.

Versican-Containing Hydrogel

Fmoc-FRGDF was prepared as above (*section 3.2.1.1*), however PBS was substituted for versican-transfected media mixed with growth media (25 mM glucose DMEM containing FBS) at a 1:4 ratio. Media was adjusted such that a final concentration of 10% FBS is achieved. *See Section 3.3.2 for versican conditioned media preparation.*

Empty Vector Control Hydrogel

Fmoc-FRGDF was prepared as above (*section 3.2.1.1*), however PBS was substituted for empty vector-transfected media mixed with growth media (25 mM glucose DMEM containing FBS) at a 1:4 ratio.

Media was adjusted such that a final concentration of 10% FBS is achieved. *See Section 3.3.2 for Empty-vector conditioned media preparation.*

3.2.2 1% Agarose Preparation

A 2% low-melting agarose (#200-0030, Progen Ind. Ltd., Australia) solution was dissolved in dH₂O and heated using a microwave to melt sample. Repeated stirring and heating was performed until the solution comes to a boil. The solution was then autoclaved before the sterile 2% agarose was cooled to 37°C prior to mixing with equal volume sterile complete DMEM medium (with 10% or 20% FBS) or 0.1 M PBS to form a 1% agarose mixture. The mixture was set at room temperature before spheroid encapsulation (in media containing gel) or mechanical analysis (in PBS containing gel).

3.2.3 Bioink Preparation

3.2.3.1 Gelatin Methacryloyl Bioinks

Gelatin Methacryloyl (GelMA) with 18% and 80% degree of functionalisation (DoF) was purchased from the University of Wollongong, Wollongong, NSW, Australia. Non-sterile GelMA was dissolved (at 37°C) in MilliQ water such that the final concentration is < 2% (w/v). Following being left for 24h to dissolve, solution (40 mL at a time) was passed through a syringe filter (0.22 µm PES Express® syringe filters, Merck Millipore Ltd. Cork, Ireland) into 50 mL, pre-weighed Mini Bioreactors (Corning, NY, USA) under aseptic conditions to sterilise solution. Permeable caps were then fitted to tubes, and sterile aliquots were frozen at -80°C. Frozen aliquots were then removed and placed into a freeze drier (Alpha 1-2 LD Plus, Martin Christ Gefriertrocknungsanlagen GmbH, Germany) for 72h. Following 72h, samples weight was recorded once an hour for 3 hours to ensure stable mass indicating samples are sufficiently dry. Sterile, dry aliquots were then sealed with fresh, sterile caps (under aseptic conditions) and stored in -80°C until use.

46% and 61% DoF GelMA (Sold as *Gelatin Methacryloyl 300 Bloom 40% DoF (900629-1G)*, and *Gelatin Methacryloyl 300 Bloom 60% DoF (900622-1G)*, respectively) was purchased from Sigma Aldrich, Australia. 46% and 61% DoF GelMA was maintained under sterile and dry conditions until time of use.

Sterile GelMA stock solutions were formed through the dissolve of dry GelMA in 0.1 M PBS such that the final LM-GelMA concentration is 15% (w/v). GelMA bioinks were prepared by dilution of GelMA stock to a final concentration of 6% (w/v) (**Chapters 7, 8, 9**) and 10% (w/v) (**Chapter 7**) in $1 \times$ PBS with 0.1% (**Chapter 7**) or 0.025% (**Chapter 8 and 9**) Lithium phenyl-2,4,6-trimethylbenzoylphosphinate (LAP) (Tokyo Chemical Industry Co. Ltd., Tokyo, Japan). Reduced LAP levels were desired when used for cell-seeding applications. Bioinks were stored at 37°C under UV-protected conditions until time of use (within 3 days).

GelMA bioinks prepared for *in vitro* cell culture experiments were made to 90% volume (through minimalization of PBS addition) to allow sufficient volume for cell inclusion. Before use, 15 million mouse primary myoblasts (**Chapter 8**) or 15 million rat cortical neurospheres (**Chapter 9**) were incorporated into the bioink via short and gentle vortex. Bioinks were then placed in incubation for 10 minutes to allow bubbles to settle.

3.2.3.2 Hybrid Fmoc-FRGDF/Fmoc-PHSRN/GelMA Bioinks (FPG-Hybrids)

Fmoc-FRGDF/Fmoc-PHSRN/GelMA (FPG-Hybrid) bioinks (**Chapter 8**) were prepared as coassembled Fmoc-SAP hydrogel (5 mg/mL Fmoc-SAP concentration), however before addition of $1 \times$ PBS, $400 \mu\text{L mL}^{-1}$ of 15% (w/v) Low-Methacryloyl Gelatin Methacrylate (LM-GelMA, 18% DoF), and $12.5 \mu\text{L mL}^{-1}$ LAP (2%) was added and briefly vortexed such that a final concentration of 6% (w/v) LM-GelMA, and 0.025% LAP exists. FPG-Hybrid bioinks were allowed to gel over 72h at 37°C under UV-protected conditions.

FPG-Hybrids prepared for *in vitro* cell culture experiments were made to 90% volume (through minimalization of PBS addition) to allow sufficient volume for cell inclusion. Bioinks were prepared under aseptic conditions and assembled over 72h. Before use, 15 million mouse primary myoblasts were incorporated into the bioink via short and gentle vortex. Bioinks were then placed in incubation for 10 minutes to allow bubbles to settle.

3.2.3.3 Hybrid Fmoc-DIKVAV/GelMA Bioinks (DIKVAV-Hybrids)

Fmoc-DIKVAV/GelMA bioinks (DIKVAV-Hybrids, **Chapter 9**) were formed similarly to FPG-Hybrid bioinks; however, 5 mg/mL Fmoc-FRGDF/Fmoc-PHSRN (1:1 ratio) was substituted for 5 mg/mL Fmoc-DIKVAV. Bioink formation was achieved as detailed above (**Section 3.2.3.2**). Fmoc-DIKVAV/GelMA bioinks were allowed to gel over 24h at 37°C under UV-protected conditions.

For DIKVAV-Hybrids prepared for casting and subsequent rat cortical neurosphere seeding, neurospheres were prepared under aseptic conditions and placed into 48-well plates (CELLSTAR®, Greiner Bio-one GmbH, Kremsmünster Austria). Hydrogels were then UV (365 nm) crosslinked at 4.5 mW cm⁻² (UVP crosslinker, analytikjena, Jena, Germany) for 8 minutes followed by a short wash with PBS. Rat cortical Neurospheres were then seeded onto the bioinks at 1×10^4 cells per well.

For DIKVAV-Hybrids prepared for *in vitro* encapsulation and bioprinting experiments, bioinks were made to 90% volume (through minimalization of PBS addition) to allow sufficient volume for cell inclusion. Bioinks were prepared under aseptic conditions and assembled over 24h. Before use 15 million rat cortical neurospheres were incorporated into the bioink via short and gentle vortex. Bioinks were then placed in incubation for 10 minutes to settle bioinks and remove any induced bubbles.

3.2.4 Circular Dichroism

Dilute samples ranging in concentration from 0.1% to 0.001% (w/v) (Diluted in MilliQ water) were scanned using a Jasco J-815 Circular Dichroism Spectropolarimeter (Jasco Inc., Maryland, USA) from 330-180 nm. 5 accumulations were averaged for each sample with a 1 nm data interval, 2 s⁻¹ integration time, and at 50 nm min⁻¹ (**Chapter 4**) or 100 nm min⁻¹ (**Chapter 4, 5, 6, 8, 9**). A 1 mm quartz cell (Starna Pty. Ltd., Australia) was used for all samples. A MilliQ (**Chapters 4 and 6**) or dilute PBS (**Chapters 5, 8, 9**) background was obtained and subtracted from each sample. Data was smoothed with inbuilt software (Jasco J-815 Circular Dichroism Spectropolarimeter).

3.2.5 Fourier Transform Infrared Spectroscopy

For **Chapters 4 and 6**, a Nicolet 6700 Fourier Transform Infrared Spectrometer (Waltham, MA, USA) in attenuated total reflection (ATR) mode was used to collect sample spectra. 12 µL of sample was

placed directly on the ATR crystal and scanned between wavenumbers 4000 cm^{-1} and 400 cm^{-1} over 64 scans. A background scan of PBS was acquired and subtracted from each sample.

For **Chapters 8 and 9**, FT-IR spectrums were acquired from a Frontier FT-IR/FIR spectrometer, Bruker D8 XRD (Bruker Co. Massachusetts, USA) from wavenumbers 4000 cm^{-1} to 400 cm^{-1} at a resolution of 1 cm^{-1} . 16 accumulations were performed, and a background ($1 \times \text{PBS}$) was acquired and subtracted from samples. Data was smoothed with inbuilt software (Frontier FT-IR/FIR spectrometer, Bruker D8 XRD).

3.2.6 Fluorescence Spectroscopy

For **Chapters 4 and 6**, fluorescence emission spectra were collected using a Cary Eclipse fluorescence spectrophotometer (Agilent Technologies CA, USA). The emission bandwidth was set to 5 nm, and scanning speed was set to 600 nm/min with a 1.0 nm data pitch. An excitation wavelength of 248 nm was selected, and emission was monitored from 300 nm to 600 nm. A quartz cuvette (Starna Pty. Ltd., NSW, Australia) of 1 mm path length was used during tests. Samples were diluted in MilliQ water to a final peptide concentration of 0.5% wt.

For **Chapter 8**, sample fluorescence emission spectra were measured on a LS55 PerkinElmer Spectrometer (PerkinElmer, Australia). An emission bandwidth was set at 2.5 nm, and a scanning speed of 50 nm/min was selected with data pitch of 0.5 nm. The excitation wavelength was set at 248 nm, and emission was monitored between 200 nm and 600 nm. A quartz cuvette (PerkinElmer, Australia) of 10 mm path length was used for scanning. Samples were diluted 1:5 in MilliQ water.

3.2.7 Atomic Force Microscopy

AFM images of the samples were collected using a Multimode 8 atomic force microscope (Bruker BioSciences Co. Massachusetts, USA). For sample preparation, peptide hydrogels (10 mg/mL) were diluted to a final peptide concentration of 0.5 mg/mL before 15 μL of each diluted solution was applied to highly ordered pyrolytic graphite (HOPG) substrates (SPI), with any excess sample being absorbed by pipet. The tips used were ScanAsyst-Air probes with silicon tip on nitride lever (Bruker BioSciences

Co. Massachusetts, USA). The scan was operated in PeakForce QNM imaging mode with a scan size of 10 μm^2 .

3.2.8 Transmission Electron Microscopy

For **Chapters 4 and 6**, A JEOL-2100 LaB6 transmission electron microscope (TEM) (JEOL Ltd., Japan) at an operation voltage of 100 kV was used for TEM imaging. Images were acquired through a Gatan Orius CCD camera (Cuddy, PA, USA). Lacey carbon coated films on 300 mesh copper grids (Emgrid Pty. Ltd., Australia) were used as sample holders. 12 μL of dilute sample (5:1 dilution in MilliQ water) was applied onto the grid and allowed to absorb for 5 minutes, following which Whatman filter paper (No.1) was used to wick off excess fluid. One drop of negative stain NanoVan (Bio-Scientific Pty. Ltd., USA) was put onto parafilm “M”, then the grid was placed on the stain with carbon side down for 5 minutes. Samples were then dried in air for 2 minutes with carbon side up before grids were placed into the grid box and left to dry overnight.

For **Chapters 5, 8 and 9**, Strong carbon grids (GSCu200C-25, ProScitech, Australia) were placed on a 15 μL droplet of sample at a 1 in 5 sample dilution (diluted in MilliQ water) for 30 s; excess was wicked away with Whatman filter paper. All droplets were deposited on parafilm. Grids were placed on a 15 μL droplet of uranyl acetate 1% stain for 5 min; excess was wicked away with Whatman filter paper and left at room temperature to air dry overnight. Bright Field TEM was performed at an accelerating voltage of 80kV (JEOL 1010 Transmission Electron Microscope). Images were captured by a Gatan Orius SC600 CCD Camera (Cuddy, PA, USA) . Fibril diameter was determined through use of the measuring tool in ImageJ, n=5. The average diameter and standard deviation were calculated for each sample.

3.2.9 Cryo-Scanning Electron Microscopy

CryoSEM was used to determine hydrogel microstructure. Fmoc-SAPs were prepared as detailed in **sections 3.2.1 and 3.2.3**; however, PBS was replaced with MilliQ water to minimise salt bridging. Although this would have some effects on network presentation;²⁴³ MilliQ substitution allowed for visualisation of network fibrils otherwise masked by salt bridging, and therefore was selected as the

best approach for comparing sample network organisation. Samples were plunge frozen into liquid nitrogen slush for ~30 seconds before being immediately transferred to a Gatan cryo-chamber and fractured at -170 °C. Samples were then sublimated at -95 °C for 2 minutes to remove amorphous surface ice and reveal structure depth. Samples were then gold sputter coated for 140 s before being imaged at 15 kV, spot size 5 (FEI Quanta 200 ESEM, Thermo Fisher Scientific). Fibril bundle diameter was determined through use of the measuring tool in ImageJ (n=5, **Chapter 5**); and average diameter and standard deviation were calculated for each sample.

3.2.10 Small-Angle X-ray Scattering

SAXS was performed at the Australian Synchrotron (Melbourne, Australia) using the SAXS/WAXS beamtime. Measurements used in **Chapter 4** were taken at a calibrated camera length of 1598 mm with X-ray energy of 11 KeV (1.12713 Å). Using this length, a scattering vector (q) could be measured across the range of 0.01 to 0.6 Å⁻¹. Measurements used in **Chapters 5, 7, 8 and 9** were acquired at a calibrated camera length of 967.667 mm with X-ray energy of 12KeV (1.03320 Å); allowing for scattering vector (q) to be measured across the range of 0.018 to 0.92 Å⁻¹. The diffraction pattern was recorded on a Pilatus 1M detector (169 mm × 179 mm, effective pixel size (172 μm × 172 μm) and processed using the Australian Synchrotron ScatterBrain Software (Melbourne, Australia). Hydrogels were prepared as detailed above (**Sections 3.2.1 and 3.2.3**) and loaded into 1.5 mm glass capillaries with a wall thickness of 0.1 mm (Hilgenberg, GmbH, Malsfeld, Germany). Where appropriate (**Chapters 7, 8, 9**), samples were crosslinked within capillaries for 8 minutes at 4.5 mW cm⁻². PBS backgrounds with and without LAP were collected before samples were loaded. Each sample (and background) was subjected to ten, 1 s⁻¹ exposures at multiple (n=3) points along the capillary to minimise sample burning (**Chapters 5, 7, 8 and 9**). Repeat measurements were summed using Scatterbrain and q calibrated using an AgBeh sample, and intensity was normalised and set on an absolute scale using water and air shots. Due to poor scattering, backgrounds were scaled by 0.9 (**Chapter 5, 8 and 9**) before subtraction from the sample scattering data. For Fmoc-SAP and coassembled Fmoc-SAP hydrogel fibril radius calculations, data was subject to indirect Fourier-transform (IFT) analysis and P(r) inversion using SASView (SASView, Australia) to calculate the

average diameter of the fibrils in the sample. For GelMA, FPG-Hybrid, and DIKVAV-Hybrid samples, data was fit to shape independent models using SASView. Specifically, the mass fractal dimension was determined through fitting with a power law model between mid q range ($0.05 - 0.2 \text{ \AA}^{-1}$, **Chapters 7, 8, 9**); correlation length was determined through fitting with correlation length model at low-mid q range ($0.018 - 0.2 \text{ \AA}^{-1}$, **Chapters 5, 7, 8**); and mesh size was determined through fitting with two-power law model at low-mid q range ($0.018 - 0.2 \text{ \AA}^{-1}$, **Chapters 5, 7, 8, 9**). All acquired scatter curves, and subsequent fits were further graphed using GraphPad Prism 7 (GraphPad Prism Software Inc., San Diego, USA, **Chapter 5, 8, 9**) for ease of graphical visualisation.

3.2.11 Small-Angle Neutron Scattering

SANS data was attained using the D33 instrument at the Institut Laue-Langevin, Grenoble, France. Scattering was measured at two sample-detector distances of 2 m and 12 m, allowing for a q range of $0.03 - 0.5 \text{ \AA}^{-1}$. A fixed wavelength mode was used with a wavelength of 6 \AA and a wavelength resolution of $\Delta\lambda = 10\%$. Data from the two detector distances were reduced using the GRASP program and joined through use of the NIST SANS package for Igor Pro. Samples were prepared at 21.5% Deuterium oxide (D_2O) to contrast match for fucoidan, leaving only scattering relating to the peptide assemblies. Fucoidan-only samples were prepared in D_2O solution for maximum contrast and background reduction. Samples were measured in sealed 1 mm path-length Hellma[®] cells (Hellma, UK). Samples were injected into cells and heated in a water bath to 70°C to nullify shear effects encountered during sample loading.

3.2.12 Oscillatory Rheology

3.2.12.1 Rheological Frequency Sweep

Chapter 4 and 6: Mechanical properties of the hydrogels at various frequencies were determined through rheological measurements taken on a Discovery Hybrid Rheometers (TA Instruments, New Castle, DE, USA) using a cone-plate geometry (40 mm , 2° $1' 37''$) with a $51 \text{ }\mu\text{m}$ truncation gap. Sample was placed onto the lower plate to cover the measured area completely and excess trimmed. To ensure the measurements were made in the linear viscoelastic regime, amplitude sweeps were performed at a constant frequency of 10 rad/s with shear strain $0.01\text{--}100\%$. Data on dynamic frequency sweeps were

collected over a range between 0.1 and 100 rad/s at a constant strain (0.4% in **Chapter 4**, 2.83% in **Chapter 4**, and 1% in **Chapter 6**). Temperature was maintained at 25°C via the use of Peltier plate control. A water trap was used to minimise sample evaporation. All measurements were carried out in triplicate to ensure reproducibility with the show of the average data.

For viscoelastic data acquired during **Chapter 5**, storage and loss moduli were acquired under oscillatory conditions using a calibrated rheometer (Anton Paar MCR 301, Austria) fitted with a 15 mm cone plate fixture with a cone angle of 1° (CP15-1, Anton Paar GmbH, Austria); a water trap was used to minimize sample evaporation and drying. Data on dynamic frequency sweeps were collected over a range between 0.1 and 20 Hz at a constant shear strain of 0.1%. The temperature was maintained at 37°C via the use of Peltier plate control. All measurements were carried out in triplicate to ensure reproducibility with the show of the average data.

3.2.12.2 Rheological Temperature Sweep

Storage and loss moduli were acquired under oscillatory conditions using a calibrated rheometer (Anton Paar MCR 301, Anton Paar Pty. Ltd. Australia) fitted with a 15 mm cone plate fixture with a cone angle of 1° (CP15-1, Anton Paar Pty. Ltd. Australia); Paraffin oil (Sigma Aldrich, Australia) was placed over the cone to avoid dehydration. Thermal dependent viscoelastic properties were acquired via temperature sweep from 37 °C to 4 °C (~0.97°C min⁻¹) and at a shear strain of 0.1% and angular frequency of 10 rad s⁻¹.

For **Chapter 7**, gradient of stiffness change in response to temperature decrease was determined as follows. Firstly, the temperature (T₁) and storage modulus (G'₁) where loss tan = 0.1 is determined; next, storage modulus (G'₂) at a temperature 4 °C below T₁ is determined. G'₁ is then subtracted from G'₂ before subsequent division by 4; as described by equation

$$\text{Gradient of storage modulus increase} = \frac{G'_1 - G'_2}{4^\circ\text{C}}$$

Equation 3-1 – Calculation of stiffness gradient in response to temperature

Where G'₁ and G'₂ are measured in kPa.

Here, gradient of stiffness change was monitored over the first 4 °C to ensure uniform sample analysis.

3.2.12.3 Rheological *In Situ* Crosslinking and Shear Resistance

Storage and loss moduli were acquired under oscillatory conditions using a calibrated rheometer (Anton Paar MCR 301, Anton Paar Pty. Ltd. Australia) fitted with a 15 mm cone plate fixture with a cone angle of 1° (CP15-1, Anton Paar Pty. Ltd. Australia); Paraffin oil (Sigma Aldrich, Australia) was placed over the cone to avoid dehydration. *In situ* UV crosslinking was performed at a wavelength of 365 nm and intensity of 4.5 mW cm⁻² for 20 minutes (OmniCure Lx400+, Lumen Dynamics Group Inc., Canada). UV intensity was verified using an OmniCure LED Light Meter System (Lumen Dynamics Group Inc., Canada). Samples were allowed to stabilise for 1-minute before UV application. Constant shear strain of 0.1%, angular frequency of 10 rad/s and temperature of 37 °C was used during UV crosslinking. Crosslinking was performed for 15 minutes (**Chapter 7**) or 20 minutes (**Chapter 8, 9**). An amplitude sweep was obtained following crosslinking via a shear strain logarithmic ramp from 0.1% - 1000% at an angular frequency of 10 rad/s and at 37 °C. For analysis of shear yield point in **Chapter 7**, the complex modulus was plotted against shear-strain, and point of peak stress calculated.

Structure-function correlations obtained in **Chapter 7** were calculated using GraphPad Prism 7 (GraphPad Prism Software Inc., San Diego, USA,). Specifically, a Pearson correlation test was performed between each sample with a 95% confidence interval and Pearson r values were calculated and plotted as a heatmap for ease of visualisation. A Pearson value of 1 indicates a perfect correlation while -1 indicates a perfect inverse correlation. For this study, anything above 0.5 or below -0.5 was considered well-correlated.

3.2.13 Printability Tests

Bioinks were prepared as above (**Section 3.2.3**), and immediately placed into 3 mL Optimum[®] syringe barrels (Nordson EFD, Ohio, USA) after which bioinks were sealed and allowed to self-assemble over 24h (**Chapter 9**) or 72 h (**Chapter 8**) in 37°C incubation. For temperature printability tests, bioinks were cooled to 10°C, 15°C, and 20°C using an ES SERIES laboratory refrigerator (Thermo Fisher Scientific). Cartridge temperatures were monitored using a FLIRone thermal camera (FLIR Systems

Australia Pty Ltd., Australia). After cooling, Cartridges were fitted with conical 22G (TT) Blue Precision Tips (Nordson EFD, Ohio, USA) and placed into an Inkredible® Bioprinter (CELLINK AB, Gothenburg, Sweden) where they were prepared for bioprinting as per manufacturers recommendations. Briefly, axis' were homed, and z-position calibrated. Pneumatic pressure was facilitated through MC mini compressor (MC90, Biltema, Helsingborg, Sweden) and further regulated to maintain consistent pressure (AD300C dispenser, Iwashita Engineering, Inc., Japan). A $4 \times 4 \times 2$ grid-like pattern (2.5 mm strut spacing) was designed via in-house G-code and verified through printing with CELLINK START (**Supplementary Figure S - 11**). Bioinks were printed and extrusion pressure was adjusted accordingly with changes in viscosity between bioinks and printing temperatures. Pressures ranged between 30 – 60 kPa. Printed grid constructs were printed onto cooled (-20°C) dishes (Greiner Bio-one GmbH, Kremsmünster Austria) and crosslinked immediately after printing at 365 nm and 4.5 mW cm^{-2} for 8 minutes (UVP crosslinker, analytikjena, Jena, Germany). Images were taken both before and after crosslinking. Following crosslinking, samples were fully submerged in PBS and shape fidelity (swelling and degradation) was monitored for 4 weeks under simulated culture conditions (PBS, 37°C).

For **Chapter 9**, and additional two grids were designed with alternate strut-spacings. Specifically, one $8 \times 8 \times 2$ grid was designed with strut spacings of 1.5 mm, and a second $10 \times 10 \times 2$ grid was designed with 1 mm strut spacings. Grids were printed and crosslinked as above.

Additionally, in **Chapter 9**, a DIKVAV-Hybrid construct was printed in a $4 \times 4 \times 2$ grid-like pattern (2.5 mm strut spacing) as above however, LM-GelMA was substituted for LM-GelMA containing 0.03% Fluorescein Isothiocyanate-labelled (FITC) GelMA for a final FITC-labelled GelMA concentration of 0.012%. FITC-GelMA was kindly donated by Dr. Zhilian Yue (University of Wollongong, Australia). Fluorescently-labelled DIKVAV-Hybrid constructs were then printed and crosslinked as above, before observation via fluorescence microscopy (EVOS FL Fluorescence Microscope, Life Technologies) to confirm GelMA isolation to structural regions.

3.2.14 Bioprinting

Bioinks were prepared as above (**Section 3.2.3**); however, measures to ensure sterility were observed. Specifically, all reagents were prepared sterile, and assembly was performed under aseptic conditions.

For bioprinting conducted during **Chapter 8**, bioinks were prepared as detailed in **section 3.2.3**. Cell incorporated bioink was transferred to previously sterilised bioink cartridge via 1 mL pipette and allowed to settle for 10 minutes under incubation at 37 °C before subsequent cooling to optimal temperature as determined in printability tests (10 °C and 15 °C for LM-GelMA and FPG-Hybrid respectively). Cartridge temperature was monitored via FLIRone thermal camera to ensure accuracy. Bioinks were printed into a grid as above, and immediately UV crosslinked at 4.5 mW cm⁻² for 8 minutes using an OmniCure LED Light Meter System (Lumen Dynamics Group Inc., Canada). Bioprinted grids were immersed in 2 mL proliferation media (Ham's F10 (Thermo Fisher) supplemented with 20% Fetal Calf Serum (Gibco), 2.5 ng bFGF (Peprotech), 2 mM L-glutamine (Gibco) and 1 × penicillin/streptomycin (Gibco)) for 10 minutes before media was removed and fresh media added. Constructs were then placed in incubation (5% CO₂) and maintained at 37 °C with 1 mL media change every 24 h. Triplicate grids were fabrication and analysed per time point.

For bioprinting conducted in **Chapter 9**, bioinks were prepared as detailed in **section 3.2.3**. Cell incorporated gel was transferred to previously sterilised bioink cartridge via 1 mL pipette and allowed to settle for 10 minutes under incubation at 37 °C before subsequent cooling to optimal temperature as determined in printability tests (10 °C and 15 °C for LM-GelMA and Fmoc-DIKVAV/GelMA Hybrid respectively). Cartridge temperature was monitored via FLIRone thermal camera to ensure accuracy. Bioinks were printed using a 25G red (TT) conical needle (Nordson EFD, Ohio, USA) into a grid as above, and immediately UV crosslinked at 4.5 mW cm⁻² for 8 minutes using an OmniCure LED Light Meter System (Lumen Dynamics Group Inc., Canada). Bioprinted grids were immersed in DMEM/F12 for 10 minutes followed by media removal and immersion in fresh neuroproliferation media (Neurocult NS-A Proliferation Kit (STEMCELL technologies) supplemented with 20 ng/mL bFGF (Peprotech), 20 ng/mL EGF (Peprotech), 2 µg/mL Heparin (STEMCELL technologies) and 1 × penicillin/streptomycin (Gibco)). Constructs were then placed in incubation (5%

CO₂) and maintained at 37 °C with 1 mL media change every 24 h. Triplicate grids were fabrication and analysed per time point.

3.3 *In Vitro* Cell Culture

3.3.1 Cell Lines and Culture Conditions

Chapter 4: Primary Human Mamillary Fibroblast Cells (HMFCs) were maintained and cultured in the fibroblast media containing 10% FBS, fibroblast growth supplement, 2% penicillin/streptomycin (ScienCellResearch Laboratories, Carlsbad, CA, USA) at 37 °C and 5% CO₂. After reaching 80–90% confluence cells were detached using Trypsin/EDTA.

Chapter 5: Murine Lewis Lung Carcinoma (LLC) cell line was provided by the Peter MacCallum Cancer Centre, Melbourne, Australia. LLC cells were cultured in complete 10 media (DMEM, 1× penicillin/streptomycin and 10% FBS). Murine skeletal muscle fibroblasts (NOR-10) were purchased from ATCC, USA, and maintained in a complete 20 media (DMEM, 2 mM Glutamine, 1× penicillin/streptomycin and 20% FBS). Cells were incubated at 37°C and 5% CO₂. After reaching 80–90% confluence LLC cells were detached using 0.05% Trypsin/EDTA and NOR-10 using 0.25% Trypsin/EDTA.

LLC and NOR-10 cells were cultured in monolayer with media described above. Spheroids were formed through seeding of LLC, NOR-10 and co-culture cell populations (LLC and NOR-10 at 1:1 ratio) at 1×10^4 cells/well using 96-well, ultra-low attachment, round-bottom plates (Corning Inc., NY, USA). After 24h culture, dense multicellular spheroids were observed. These spheroids were termed 3D. 3D+ECM spheroids were formed through spheroid encapsulation in a coassembled Fmoc-SAP. For 2D cultures, cells were cultured in tissue culture 96-well flat-bottomed plates (Corning Inc., NY, USA) using the same culture media and at the same cell concentration.

Chapter 6: HEK-293T cells were cultured in DMEM containing 10% (v/v) FBS and 0.4% (v/v) penicillin/streptomycin in atmospheric O₂ plus 5% CO₂ at 37°C. C2C12 myoblasts were cultured in growth media (25 mM glucose DMEM plus 10% FBS, (Thermo Fisher, Australia)) in atmospheric O₂ with 5% CO₂ at 37°C and passaged when 70 – 80% confluent.

Chapter 8: Primary myoblasts isolated from C57Bl/6 mice (ARC, Western Australia) were generously donated by Dr Anita Quigley (St. Vincent's Hospital Melbourne, Australia). Myoblasts were cultured in growth media (HamsF10 (Gibco), 20% FCS (Gibco), 2.5ng/ml bFGF (Peprotec), 2mM L-glutamine (Thermo)), 100 units/mL penicillin and 100 µg/mL streptomycin (Thermo)) in atmospheric O₂ with 5% CO₂ at 37°C and passaged when 70 – 80% confluent. Myoblasts were differentiated in DMEM (Lonza), 2% Horse Serum (Gibco), 2mM L-glutamine and 100 units/mL penicillin and 100 µg/mL streptomycin (Thermo).

Chapter 9: Cortical neurosphere cultures isolated from E18 Sprague Dawley rat pups were generously donated by Dr Anita Quigley (St. Vincent's Hospital Melbourne, Australia). Neurospheres were propagated using a Neurocult NS-A Proliferation Kit (STEMCELL Technologies), supplemented with 20 ng/ml EGF (Peprotec) and 20ng/ml bFGF (Peprotec), according to manufacturer instructions. Neurospheres were differentiated in DMEM/F12 (Lonza) supplemented with 1% Stempro (Thermo Fisher), 0.5% N2 (Thermo Fisher), 20 ng/mL BDNF (Peprotech), 100 units/mL penicillin and 100 µg/mL streptomycin (Thermo).

3.3.2 Preparation of Versican and Empty Vector Conditioned Media

Lipofectamine 2000 (Life Technologies) was used to transfect cells with constructs encoding the V1 versican construct (provided by Professor Dieter Zimmermann) or the empty vector control (pcDNA3.1MycHisA, Life Technologies). Conditioned medium was produced as previously described.²⁴⁴ The conditioned media was collected into 1.5 mL Eppendorf tubes at 48 h post-transfection and stored at –80°C. 10% FBS was added to the conditioned media before use.

3.3.3 Western Blotting of Versican Enriched Conditioned Media

Versican was deglycosylated through addition of Chondroitinase ABC to aliquots of conditioned media improving V1/V0 versican anti-GAG-β antibody (AB1033, Merck Millipore Ltd. Pty., Australia) binding affinity to V1 versican. To prepare conditioned media samples for immunoblotting, Chondroitinase ABC was added to versican or empty vector conditioned media at a 1:30 ratio and incubated at 37°C for 2 h. Samples were then diluted with a 4 × loading buffer (Bio-Rad Laboratories

Inc., NSW, Australia) containing β -mercaptoethanol and incubated for 5 minutes at 95°C. Samples were run at 120 V on mini-protean TGX stain-free gels (Bio-Rad Laboratories Inc., NSW, Australia). Gels were then activated, and proteins visualised using the ChemiDoc XRS+ system (Bio-Rad Laboratories Inc., NSW, Australia). Gels were then transferred to Polyvinylidene difluoride (PVDF) membranes using the Trans-Blot Turbo system (Bio-Rad Laboratories Inc., NSW, Australia) as per manufacturer's recommendations. PVDF membranes were blocked in 5% (w/v) skim milk in tris-buffered saline with tween (TBST) for 1h at room temperature, then incubated overnight at 4°C with versican anti-GAG- β antibody (AB1033, Merck Millipore Ltd. Pty., Australia) (1:500 dilution in 1% skim milk). Samples were then incubated for 1h with a secondary goat anti-rabbit HRP antibody in 1% skim milk in TBST (1:5000). Bands were observed using an ECL substrate (Bio-Rad Laboratories Inc., NSW, Australia), and blots were imaged through the ChemiDoc XRS+ system.

3.3.4 Immunofluorescence to Confirm Media Incorporation to Scaffolds

Hydrogels were prepared with either versican or empty vector conditioned media as outlined in **Section 3.2.1.3**. Aliquots of gel samples were air-dried on poly-L-lysine microscope slides before fixing with 4% paraformaldehyde in PBS for 5 minutes at room temperature. Immunostaining was performed using the V1/V0 versican anti-GAG- β antibody, as previously described.²⁴⁵ Stained gels were imaged on a benchtop confocal microscope (Fluoview FV10i, Olympus, Australia) at 600 \times magnification.

3.3.5 Live/Dead Cell Staining

Chapter 6: C2C12 cells were stained using calcein AM and propidium iodide (Sapphire Bioscience Pty. Ltd., NSW, Australia) as per manufacturer's instructions to show the relative percentage of live/dead cells at 24 and 72h post seeding onto the four hydrogel groups. Following 60 minutes incubation in atmospheric O₂ with 5% CO₂ at 37°C, live and dead cells were imaged using a ZOE fluorescence cell imager (Bio-Rad Laboratories Inc., NSW, Australia) at 200 \times magnification. Live cells stained green with calcein AM, and dead cells stained red with propidium iodide. Cell-size was monitored as an indicator of cell spreading and was measured using ImageJ. N = 3 biological replicates were performed in duplicate wells for each scaffold at each time point. Total cell area was determined for an average of 880 cells per scaffold.

Chapters 8 and 9: At 24 and 72 h in culture 1 mL media was gently removed and Ethidium bromide and Calcein AM stains were added to constructs as per manufacturers instruction. Cells were stained for 15 minutes (**Chapter 8**) and 30 minutes (**Chapter 9**) to ensure sufficient fluorescence. Stained cells were observed under a fluorescent microscope (EVOS FL Fluorescence Microscope, Life Technologies) and imaged at 100x (**Chapter 8**) or 200x (**Chapter 9**) magnification. A Live/Dead cell count was performed manually using ImageJ cell counter and the relative proportion of live cells determined.

3.3.6 Cell Proliferation and Metabolic Activity

Chapter 4: Hydrogels were seeded with HMFC cells (4000 per well in 100 μ L of media) and cultured for 24, 48 and 72h on Fmoc-FRGDF, Fmoc-FRGDFPHSRN, and coassembled Fmoc-FRGDF/Fmoc-PHSRN (1:1, w/w) samples. Live cell quantification was performed through a colourimetric method by adding MTS reagent (Promega, Madison, WI, USA) to cells at each timepoint. MTS (20 μ L) was added to samples and gently mixed. Cells were then incubated for 4 h at 37 °C before reading absorbance values at 490 nm using spectrophotometer (Bio-Rad, Hercules, CA, USA).

Chapter 5: LLC, NOR-10 and co-culture 3D+ECM spheroid metabolic activity was determined to investigate cell response to encapsulation within Fmoc-SAP hydrogels. A CellTiter 96[®] AQueous One Solution Cell Proliferation Assay (Promega, Madison, WI, USA) was used and samples were compared to non-encapsulated 3D spheroids, according to manufacturer's instructions. Briefly, after 3D+ECM and 3D spheroid formation and incubation, MTS solution was added to each well and incubated at 37°C for 4 hours. Supernatant (100 μ L) was then transferred to a clean flat-bottom 96-well plate (Corning Inc., NY, USA) and cell metabolic activity was quantified through absorbance measurement at 490 nm using a plate reader (Clariostar plate reader, BMG LABTECH, Australia)

Chapter 6: Following 72h seeding, cell number was determined using a commercially available cytotoxicity kit (Vybrant Cytotoxicity AssayKit (Glucose-6-phosphatedehydrogenase (G6PD) Release Assay, V231111, Thermo Fisher Scientific), as per manufacturer's recommendation with the following modifications. Hydrogel samples were solubilised in 15 mL PBS and centrifuged for 5 minutes at 3202g

to pellet cells. 12 mL of PBS was then removed, and myoblasts were washed and recentrifuged in 15 mL of fresh PBS. The resultant cell pellet was then resuspended in 1 mL of PBS and centrifuged for 5 minutes at 11688g. The cell pellet was then lysed using 1% lysis buffer for 15 minutes on ice. Samples were then diluted at 1:10 to assay glucose-6phosphate activity (a marker of cell number) using a multimode microplate reader Flexstation II384 (Molecular Devices, San Jose, CA, USA) at an excitation wavelength of 544 nm emission wavelength of 590 nm. Remaining cell lysate was used to assess total protein content as an indicator of cell growth through use of a Pierce BCA Protein Assay Kit (Thermo Fisher Scientific), as per manufacturer's instructions. N = 3 biological replicates were performed in triplicate wells for each experiment, and the results were normalised to the respective control scaffolds (Fmoc-FRGDF, or Fmoc-FRGDF coassembled with empty vector conditioned media).

3.3.7 Flow Cytometry

Chapter 5: After culturing samples for 72 hours, vinculin and α -SMA expression levels were quantified via flow cytometry. Harvested spheroids and cells in 2D cultures were trypsinised using 0.25% trypsin-EDTA, and spheroids were dissociated through repeated pipetting. Dissociated cells were then fixed using 2.5% paraformaldehyde for 20 minutes followed by permeabilisation using 0.5% saponin in PBS and subsequent blocking with 0.5% Bovine Serum Albumin (BSA) in PBS. Immunostaining was completed through incubation of cells with either mouse monoclonal anti-vinculin primary antibody (1:100 dilution, ab18058, Abcam, Cambridge, UK) followed by Alexa Fluor 594-conjugated secondary antibody (1:200 dilution, A11005, Goat Anti-Mouse IgG (H+L); Life Technologies Pty Ltd., Australia); or mouse monoclonal anti- α -Smooth Muscle Actin primary antibody (1:100 dilution, ab7817, Abcam, Cambridge, UK) followed by Alexa Fluor 488-conjugated secondary antibody (1:200 dilution, A11059, Rabbit Anti-Mouse IgG (H+L); Invitrogen, USA). Following incubation, cells were washed with PBS and resuspended in 500 μ L fluorescence-activated cell sorting (FACs) fix buffer. Negative controls (incubation in secondary antibody only) were prepared for each experimental condition. Flow cytometry analysis was performed using a FACS Canto™ II Flow Cytometer (BD Biosciences, San Jose, CA, U.S.A.) and data was analysed through use of Flowing software 2 (V 2.5.1, University of Turku, Finland). Each experiment was performed three times in duplicate.

3.3.8 Nucleus (DAPI) and Actin (Phalloidin) Staining

Chapter 4: Following 48 h culture, cells seeded on hydrogel samples were fixed using 4% paraformaldehyde for 10 minutes at room temperature. Cells were then gently washed twice with $1 \times$ PBS and subsequently permeabilised with 0.1% tritonX-100 for 15 minutes at room temperature. Cells were again gently washed twice with $1 \times$ PBS with care taken to avoid gel damage. Rhodamine-phalloidin (Life Technologies, Mulgrave, Australia) was used to stain cell actin as per manufacturer's recommendation, and stained cells were observed using fluorescent microscopy (Nikon, Tokyo, Japan). ImageJ analysis (Bethesda, MD, USA) was used to determine cell area and intensity as per the software instructions. GraphPad prism (version 3.03, San Diego, CA, USA) was used to calculate the significant student t-test for the values obtained using ImageJ.

Chapter 6: To visualise cell actin and nuclei, C2C12 myoblasts were stained with Rhodamine phalloidin (Life Technologies) and 4',6-diamidino-2-phenylindole (DAPI, Life Technologies) respectively. Cells were stained following 72 h culture to assess hydrogel effect on cell morphology and formation of multinucleated syncytia as an indication of cell differentiation. Briefly, samples were fixed using 200 μ L of 4% paraformaldehyde in PBS (ProSciTech Pty. Ltd.) for 20 minutes at room temperature. Next, samples were washed in PBS and solubilised in 200 μ L of 0.1% Triton \times 100 (ProSciTech Pty. Ltd.) for 15 min. Cells were then stained with DAPI (1:200 dilution in PBS) and phalloidin (1:150 dilution in PBS) for 60 minutes. Following staining, cells were imaged using a ZOE fluorescence cell imager (BioRad) at $200\times$ magnification, and the number of myonuclei in a cell or syncytium was counted using ImageJ. $N = 3$ biological replicates were performed in duplicate wells for each sample following 24 and 72 h culture. An average of 450 cells or syncytia were analysed to determine average number of nuclei per cell or syncytia per scaffold. Furthermore, to verify cell-size calculations acquired through calcein AM staining, cell-size was determined using ImageProPlus. A reverse mask was used to identify fluorescently labelled red and blue cells through selection of the black background, allowing for automated cell counting and determination of cell area. Cells at the edge of the image were excluded, and a minimum area of $40 \mu\text{m}^2$ was set.

Chapter 8: Primary myoblasts were stained using Alexa Fluor 488[®] phalloidin (Life Technologies, Australia) and DAPI (Life Technologies, Australia) to observe cell actin and nuclei, respectively, at day 0 and day 14 differentiation. Briefly, following 3 days differentiation, proliferation media (Ham's F10 (Thermo Fisher, Australia) supplemented with 20% Fetal Calf Serum (Gibco), 2.5 ng bFGF (Peprotech), 2 mM L-glutamine (Gibco) and 1× penicillin/streptomycin (Gibco)) was replaced with differentiation media (DMEM supplemented with 2% horse serum, 2 mM L-glutamine (Gibco), and 1% penicillin/streptomycin (Gibco)). Cells were cultured in differentiation media for 14 days with a half media change every 2 days. Media was removed following 14 days differentiation, and cells were fixed with 4% formalin overnight. Formalin was then removed, and constructs washed twice with PBS followed by a 1h PBS soak. PBS was then removed, and phalloidin was added as per manufactures instructions. Phalloidin was left overnight to ensure good stain penetration through the depth of the print. Again, constructs were washed twice with PBS before a subsequent 1h PBS soak. PBS was then removed and DAPI was added as per manufactures recommendation. DAPI was stained for 1h to ensure good stain penetration through the depth of the scaffold. Finally, constructs were washed twice followed by two 1h PBS soaks. Constructs were then imaged *via* confocal analysis (Nikon A1R Confocal laser microscope) and morphology assessed as an indication of myogenic differentiation.

Chapter 9: Dissociated rat cortical neurospheres were stained using Alexa Fluor 488[®] phalloidin (Life Technologies, Australia) and DAPI (Life Technologies, Australia) to visualise cell actin and nuclei, respectively, following 3 days proliferation and following 14 days differentiation. For proliferative studies, cells were cultured in proliferative media (Neurocult NS-A Proliferation Kit (STEMCELL technologies) supplemented with 20 ng/mL bGNF (Peprotech), 20 ng/mL EGF (Peprotech), 2 µg/mL Heparin (STEMCELL technologies) and penicillin/streptomycin (Gibco)) for 3 days following printing; while for differentiation studies, cells were cultured in proliferation media for 7 days following which media was substituted for differentiation media (DMEM/F12 supplemented with 1% Stempro (Thermo Fisher), 0.5% N2 (Thermo Fisher), 20 ng/mL BDNF (Peprotech), and 1 × penicillin/Streptomycin (Gibco)) and cells were cultured for a further 14 days with a half media change every 48h. Following desired culture (3 days proliferation or 14 days differentiation), media was removed, and cells were

fixed with 4% formalin overnight. Formalin was then removed, and constructs washed twice with PBS followed by a 1h PBS soak. PBS was then removed, and phalloidin was added as per manufactures instructions. Phalloidin was left overnight to ensure good stain penetration through the depth of the print. Again, constructs were washed twice with PBS before a subsequent 1h PBS soak. PBS was then removed and DAPI was added as per manufactures recommendation. DAPI was stained for 1h to ensure good stain penetration through the depth of the scaffold. Finally, constructs were washed twice followed by two 1h PBS soaks. Constructs were then imaged via confocal analysis (Nikon A1R Confocal laser microscope) and morphology assessed.

3.3.9 Immunofluorescence Staining for DAPI, Vinculin and F-actin

Chapter 5: Vinculin and filamentous-actin (F-actin) co-localisation was observed in 2D, 3D and 3D+ECM co-cultures through immunofluorescence staining. Following 72 h culture, cells were fixed in 4% paraformaldehyde and washed twice in 0.05% Tween-20 in PBS. Cells were then permeabilised using 0.5% Triton X-100 solution in PBS and blocked with 1% BSA in PBS. Cells were then immersed in mouse monoclonal anti-vinculin primary antibody (1:100 dilution, ab18058, Abcam, Cambridge, UK) at 4°C overnight. Samples were then washed with 0.05% Tween-20 in PBS and spheroids were incubated with Alexa Fluor 488-conjugated secondary antibody (1:200 dilution, A11059, Rabbit Anti-Mouse IgG (H+L); Invitrogen, USA) and tetramethylrhodamine isothiocyanate (TRITC)-conjugated phalloidin (1:200, R415; Life Technologies Pty Ltd., Australia). Finally, DAPI (R37606, Life Technologies, and Grand Island, NY) was used to stain cell nuclei for 5 minutes following which samples were washed using 0.05% Tween-20 in PBS. Samples were then immersed in PBS to avoid sample drying and imaged through confocal microscopy (A1R+ confocal microscope system; Nikon, Tokyo, Japan).

3.3.10 Cell Migration Tracking

Chapter 5: To investigate cell migration through agarose and Fmoc-SAP hydrogels, LLC cells were fluorescently labelled red (CellTracker™ Red CMTPX Dye, C34552, Invitrogen, USA), and NOR-10 cells were fluorescently labelled green (MitoTracker Green FM, M7514, Invitrogen, USA) prior to co-culture and spheroid formation. Briefly, cell concentrations were adjusted to $1 \times 10^6 \text{ mL}^{-1}$ in PBS and

CMPTX red (LLC cells) and MitoTracker Green (NOR-10 cells) were added at a final working concentration of 5 μ M and 10 μ M, respectively. Cells were then incubated for 37°C under light protected conditions, followed by fluorescence quenching using two volumes of complete media and washed thrice. Fluorescently labelled cells were co-cultured into spheroids as described in **section 3.3.1**. Subsequently, spheroids were encapsulated within coassembled Fmoc-SAP hydrogel or 1% agarose (prepared as detailed in **section 3.2.1** and **3.2.2**). Finally, cell migration was observed as tracked by confocal microscopy after 72 hours of incubation.

3.3.11 SEM Observation of Cell Interaction with Bioinks

Chapter 8: Primary myoblast interaction with printed bioinks was assessed via SEM following 14 days differentiation. Briefly, cells were fixed in formalin overnight followed by washing thrice in PBS. Samples were then washed three times in 0.1 M cacodylate buffer to avoid salt precipitation. Next, 1% osmium tetroxide was added to samples and samples were soaked for 30 minutes. Osmium tetroxide was then removed, and samples were washed 3 times with MilliQ water. Samples then underwent various drying steps through sequential increase in ethanol content. Specifically, samples were immersed in 50% ethanol for 10 minutes, followed by soaking in 70% ethanol for 10 minutes. Samples were then soaked in 90% ethanol for 30 minutes followed by further soak in 100% ethanol for 30 minutes. 100% ethanol was then removed, and samples were placed in fresh 100% ethanol overnight at 4°C. Finally, samples were removed from ethanol and placed onto SEM stubs where they were allowed to dry for a minimum of 1 hour. Samples were then gold sputter coated and stored in a sealed environment prior to imaging. Samples were imaged using a FEI Scios Dualbeam FIBSEM and/or FEI Verios 460L FEGSEM at an operating voltage of 5 kV and 3 kV, respectively.

Chapter 9: Rat cortical neurosphere interaction with printed bioink constructs was observed via SEM following 3-days culture to investigate cell protrusion and material interaction. Constructs were prepared as above. Briefly, cells were fixed in formalin overnight followed by washing thrice in PBS. Samples were then washed three times in 0.1 M cacodylate buffer to avoid salt precipitation. Next, 1% osmium tetroxide was added to samples and samples were soaked for 30 minutes. Osmium tetroxide was then removed, and samples were washed 3 times with MilliQ water. Samples then underwent

various drying steps through sequential increase in ethanol content. Specifically, samples were immersed in 50% ethanol for 10 minutes, followed by soaking in 70% ethanol for 10 minutes. Samples were then soaked in 90% ethanol for 30 minutes followed by further soak in 100% ethanol for 30 minutes. 100% ethanol was then removed, and samples were placed in fresh 100% ethanol overnight at 4°C. Finally, samples were removed from ethanol and placed onto SEM stubs where they were allowed to dry for a minimum of 1 hour. Samples were then gold sputter coated and stored in a sealed environment prior to imaging. Samples were imaged using a FEI Scios Dualbeam FIBSEM at an operating voltage of 5 kV.

3.4 Statistical Analysis

A student paired, two-tailed t test was performed between control and test groups for all cell culture experiments in **Chapter 4** and **6**. GraphPad Prism (Version 3.03 and 7 for **Chapter 4** and **6**, respectively) was used for statistical analysis and samples were prepared in triplicate with 3 biological repeats. For **Chapter 5**, 3 biological repeats were performed in duplicate for all samples and statistical analysis performed through Graphpad Prism (Version 7.0, GraphPad Software, San Diego, CA, USA). Student unpaired, two-tailed t test was used to determine statistical significance between two samples, whilst Two-Way Analysis of Variance (ANOVA) with Tukey post-hoc tests was used for multiple comparisons. For **Chapter 7**, all correlation analysis was performed using GraphPad Prism (Version 7.0, GraphPad Software, San Diego, CA, USA). Specifically, a Pearson correlation test was performed between each sample with a 95% confidence interval and Pearson r values were calculated and plotted as a heatmap for ease of visualisation (**Supplementary Figure S - 6**). One-way ANOVAs with Tukey post-hoc tests were used to identify statistically significant changes between groups in **Chapter 8** and **9**, all *in vitro* data was completed in triplicate. In all chapters, statistical significance was set at a value of $P < 0.05$. All data was presented with mean \pm standard error of the mean (SEM), or data \pm standard deviation (σ). In **Chapters 5, 7, 8**, and **9**, SAXS data presented as calculated value \pm uncertainty. For all correlations in **Chapter 7**, a Pearson value of 1 indicates a perfect correlation while -1 indicates a perfect inverse correlation; anything above 0.5 or below -0.5 was considered well-correlated.

Chapter Four:

TUNING THE BIOMECHANICAL AND BIOCHEMICAL PROPERTIES OF SCAFFOLDS VIA COASSEMBLY

4.1 Preview

In this chapter we tune the biomimetic properties of SAP materials through the development of multi-component scaffolds. Firstly, synergistic epitopes from fibronectin were incorporated into rationally designed SAPs (Fmoc-FRGDF, Fmoc-PHSRN). These were then assembled into nanofibrils, where they were synergistically presented to promote a more ECM-like environment that enhanced attachment during *in vitro* cell culture. A sulphonated polysaccharide, Fucoidan, was then investigated as a means of influencing nanofibrillar supramolecular organisation. Results show that these two distinct mechanisms of multicomponent assembly enable tuneable control over mechanical properties and network orientation, and enhance cell adhesion and spreading. This chapter forms foundations for subsequent studies including **Chapter 5**, and those investigating macromolecule functionalisation on cell-behaviour (**Chapter 6**), and bioink development (**Chapter 8**).

Contribution of the candidate:

- Involvement in analysis regarding material properties and assembly mechanisms.
- Contributed in manuscript preparation.

Publications relevant to this chapter

Figures within this chapter reprinted (adapted) with permission from:

Aye, S.S., Li, R., **Boyd-Moss, M.**, Long, B., Pavuluri, S., Bruggeman, K., Wang, Y., Barrow, C., Nisbet, D. and Williams, R., (2018). Scaffolds formed via the non-equilibrium supramolecular assembly of the synergistic ECM peptides RGD and PHSRN demonstrate improved cell attachment in 3D. *Polymers*, 10(7), p.690.

Li, R., **Boyd-Moss, M.**, Long, B., Martel, A., Parnell, A., Dennison, A.J., Barrow, C.J., Nisbet, D.R. and Williams, R.J., (2017). Facile Control over the Supramolecular Ordering of Self-assembled Peptide Scaffolds by Simultaneous Assembly with a Polysaccharide. *Scientific reports*, 7(1), p.4797.

Oral Presentation:

27-29th June 2016, 7th international Nanomedicine Conference, Coogee Beach, Sydney, Australia.

Abstract:

The native ECM is a complex, protein-rich milieu which varies in mechanical and biological properties between tissue types. Current tissue engineering approaches aim to replicate these conditions; however, despite research efforts, few researchers have engineered suitable materials which present controlled biological and mechanical tunability under physiological conditions. Here, we investigate two separate mechanisms for simultaneous mechanical and biological tunability. The first takes advantage of simple peptide synthesis techniques to selectively engineer biologically relevant epitopes within a stable SAP. Natively, fibronectin presents the attachment motif RGD synergistically with PHSRN; however, many functionalisation approaches focus solely RGD presentation. As such, we aim to address these shortcomings through combination of fibronectin-inspired Fmoc-FRGDF with PHSRN. This is achieved through two approaches: a) concatenated peptide Fmoc-FRGDFPHSRN, and b) coassembly of Fmoc-FRGDF with Fmoc-PHSRN. The second half of this chapter focuses on introducing mechanical tunability through macromolecule incorporation. Here, the anti-inflammatory polysaccharide fucoidan is coassembled with Fmoc-FRGDF.

Assembly mechanisms and their influence on mechanical characteristics are investigated through spectroscopic analysis and electron microscopy. Fucoidan influence on network architecture is further observed through SANS; while underlying nanostructure of multisequence scaffolds is observed using SAXS. Preliminary *in vitro* cell response is also investigated for multisequence scaffolds through seeding of HMFCs. Results show maintenance of self-assembly in both cases. Fucoidan addition altered

fibril supramolecular ordering – resulting in increased bundling proportional to fucoidan concentration. Alternatively, Fmoc-PHSRN addition to Fmoc-FRGDF did not significantly alter network topology; and cells cultured on Fmoc-FRGDF/Fmoc-PHSRN coassembled scaffolds demonstrated enhanced adhesion and spreading compared to Fmoc-FRGDF alone.

4.2 Introduction

Recent advances in materials engineering has enabled tailored tissue regeneration previously unobtainable through conventional treatment protocols.²⁴⁶ The potential for these biomaterials to mimic aspects of the native ECM has inspired significant research through fields transcending tissue engineering, regenerative medicine, and drug delivery.²⁴⁷⁻²⁴⁸ However, despite some success, there is still substantial research to be undertaken if we are to truly mimic the complexities of natural tissue microenvironments.

The native ECM is a complex cellular microenvironment which provides structure and signalling to tissue through the mediation of interactions between cells and various bioactive proteins, polysaccharides and other biological macromolecules.¹ Fibronectin is a fibrous glycoprotein found in abundance within the native ECM which plays a crucial role in facilitating cell-ECM interactions.²⁴⁹ Significant research into fibronectin's cell-attachment region has revealed short sequences of amino-acids responsible for promoting cell attachment through integrin binding.²⁴⁹ In particular, research has centred on the minimalistic peptide motif RGD, a key attachment site which numerous materials engineering approaches have incorporated to facilitate successful biomaterial functionalisation.²⁵⁰ However, in native fibronectin, this amino acid sequence does not work in isolation, rather it works synergistically with another minimalistic cell attachment motif, PHSRN, to promote cell adhesion.^{249, 251-252} Despite this, few approaches have investigated material functionalisation through PHSRN addition.

ECM mechanical properties are also known to differ significantly between tissue types and as such advanced biomaterials are required to possess simplistic and tuneable ways of controlling material stiffness.²⁵³⁻²⁵⁵ One potential resolve is offered through structural macromolecule integration to

hydrogel systems. Previously, the oligosaccharide agarose has been combined with low-molecular-weight gelators to increase hydrogel stiffness substantially.²⁵⁶ Similarly, to investigate macromolecule incorporation in this peptide system and its subsequent influence on mechanical properties, the polyanionic polysaccharide fucoidan was selected.²⁵⁷ Fucoidan is a highly sulphated, seaweed-derived biomacromolecule which demonstrates anti-inflammatory and anti-coagulant activity.²⁵⁸⁻²⁵⁹ Furthermore, fucoidans have shown success in hemopoietic expansion cultures,²⁶⁰ as wound healing accelerators,²⁶¹⁻²⁶² and are known to bind heparin-binding growth factors.²⁶³⁻²⁶⁴ However, unlike agarose, fucoidan alone has not demonstrated the propensity to form hydrogels, and therefore, needs to incorporate gelling components for wound care applications.²⁶¹ Consequently, fucoidan can be considered as a polyelectrolyte, which at low concentrations, interacts with supramolecular bundles and is subsequently presented on the surface of the fibrillar scaffold in a bioactive fashion.²⁶⁵

Biomimetic artificial tissue microenvironments must adhere to stringent design rules. Here, biocompatible materials are required to provide cells with a 3D microenvironment, while providing the necessary structural and biochemical signals to cells directing cell fate.^{143, 266} These materials should be tuneable (both mechanically and biologically), should present optimised biodegradation profiles, and should control the local inflammatory environment.^{141, 267-268} SAPs are unique biomaterials capable of spontaneous self-organisation into larger hierarchical structures through mechanisms similar to those in nature.^{128, 141} The ability of these materials to be easily biofunctionalised through sequence selection, combined with their ease of synthesis and mechanical tunability, have made them promising candidates as artificial ECMs.^{26, 243, 265}

Previous work in our laboratory has developed the fibronectin inspired, RGD presenting SAP, Fmoc-FRGDF.¹⁴³ Recently, the coassembly of this peptide with other SAPs or polysaccharides has resulted in optimised tissue engineering scaffolds.^{26, 265} Therefore, in this chapter, we investigate the ability of Fmoc-FRGDF enhancement through mechanical and biological manipulation. Biological optimisation is investigated through the incorporation of the synergistic sequence, PHSRN. Here, two assembly mechanisms are detailed – the first is enabled through the synthesis of the decapeptide, ‘Fmoc-FRGDFPHSRN’, while the second approach focuses on coassembly of Fmoc-FRGDF with a second

SAP, 'Fmoc-PHSRN'. Mechanical tunability is investigated through fucoidan coassembly with Fmoc-FRGDF at three different fucoidan concentrations (2 mg/mL, 5 mg/mL, and 10 mg/mL), and compared to Fmoc-FRGDF alone.

In all functionalisation approaches, material assembly mechanisms, network topology, and resultant mechanical properties are investigated. Additionally, material bioactivity is investigated for PHSRN-containing scaffolds.

4.3 Results and Discussion

4.3.1 Development of Multi-Sequence Self-Assembled Peptide Hydrogels

4.3.1.1 Formation of Hydrogels

To investigate the propensity of Fmoc-based SAPs to form advanced biomimetic, multisequence scaffolds, three fibronectin inspired peptide sequences were developed (**Figure 4-1A-C**). Fmoc-FRGDF, Fmoc-PHSRN, and Fmoc-FRGDFPHSRN were synthesised via SPPS, resulting in the formation of a white crystalline powder in each case. A fourth peptide mixture was also developed through mixing of Fmoc-FRGDF and Fmoc-PHSRN powders at a 1:1 ratio. Peptides hydrogels (10 mg/mL) were developed from each of the four samples via a well-characterised pH switch method (**Figure 4-1D**).⁸ Here, Fmoc-FRGDF formed a clear, stable hydrogel within 2 hours. Alternatively, Fmoc-PHSRN was unable to form a stable hydrogel under all tested conditions. This is likely due to the presence of proline residues, which literature shows is unable to form effective hydrogen bonds owing to its cyclic structure which lacks the normal NH₂ backbone; subsequently limiting its ability to form α -helix or β -sheet conformations.²⁶⁹⁻²⁷⁰ The concatenated decapeptide sequence 'Fmoc-FRGDFPHSRN' formed a hydrogel over 10 days; whilst the coassembled peptide mixture (Fmoc-FRGDF + Fmoc-PHSRN, 1:1 ratio) required 3 days to form a stable hydrogel. The ability of these peptides, containing both 'PHSRN' and 'FRGDF' epitopes to form hydrogels is interesting, as it shows that interactions within the 'FRGDF' component are stable enough to maintain sufficient self-assembly, despite the presence of proline. The delay in hydrogel formation in these samples, however, may explain the relatively limited research into PHSRN-containing, SAP hydrogels.

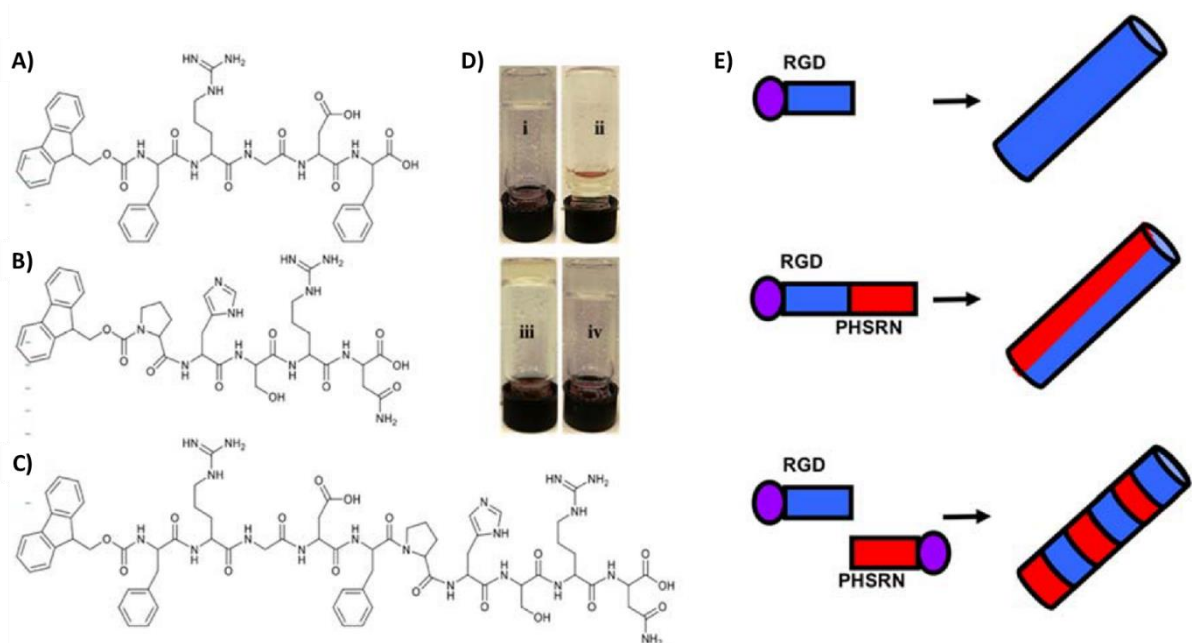


Figure 4-1 – Structure of three Fmoc-based self-assembling peptides. A) Fmoc-FRGDF; B) Fmoc-PHSRN; C) Fmoc-FRGDFPHSRN and D) hydrogels formed of (i) Fmoc-FRGDF; (ii) Fmoc-PHSRN; (iii) Fmoc-FRGDFPHSRN and (iv) peptide mixture of Fmoc-FRGDF/Fmoc-PHSRN (1:1, w/w). E) Cartoon Schematic of peptide assembly mechanisms. Reproduced with permission ³¹⁴

4.3.2 Investigation into Network Topology of Engineered SAP Hydrogels.

All hydrogels were allowed to gel over 10 days; after which their resulting nano- and microarchitectures were analysed using microscopy techniques. TEM analysis was employed to analyse hydrogel nano-structure (**Figure 4-2A-D**). Here, Fmoc-FRGDF, Fmoc-FRGDFPHSRN, and the coassembled hydrogel, Fmoc-FRGDF/Fmoc-PHSRN, all demonstrated nanofibers of width 5-10 nm and length several micrometres as analysed via ImageJ; while no fibrillar structures were evident in Fmoc-PHSRN samples. Fmoc-PHSRN's lack of fibrous structure provides insight into the inability of this peptide to gel on its own – as there are no structures capable of effectively immobilising surrounding water (**Figure 4-2B**). Analysis of Fmoc-FRGDF alone showed the formation of a highly ordered network with a lateral association between many peptide fibrils resulting in the formation of 'bundles' (**Figure 4-2A**). Alternatively, TEM analysis of Fmoc-PHSRN showed no fibrils, rather, granules or clusters are present. The long peptide, Fmoc-FRGDFPHSRN, demonstrates short peptide fibrils with no noticeable bundling (**Figure 4-2C**); these short fibrils provide a potential explanation for the long hydrogelation time, as these truncated structures would be ineffective at trapping surrounding water, and as such would require more time to trap sufficient water. Further analysis of Fmoc-FRGDFPHSRN structures show the coexistence of globular structures which may be due to unassembled peptide particles. Finally, TEM analysis of the coassembled hydrogel, Fmoc-FRGDF/Fmoc-PHSRN shows the formation of a well-ordered fibrillar network (**Figure 4-2D**).

AFM provides insight into network orientation (**Figure 4-2E-H**). Fmoc-FRGDF shows a well-ordered network which confirms the highly-structured nature of this hydrogel (**Figure 4-2E**).¹⁴³ Alternatively, Fmoc-PHSRN is once again shown to have no observable fibrils, rather aggregates in an array of sizes are visible (**Figure 4-2F**). Here, it is likely that the presence of the proline residue perturbs stable fibril formation. Fmoc-FRGDFPHSRN shows a highly dense network consisting of short truncated fibrils compared to Fmoc-FRGDF alone (**Figure 4-2G**). Observation of the mixed hydrogel formed through coassembly of Fmoc-FRGDF and Fmoc-PHSRN shows a highly branched network similar in topology to Fmoc-FRGDF alone (**Figure 4-2H**).

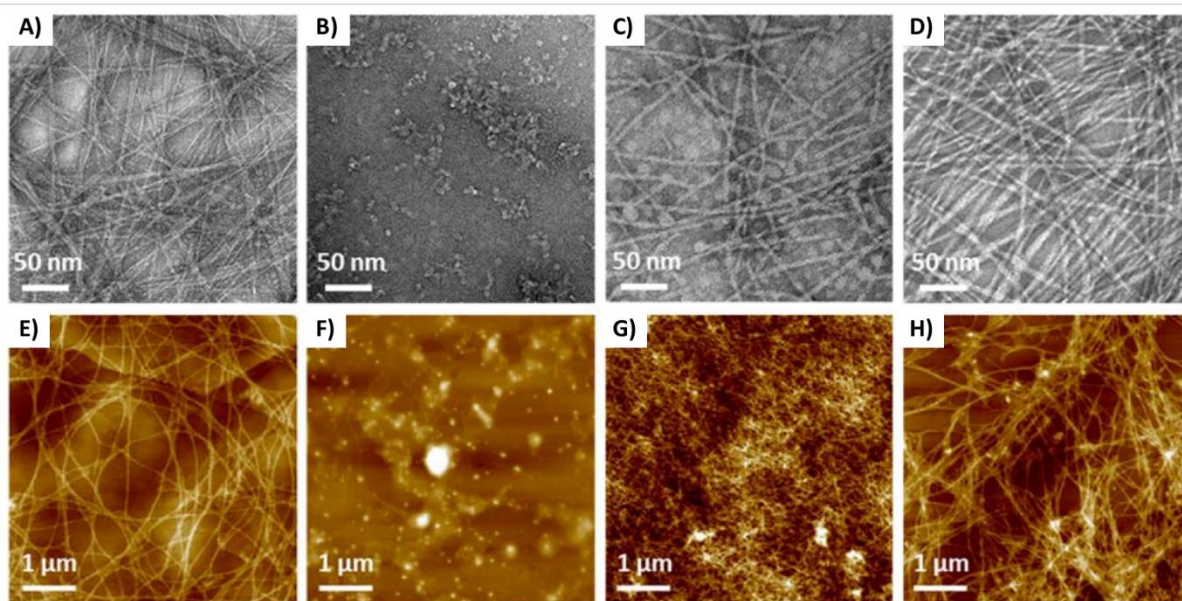


Figure 4-2 –Hydrogel Nano/Microtopology observations in response to assembly mechanism. (top panel TEM images and bottom panel AFM images). A,E) Fmoc-FRGDF; B,F) Fmoc-PHSRN; C,G) Fmoc-FRGDFPHSRN and D,H) peptide mixture of Fmoc-FRGDF/Fmoc-PHSRN (1:1, w/w). Reproduced with permission ³¹⁴

Further analysis of material nanoarchitecture was performed using SAXS (**Figure 4-3**). As Fmoc-PHSRN failed to form a suitable hydrogel, it was excluded from SAXS analysis and subsequent *in vitro* investigation. AFM and TEM analysis revealed fibrillar structures, and therefore we anticipate that SAXS analysis will demonstrate similar findings. All remaining samples showed SAXS spectra characteristic of cylindrical structures, indicated by q^{-1} angle dependence in low q values (**Figure 4-3A**). Length of each fibril could not be established as the length lies outside the range tested (q range). As such, the length can be considered infinite during this analysis, and all calculated values can be attributed to the radius of structures within the hydrogel. To determine radius, an IFT method was employed. As we have previously determined the cylindrical nature of these structures, and, as the length is known to be outside the q range, analysis of the max $P(r)$ of IFT functions indicates the average radius (**Figure 4-3B**). The resulting fibril diameter is found to be 8.4 nm (41.8 Å, $\sigma = 0.7$ Å), 6.3 nm (31.3 Å, $\sigma = 1.2$ Å), and 7.1 nm (35.3 Å, $\sigma = 1.2$ Å) for Fmoc-FRGDF, Fmoc-FRGDF/Fmoc-PHSRN (coassembled), and Fmoc-FRGDFPHSRN respectively. However, TEM analysis of Fmoc-FRGDFPHSRN also indicated the presence of spherical structures which may convolute the determined fibril radius. Despite this, all results are consistent with previous TEM observations relating to fibril diameter.

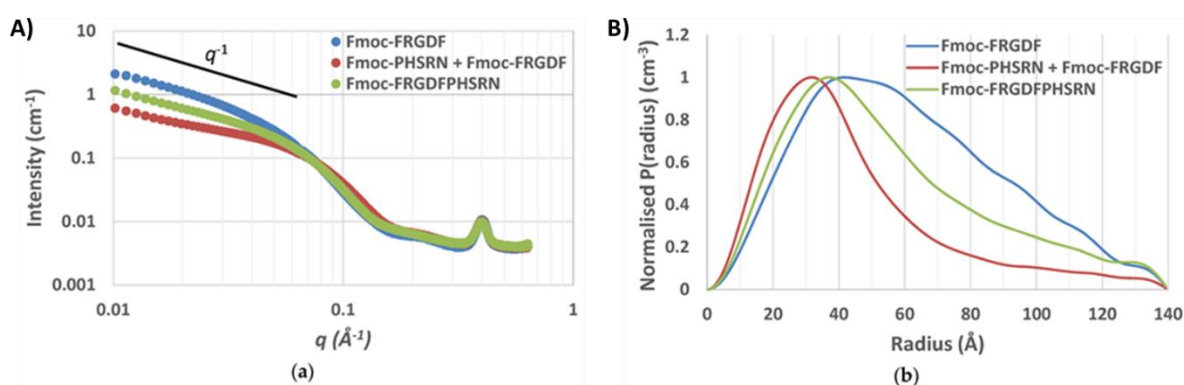


Figure 4-3 – Investigation of material nanostructure via SAXS A) Scattering curve of Fmoc-FRGDF, Fmoc-FRGDFPHSRN, and Fmoc-FRGDF/Fmoc-PHSRN displaying q^{-1} relationship at low q angles. B) $P(r)$ inversion of RGD-containing SAPS. Reproduced with permission ³¹⁴

4.3.3 Investigation of Self-Assembly Mechanisms

Spectroscopic analysis, including FT-IR, CD, and fluorescence spectroscopy was employed to analyse the driving mechanisms of assembly in each case. All samples showed similar self-assembly mechanisms driven through Fmoc-interactions and stabilised via various hydrogen bonds.²⁷¹ FT-IR analysis indicates the dominant organisation of the peptide backbone. Here, Fmoc-FRGDF, Fmoc-FRGDFPHSRN, and the coassembled hydrogel, Fmoc-FRGDF/Fmoc-PHSRN all demonstrated two distinct absorption peaks within the amide I region, occurring at approximately 1627cm^{-1} and 1690cm^{-1} corresponding to the formation of stable β -sheet conformations (**Figure 4-4A**).²⁷² These peaks were not evident in samples containing Fmoc-PHSRN alone, instead, a broad transition is evident which centres near 1667cm^{-1} indicating the presence of randomly coiled conformations.²⁷³ Interestingly, the coassembled peptide sequence, Fmoc-FRGDF/Fmoc-PHSRN, demonstrated an additional peak at $\sim 1664\text{cm}^{-1}$ indicative of random coils; this additional peak in conjunction with those centred around 1627cm^{-1} and 1690cm^{-1} indicate that in addition to β -sheet formation, random coils are also evident. The presence of random coils is likely a result of non-ideal assembly, owing to the presence of proline residues which necessitate differing spatial requirements and therefore are unable to pack efficiently during self-assembly. The same peak, centred around 1664cm^{-1} , is not observed in samples constituting Fmoc-FRGDF alone, and therefore, it can be reasoned that any disruption in β -sheet formation is due to the presence of the PHSRN motif. Findings gained in FT-IR analysis support observations made in TEM and AFM analysis, where Fmoc-PHSRN addition was found to influence assembly mechanisms.

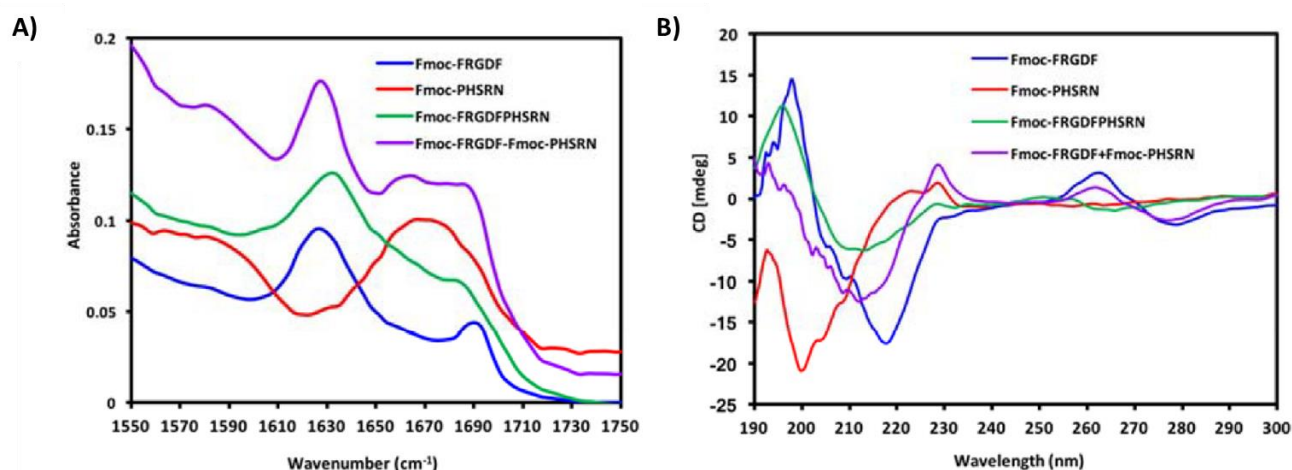


Figure 4-4 – Spectroscopic characterisation of the peptide hydrogels. A) Truncated FT-IR absorption spectra in amide I region, and B) CD spectra. Reproduced with permission ³¹⁴

CD allowed for further analysis of amino acid secondary structure. Investigation into Fmoc-FRGDF assembly shows a strong, positive peak centred on 198 nm and a second, negative peak located at 220 nm (**Figure 4-4B**). These peaks indicate a negative cotton effect induced by $n\text{-}\pi$ transitions.²⁷⁴⁻
²⁷⁵ The combination of these peaks indicates the presence of stable β -sheet conformations.²⁷⁴⁻²⁷⁵ Another positive peak is evident at ~ 263 nm in the Fmoc-FRGDF sample spectrum, signifying induced chirality of aromatic-stacking moieties and relating to the stacking of Fmoc-groups.²⁷⁶ Contrastingly, Fmoc-PHSRN establishes a strong negative peak at 200 nm and a weak positive peak at 223 nm; as such, this peptide is likely to assume a non-hydrogen bonded polyproline type II helical structure and present as random coils in dilute solution (10 mg/mL).²⁷⁷⁻²⁷⁸ Interpretation of Fmoc-PHSRN CD spectra is in agreeance with findings gained in FT-IR analysis and provides further explanation for the fluidic state observed in this sample during hydrogel synthesis (**Figure 4-1D**). Fmoc-FRGDFPHSRN demonstrated a comparable trend to Fmoc-FRGDF alone, demonstrating a positive peak at 196 nm and a negative peak at 213 nm, once again indicating the formation of β -sheet structures.²⁷⁴ Finally, CD analysis of the Fmoc-FRGDF/Fmoc-PHSRN hydrogels demonstrated a strong negative peak at 212 nm yet lacked a prominent positive peak at 218 nm, indicating the presence of indistinct β -sheet structures which might be due to the incidence of random coils identified in FT-IR analysis. Another peak evident at approximately 260 nm indicates Fmoc-group stacking.²⁷⁶ The evidence of β -sheets in this sample shows

that despite prolines inability to form β -sheet conformations, the remaining moieties can maintain these structures.

Analysis through fluorescence spectroscopy provides insight into emission of fluorenyl moieties and further enforces understandings gained in FT-IR and CD analysis.²⁷⁹ Peaks at ~330 nm indicate Fmoc-monomer interactions and consequently indicate the relative amount of Fmoc-monomers in solution.²⁷⁹ As expected, Fmoc-PHSRN showed the most significant peak at this wavelength indicating the highest amount of Fmoc-monomers present compared to the remaining samples (**Figure 4-5A**). Alternatively, Fmoc-FRGDF and Fmoc-FRGDF/Fmoc-PHSRN samples showed decreased Fmoc-monomers, likely a result of stable hydrogel assembly. Fmoc-FRGDFPHSRN was shown to demonstrate the smallest peak around this wavelength and subsequently shows the least number of Fmoc-monomers present out of all four samples. Further analysis of the fluorescent spectra shows all samples demonstrate a broad peak centred around 450 nm, relating to extensive stacking between aromatic groups (J-aggregates) and owing to contributions from both phenylamine and fluorenyl groups.²⁸⁰ Specifically, this peak relates to π - π stacking between multiple fluorenyl rings during efficient hydrogel formation and subsequently, indicates fibre formation.²⁸⁰ Excimer peaks are more noticeable in Fmoc-FRGDFPHSRN and the coassembled, Fmoc-FRGDF/Fmoc-PHSRN sample, suggesting increased Fmoc-stacking despite evidence of random coil structures in CD and FT-IR analysis techniques. Contrastingly, this peak is hardly evident in Fmoc-PHSRN samples, signifying a lack of apparent J-aggregate formation in this sample possibly resulting from the steric effect of proline residues;²⁷⁰ subsequently, Fmoc-organisation in self-assembly is likely to be negatively influenced, and the resultant self-assembled structure is expected to be interrupted. The coassembled Fmoc-FRGDF/Fmoc-PHSRN system demonstrates the greatest peak at this wavelength; therefore, it can be deduced that weak hydrogen bonds relating to the proline-containing PHSRN sequence are compensated by increase Fmoc-stacking to maintain stable fibril formation.

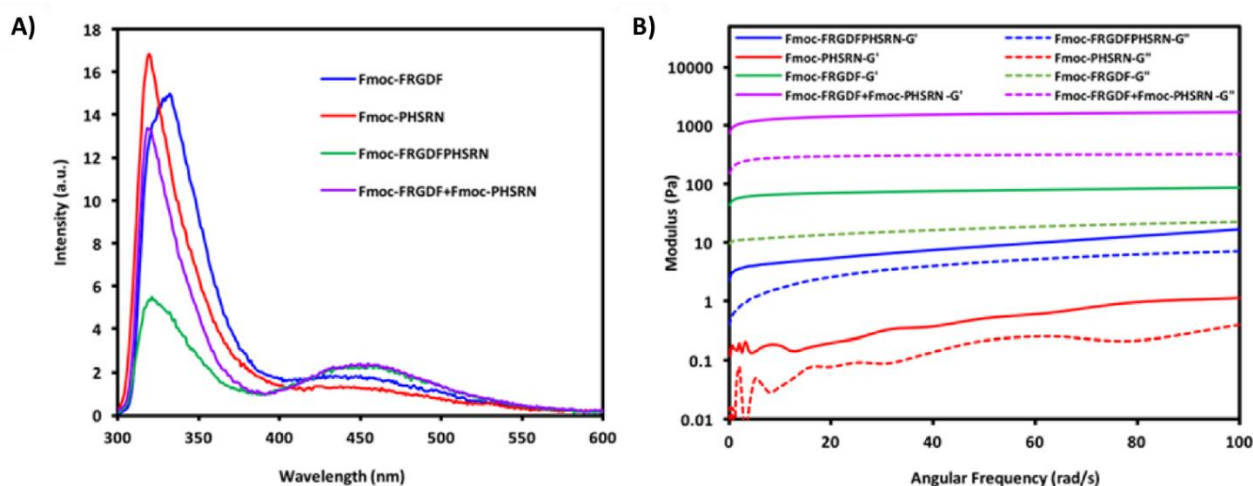


Figure 4-5 – Spectroscopic and rheological characterisation of the peptide hydrogels. A) fluorescence spectra, and B) rheological analysis of peptides showing viscoelastic characteristics. Reproduced with permission ³¹⁴

Oscillatory rheological analysis was employed to analyse the broad viscoelastic properties of the developed hydrogel systems. For all samples, the storage modulus was found to be greater than the loss modulus indicating the successful formation of a stable hydrogel (**Figure 4-5B**); however, despite this, Fmoc-PHSRN demonstrated an extremely low storage modulus of 0.5Pa (at 50 rad/s), and as such, exhibited a fluidic state in macroscopic analysis. The observations gained in spectroscopic and microscopic analysis show structures are formed during Fmoc-PHSRN self-assembly, and this may contribute to the perceived storage modulus being above that of the loss modulus in this sample, despite this, these structures are shown to be non-conductive to self-supporting gel formation. Contrastingly, Fmoc-FRGDF was shown to form a soft hydrogel with a storage modulus of approximately 50 Pa at 50 rad/s. The long peptide Fmoc-FRGDFPHSRN, demonstrated a relatively low storage modulus of approximately 8.5 Pa at 50 rad/s. Interestingly, the coassembled Fmoc-FRGDF/Fmoc-PHSRN system demonstrated the most robust hydrogel, exhibiting a storage modulus of ~1600 Pa at 50 rad/s.

4.3.4 Biological Effect of Synergistic Scaffolds

Finally, synergistic scaffold bioactivity is investigated via *in vitro* analysis of seeded cell viability, proliferation, and spreading. As Fmoc-PHSRN alone could not form an adequate hydrogel under all tested conditions, it was excluded from cell-culture investigation. All hydrogels were allowed to undergo sufficient gelation over 10 days, after which HMFCs were seeded onto the hydrogel surface. Cell viability and proliferation was analysed over 3 days through colourimetric MTS Assay. Fmoc-FRGDF alone at day 1 was used as a control, and all samples were normalised to this result; Fmoc-FRGDF was selected for use as a control as it has previously proved suitability for cell culture conditions.^{143, 281} Fmoc-FRGDF alone was found to proliferate steadily over 3 days (**Figure 4-6A**). Alternatively, the long peptide, Fmoc-FRGDFPHSRN, showed a decrease in cell viability resulting in a significant difference between Fmoc-FRGDFPHSRN and Fmoc-FRGDF alone after 3 days. This observation may be a result of weak assembly and/or insufficient cell attachment. Contrastingly, the coassembled peptide, Fmoc-FRGDF/Fmoc-PHSRN demonstrated a substantial increase in cell proliferation over three days; being significantly higher than that of Fmoc-FRGDF and Fmoc-FRGDFPHSRN by day 3.

Cell attachment and spreading was analysed through actin staining after 48h culture (**Figure 4-6B, C**), this time point was selected as it allows cells to react and integrate within their respective environments. Fmoc-FRGDF alone shows viable cells with a typical fibroblast morphology demonstrating slight focal adhesions to the peptide. Fmoc-FRGDFPHSRN did not show such projections; alternatively, cells appeared more rounded in structure indicative of poor cell attachment. Finally, the mixed peptide coassembly, Fmoc-FRGDF/Fmoc-PHSRN demonstrated substantially more spreading when compared to Fmoc-FRGDF alone; indicating cell attachment is significantly increased in this sample by 48h. Such differences between Fmoc-FRGDFPHSRN and the coassembled system may be a result of epitope spacing, as research into fibronectin shows RGD and PHSRN are separated by approximately 30-40 Å and that this distance is important for correct synergistic signalling.²⁸²

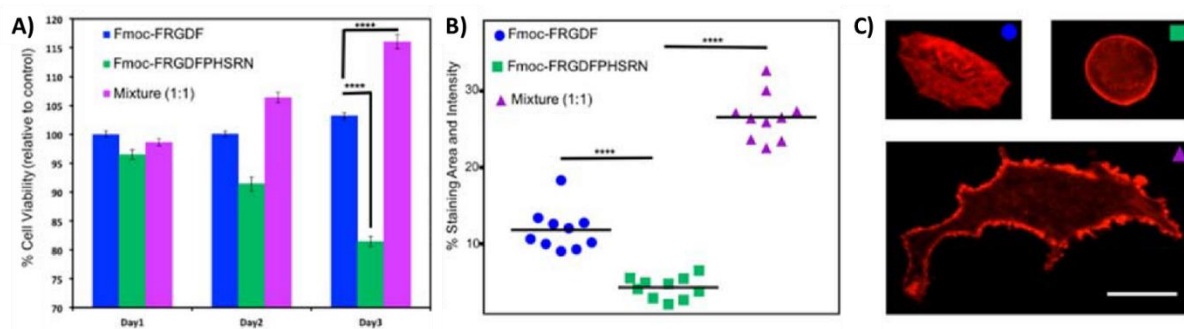


Figure 4-6 – Cytocompatibility of HMFCs on Fmoc-SAP hydrogels A) Cell viability of HMFCs on peptide hydrogels over three days as assessed through MTS assay (absorbance wavelength of 490 nm). Absorbance value of cells grown on Fmoc-FRGDF was considered as control and a p-value of <0.05 was considered significant. B) Analysis of spreading area: following 48h of HMFCs on peptide surface, cells were stained with actin, and images were obtained using through fluorescence microscopy (20x magnification). ImageJ analysis was performed, and values were plotted using GraphPad Prism, the p-value**** <0.05 was considered statistically significant. C) Typical morphologies of HMFCs following actin staining for samples measured in (b) scale bar 10 μ m. Reproduced with permission ³¹⁴

4.4 Enabling Mechanical Tunability Through Macromolecule Addition

4.4.1 Formation of Hydrogels

Fmoc-FRGDF based hydrogels were used to investigate network tuning through bioactive polysaccharide addition. Here, Fmoc-FRGDF (10 mg/mL) assembly was triggered in a solution containing the highly sulphated polysaccharide fucoidan to observe the mechanical effect of the process (**Figure 4-7A-D**). Here, we added varying amounts of fucoidan to form 4 distinct hydrogels: Fmoc-FRGDF (+0 mg/mL fucoidan), +2 mg/mL, +5 mg/mL, and +10 mg/mL. In each case – fucoidan containing samples were combined before assembly via a pH switch method, resulting in a coassembled peptide network. We hypothesise that fucoidan integration during the assembly process allows for modification of the assembly process, while fucoidan addition post-assembly does not facilitate such tunability. Therefore, a fifth hydrogel was developed as a control; this hydrogel consisted of Fmoc-FRGDF (10 mg/mL) which was allowed to assemble to completion before subsequent addition of 10 mg/mL fucoidan – resulting in a post-assembled fucoidan-containing network. In coassembled hydrogels, gelation occurs within 2 hours of assembly. Interestingly, fucoidan containing samples are found to assemble more rapidly compared to Fmoc-FRGDF alone; therefore, we anticipate that fucoidan addition is effectively able to influence fibril interactions. Increase in rate of self-assembly has previously been observed as a function of the extent of stimulus during early self-assembly stages.²⁷⁹

²⁸³ Previously, studies using similar peptides have found that although pK_a was unaffected by macromolecule addition, the rate of pH change was effected, and subsequently, hydrogels formed more rapidly.²⁸⁴ Likewise, fucoidan addition influenced rate of gelation, however, was found to have no effect on hydrogel pK_a , and subsequently, did not change the pH of hydrogelation.¹⁴⁰ All gels formed optically transparent hydrogels, however, the hydrogel coassembled with 10 mg/mL fucoidan demonstrated slightly increased opacity (**Figure 4-7E**).

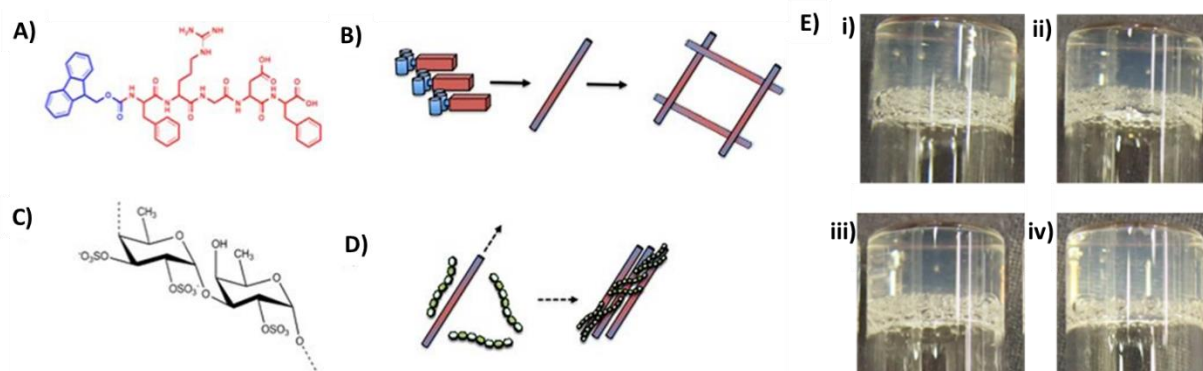


Figure 4-7 – Peptide self-organisation in the presence of fucoidan. A) Chemical structure of Fmoc-FRGDF. B) schematic of peptide assembly showing fibril formation and subsequent entanglement to form a hydrogel network. C) repeating fucoidan subunit D) Schematic of proposed supramolecular ordering through interactions between fucoidan and individual fibrils to produce organised fibre bundles of thicker morphology.. E) Gel macromorphology as formed from i) Fmoc-FRGDF, ii) +2, iii) +5, iv) +10 mg/mL fucoidan. Reproduced with permission ³³⁷

4.4.2 Investigation into Network Topology of Macromolecule Functionalised SAPs

To analyse fucoidans influence on network topology, TEM and AFM techniques are employed (**Figure 4-8**). TEM analysis of Fmoc-FRGDF once again shows the development of nanofibers with a diameter of ~10 nm and microns in length (**Figure 4-8A**). Fucoidan addition during assembly is found not to interrupt the formation of nanofibrils, with fibrils comparable to those seen in Fmoc-FRGDF alone present in all samples (**Figure 4-8B-D**). Despite this, TEM analysis of fucoidan-containing samples demonstrates greater fibre bundling compared to Fmoc-FRGDF alone. Alternatively, analysis of network microstructure through AFM shows a significant difference between samples. Fmoc-FRGDF demonstrates a highly interconnected network of individual fibrils (**Figure 4-8E**). Observation of coassembled Fmoc-FRGDF + 2 mg/mL fucoidan samples shows no significant increase in fibre bundling; however, there is a notable increase in fibril alignment (**Figure 4-8F**). As the concentration of fucoidan increases from 2 mg/mL to 5 mg/mL, fibre bundling is observed, with bundles ranging in diameter from 50 nm – 100 nm (**Figure 4-8G**). Further increase in fucoidan concentration to 10 mg/mL results in a further increase in fibril bundling, resulting in large bundles of approximately 150 nm in diameter (**Figure 4-8H**). Additional analysis of this sample shows a greater degree of fibre alignment, resulting in features up to 1 μm in width. Subsequently, fucoidan addition is found to influence the ordering of Fmoc-FRGDF in both nano- and micro-environments, with the degree of ordering proportional to fucoidan concentration. These observations are in agreeance with similar investigations which found that peptide assembly driven via biocatalytic induction or increased ionic concentration results in an increase in fibre bundling;^{243, 285} however, to our knowledge, this is the first time a polyanionic polysaccharide has been employed to increase supramolecular ordering in Fmoc-SAP systems using pH switch driven assembly under physiological gelation.

Observation of the post-assembled hydrogel via TEM and AFM analysis reveals thinner, more flexible fibrils coexistent with globular artefacts (**Supplementary Figure S - 1A**). These artefacts are likely a result of free fucoidan precipitation upon drying, resulting in dried fucoidan aggregates. This effect is not visible in coassembled samples and therefore indicates that fucoidan addition post-assembly does not allow for sufficient association with peptide fibrils).

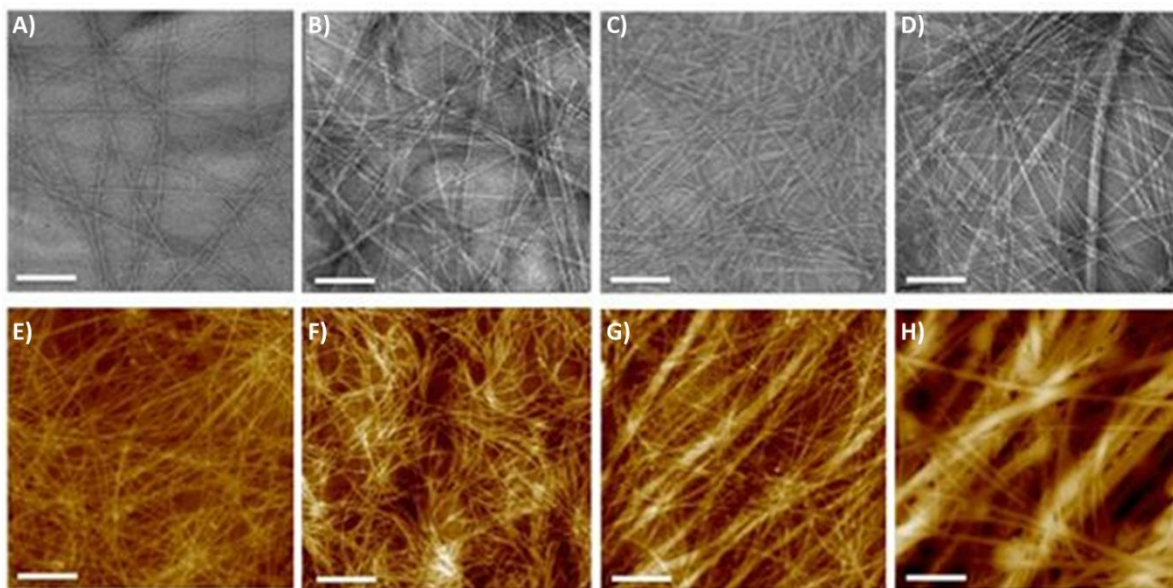


Figure 4-8 –Hydrogel Nano/Microtopology changes upon macromolecule addition (top panel TEM and bottom panel AFM) A, E) 10 mg/mL Fmoc-FRGDF shows scaffold formation through random interaction of fibrils; B, F) +2 mg/mL shows a small increase in supramolecular organisation yielding thicker bundles where individual fibrils have aligned C, G) +5 mg/mL and D, H) +10 mg/mL fucoidan show a large number of thick bundles and consequently fewer individual fibrils. TEM scale bar represents 50 nm, AFM 1 μ m. Reproduced with permission ³³⁷

SANS was performed to verify hydrogel nanoarchitecture and observe fucoidans effect on hydrogel properties further (**Figure 4-9**). Fucoidan containing samples were analysed and compared to Fmoc-FRGDF alone (**Figure 4-9A**), while further analysis was performed on fucoidan solutions dissolved in D₂O to determine if fucoidan alone contributes to structural observations or if such characteristics are resultant of fucoidan-driven supramolecular assembly (**Figure 4-9B**). Analysis of fucoidan only samples demonstrated weak scattering curves owing in part to a large number of exchangeable hydrogen atoms as well as the relatively low fucoidan concentration. Fucoidan dissolved free of peptide demonstrated a concentration-dependent behaviour similar to observations noted in other polyelectrolytes.²⁸⁶⁻²⁸⁷ Higher fucoidan concentrations (5 mg/mL and 10 mg/mL) demonstrated broad correlation peaks. q scattering results in $I(q) \propto q^{-2.7}$ and $I(q) \propto q^{-3}$ for 5 mg/mL and 10 mg/mL samples respectively, with correlation peaks centred at $q^*5 = 0.028$ and $q^*10 = 0.032$. Interpretation of these results reveals mesh sizes of diameter 22.4 nm and 9.8 nm for 5 mg/mL fucoidan and 10 mg/mL fucoidan samples respectively.²⁸⁸ The presence of a mesh in solutions prior to peptide assembly potentially describes some morphological differences between samples coassembled in the presence of fucoidan and those assembled after (post-assembled). The Debye screening effect of the pH switch used to trigger assembly, and the subsequent neutralisation of solution to pH 7.4 means a final ionic concentration of 0.1 M is achieved; this concentration is sufficient for fucoidan in solution to form random coil conformations.²⁸⁹ Despite this, emerging SAP fibrils with high affinity for fucoidan would potentially influence this structure.

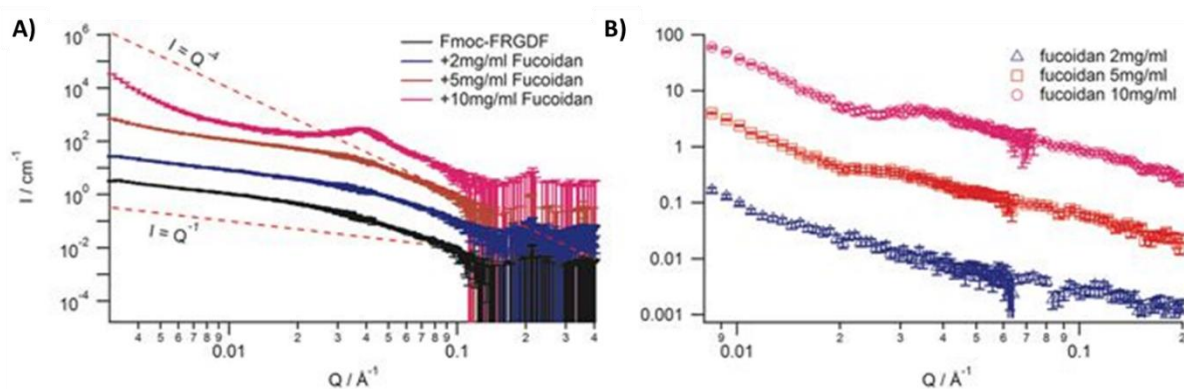


Figure 4-9 – Characterisation of nanostructured changes as observed through SANS A) Scatterplots from hydrogels formed with fucoidan under fucoidan contrast matching conditions, here, increases in low q scattering at higher fucoidan concentration result from an increased density of large objects within the sample. B) SANS

plots from pure fucoidan solutions in D₂O shows polyelectrolyte scattering with a single broad peak Q*. Reproduced with permission ³³⁷

Further analysis of the assembled peptide hydrogels shows trends in agreement with TEM and AFM findings. A low q scattering in samples of higher fucoidan concentration results from the presence of larger hierarchical structures with properties too large for the range of SANS analysis. SANS analysis of structures formed during hydrogelation in the presence and absence of fucoidan is analysed under two separate conditions. The first condition takes advantage of isotropic contrast monitoring to render fucoidan scattering invisible, here, hydrogels are dissolved in 21.5% D₂O; the second technique dissolves hydrogels in ‘pure’ D₂O enabling sufficient contrast for all components to display adequate scattering. Scattering in 21.5% D₂O samples for fucoidan free, 2 mg/mL, and 5 mg/mL samples demonstrated rod-like structures with intermediate q scattering which is proportional to q^{-1} shifting to q^{-4} ; this shift is indicative of fibril radius. Alternatively, samples containing 10 mg/mL fucoidan demonstrate a similar trend; however, in this case, scattering is convoluted as additional structures are influencing sample spectrum. Shape independent analysis of samples gives insight into fibril diameter. Here, the fibril radius is found to decrease upon fucoidan introduction, from an initial 4.9 nm (± 0.1 nm) to 3.6 nm (± 0.1 nm). Investigation of the intermediate q region indicated the average structure of individual SAP fibrils is maintained over the tested fucoidan concentrations. Despite this, analysis of low q range in samples of higher fucoidan concentrations (5 mg/mL and 10 mg/mL) demonstrates more significant structural differences. Observations in this region can be attributed to the presence of larger structures which are likely a result of fibril bundling. These observations are in agreeance with those made during microscopic and spectroscopic analysis.

Fitting using a power law model shows different contributions to scattering in each system. Fucoidan samples containing 5 mg/mL show increased intensity at low q values and a clear deviation from $I \propto q^{-1}$ to q^{-4} . We interpret this as the presence of dilute large aggregates. Alternatively, the 10 mg/mL fucoidan coassembled sample shows a drastic trend following a q^{-4} decline which we believe is indicative of Porod scattering from the increased density of large bundles. However, the limited q range renders us unable of determining lateral bundle size. Despite this, the presence of a Braggs peak at $q =$

0.0376 \AA^{-1} provides evidence of a characteristic length of approximately 16.7 nm; which is roughly 2x fibril diameter, and therefore we attribute this to the lateral association of two peptide fibrils in the presence of fucoidan. These observations agree with observations made during microscopy analysis.

The altered bioactivity of fucoidan-containing samples was not investigated in this chapter as the focus of this chapter was to investigate the ability to enable mechanical tunability through peptide sequence engineering or macromolecule addition. Extensive analysis of macromolecule-modified Fmoc-FRGDF hydrogels is investigated in **Chapter 6**.

4.4.3 Investigation of Self-Assembly Mechanisms and Impact on Mechanical Properties

Spectroscopic techniques are used to investigate fucoidans influence on molecular ordering, and specifically, if the addition of fucoidan to the self-assembled peptide network maintained stable fibril formation (**Figure 4-10**). CD analysis shows chiral spectrums relating to intra- and interfibrillar interactions involved in peptide assembly.^{140, 279, 290} Fmoc-peptides are chiral molecules which produce pronounced CD signals when hierarchically organised into self-assembled structures.²⁹¹ In all samples, CD analysis demonstrates a maintenance of β - π hierarchical assemblies indicated by transitions over three distinct regions (**Figure 4-10A**). The amide region, (200-230 nm), provides insight into protein secondary structure, and specifically (in the context of Fmoc-self-assembly) relates to the formation of β -sheet structures.^{8, 279} Here, there was a noticeable noise effect on scattering in high fucoidan samples (below 220 nm).^{8, 279} Next, the region between 300 – 310 nm is indicative of aromatic π - π stacking between Fmoc groups, here our results suggest this mechanism is maintained in accordance with findings of other assemblies.^{8, 140} Finally, the region between 230 nm and 270 nm indicates degree of supramolecular ordering and subsequently, provides insight into fibril bundling.²⁷⁹⁻²⁸⁰ Here, it is evident that fibril bundling increases at high fucoidan concentrations. Importantly, the spectra relating to the post-assembled control containing 10 mg/mL fucoidan demonstrated no significant difference compared to the Fmoc-FRGDF alone; therefore, it can be deduced that fucoidan induced supramolecular ordering only occurs during coassembly with Fmoc-FRGDF, not post-assembly (**Supplementary Figure S - 1B**). FT-IR is used to analyse vibrations within the amide I region (1600-1700 cm^{-1}) to observe secondary structure formation between peptides (**Figure 4-10B**).²⁷³ All samples demonstrate conserved self-assembly features demonstrated by a major peak at 1690 cm^{-1} and a second minor peak at 1630 cm^{-1} , indicative of β -sheet formation and carbamate characteristic to this class of assembly.²⁷³

Fluorescence spectroscopy observes interactions between Fmoc-groups.²⁷⁹ Here, all samples showed trends characteristic of this class of assembly, once again indicating a broad maintenance of self-assembly despite the presence of fucoidan (**Figure 4-10C**). The peak centred at 310 nm represents the fluorenyl excimer, and is shown to increase proportionately to fucoidan concentration up until a

fucoidan concentration of 10 mg/mL, wherein it decreases; this is likely due to quenching effect (**Supplementary Figure S - 1C**).²⁸⁰ Another peak at 495 nm is representative of excimer species and can provide insight into the formation of J-aggregates.^{8, 280} Once again, this peak increases proportionately to increase in fucoidan concentration within the coassembled peptides. A peak in this range is indicative of supramolecular ordering, and as such supramolecular ordering is found to increase alongside fucoidan concentration, reinforcing observations gained in CD and microscopic analysis.^{8, 279} Once again, the post-assembled control showed a significantly smaller peak in this region, indicating supramolecular assembly via macromolecule addition is only effective when coassembled with the Fmoc-SAP (**Supplementary Figure S - 1D**).

Finally, the mechanical properties of the developed systems were investigated via parallel-plate oscillatory rheology. All samples showed a conserved hydrogel structure indicated through a storage modulus of magnitude higher than that of the loss modulus for the tested frequencies (**Figure 4-10**). Furthermore, a slight increase in viscoelasticity was observed at high frequencies owing to water loss; this observation is characteristic of non-covalent networks.^{290, 292} Fmoc-FRGDF alone demonstrated a soft hydrogel with a storage modulus of approximately 1 kPa. In fucoidan containing samples, storage modulus was significantly increased ($G' \sim 1600\text{Pa}$); with further fucoidan increase resulting in stiffness (relating to G') stabilisation at approximately 2kPa. Here, it is thought that stiffness attributing to increased bundling is compromised by reduced entanglement and junctions, resulting in solitary fibrils existent within the hydrogel. Analysis of a separate fucoidan solution showed no significant contribution to stiffness (**Supplementary Figure S - 1E**); therefore, the increase in stiffness in fucoidan containing samples is likely due to increased supramolecular ordering facilitated through fibril/fucoidan interactions as observed through spectroscopic analysis.

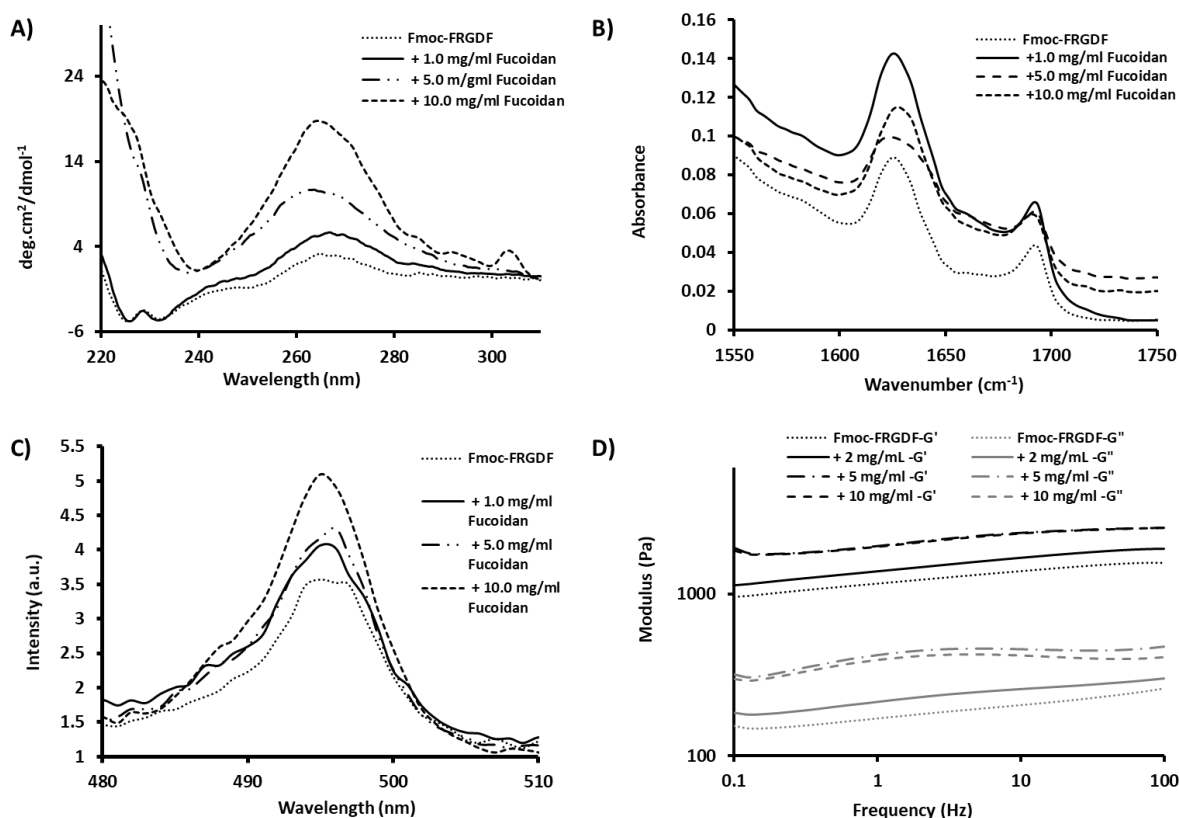


Figure 4-10 – Spectroscopic and rheological analysis of peptide assembly with increasing fucoidan concentration A) CD spectra showing increased magnitude in the region located at 260–270 nm associated with increasing supramolecular organisation; B) FT-IR spectra showing consistent β -sheet formation in all samples, suggesting the maintenance of assembly despite an increase in fucoidan concentration C) Fluorescence spectra of the region 480–510 nm showing increasing fluorescence from Fmoc ordering upon fucoidan increase. D) Rheological Characterisation of the hydrogels. Typical frequency sweeps showing storage (G') and loss (G'') moduli, where the increase in fucoidan is associated with an increase in stiffness. Reproduced with permission ³³⁷

4.5 Conclusion

Alteration of hydrogel biological and structural properties was successfully achieved through incorporation of selectively engineered peptide sequences, or through macromolecule addition. In both cases, the fibronectin-derived, short peptide sequence Fmoc-FRGDF was employed as a relative control.

Control of biological properties through peptide sequence focused on the incorporation of a synergistic fibronectin attachment motif, PHSRN. Scaffolds were formed from this bioactive sequence in one of three ways: 1) synthesis of Fmoc-PHSRN alone, 2) synthesis of Fmoc-FRGDFPHSRN, and finally, 3) coassembly between Fmoc-FRGDF and Fmoc-PHSRN at a 1:1 ratio. Analysis of these hydrogels found Fmoc-PHSRN alone was unable to form a self-supporting hydrogel – likely due to the conformational constraints of proline residues when placed in the environment of self-assembly. Alternatively, the decapeptide, Fmoc-FRGDFPHSRN, formed a weak hydrogel with undesirable mechanical properties. Finally, the coassembled scaffold, containing fibrils constituting both Fmoc-FRGDF and Fmoc-PHSRN, resulted in the formation of an enhanced hydrogel with robust mechanical and structural properties. Preliminary *in vitro* analysis of hydrogel bioactivity revealed enhanced results in the coassembled system, showing significantly greater cell spreading and proliferation compared to the Fmoc-FRGDF control.

Integration of mechanical tunability was investigated through macromolecule incorporation during self-assembly. Here, Fmoc-FRGDF was coassembled with the highly sulphated polysaccharide, fucoidan, at various concentrations. Analysis of self-assembly mechanisms and subsequent microarchitecture demonstrated a correlation between fucoidan concentration and supramolecular fibril ordering; resulting in increased fibre bundling proportional to an increase in fucoidan concentration. Importantly, the presence of fucoidan during self-assembly was found to maintain fibril formation at these concentrations. Samples allowed to gelate in the absence of fucoidan did not demonstrate increased fibre bundling even when fucoidan is added after assembly (post-assembly); therefore, increased supramolecular ordering using this system requires fucoidan inclusion during the assembly process (coassembly). In all tested conditions, fucoidan addition was shown to increase material

viscoelastic properties; however, interestingly, high fucoidan concentrations did not result in a substantial increase in stiffness (as indicated by material storage modulus). We anticipate that although there is a substantial increase in fibre bundling, stiffness is compromised by a reduction in fibre intersections.

In this chapter, we have successfully introduced and extensively characterised two novel methods for influencing mechanical and biological tunability in SAP systems. Overall, both approaches resulted in alterations in fibre presentation either in the micro- or nano-scale which lead to transient effects on material stiffness. Preliminary biological effects were investigated in PHSRN-functionalised scaffolds, while the effect of macromolecule addition on scaffold bioactivity will be comprehensively analysed in consequential chapters (**Chapter 6**).

Chapter Five:

INVESTIGATION OF MULTISEQUENCE MATERIAL AS AN ADVANCED TUMOUR MICROENVIRONMENT

5.1 Preview

In this chapter, an advanced modular cancer model is developed through the culturing of heterogeneous cancer spheroids within a coassembled Fmoc-SAP hydrogel. Specifically, heterogenous spheroids were formed through the co-culturing of LLC cells and NOR-10 fibroblasts and subsequently encapsulated within a fibronectin/laminin-inspired Fmoc-FRGDF/Fmoc-DIKVAV hydrogel. Fmoc-SAP encapsulated spheroids were compared to 2D controls and 3D non-encapsulated spheroids. Results show spheroids encapsulated within the Fmoc-SAP hydrogel demonstrate enhanced metabolic activity and increased motility compared to non-encapsulated counterparts. Furthermore, Fmoc-SAP encapsulated spheroids demonstrated higher levels of cancer-associated fibroblast (CAF) differentiation and greater endothelial to mesenchymal transition compared to the 2D control and non-encapsulated spheroids. Finally, Fmoc-SAP encapsulated spheroids were compared to agarose encapsulated spheroids, with results showing enhanced migration in Fmoc-SAP hydrogels compared to the agarose control.

Contribution of the candidate:

- Material Analysis (CryoSEM, Rheology), and assembly mechanisms (SAXS, CD).
- Manuscript preparation.

- Prepared proposal, successful Funding for Synchrotron Experiments (ANSTO, AUS)

Publications relevant to this chapter

Al Balushi, N., **Boyd-Moss, M.**, Firipis, K., Darby, I., Nisbet, D., Pouniotis, D., Williams, R., (2019)
'Bioactive Peptide Microenvironments as functional lung tumour models.' Manuscript in preparation.

Abstract

Effective modelling of tumours *in vitro* will provide rapid, cost-effective systems for the testing of anti-cancer therapeutics. Currently, cancer modelling is routinely conducted in 2D cultures; although these systems are simple, they lack multidimensional cell-cell and cell-matrix interactions which govern cellular behaviour. Cancerous tumours exist within a supportive microenvironment which encourages development; thus, we hypothesise that spheroids placed within a 3D, functionalised artificial microenvironment would mimic *in vivo* tumours to a greater degree compared to those cultured in 2D or the absence of a functionalised microenvironment. Here, we develop a novel system, whereby we encapsulate heterogenous cancer spheroids within a functionalised, multi-epitope SAP scaffold. Specifically, we coassemble a fibronectin-inspired SAP, Fmoc-FRGDF; with a laminin-inspired SAP, Fmoc-DIKVAV to better mimic the cancer microenvironment. Encapsulated spheroids were compared to non-encapsulated spheroids and a 2D co-culture control. Environment functionalisation was further investigated through comparison with agarose-encapsulated spheroids. We selected agarose as a control owing to its comparable network orientation yet lack of cell-recognised sequences. The physical properties of the developed hydrogels were discussed concerning assembly mechanisms, network organisation, nanoscale morphology, and viscoelastic properties; whilst influence of functional matrix incorporation was investigated regarding cell metabolic activity, motility, migration, and CAF fibroblast differentiation. Results showed cancer cell, and co-cultured spheroid motility was enhanced in encapsulated spheroid samples compared to non-encapsulated counterparts. This part of the work demonstrated the potential of multi-sequence Fmoc-SAPs in cancer modelling applications and confirms the versatility of these materials.

5.2 Introduction

Traditionally, cancer studies performed *in vitro* have been conducted in 2D environments. These conventional models are cheap, simple, and have substantially increased understanding of cancer behaviour; yet they fail to sufficiently capture the complexities of the *in vivo* tumour microenvironment (TME). Notably, these models are limited as they lack direct, multidimensional cell-cell contact and cell-matrix interactions required to drive major cellular processes, including tumour initiation, proliferation, migration, and invasion.^{49, 293-294}

The natural TME is a complex system which consists of the ECM, blood vessels, tumour cells, soluble factors, and numerous other stromal cell types, including endothelial cells, fibroblasts, and immune cells.²⁹³ During tumour progression, the stroma surrounding epithelial tissue undergoes substantial changes. The stroma contains predominantly collagen-I, which appear ‘curly’ and anisotropic, however in the early stages of cancer progression, the amount of collagen within the stroma increases and collagen fibres transform into straighter, more aligned morphologies.²⁹⁵⁻²⁹⁶ In invasive cancers, these collagen fibres become more bundled and orientate perpendicularly to the basement membrane; promoting the migration of cancer cells away from the primary tumour, and subsequently, decreasing patient survival rates.²⁹⁷ Stromal network reorganisation by CAFs also increases network stiffness through the secretion of ECM proteins and enzymes which crosslink collagen fibrils.^{295, 298} This increase in stiffness, combined with the track-like organisation of collagen, significantly increase cancer cell migration, leading to later metastasis.^{295-296, 298}

The ECM is an essential component of the TME which supports cells while providing necessary biochemical and biomechanical cues essential for cell-cell communication and cell-matrix interactions.²⁹³ Therefore, 3D *in vitro* models for cancer progression have become increasingly popular with researchers, as they allow for the controlled presentation of biochemical and biomechanical signals in a biomimetic fashion.²⁹⁹ These systems effectively bridge the gap between 2D cancer models and *in vivo* studies, enabling effective investigation into cancer progression and allowing for better evaluation into drug therapies.²⁹³

In cancer research, tumour spheroid models have been extensively used as a popular technique to model 3D cancer progression and behaviour *in vitro*; owing to their high similarities to solid tumours *in vivo*. In particular, tumour spheroids present similar structural characteristics to solid tumours, having proliferative zones and necrotic zones (**Figure 5-1A**).²⁹⁹ Furthermore, tumour spheroids allow biomimetic cell-cell communication, present similar oxygen and nutrient gradients and allow for the development of heterogeneous models.²⁹⁹⁻³⁰⁰ However, unlike clinical tumours, tumour spheroid models often lack a suitable ECM, resulting in the spheroids existing in an attachment-free microenvironment, and therefore, experiencing very different mechanical and biochemical properties than that provided by the native ECM.²⁹⁹

Mimicking the *in vivo* environment *in vitro* requires the use of advanced biomimetic scaffolds which are capable of supporting cell-cell and cell-matrix interactions. Recently, studies have placed patient-derived tumoroids within Matrigel environments, allowing for highly biomimetic behaviour analysis.³⁰¹ However, organoids are complex and difficult to reproduce accurately, and Matrigel is difficult to tune and suffers from batch-to-batch variability.³⁰² Similarly, Lan et al. took the advantage of alginate hydrogels for liver cancer cell encapsulation to study cancer cell viability, morphology and drug metabolism. Despite alginate hydrogels allowing ease of encapsulation and cell recovery, these materials are highly soluble in solution and lack cell-adhesion sites essential for cell development.³⁰³

One recent class of materials which have offered significant promise to tissue engineering applications are SAPs. Hydrogels developed from these materials allow for high biomimicry, boasting the ability to form highly similar structures to the native ECM while enabling for substantial control over biochemical signalling through amino-acid sequence selection.^{143, 304} Furthermore, these materials are inherently biocompatible owing to their formation from amino acid building-blocks.. Using these materials, researchers have seen success in a range of tissue-regeneration applications, including muscle, nerve, and bone regeneration;^{26, 305-307} as well as cancer modelling.³⁰⁸ Fluorenylmethyloxycarbonyl self-assembling peptides (Fmoc-SAPs) are promising biomaterials which are easily functionalised through sequence selection. These short aromatic peptide sequences allow for triggered self-assembly through π - π stacking between Fmoc-groups and β -sheet formation between

short peptide sequences.⁸ Importantly, this class of SAP allows for the formation of biocompatible hydrogels from highly decorated, bioactive nanofibrous structures similar to the *in vivo* ECM.¹²⁸

In this chapter, a complex, multidimensional *in vitro* lung cancer model is developed through the formation of heterogenous spheroids placed within a highly biomimetic self-assembled microenvironment. Specifically, tumour spheroids are developed through the co-culturing of LLC lung cancer cells and murine NOR-10 fibroblasts (NOR-10); while an artificial microenvironment is formed through the coassembly of Fmoc-DIKVAV and Fmoc-FRGDF. Previous investigations using Fmoc-DIKVAV and Fmoc-FRGDF have shown good biocompatibility, suitable mechanical properties, and high bioactivity facilitated through the presentation of IKVAV and RGD motifs.²⁶

5.3 Results and Discussion

5.3.1 Formation of Spheroids and Artificial Microenvironments

5.3.1.1 Formation of Spheroids

Cancer cells cultured in a 3D microenvironment illicit significant behavioural differences compared to those cultured in 2D models.²⁹⁴ Tumour spheroids are 3D spherical clusters of cells which better present *in vivo* tumours, allowing for cancer models of increased accuracy.³⁰⁹ The proximity of these cells in a 3D configuration allows for biomimetic cell-cell communication, while the ability to culture spheroids from multiple cell types facilitates better replication of the heterogeneous tissue microenvironment.^{299-300, 309} Heterogenous co-cultures of murine LLC cancer cells and murine NOR-10 fibroblasts (NOR-10) were used for subsequent spheroid formation. 2D co-cultures were also developed through co-culture of LLC and NOR-10 cells on tissue culture plastic (**Figure 5-1B i**) and compared to non-encapsulated 3D spheroids (**Figure 5-1B ii**) and 3D spheroids encapsulated in hydrogels (**Figure 5-1B iii**). Within this chapter, hydrogel-encapsulated spheroids are termed 3D+ECM.

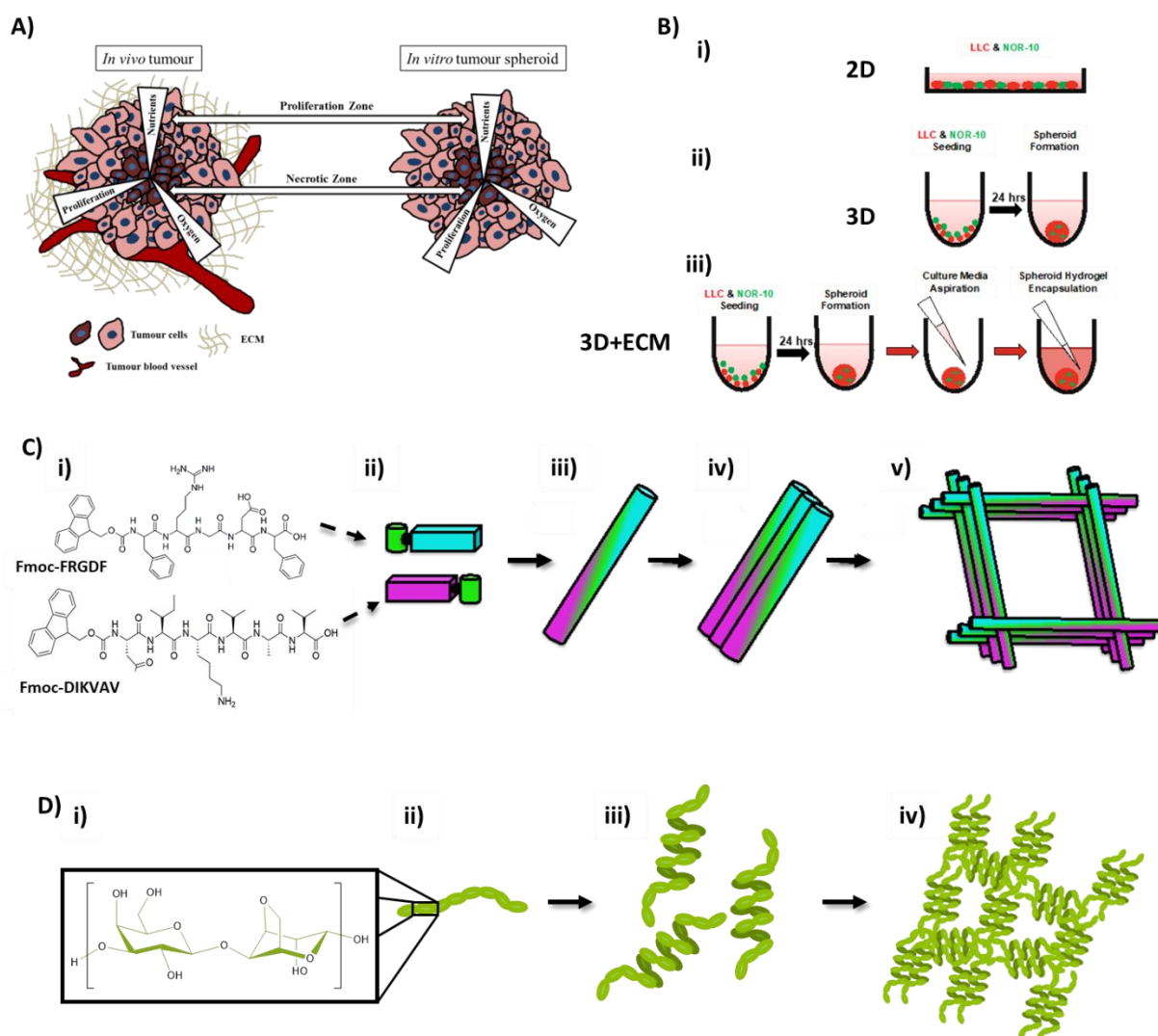


Figure 5-1 – Schematic of spheroid and hydrogel formation A) Cartoon comparison of similarities between *in vivo* tumour and spheroids, B) schematic of spheroid preparation showing 2D co-culture, 3D spheroid, and 3D+ECM spheroid, C) Cartoon showing Fmoc-SAP hydrogel assembly (i) Chemical structure of Fmoc-FRGDF and Fmoc-DIKVAV, (ii) individual subunit in schematical depiction, (iii) formation of fibril, (iv) supramolecular ordering of fibrils, (v) entanglement of fibrils into network. D) Cartoon depiction of Agarose hydrogel formation. (i) chemical structure of agarose, (ii) artistic depiction of polymer, (iii) formation of helical structures, (iv) polymer association and formation of network.

5.3.1.2 Formation of Hydrogels

The development of an artificial TME is enabled through the coassembly of a fibronectin-inspired SAP, Fmoc-FRGDF with a laminin-inspired SAP, Fmoc-DIKVAV, to form the coassembled hydrogel – Fmoc-FRGDF/Fmoc-DIKVAV as previously reported (**Figure 5-1C i**).²⁶ Previously, these systems have been shown to present both peptides within a single fibrils within a coassembled network (assessed through FT-IR, SAXS, CD) which drives enhanced cell spreading and morphology.²⁶ Peptides were

combined at 1:1 ratio prior to self-assembly, allowing for the formation of fibrils that present both epitopes simultaneously. Previous investigation into Fmoc-based SAPs finds short peptide sequences capped with the Fmoc-group undergo spontaneous self-assembly triggered by a well-characterised pH switch method, resulting in the formation of larger hierarchical structures through π - β assembly.¹⁴⁰ Specifically, fibril formation is facilitated through π - π stacking of Fmoc-groups and anti-parallel β -sheet formation between short peptide sequences, resulting in the controlled self-organisation of short sequences into long fibrillar structures (**Figure 5-1C ii – iv**).⁸ Further association and entanglement of fibrillar structures results in the formation of a hydrogel network (**Figure 5-1C v**). Coassembled Fmoc-FRGDF/Fmoc-DIKVAV hydrogels were formulated at 10 mg/mL (1% (w/v)) and used to encapsulate spheroids in 3D+ECM samples.

A control artificial TME was developed through the gelation of low-melt agarose (1% (w/v)). Agarose is a seaweed-derived polysaccharide comprised of repeating agarobiose units (**Figure 5-1D i**).⁹³ Hydrogel formation from agarose is facilitated through hydrogen bonding and electrostatic interactions resulting in the formation of helical structures which associate with one another to form networks, specifically upon cooling from melted state (**Figure 5-1D ii – iv**).⁹³ Hydrogels developed from both agarose and coassembled SAPs were able to maintain stable gel formation under physiological conditions (pH 7.4, 37° C); with both hydrogels eliciting self-supporting properties as demonstrated through hydrogel inversion (**Supplementary Figure S - 2**). In both cases, the resultant hydrogel was slightly opaque (**Supplementary Figure S - 2A**), and spheroids were encapsulated within hydrogels as indicated (**Figure 5-1B**).

Despite both artificial microenvironments being characterised in regard to mechanical properties in the following section, agarose is not used for comparison of 2D, 3D and 3D+ECM samples until the peripheral sections of this chapter (see *Section 5.3.4*).

5.3.2 Mechanical Characterisation of Formulated Materials

5.3.2.1 Observation of Network Topology of Engineered SAP Hydrogels.

Investigation into hydrogel morphology was facilitated through TEM, allowing direct visualisation of underlying hydrogel nanostructures (**Figure 5-2A i, ii**). The coassembled system presented as long

fibrils as has been previously noted (**Figure 5-2A i**).²⁶ Contrastingly, agarose samples presented as aggregates with no noticeable structural organisation as previously observed (**Figure 5-2A ii**).³¹⁰ Coassembled Fmoc-SAP fibrils were measured using ImageJ and an average fibril diameter of 14.72 nm ($\sigma = 2.10$) was calculated. The lack of visible hierarchical order in the agarose hydrogel suggests agarose structures lies outside the range of TEM.

Hydrated microscale network topology was investigated qualitatively through CryoSEM techniques allowing for observation of sample microscopic structure under hydrated conditions (**Figure 5-2A iii, iv**). The coassembled hydrogel containing both Fmoc-FRGDF and Fmoc-DIKVAV sequences presented as a typical fibrous hydrogel with high porosity and morphological similarities to the native ECM (**Figure 5-2A iii**). A bundle width of 0.61 μm ($\sigma = 14 \mu\text{m}$) was observed in the coassembled sample as calculated using ImageJ. Alternatively, agarose samples presented as thicker bundles (1.77 μm width, $\sigma = 0.56 \mu\text{m}$), yet retained the highly porous structure observed in the coassembled hydrogel (**Figure 5-2 A iv**). Despite agarose samples appearing as denser structures, both networks demonstrate comparable network organisations.

5.3.2.2 Nanoscale Investigation of Local Polymer Organisation

Sample structure was quantitatively investigated via SAXS (**Figure 5-2B**). Considering the SAXS curve follows a trend comparable to characteristic cylinders as is evident by a transition from q^{-4} at low q range to q^{-1} at mid q range, IFT scattering curves can be fitted with a $P(r)$ model which provides insight into average fibril radius (**Supplementary Figure S - 2B**). TEM analysis of fibrils finds fibril length lies outside SAXS q range; as a result, the maximum intensity in the $p(r)$ curve can be correlated to fibril radius, rather than length. Through $P(r)$ fitting, an average fibril diameter of 14.2 nm ($r = 71.04 \text{ \AA}$) was calculated, reinforcing results gained in TEM analysis. Agarose samples did not demonstrate a suitable trend for $P(r)$ fitting. Consequently, agarose scattering curves were modelled with shape independent models and compared to coassembled hydrogels regarding correlation length, and mesh size (via two-power model fitting).

Analysis of scattering curves over mid-low q range allows for the determination of correlation length (**Figure 5-2B i**), as described by **Equation 5-1**.

$$I(q) = \left(\frac{C}{(1 + Q\xi)^m} \right) + bkg$$

Equation 5-1 SAXS Fitting for correlation length

Where the Porod scaling factor (C) is deduced from the scattering vector $q = 0$ and relates to scattering intensity. The Porod exponent (m) relates to the local polymer structure and provides information about polymer conformation. Correlation length (ξ) provides a reasonable estimate of the average length of entanglement in semi-dilute polymer solutions;³¹¹ and bkg takes into account background scattering. The agarose sample demonstrates a correlation length of 5.0 nm ($\pm <1\%$) while the coassembled sample shows a correlation length of 4.7 nm ($\pm <1\%$). These results suggest agarose has a slightly larger distance between entanglements compared to the coassembled hydrogel.

Determination of mesh size provides insight into polymer spatial association within the network, and specifically, into nanoscale polymer mesh organisation. Mesh size can be determined through calculation of the crossover point (q_c) when scattering profiles are modelled using a two-power law (**Figure 5-2B ii**). The point of crossover can also be described as the position of a shoulder formed at low-scattering vectors in self-similar structures of comparable dimensions and is indicated by the intercept of two-power laws, one in the low q range (before shoulder) and another in mid q range (following shoulder).³¹² Mesh size is related to crossover as indicated by arrows (**Figure 5-2B ii**) and as described by **Equation 5-2**.

$$Mesh\ Size = \frac{2\pi}{q_c}$$

Equation 5-2 – SAXS Fitting for Mesh Size

Analysis of mesh size using a two-power law found agarose samples to have a mesh size of 10.2 nm (± 0.047 nm), while the coassembled sample presented a mesh size of 19.4 nm (± 0.14 nm). The agarose sample presented two-power laws of 2.50 ($\pm <1\%$) and 3.27 ($\pm <1\%$) for the low and mid- q range respectively. A similar trend was evident in the coassembled sample, returning a power law of

2.46 ($\pm 1.4\%$) for low q range and 3.85 ($\pm <1\%$) for mid q range. Power law model fitting provides insight into the mass fractal dimension and correlates to polymer conformation. Mass fractal dimensions range from 1 to 3.³¹² A mass fractal dimension of 1 indicates a linear object - such as a mathematical line; while a mass fractal dimension near 1.67 indicates a swollen polymer in a good solvent.³¹¹ Mass fractal dimensions between 2 and 3 indicate the formation of branched polymer conformations and network formation.³¹¹ Power laws which return values greater than 4 indicate a density change is finite but discontinuous at the boundary of scattering.³¹³ Therefore, the similarity of power laws presented at low q range (2.50 and 2.46 for agarose and coassembled respectively) indicates a similarity of polymer conformation between the two samples, relating to the presence of highly branched polymer polymer conformations and indicating the similarity of network formation; while power laws at mid q indicate the presence of structures outside the range of scattering.

Assembly mechanisms were verified using CD to provide insight into chiral interactions and subsequently, provide information of assembly mechanisms and polymer/protein backbone conformation (**Figure 5-2C**). Absorption peaks in the amide I region indicate peptide folding, and specifically, the formation of β -sheets, α -helix and random coil conformations. A strong negative peak is evident in the coassembled peptide hydrogel centred around 209 nm, indicating the presence of indistinct β -sheets as is characteristic of Fmoc-assemblies. A positive peak centred at 261 nm is representative of supramolecular ordering, while a positive peak between 300 nm and 310 nm is indicative of Fmoc-stacking through J-aggregate interactions. Contrastingly, the agarose hydrogel shows no dominant structural organisation. CD results confirm the highly ordered structure of the coassembled Fmoc-FRGDF/Fmoc-DIKVAV system.

5.3.2.3 Determination of Material Viscoelastic Properties

Following determination of assembly mechanisms, hydrogel viscoelastic properties were analysed via oscillatory rheology (**Figure 5-2D**). A frequency sweep was applied from 0.1 Hz to 20 Hz to investigate material stability in response to shear. In both hydrogels, the storage modulus was of greater magnitude than loss modulus, indicating the formation of a stable hydrogel. The agarose sample demonstrated a storage modulus of approximately 1 kPa. Contrastingly, the coassembled hydrogel demonstrates a

storage modulus of approximately 10 kPa, being approximately one order of magnitude stiffer than agarose. A slight thickening effect is evident in both samples with increasing frequency, as is characteristic of non-covalent hydrogel systems.^{292, 314}

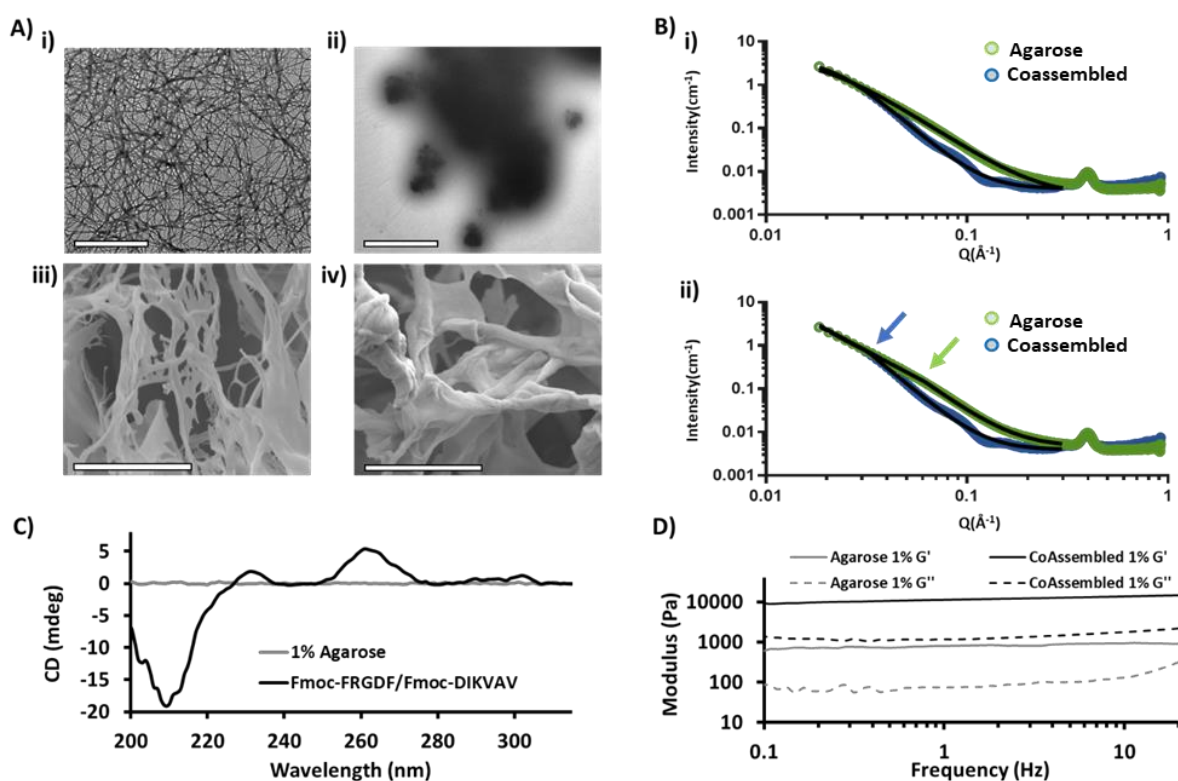


Figure 5-2 – Material characterisation A) investigation of material architecture and network topology, i) TEM imaging of Fmoc-SAP fibrils, ii) TEM imaging of Agarose aggregates, (TEM Scalebar 1 μm) iii) CryoSEM imaging of coassembled peptide network showing fibres, and iv) CryoSEM imaging of 1% agarose sample showing bundled network topology (SEM Scalebar 20 μm) B) Fitting of scattering curves attained during SAXS investigation, i) fitting for correlation length, and ii) fitting to two-power model used for the determination of mesh size (arrows point to power intercept), C) CD spectra of agarose and Fmoc-FRGDF/Fmoc-DIKVAV, D) Rheological analysis of material viscoelastic properties of agarose and Fmoc-FRGDF/Fmoc-DIKVAV as indicated through storage (G') and loss (G'') modulus.

5.3.3 Comparisons of 2D, 3D and Encapsulated 3D Cultured Conditions

5.3.3.1 Analysis of Spheroid Metabolic Activity and Adhesion

The preliminary aim of this study is to investigate the effect cell organisation has on cell metabolic activity, adhesion and migration. LLC and NOR-10 mono-spheroids and co-cultures (1:1 ratio) were placed within a Fmoc-FRGDF/Fmoc-DIKVAV coassembled microenvironment (3D+ECM) and compared to spheroids placed within media (3D) and monolayer cells cultured in 2D. Cell metabolic activity was investigated through MTS assay analysis over 72 hours (**Figure 5-3A**). Following 24h culture, mono-spheroids (LLC, and NOR-10) and co-cultured 3D+ECM spheroids (LLC/NOR-10, 1:1 ratio) demonstrated significantly greater metabolic activity compared to their non-encapsulated spheroid counterparts (LLC $p < 0.0001$, NOR-10 $p = 0.0125$, co-culture $p = 0.0004$, **Figure 5-3A**). A similar trend is evident following 72-hours culture, with NOR-10 and co-cultured spheroids demonstrating a significant increase in metabolic activity compared to non-encapsulated spheroid counterparts (NOR-10 $p < 0.0001$, co-culture $p < 0.0001$, **Figure 5-3A**). LLC monospheroids did not see a significant difference in metabolic activity at this time point.

Investigation of general cell health was facilitated through the investigation of cell metabolic activity as determined through MTS assay analysis. 3D+ECM spheroids demonstrated enhanced metabolic activity compared to those cultured in media alone following 72-hour incubation, indicating that the artificial microenvironment is biocompatible and promotes healthy cell growth. This is in accordance with previous investigations which found Fmoc-FRGDF hydrogels support oral tongue squamous carcinoma cells (SCC25) and hMFCs viability over 3 and 5 days respectively.^{143, 265} Collectively, these results demonstrate the inherent biocompatibility of functionalised Fmoc-SAPs and highlight their potential for use as artificial TMEs. Furthermore, our findings support the use of encapsulated spheroids to better monitor tumour progression, underlining the significance of cell-ECM interaction on cellular behaviour.

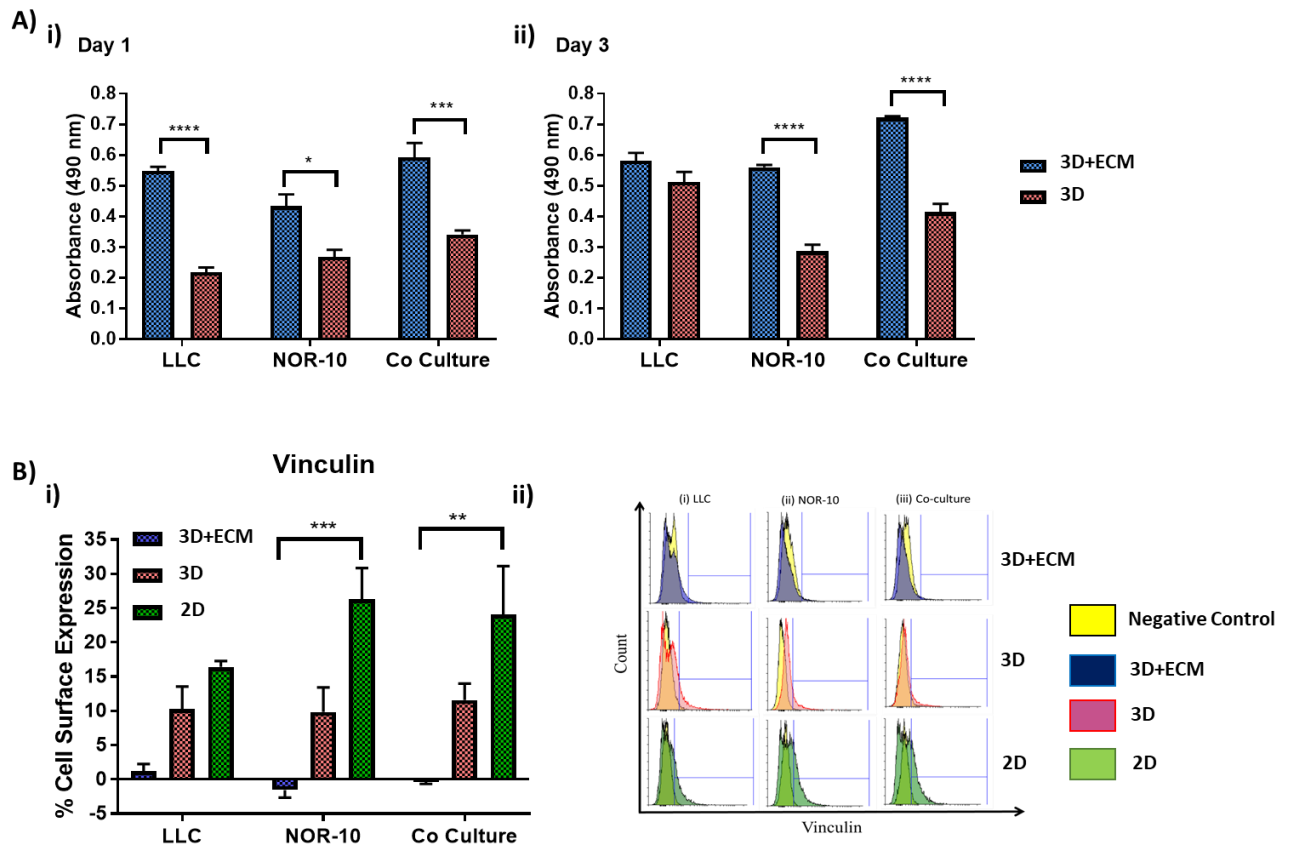


Figure 5-3 – Biological activity of spheroids in response to hydrogel microenvironment A) Metabolic activity of spheroids encapsulated within Fmoc-SAP hydrogels (3D+ECM) and non-encapsulated spheroids (3D) measured by MTS assay on i) day 1 and ii) day 3 post-cultivation. Statistics were obtained by two-way ANOVA and Tukey's post hoc test. Error bars represent the SEM; $n = 3$, $*p < 0.05$, $***p < 0.001$, $****p < 0.0001$. B) i) Percentage of cell expressing vinculin in 3D LLC, NOR-10 and co-culture spheroids post encapsulation (3D+ECM) within hydrogel for 3 days compared to non-encapsulated 3D spheroids and 2D cell culture and ii) representative histograms images of vinculin expression are shown. Statistics were obtained by two-way ANOVA and Tukey's post hoc test. Error bars represent the SEM; $n = 3$, $**p < 0.01$, $***p < 0.001$.

The ECM plays an important role in cancer cell invasion to surrounding tissue. Vinculin is a 116 kDa protein which is highly enriched in regions in which cells contact one another and the underlying substratum.³¹⁵ Subsequently, vinculin plays crucial roles in governing cell-ECM adhesion (mediated through integrin receptors) and cell-cell adhesion (mediated through cadherin).³¹⁵ A down-regulation of vinculin expression is also observed in many invasive cancers, including colorectal cancer, melanoma, vaginal, and cervical carcinomas.³¹⁶⁻³¹⁸ Therefore, vinculin expression was also investigated as an indication of cell attachment and functional association between cancer cells and the ECM. Vinculin expression of 3D+ECM spheroids (mono- and co-cultured) was compared to that of non-encapsulated spheroids (3D) and cells cultured on 2D tissue culture plastic via flow cytometry (**Figure 5-3B**). Following 72h culture, a significant down-regulation of vinculin is observed in 3D+ECM NOR-10 and co-cultured spheroids compared to the 2D control, demonstrating a vinculin surface expression of 0% for 3D+ECM encapsulated samples compared to 26.3% for 2D NOR-10 and 24.1% for 2D co-cultured cells (NOR-10 $p=0.0004$, co-culture $p=0.0019$, **Figure 5-3B**). Non-encapsulated spheroids demonstrated no significant difference in vinculin expression levels (10.3% LLC, 9.8% NOR-10, and 11.6% co-cultures) compared to 3D+ECM spheroids and the 2D control ($p \geq 0.05$, **Figure 5-3B**).

A reduction in vinculin expression has been shown to result in a decrease of cell adhesion and induction of motility, thus promoting cancer cell invasion and metastasis. Our results demonstrate a reduction in vinculin expression in 3D+ECM NOR-10 and co-cultured spheroids compared to the 2D control; indicating cancer cell culturing within this self-assembled, biomimetic microenvironment leads to increased motility as is characteristic of cancer cells *in vivo*. Furthermore, the elevated vinculin expression in 2D cultures and non-encapsulated spheroids indicates that the cells are more adherent to tissue culture plastic or themselves compared to those cultured within the coassembled microenvironment. Our results echo a study by Li et al. who observed a significant down-regulation of vinculin in patient-sourced metastatic colon cancer tissue samples and various invasive human colon cancer cell lines (HT116, Caco2, HT29, SW620, and SW480).³¹⁶ These results combined with observations in this study indicate that spheroid adhesion, motility, and invasiveness is significantly

impacted by a reduction in vinculin expression when cultured in a functionalised artificial microenvironment compared to 2D cell cultures.

5.3.3.2 Vinculin and F-actin Co-localisation

Cell migration and cytoskeleton organisational changes are further investigated through observation of vinculin and F-actin co-localisation as indicated through immunostaining and confocal analysis (**Figure 5-4**). Following 72 hours in culture, cells cultured onto tissue culture plastic (2D) demonstrated highly flat morphologies with multidirectional stretched F-actin filaments (arrows showing filaments) (**Figure 5-4A, iii**). Alternatively, non-encapsulated spheroids showed round F-actin filaments which were localised along the spheroid periphery (**Figure 5-4B iii**). Interestingly, 3D+ECM spheroids in the coassembled hydrogel presented more protrusive, round branched F-actin filaments compared to non-encapsulated counterparts (**Figure 5-4C iii**). Despite an absence of observable focal adhesion points localised to the outer plasma membrane in co-cultured conditions, vinculin is clearly observed in all conditions.

Integrin association with surrounding ECM proteins, including laminin and fibronectin, results in cytoskeleton changes through the formation of focal adhesion complexes comprising many cytoplasmic proteins, including vinculin and F-actin.³¹⁹ Cell interaction with the ECM results in motility, allowing the migration of cells through the ECM.³¹⁹ These interactions are complex and require coordinated changes in actin cytoskeleton organisation, resulting in the development of focal adhesion points and alteration of cell morphology.³¹⁹ Our results find that culturing cells under different organisational conditions (2D culture, non-encapsulated spheroid, encapsulated spheroid) results in dramatic changes in F-actin distribution in co-cultured spheroids. 3D+ECM co-cultured spheroids demonstrated round, branched F-actin filaments which were substantially different in appearance to those observed in 2D cultures and non-encapsulated spheroids. These findings are supported by Zhou and colleagues who demonstrated that MSCs displayed stretched out F-actin filaments in 2D culture, yet presented along the periphery in spheroid samples.³²⁰ These results illustrate the importance of functional matrix incorporation and suggest that Fmoc-SAP hydrogels enhance the migratory phenotype of co-cultures in 3D spheroids.

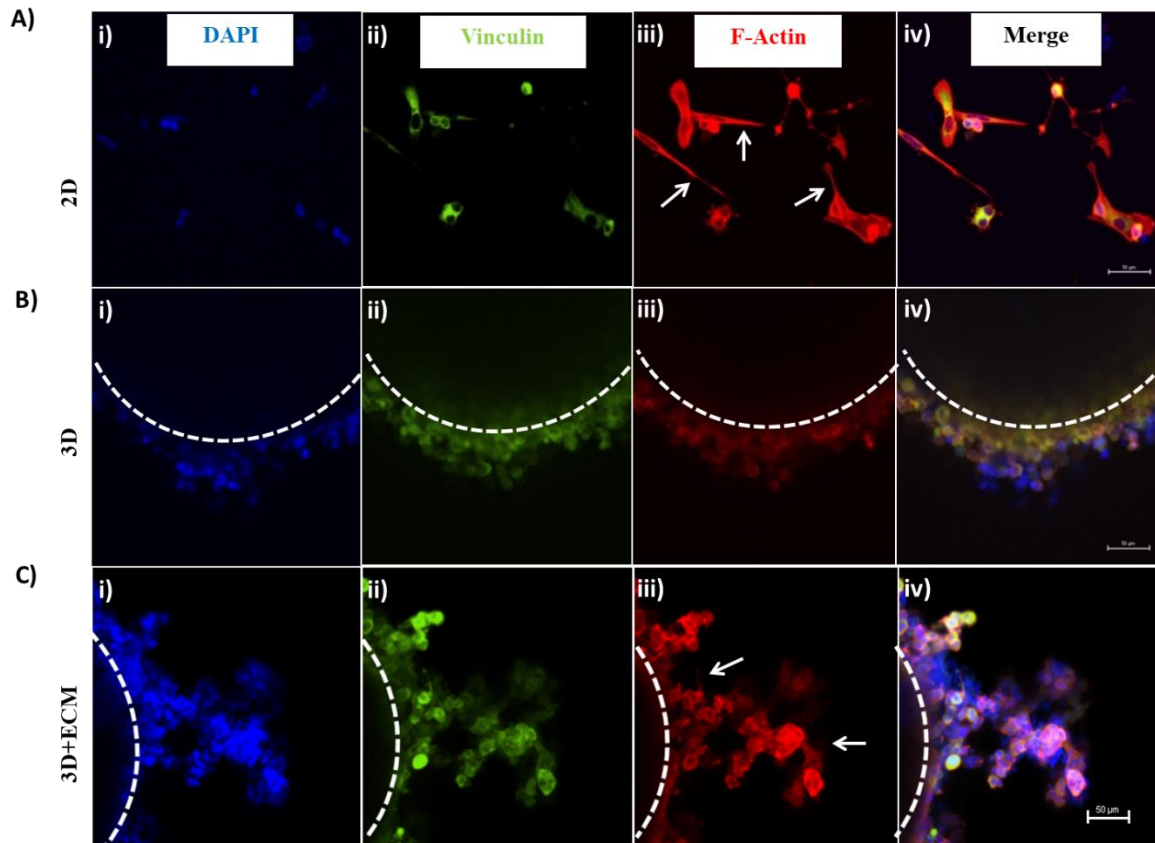


Figure 5-4 – Cytoskeleton in A) 2D cultures, B) non-encapsulated spheroids and C) 3D+ECM spheroids. F-Actin and vinculin/focal adhesion organization in co-culture spheroids encapsulated within hydrogel (3D+ECM) for 3 days compared to non-encapsulated spheroids (3D) and 2D co-culture cells. Dashed line indicates the original spheroid border as internal margin for reference (scale bar, 50 μ m).

5.3.3.3 *Alpha-Smooth Muscle Actin Expression*

Epithelial to mesenchymal transition (EMT) is a process during cancer development wherein epithelial-like cancer cells switch toward a more motile mesenchymal phenotype.³²¹ During EMT, epithelial markers are downregulated (such as E-cadherin) whereas mesenchymal markers (such as α -SMA) are upregulated;³²¹ therefore, α -SMA expression is commonly monitored to assess EMT transition.³²¹ α -SMA expression is also used to assess differentiation of fibroblasts into CAFs, as α -SMA is normally expressed by differentiating CAFs in the TME.³²² In this study, α -SMA expression was determined using flow cytometry following 72h cell culture as a measure of CAF differentiation and EMT induction (**Figure 5-5**). LLC, NOR-10 and co-culture spheroids were encapsulated within the coassembled Fmoc-FRGDF/Fmoc-DIKVAV hydrogel and compared to non-encapsulated spheroids and 2D cells cultured on culture plastic. A noticeable reduction in α -SMA expression was observed in NOR-10 cells compared to LLC cells and co-culture in all conditions (**Figure 5-5**), signifying reduced fibroblast activation in the absence of cancer cells. Furthermore, there was a significantly greater percentage (36.3%) of α -SMA expression in 3D+ECM co-cultured spheroids following 72 hours in culture compared to non-encapsulated spheroids and 2D co-cultures ($p < 0.0001$ in both conditions, **Figure 5-5**). Similarly, LLC spheroids in 3D+ECM and non-encapsulated environments expressed significantly higher percentages (21.2% and 22.9%, respectively) of α -SMA expression compared to the 2D control, indicating that the 3D+ECM spheroids may have undergone EMT ($p = 0.0005$ and 0.0001 , respectively, **Figure 5-5**). Analysis of α -SMA expression in this study indicate that encapsulating cancer cells within a bioactive, Fmoc-SAP hydrogel results in increased induction of mesenchymal phenotypes compared to 2D culture and non-encapsulated spheroids.

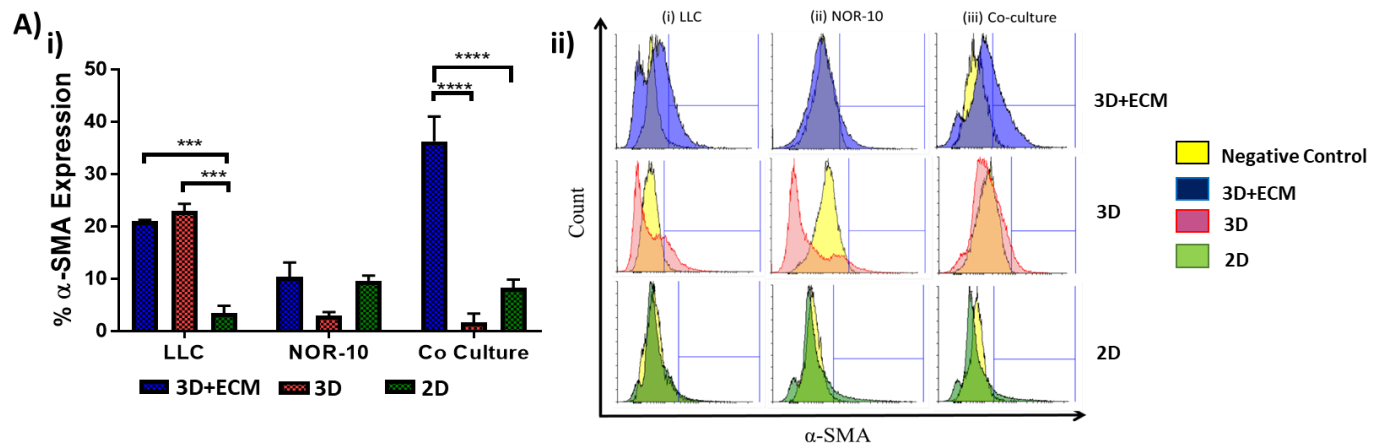


Figure 5-5 – Analysis of α -SMA expression. A) i) α -SMA expression of LLC, NOR-10, and co-cultured encapsulated spheroids (3D+ECM) compared to 3D non-encapsulated and 2D cultures following 72h culture; measured by flow cytometry ii) representative histograms images of α -SMA expression are shown.

5.3.4 Effect of Microenvironment

5.3.4.1 Monitoring Migration in Encapsulated co-culture Spheroids

Migration within artificial microenvironments was further analysed through comparison of spheroids encapsulated in Fmoc-FRGDF/Fmoc-DIKVAV hydrogels to spheroids encapsulated in a 1% agarose hydrogel (**Figure 5-6**). Agarose was selected as a control owing to its structural similarities yet lack of cell-recognisable, bioactive epitopes.⁹³ Cells within co-cultured spheroids were tracked to monitor migration in RGD and IKVAV functionalised hydrogels and compared to the agarose control. Following 72-hour culture, confocal imaging was performed on LLC cells loaded with cell CMTPIX dye (red) and NOR-10 cells loaded with MitoTracker™ Green FM. Results show that both LLC and NOR-10 cells migrate into the coassembled hydrogel yet remain stationary within the 1% agarose hydrogel (**Figure 5-6A**). Expression of vinculin and α -SMA was investigated for co-cultured spheroids encapsulated within the coassembled hydrogel and compared to the agarose control (**Figure 5-6B**). Flow cytometry was employed to analyse expression levels following 3-days culture. A significant down-regulation in vinculin expression was measured for spheroids cultured in the coassembled Fmoc-SAP hydrogel compared to spheroids cultured in the agarose control (0% compared to 23.6% respectively, $p=0.0003$, **Figure 5-6B**). Contrastingly, a significantly higher expression of α -SMA was evident in spheroids cultured in the coassembled hydrogel compared to those cultured in agarose (36.3% and 12.4% respectively, $p = 0.00078$, **Figure 5-6B**).

Results show enhanced motility of CMTPIX-labelled LLC cells and MitoTracker™ Green FM-labelled NOR-10 cells when cultured in the coassembled hydrogel compared to a 1% agarose control. Furthermore, cancer cell motility in the coassembled hydrogel demonstrated a significant down-regulation of vinculin expression compared to the agarose control, indicating a loss of cell adhesion. Ulrich et al. made similar observations, wherein U373-MG human glioma spheroid cell migration was inhibited when cultured in agarose compared to collagen or collagen-agarose blends.³²³ Therefore, results from this study indicate that cellular response to the coassembled artificial microenvironment is likely due to integrin interactions with bioactive motifs, highlighting the potential of this model to replicate lung cancer cell adhesion and migration *in vitro*.

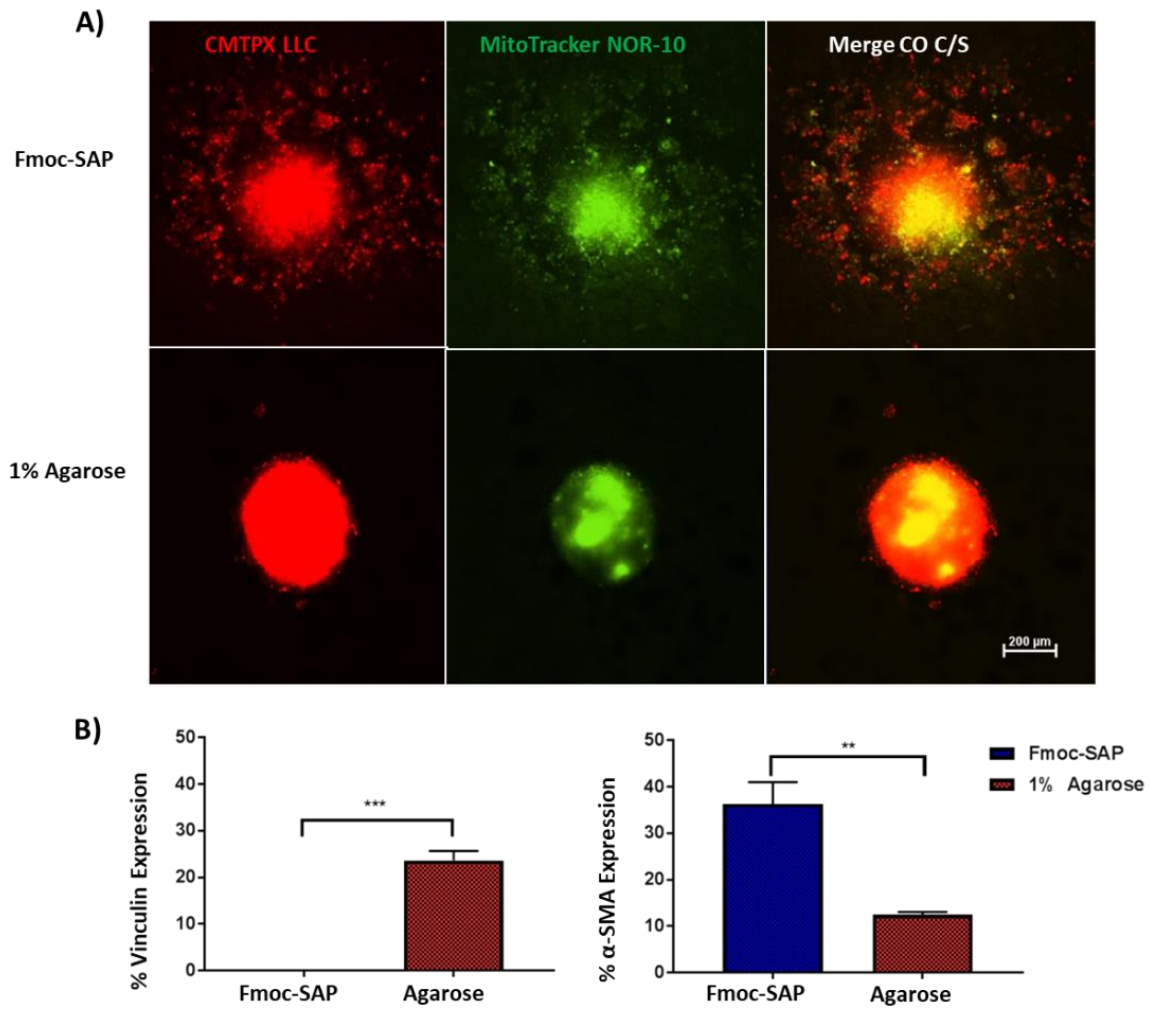


Figure 5-6 – Investigation of cell motility A) LLC (labelled with CMPTX red) and NOR-10 (labelled with Mitotracker green) in 3D co-culture spheroids encapsulated within Fmoc-SAPs and 1% Agarose hydrogels for 3 days; images were acquired by confocal microscopy (scale bar, 200 μ m). B) Vinculin expression level in co-culture spheroids encapsulated within Fmoc-SAPs hydrogels and 1% Agarose for 3 days; measured by flow cytometry. Results are shown as mean \pm SEM (n=3, ***p<0.001, Student's unpaired t-test).

5.4 Conclusion

A biomimetic Fmoc-SAP hydrogel has been developed for use as part of an advanced TME for cancer modelling applications. Spheroids cultured in the hydrogel presenting fibronectin's RGD, and laminin's IKVAV sequences demonstrated high cell viability, supporting previous observations into material biocompatibility. Furthermore, spheroids containing Lewis lung cancer cells co-cultured with NOR-10 fibroblasts demonstrated enhanced motility compared to non-encapsulated spheroids or those cultured on 2D tissue culture plastic. Co-cultured spheroids also demonstrated a greater degree of fibroblast differentiation into CAF when encapsulated in the Fmoc-SAP microenvironment compared to the 2D control as observed via assessment of α -SMA expression. Finally, the encapsulation of co-cultured spheroids within the Fmoc-SAP coassembled hydrogel was found to enhance metabolic activity of tumour spheroids and promoted the invasiveness of cancer cells via a reduction in vinculin expression compared to a control. Our results demonstrated the effectiveness of this system as a lung cancer model *in vitro*.

Chapter Six:

FUNCTIONALISING SCAFFOLDS VIA INCORPORATION OF MACROMOLECULES

6.1 Preview

This chapter aims to influence cellular behaviour through the functionalisation of the biomaterial scaffold via coassembly of biomacromolecules into the peptide networks. Here, a developmentally important proteoglycan, Versican and an anti-inflammatory polysaccharide, fucoidan were selected as macromolecule candidates. We hypothesise that macromolecules would be incorporated via a conserved mechanism owing to their similar molecular properties (charge, highly sulphated nature) and yet would provide distinct biological influences. The physical and mechanical properties of the functionalised Fmoc-FRGDF hydrogel networks are discussed with respect to macromolecule presentation, assembly mechanisms, viscoelastic properties, and fibre/network topology; whilst influence of macromolecule incorporation is investigated through analysis of cell number, protein content, cell morphology, cell viability, and finally, formation of multinucleated syncytia as an indication of myogenic differentiation. The results showed successful macromolecule decoration on Fmoc-FRGDF nanofibers, resulting in a homogenous presentation of each respective macromolecule in a 3D environment. Furthermore, macromolecule inclusion led to changes in structural and biological properties, ultimately altering the biological outcomes of a muscle cell progenitor line, C2C12. This part of the work is a prerequisite for understanding mechanisms of macromolecule association for later bioink development (**Chapter 8**).

Contribution of the candidate:

- Involvement in analysis regarding material properties and assembly mechanisms.
- Contributed in manuscript preparation.

Publications relevant to this chapter

Li, R., McRae, N. L., McCulloch, D. R., **Boyd-Moss, M.**, Barrow, C. J., Nisbet, D. R., ... & Williams, R. J. (2018). Large and small assembly: Combining functional macromolecules with small peptides to control the morphology of skeletal muscle progenitor cells. *Biomacromolecules*, 19(3), 825-837.

Reprinted (adapted) with permission from (Li, R., McRae, N. L., McCulloch, D. R., **Boyd-Moss, M.**, Barrow, C. J., Nisbet, D. R., ... & Williams, R. J. (2018). Large and small assembly: Combining functional macromolecules with small peptides to control the morphology of skeletal muscle progenitor cells. *Biomacromolecules*, 19(3), 825-837) Copyright (2018) American Chemical Society.

Abstract:

Advanced functionalised biomaterial scaffolds which better mimic the structural and biological complexities of the native ECM provide significant potential for tissue engineering and regenerative medicine applications. The complex nature of the ECM provides developing cells with a variety of signals simultaneously to effectively control cell-fate. Therefore, progressive biomaterial scaffolds must also provide an array of biomechanical and biochemical signals to cells in a dynamic yet synergistic nature. Fmoc-SAPs have emerged as promising candidates for tissue engineering applications owing to their ability to incorporate functional, bioinspired motifs within short, structurally relevant sequences. Despite this, further functionalisation is often desired to better mimic native cellular microenvironments. Macromolecule functionalisation offers an additional means of providing artificial scaffolds with complex, bioactive signals presented in high affinity throughout a 3D environment. In this chapter, a novel tissue engineering hydrogel is presented that takes advantage of a simultaneous ‘large and small’ assembly to non-covalently incorporate functional macromolecules. ‘Small assembly’ is enabled through peptide self-assembly, wherein the fibronectin inspired SAP, Fmoc-FRGDF, is self-organised via π - β organisation. Alternatively, in ‘large assembly’, structurally and developmentally important macromolecules are constrained on fibril surfaces via supramolecular interactions, including electrostatic forces, hydrophobic forces, and physical entrapment. Results show macromolecule inclusion - using fucoidan and versican – enables controlled structural and biological tunability. C2C12 skeletal muscle progenitor cells seeded onto macromolecule scaffolds demonstrate altered cellular processes, yet cell viability and proliferation remain unaffected.

6.2 Introduction

Advanced tissue engineering applications require optimally functionalised biomaterials; providing the necessary physical and biochemical cues to cells in a biomimetic fashion. The native ECM presents numerous cell-signalling proteins and bioactive polysaccharides to developing tissues; providing an effective cocktail of biological cues which regulate cellular fate.¹ These large molecules rarely work in isolation and the relative proportion of each macromolecule - including laminins, fibronectins, collagens and proteoglycans - differs significantly between tissue types.^{1, 324}

Fibronectin is a highly expressed glycoprotein which regulates a variety of interactions between cells and the ECM.²⁴⁹ Extensive research into fibronectin's structure has revealed distinct, short regions responsible for promoting cell attachment through integrin $\alpha_5\beta_1$ binding.²⁴⁹ The most well-understood of these attachment sites is the minimalistic attachment motif, arginine–glycine–aspartic acid (RGD); subsequently, through integration of this bioactive motif within an artificial cellular microenvironment, various materials have been successfully functionalised for drug delivery³²⁵⁻³²⁶ and tissue engineering applications.³²⁷⁻³³¹

Similarly, SAP biomaterials have seen improved cellular 3D outcomes from the incorporation of RGD sequences.³³²⁻³³⁴ These peptides may be categorised by the mechanism of assembly; including PAs and aromatically-capped peptide derivatives.⁷ One particular advantage of aromatically-capped peptide derivatives is their ability to form very short bioactive sequences via routine peptide synthesis techniques, including SPPS.⁷ Within this class of peptide lies Fmoc-SAPs, here, assembly is driven through π - β interactions, resulting in π - π stacking between Fmoc-groups and subsequent β -sheet formation between short peptide sequences.⁸ Using this approach, researchers in our lab have successfully presented a wide range of biochemical signals at high density, including biologically relevant peptide derivatives, RGD,^{141, 143, 243} IKVAV,^{141, 335} and YIGSR,¹⁴¹ as well as synergistic combinations, including RGD-PHSRN³¹⁴, and RGD-IKVAV²⁶. However, despite this unique ability, peptide functionalisation through sequence engineering forms only part of the solution; with complex material functionalisation in a truly biomimetic fashion remaining a significant challenge.

One approach which offers substantial promise focuses on the incorporation of whole macromolecules within biocompatible SAP scaffolds.³³⁶ Unlike many current macromolecule functionalisation techniques which focus on 2D surface functionalisation; the resulting network can present complex large biological molecules in a constrained 3D manner. Using this approach, our laboratory has previously functionalised Fmoc-SAP networks with the anti-inflammatory polysaccharide 'fucoidan'; resulting in a network of altered biological and structural characteristics.^{265,}

335, 337

Similarly, here we investigate the incorporation of structurally and developmentally important macromolecules within a SAP hydrogel network. Namely, we investigate the biological and structural effects of two highly sulphated biomacromolecules, fucoidan and versican, incorporating each macromolecule within a Fmoc-FRGDF hydrogel. These biomacromolecules were selected owing to their similar bulk macromolecular properties (charge, sulfonated nature) that control supramolecular assembly yet different biological functions. Fucoidan is a seaweed-derived polysaccharide which has previously shown excellent anti-inflammatory properties and has demonstrated the propensity to induce apoptosis in epithelial cancer cells.²⁶⁵ Furthermore, fucoidan addition within a SAP hydrogel network grants the ability to tune network microtopology; resulting in increased fibril supramolecular ordering and subsequent increase in network stiffness.³³⁷ Contrastingly, versican is a developmentally important ECM proteoglycan involved in regulating various cell-behaviours.³³⁸ This large proteoglycan is broken-down by cell-secreted ADAMTS versicanases, resulting in the production of versikine, a bioactive peptide fragment which has demonstrated importance in myoblast differentiation and proliferation.²⁴⁴

In this investigation, supramolecular network functionalisation is achieved through biomacromolecule addition during peptide self-assembly. Macromolecule interactions with SAP fibrils take advantage of various intermolecular forces, including electrostatic interactions,³³⁹ hydrophobic interactions,²⁹⁰ and physical entrapment.¹²⁹ The resultant network is robust, in that fibril nucleation and development is stable and conserved, while introduced macromolecules are tightly associated with the fibril surface.²⁶⁵ The ensuing bonds are non-covalent, and as such do not require commonly used cytotoxic crosslinking agents or crosslinking conditions. Additionally, the inclusion of large molecules to the assembly can be tuned as not to disrupt network ordering – retaining the nanofibrillar peptide structure.³³⁷ Macromolecule influence on self-assembling mechanism is investigated through spectroscopic practices including CD and FT-IR; while viscoelastic characterisation is completed through rheological analysis. TEM and AFM were employed to analyse macromolecule induced change in network nano-/microtopology.

C2C12 cells were used to analyse the effects of macromolecule functionalised coassembled hydrogels on cell number, protein production, cell morphology, and formation of multinucleated

syncytia. C2C12 cells were selected as they are a well characterised murine skeletal muscle progenitor cell line which are routinely used to investigate cellular processes relevant to myogenesis during skeletal muscle development and regeneration.³⁴⁰ Our results show that macromolecules may be incorporated within Fmoc-SAP networks, enabling controlled tunability of network biological and structural properties. Furthermore, we find ‘large and small’ assembly mechanisms can be used in conjunction to form more complex biomimetic scaffolds for use in advanced tissue engineering approaches.

6.3 Results and Discussion

6.3.1 Formation of Hydrogels

Fibronectin plays a key role in mediating a variety of interactions between cells and the ECM, providing chemical signals to cells in the form of recognised amino acid sequences, and contributing to the overall structural characteristics of the ECM through binding with other ECM proteins and proteoglycans.²⁴⁹ This developmentally important ECM glycoprotein is secreted by a variety of cells and plays important roles controlling cell attachment, differentiation, growth and migration.²⁴⁹ Similarly, the fibronectin-derived cell-attachment motif, RGD, is able to facilitate cell attachment.²⁵⁰ Despite RGD's success in promoting cell attachment, RGD does not act alone in the native ECM, and therefore consideration needs to be placed into facilitating further functionalisation of these peptides.³⁴¹ One approach which has been seen some success is the integration of biomacromolecules within hydrogel networks.³⁴²⁻³⁴³ Therefore, in this study, the fibronectin-inspired SAP, Fmoc-FRGDF (**Figure 6-1A, B**), containing the cell attachment domain RGD was synthesised using SPPS as previously detailed.^{243, 265} Four hydrogel groups were developed from this Fmoc-SAP: 1) Fmoc-FRGDF, 2) Fmoc-FRGDF + 0.5 mg mL⁻¹ fucoidan, 3) Fmoc-FRGDF + empty vector conditioned media, and 4) Fmoc-FRGDF + versican conditioned media. Fmoc-FRGDF is self-assembled, while hydrogels 2, 3 and 4 are coassembled. All gels have a Fmoc-FRGDF concentration of 1% (w/v). and assembly is triggered via the well-characterised pH switch method.²⁴³ In the coassembled hydrogel system 2, fucoidan powder (0.05% (w/v)) was mixed with Fmoc-FRGDF powder before assembly (**Figure 6-1C, D**). Fmoc-FRGDF was used as a control for fucoidan investigations, while a Fmoc-FRGDF hydrogel containing empty vector media was used as a control for versican investigations. Versican enriched media and versican free (or empty vector) media were obtained via culturing of HEK-293T cells transfected with V1 versican construct or an empty vector (pcDNA3.1MycHisA) respectively (**Figure 6-1E, F**).²⁴⁵

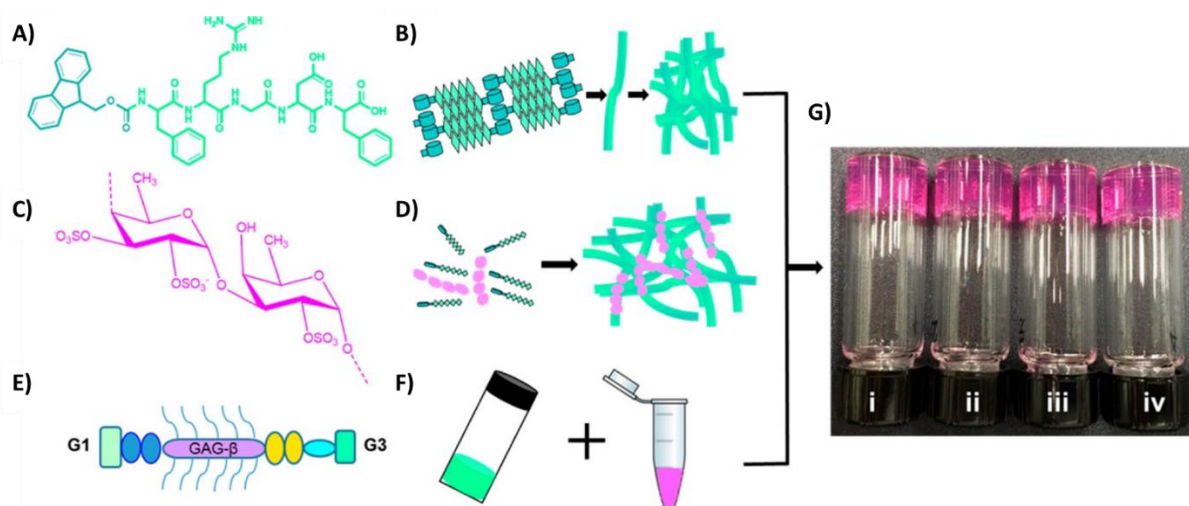


Figure 6-1 – Schematic of peptide self-assembly, macromolecule co-assembly and resultant hydrogel formation. A) Fmoc-FRGDF chemical structure. B) Schematic representation of Fmoc-FRGDF self-assembly driven through π - π stacking between Fmoc-groups and β -sheet formation between short peptide sequences resulting in the formation of peptide nanofibrils which further entangle to form a hydrogel scaffold. C) Chemical structure of the fucoidan subunit. D) Schematic of Fmoc-FRGDF/fucoidan co-assembly. E) Schematic of V1 versican showing the G1 and G3 globular domains and the chondroitin sulphate side chains bound to the GAG- β subunit. F) Schematic of co-assembly between Fmoc-FRGDF and versican conditioned media or empty vector conditioned media, resulting in the presentation of molecules on the surface of the peptide nanofibrils. G) Macroscopic observations of hydrogels showing self-supporting properties (i) Fmoc-FRGDF, (ii) + fucoidan, (iii) + empty vector conditioned media, and (iv) + versican conditioned media. Reproduced with permission ³⁸¹

6.3.2 Confirmation of Macromolecule Presentation

The incorporation of fucoidan within a Fmoc-SAP hydrogel has been previously confirmed.²⁶⁵ To assess the incorporation of versican, the effectiveness of versican production by V1 versican transfected HEK-293T cells were analysed via western blotting (**Figure 6-2A**). As expected, a prominent band was observed at a molecular weight greater than 250 kDa in the versican conditioned media; the same band was not evident in the empty vector conditioned media.³⁴⁴ A second band was also observed in the V1 versican conditioned media at around 70 kDa. This band correspond to versikine – a product of versican proteolysis by ECM ADAMTS versicanases.³⁴⁵ The presence of other protein bands in the empty vector conditioned media indicates HEK-293T cells secrete other proteins and therefore justifies the need for an empty-vector control (**Figure 6-2B**). The inclusion of versican within the coassembled Fmoc-FRGDF/versican hydrogels was assessed using immunofluorescent and confocal analysis. Gels were stained with Anti-GAG- β versican anti-body to enable the observation of versican. Versican was not detected in the empty-vector control (**Figure 6-2B**). Alternatively, the hydrogels assembled with versican-containing media showed versican localised to peptide nanofibers (red) throughout the 3D environment (**Figure 6-2B**), indicating the successful inclusion of versican in the coassembled versican network.

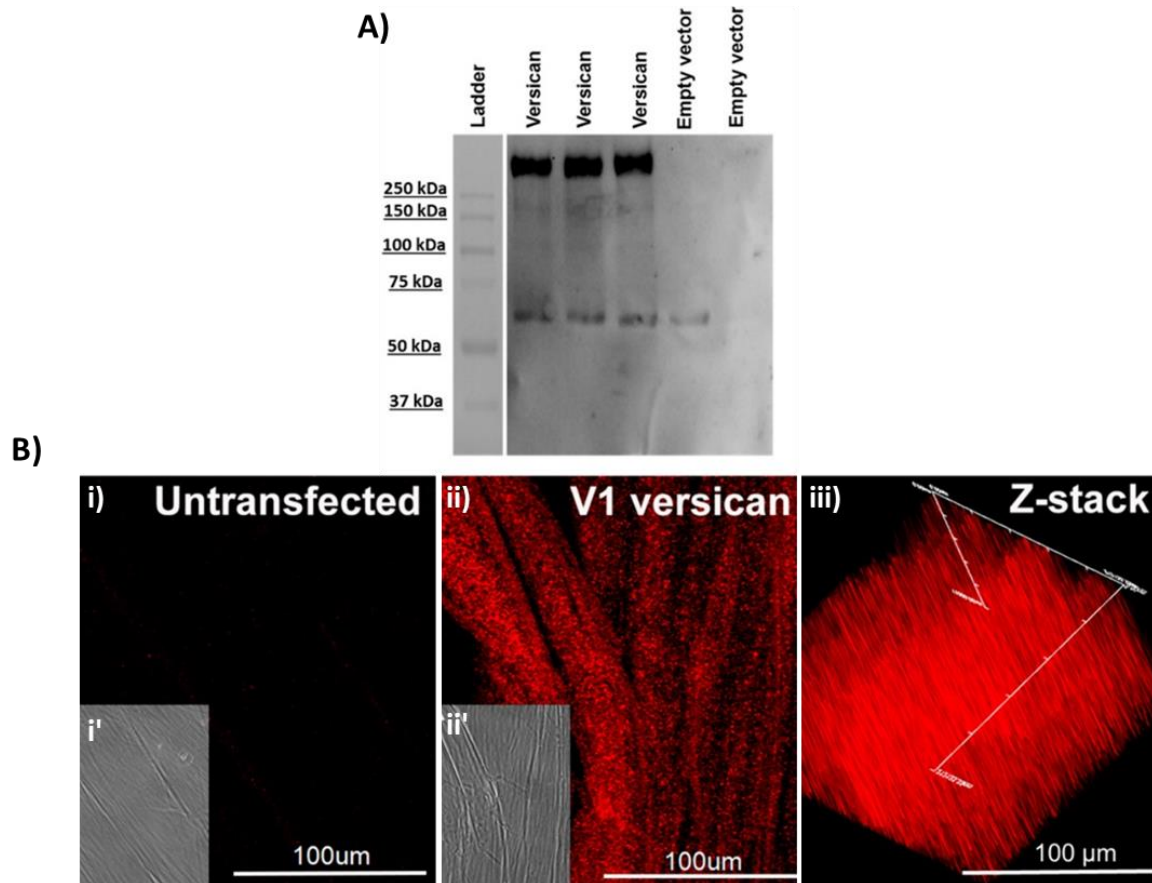


Figure 6-2 – Verification of versican production by HEK-293T cells and visualisation of versican incorporation in Fmoc-FRGDF scaffolds. A) Western blot analysis showing presence of versican in versican transfected media but not in empty vector transfected, conditioned media as indicated by a prominent band greater than 250 kDa. A smaller band located around 70 kDa is likely to indicate cleaved versikine. B) Confocal observations of labelled V1 versican complex in the hydrogel as stained with the V1/V0 versican anti-GAG- β antibody (red), i) Fmoc-FRGDF hydrogel containing untransfected media; (i') corresponding bright field image. ii) Fmoc-FRGDF hydrogel containing transfected V1 versican conditioned media; (ii') corresponding bright field image. iii) Z-Stack of (ii) showing 3D fibres and network orientation. Reproduced with permission ³⁸¹

6.3.3 Investigation of Hydrogel Architecture.

The nano- and microstructure of the developed hydrogel scaffolds were analysed through TEM and AFM imaging to determine how macromolecule inclusion during the assembly process alters scaffold architecture. It should be noted that samples were dried prior to imaging; however care has been taken to use representative images free of artefacts which may be encountered during the drying process.³⁴⁶ TEM images showed highly similar, nanofibril structures in all four hydrogels (**Figure 6-3A-D**). These nanofibrils are ~10 nm in diameter and micrometres in length. These findings are in agreeance with SANS data acquired in a previous study.³³⁷ AFM images show Fmoc-FRGDF has a highly interwoven homogeneous network (**Figure 6-3E-H**), reinforcing previous findings.²⁴³ The addition of fucoidan is shown to increase the degree of fibre bundling; once again, this is expected as a previous investigation into fucoidan incorporation showed increased bundling proportional to fucoidan concentration.³³⁷ Samples coassembled with versican or the empty-vector conditioned media showed scaffold morphologies which were different to Fmoc-FRGDF and fucoidan-containing hydrogels. Here, the hydrogel network appears to be less linear with more flexibility and greater densification; this is likely due to the inclusion of proteins excreted by HEK-293T cells, or proteins found within FBS, which may interfere with scaffold morphology when included during hydrogel assembly. Our observations are consistent with previous studies concerning the inclusion of laminin²⁹⁰ or dextran within composite networks.²⁸⁴

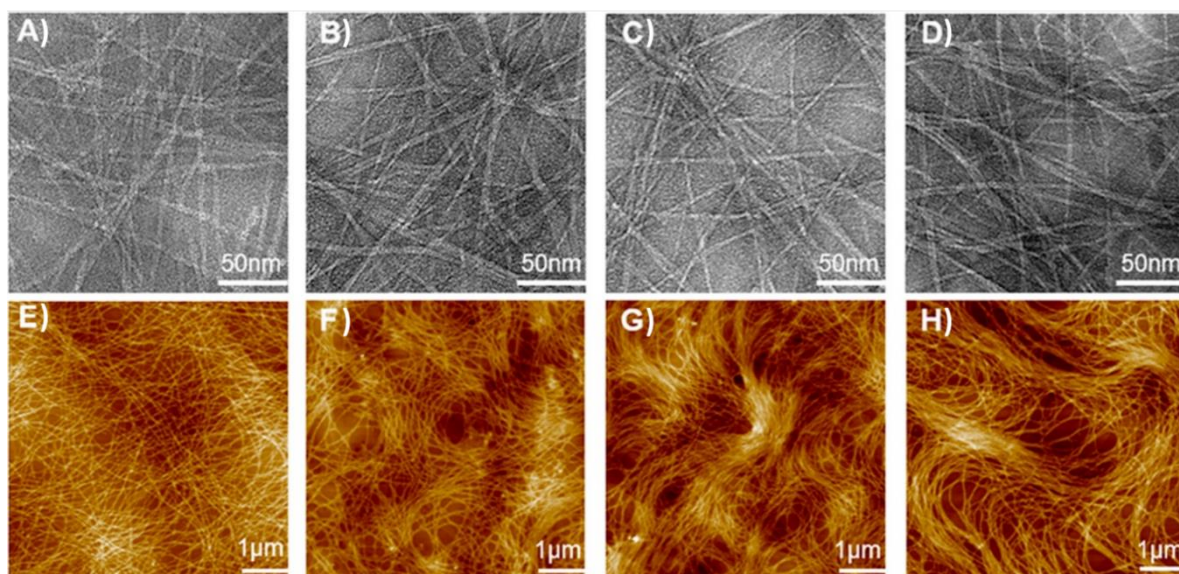


Figure 6-3 – Hydrogel Nano/Micromorphological changes in response to macromolecule incorporation. TEM shows nanostructure of fibrils formed (top panel), AFM shows microstructure network formation (bottom panel) of A, E) Fmoc-FRGDF, B, F) + fucoidan, C, G) + empty vector, and D, H) + versican hydrogels. TEM scale bar represents 50 nm, AFM 1 μm. Reproduced with permission ³⁸¹

6.3.4 Characterisation of Coassembled Structure, Mechanisms, and Mechanical Properties

FT-IR and CD analysis techniques were employed to investigate the effect of macromolecule addition on the secondary structure of Fmoc-FRGDF hydrogels; while bulk mechanical properties of hydrogels were assessed through oscillatory rheology. Analysis of the FT-IR spectrum demonstrates a consistent large single peak at 1630 cm^{-1} in the amide I region and another smaller, shouldered peak at 1690 cm^{-1} for all samples (**Figure 6-4A**); characteristic of β -sheet peptide organisation.³⁴⁷ The lack of spectrum shift between samples signifies that the presence of fucoidan, versican or empty vector condition media does not disturb the broad self-assembly of these hydrogels. Analysis of CD absorption below 240 nm provides insight into secondary protein structures; a large negative peak is observed at $\sim 220\text{ nm}$ (**Figure 6-4B**), indicating a cotton effect induced via the presence of $n\text{-}\pi$ interactions.²⁷⁴⁻²⁷⁵ This indicates the formation of predominately β -sheet-like structures – reinforcing findings found in FT-IR analysis. A second, positive broad peak is evident at $\sim 260\text{ nm}$, indicating supramolecular ordering between nanofibrils in hydrogel samples; these results agree with CD spectra of similar SAP hydrogel structures.^{143, 290}

Rheological analysis was employed to test the viscoelastic properties of the developed hydrogels. A cone-plate rheometer configuration under oscillatory conditions was used to perform a frequency sweep to analyse shear stiffness and shear thinning of hydrogels. In each of the four samples, the storage modulus, is larger than the loss modulus, over the frequency range tested (**Figure 6-4C, D**); indicating the formation of a stable, self-supporting hydrogel. Fmoc-FRGDF co-assembly with fucoidan, versican, or the empty vector conditioned media results in an increase in stiffness by approximately one order of magnitude when compared to Fmoc-FRGDF alone. The increased stiffness in fucoidan containing hydrogels is due to increased fibre bundling; this is in accordance with previous studies in our laboratory which found macromolecule addition results in increased fibre alignment, bundling, and fibril densification.^{265, 337} Hydrogels containing versican conditioned media demonstrated comparable viscoelastic properties to hydrogels incorporating the empty vector conditioned media; therefore, it is likely that the increase in stiffness is due to proteins and macromolecules secreted by HEK-293T cells. There was no significant difference in stiffness between coassembled hydrogels

containing fucoidan, versican, and empty vector control; indicating a maintenance of assembly mechanism across these three samples, and therefore, differences in biological activity between samples are due to hydrogel bioactivity, rather than differences in material stiffness.

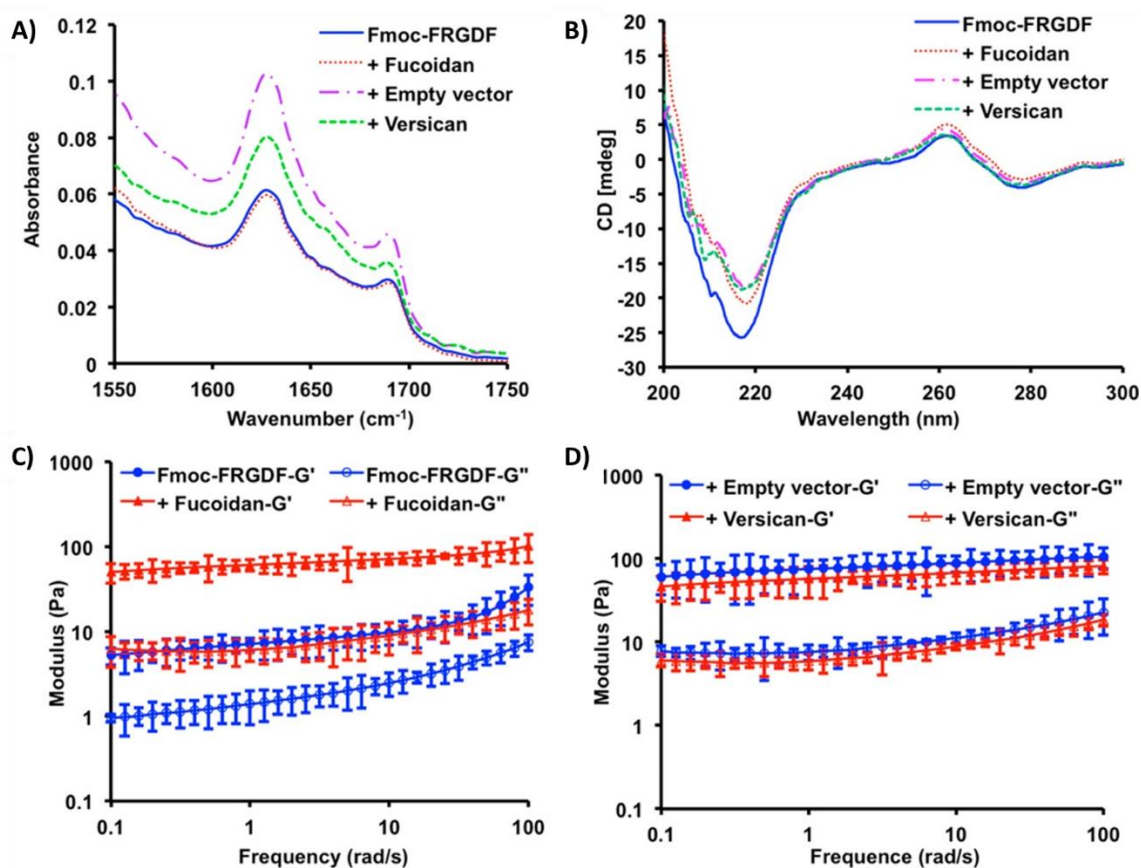


Figure 6-4 – Hydrogel assembly and mechanical properties. A) FT-IR spectroscopic analysis showing the amide I region with peaks characteristic of anti-parallel β -sheet structure present in all samples. B) CD analysis confirms the presence of β -sheet structures and indicates supramolecular ordering between nanofibrils in each sample. C) Rheological analysis showing storage and loss moduli over a range of frequencies for hydrogels formed by Fmoc-FRGDF and + fucoidan and D) Rheological analysis showing storage and loss moduli over a range of frequencies for hydrogels formed by Fmoc-FRGDF + versican conditioned media and + empty vector conditioned media. Reproduced with permission ³⁸¹

6.3.5 Effect of Macromolecule Functionalisation on Cell Viability and Protein Production.

Influence of scaffold functionalisation on bioactivity and biocompatibility is assessed through seeding of C2C12 cells on hydrogels. Following 72h culture, a similar cell number was observed between fucoidan-incorporated Fmoc-FRGDF hydrogels and the fucoidan-free Fmoc-FRGDF control (**Figure 6-5A**); complimenting observations noted by Kim et al. wherein fucoidan addition (>0.1 mg/mL) had no effect on cell viability during C2C12 myogenic differentiation following 48h culture.³⁴⁸ The relative total protein content is also found to be similar between the two samples (**Figure 6-5B**), indicating a negligible effect of fucoidan on cell number and protein synthesis at this concentration .

Versican was selected for matrix functionalisation owing to its native importance in skeletal muscle development; playing a vital role in myoblast proliferation and differentiation in developing tissue.³⁴⁹ Versican is remodelled by cell-secreted ADAMTS versicanases, resulting in the generation of versikine – a 70 kDa bioactive peptide fragment.³⁴⁵ Remodelling of versican is important for myoblast fusion and myofiber maturation;^{244, 349} however, the presence of versikine has also been shown to stimulate apoptosis in some cells, and subsequently may influence cell viability when cultured in a versican functionalised network.²⁴⁵ C2C12 cells secrete ADAMTS versicanases, potentially allowing for remodelling of scaffold-presented versican into versikine;²⁴⁴ however, versican functionalisation had no visible effect on cell viability, as cell lysate G6PD activity was observed to be similar between versican containing hydrogels and the empty vector control (**Figure 6-5C**). Similarly, total protein content was relatively indifferent between the two samples (**Figure 6-5D**).

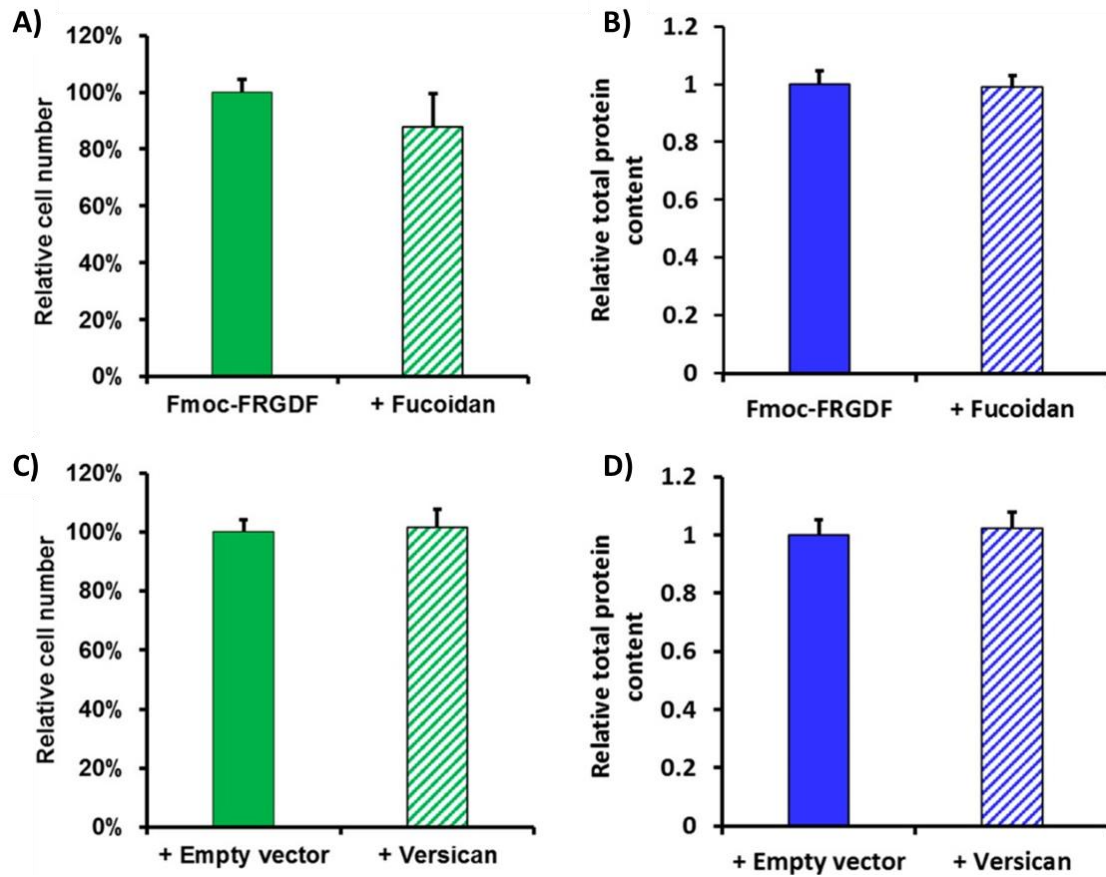


Figure 6-5 – Analysis of material cytocompatibility A) Relative cell viability and B) relative total protein content (as an indicator of cell growth) of cells seeded in Fmoc-FRGDF and Fmoc-FRGDF + fucoidan hydrogels. Data was normalized to the Fmoc-FRGDF control group. C) Relative cell viability and D) relative total protein content of cells seeded in Fmoc-FRGDF + empty vector and Fmoc-FRGDF + versican hydrogels. Data was normalized to the empty vector control group. Reproduced with permission ³⁸¹

6.3.6 Effect of Macromolecule Functionalisation on Cell-Size and Spreading

Analysis of cell spreading and morphology can be used to indicate cell attachment in artificial scaffolds.³⁵⁰ Live/dead staining of cells was implemented using Calcein AM/Propidium iodine stain respectively, to determine cell viability and analyse morphology and integration at 24h and 72h post seeding (**Figure 6-6A**). In all four gels, cells were found to possess high viability (>85%); furthermore, cells were found to migrate into the hydrogel and spread evenly within the scaffold. At 24h, viable cells in all four hydrogels demonstrated similar rounded morphologies; however, following 72h culture, cells in Fmoc-FRGDF, versican, and empty-vector containing hydrogels showed a significant change in morphology with large cells demonstrating numerous cytoplasmic extensions evident. Conversely, myoblasts within the fucoidan-containing hydrogel demonstrated consistent small, rounded or spindle morphologies with few cytoplasmic extensions.

Image analysis techniques (Image J) were used to assess cell spreading objectively. Average cell-size was found to increase significantly between 24h and 72h, resulting in an overall increase in cell area of 225%, 465%, and 1227% in Fmoc-FRGDF, Empty-vector, and versican-containing hydrogels, respectively (**Figure 6-6B-E**).

Further analysis of average cell-size found fucoidan incorporated hydrogels resulted in a more significant proportion of small cells (cell area <500 μm^2) and a lower proportion of cells of area greater than 1000 μm^2 following 24h culture (**Figure 6-6B i**). This effect was maintained after 72h culture, with fucoidan incorporated hydrogels showcasing more cells of area below 1000 μm^2 and fewer cells of area above 3000 μm^2 (**Figure 6-6B ii**). Contrastingly, versican-functionalised hydrogels demonstrated no significant difference in average categorised cell-size compared to the empty-vector control following 72h culture (**Figure 6-6C**).

Seeded cells were also stained using phalloidin and DAPI following 72h culture. Phalloidin is an actin stain widely used for analysis of cell morphology, while DAPI is a nuclear stain often used to determine nuclei count and position; in combination, the two are commonly used to determine myotube formation.³⁵¹ Cells-size was again determined through the use of ImageJ (**Figure 6-6D**); here, fucoidan

functionalised scaffolds demonstrated more small cells ($<1000\ \mu\text{m}^2$) and fewer larger cells ($>3000\ \mu\text{m}^2$) when compared to the Fmoc-FRGDF control (**Figure 6-6D i**). Alternatively, versican hydrogels did not show a significant difference in average cell area when compared to the empty-vector control (**Figure 6-6 ii**); reinforcing live/dead cell staining observations.

Myoblast attachment to fibronectin is heavily regulated by biological signalling of integrin $\alpha 5\beta 1$.³⁵²⁻³⁵³ The addition of polysaccharides has been shown to influence cell attachment to fibronectin, therefore, it is unsurprising that fucoidan incorporation into fibronectin inspired SAP networks results in decreased cell attachment and spreading of C2C12 cells over 72h.³⁵⁴ Cell attachment findings in this work echo those of Kim et al. wherein the degree of cell attachment was inversely proportional to fucoidan concentration.³⁴⁸

Versican addition demonstrated a far more elusive effect on cell attachment, with the only noticeable difference occurring in 24h samples – in which there was a greater proportion of small cells ($>500\ \mu\text{m}^2$) and a lower occurrence of large cells between 5000 and 8000 μm^2 . These results indicate that versican may attenuate C2C12 cell attachment in hydrogel networks; an observation which is comparable to findings by Evanko et al., wherein versican addition hindered spreading of human primary T cells seeded on a hyaluronan coated culture dish.³⁵⁵ C2C12 cells seeded on the versican functionalised scaffold demonstrated comparable cell spreading to the empty vector control after 72h, this is potentially due to the break-down of versican into versikine via ADAMTS versicanases, however this hypothesis needs to be further investigated.

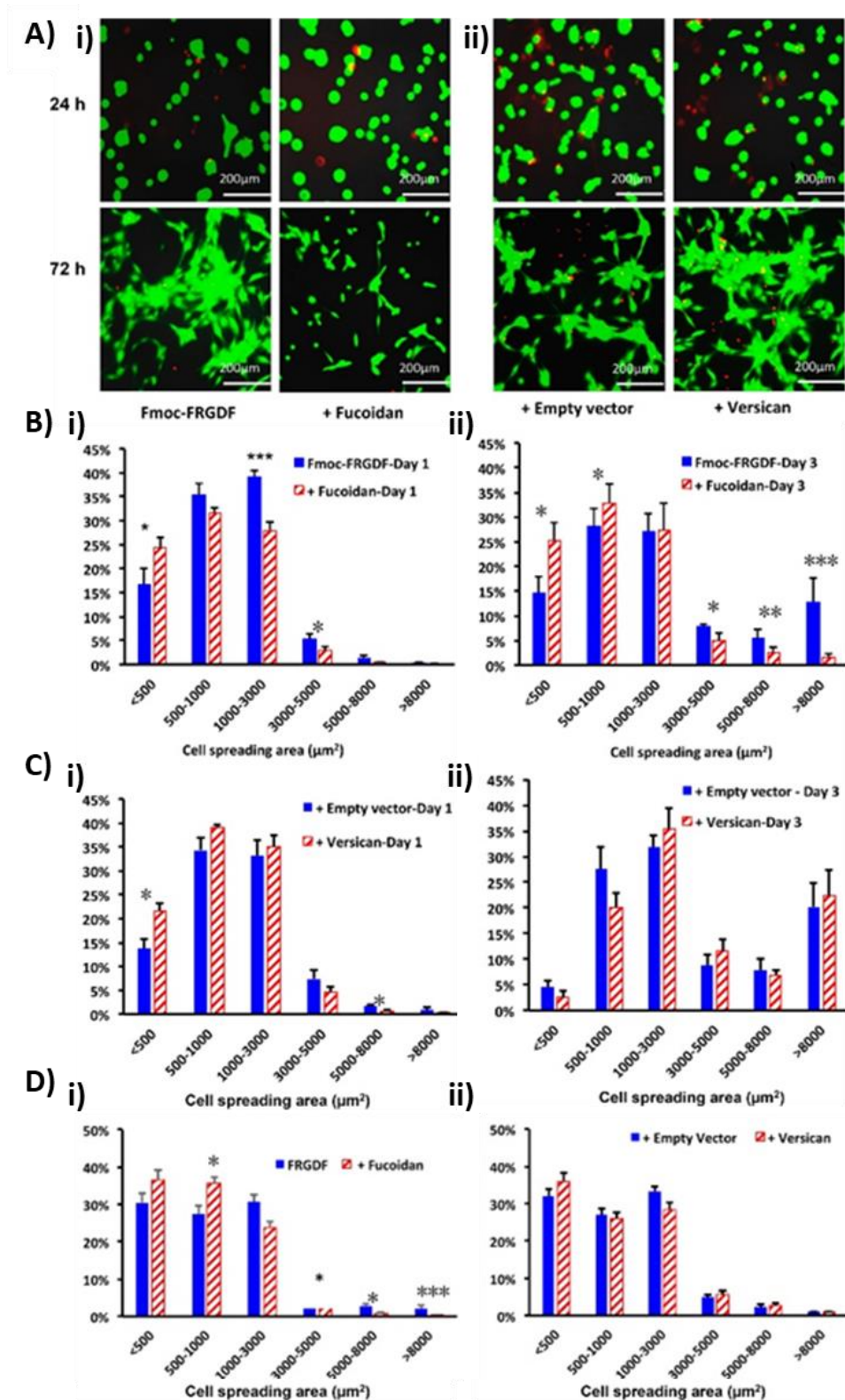


Figure 6-6 –Determination of cell morphology and spreading A) representative image of live/dead staining of C2C12 cells at 24 h and 72 h post seeding for each of the 4 hydrogel samples. Live cells stained using Calcein AM (green), and dead cells stained using propidium iodine (red). B) Calculation of cell spreading area as determined through ImageJ analysis on Fmoc-FRGDF hydrogels as compared to the fucoidan containing systems i) on day 1 and ii) on day 3. C) Cell spreading on the empty vector and versican hydrogels i) on day 1 and ii) on day 3. D) Cell spreading area on day 3 of C2C12 cells on i) Fmoc-FRGDF and + fucoidan groups and ii) + versican and + empty vector groups as above. * $p < 0.05$, ** $p < 0.01$, *** $p < 0.001$. (B) and (C) areas

calculated using ImageJ based on the live/dead staining images, (D) area calculated using DAPI and Phalloidin stains. Reproduced with permission ³⁸¹

6.3.7 Effect of Macromolecule Functionalisation on Formation of Multinucleated Syncytia

C2C12 cells were stained Phalloidin and DAPI to visually determine the degree of myogenic differentiation into multinucleated syncytia following 72h culture (**Figure 6-7A, B**). Fucoidan-functionalised scaffolds are observed to possess significantly more mononuclear C2C12 myoblasts compared to Fmoc-FRGDF alone (**Figure 6-7C**). Furthermore, a significantly lower proportion of multinucleated syncytia containing greater than five nuclei were observed in fucoidan containing samples compared to the Fmoc-FRGDF control (**Figure 6-7C**). Alternatively, versican-containing hydrogels demonstrated a similar degree of multinucleated syncytia formation compared to the empty-vector control hydrogel (**Figure 6-7D**).

The hindered development of multinucleated syncytia in fucoidan samples following 72h culture is potentially a result of reduced cell spreading; as disruption in cell morphological changes has previously been correlated with reduced myotube formation through myoblast fusion.³⁴⁸ Alternatively, versican addition did not increase the occurrence of multinuclear syncytia, despite previous studies highlighting the key role of versican in myotube formation; this may be attributed to versican degradation through ADAMTS versicanase.²⁴⁴ Notably, the total number of DAPI-stained nuclei remains consistent in all four samples – indicating that although macromolecule functionalisation influences C2C12 cellular processes, cell viability and proliferation remain unaffected.

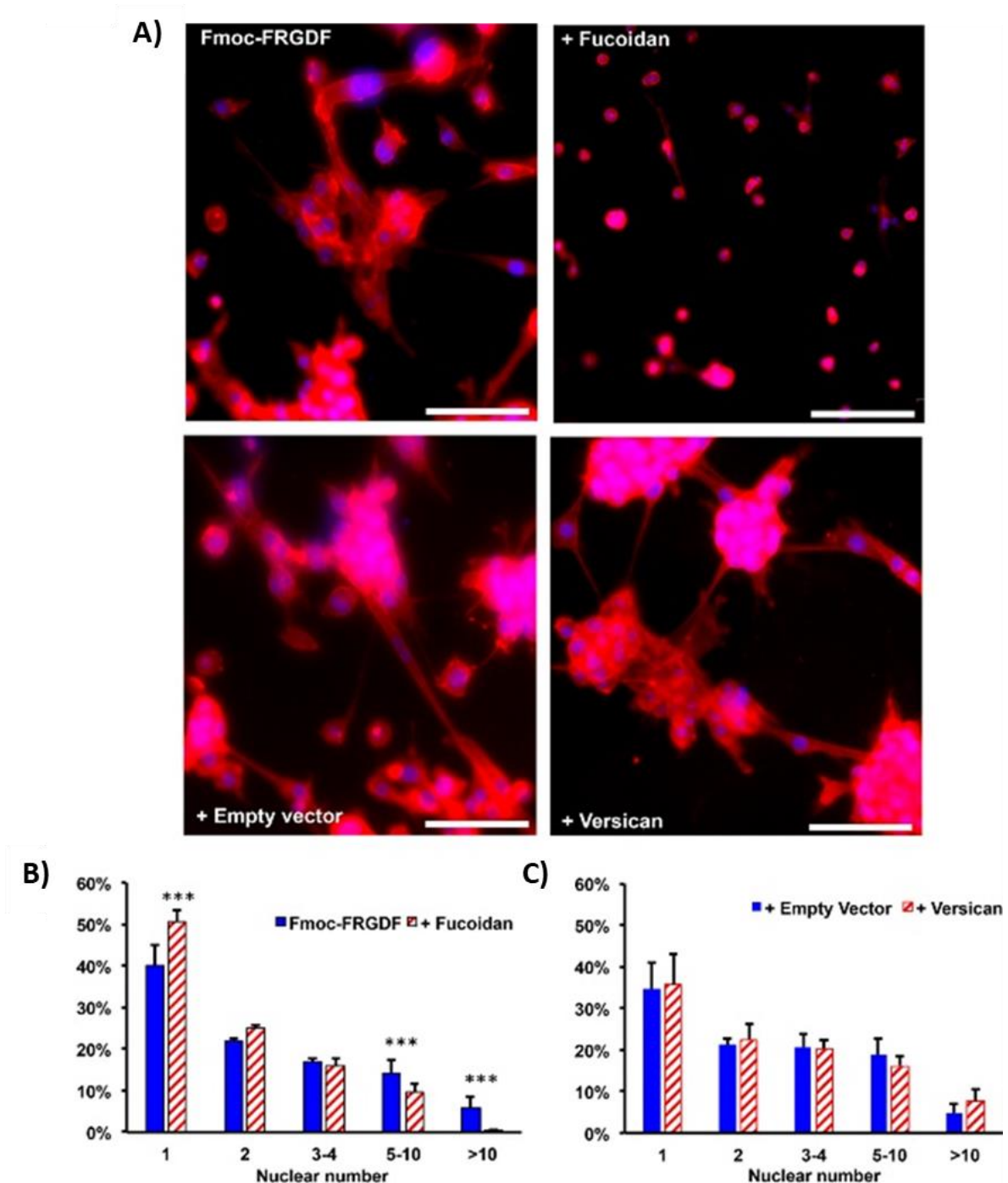


Figure 6-7 – Observation of cell morphological characteristics as determined through DAPI/actin staining and determination of multinucleation as an indication of cell maturity. A) DAPI/actin staining of C2C12 muscle cells on 72 h post seeding. Scale bar 200 μ m. B) Relative proportion of nuclei (blue) per cell or syncytium (red) for Fmoc-FRGDF and Fmoc-FRGDF + fucoidan groups C) and relative proportion of nuclei (blue) per cell or syncytium (red) for the + versican and + empty vector groups. * $p < 0.1$, ** $p < 0.01$, *** $p < 0.001$. Number of nuclei and syncytium were calculated using ImageJ. Reproduced with permission ³⁸¹

6.4 Conclusion

Macromolecule incorporation into SAP hydrogels through versican and fucoidan coassembly was successful and the underlying peptide self-organisation mechanisms were conserved. In this investigation, macromolecule coassembly is enabled through the addition of soluble large-molecules in the media during peptide assembly, making them available to interact with peptide nanofibers during the early stages of self-assembly. Using this technique, fucoidan, versican-transfected (V1) media, and empty-vector transfected media was coassembled with the fibronectin inspired SAP, Fmoc-FRGDF. For fucoidan samples, Fmoc-FRGDF alone was used as a control; while for versican-functionalised samples, an empty vector control was used. The use of an empty-vector control was important, as any candidate proteins excreted by HEK-293T cells may influence bulk network physical and biological characteristics. Versican inclusion within the coassembled scaffold was confirmed through immunostaining with anti-GAG- β . Fucoidan incorporation within the SAP network has previously been established (**Chapter 4**).²⁶⁵ The characteristic SAP fibrillar nanostructure is conserved in all samples while microscopic network topology is found to be altered upon macromolecule addition. Fucoidan addition was shown to result in increased fibre bundling. Alternatively, versican addition resulted in network densification and the formation of less linear, more flexible fibrils; as this effect is maintained in the empty vector control, it is likely due to the presence of macromolecules secreted by HEK-293T cells. Secondary structure analysis through FT-IR and CD techniques revealed all samples formed stable anti-parallel β -sheet conformations. Further analysis of the resultant spectrums indicates that although macromolecule incorporation leads to alteration of fibril supramolecular ordering, it does not interrupt peptide self-assembly mechanisms. Rheological analysis of hydrogels found macromolecule addition led to an increase in material stiffness of approximately one order of magnitude for all samples – including the empty-vector control. The increase in fucoidan-containing samples is well documented and is likely a result of increased fibre bundling, whilst an increase in versican-containing and empty-vector containing hydrogels is likely due to the presence of HEK239T secreted molecules.

The biological influence of macromolecule functionalised hydrogels was investigated through seeding of C2C12 cells. In this study, macromolecule addition to SAP hydrogel scaffolds was found to

have no influence on cell number and total protein content. However, fucoidan containing samples demonstrated differences in cell morphology compared to the Fmoc-FRGDF control, with seeded cells demonstrating smaller, rounder morphologies after 72 hours in culture. The difference in cell spreading was subtler in versican-containing samples, with cells only demonstrating smaller morphologies at 24h culture. After 72h, cells seeded in the versican-containing scaffolds demonstrated morphologies similar to the empty-vector control. This attenuation of cell spreading is possibly due to surface presented versican inhibiting cell attachment to the scaffolds; we hypothesise that ADAMTS secreted from C2C12 cells degrade versican into versikine, after which cell adhesion continues uninterrupted, allowing the material to change in response to cellular activity over time. This feature is exceptionally novel and warrants further investigation. Both versican and empty vector containing hydrogels facilitate myogenic differentiation, resulting in the formation of multinucleated syncytia.

In this study, we have successfully incorporated advanced functionalisation using small and large assembly through epitope sequence selection and macromolecule functionalisation respectively. Finally, macromolecule addition is found to impact cell processes without altering cell viability or proliferation.

Chapter Seven:

CHARACTERISATION OF GELATIN METHACRYLOYL MACROMOLECULES AS A HYDROGEL FOR BIOENGINEERING

7.1 Preview

This chapter aims to investigate the structure-function relationship of GelMA hydrogels, determining the correlations between nanostructured SAXS observations and the resultant mechanical properties as assessed through rheology. Here, commercially available GelMA nanostructure and viscoelastic properties were assessed at two commonly used concentrations (6% and 10%) and four different degrees of functionalisation (18%, 46%, 61% and 80%). Degree of functionalisation (DoF) refers to the relative percent of crosslinkable methacryloyl side-chains attached to the polymer backbone. It was hypothesised that control over DoF and concentration would highlight clear correlations between nanostructure and final mechanical properties. The physical and mechanical properties of crosslinked and non-crosslinked GelMA are discussed in respect to material nanostructure (Mass fractal dimension, correlation-length, and mesh-size) and material viscoelasticity. The results showed clear correlations between nanostructured morphologies and the resultant mechanical properties observed via rheological analysis. This part of the work is a prerequisite for subsequent bioink development chapters and aids in GelMA selection.

Contribution of the candidate:

- Developed concept and designed experiment
- Acquired, modelled, analysed, interpreted and discussed all data
- Presented whole manuscript, including all figures and content. (First Author)
- Prepared proposal, successful Funding for Synchrotron Experiments (ANSTO, AUS)

Publications relevant to this chapter

Boyd-Moss, M., Firipis, K., O'Connell CD., Long, B., Nisbet, D., Williams, R (2019) '*SAXS investigation into Gelatin Methacryloyl Structure-function Relationships*'. **Manuscript in preparation.**

Abstract

GelMA is a functionalised, collagen-derived biomaterial which has seen substantial use in bioprinting applications. This gold-standard bioink possesses highly favourable mechanical and biological properties, boasting mechanical tuneability through control over DoF or polymer concentration. DoF refers to the proportion of crosslinkable methacryloyl groups introduced into the gelatin backbone. Mechanical properties of GelMA are well understood; however, biologically-important nanostructured properties are poorly characterised and the effect of DoF and polymer concentration on network topology have not yet been investigated. Here, for the first time, SAXS is used to investigate structural changes in GelMA. Specifically, we observe hydrogel nanostructure pre- and post-crosslinking, with emphasis on assessing structural changes in response to increased DoF and polymer concentration. Samples are modelled regarding local-polymer conformation (mass fractal dimension), distance between entanglements (correlation length), and mesh size. Effect on viscoelastic properties are observed and conclusions drawn based on shared correlations. Importantly, we show a clear increase in polymer conformation upon crosslinking, with high DoF samples demonstrating the greatest increase in mass fractal dimension. Similarly, increasing GelMA DoF is strongly inversely correlated with mesh-size, with 80% DoF samples demonstrating the lowest mesh size. Clear correlations are also evident between polymer concentration and correlation length, likely a result of increased entanglement density. Finally, physical entanglements are also found to be influenced, with concentration and DoF altering the temperature required for stable gel formation; while chemical crosslinks are influenced by DoF with high DoF samples resulting in reduced strain tolerance.

7.2 Introduction

Collagen-based biomaterials have seen substantial use in tissue engineering applications, owing to their inherent bioactivity and high abundance in the ECM; however, collagen is severely limited in many tissue engineering applications, owing to its relative instability under physiological conditions.³⁵⁶ As a result, frontier materials scientists have focused on developing new ways of processing and handling this material. Consequently, gelatin-based biomaterials are increasingly popular, owing to their inherent biocompatibility, biodegradability, low-cost and ease of manipulation.⁶⁵ Gelatin is a denatured collagen-derived protein with a sol-gel transition temperature below 37°C, above this transition temperature, gelatin elicits high solubility enabled through the collapse of single strands into random coils.³¹² When cooled below the sol-gel transition temperature, gelatin can partially recombine forming noncovalent triple-helix structures which are stabilised by hydrogen bonds, enabling the formation of a soft hydrogel.³⁵⁷

However, considering the instability of gelatin under physiological conditions, substantial research has focused on introducing chemical crosslinks to gelatin, enabling the formation of collagen-mimicking materials which are stable even under physiological conditions (37°C), and providing further mechanical control allowing for tuning of viscoelasticity and control over degradation profile.³⁵⁸⁻³⁵⁹ Various Chemical crosslinkers, including formaldehyde, glutaraldehyde, carbodiimide, genipin and dextran dialdehyde have been used to crosslink gelatin-based biomaterials.³⁶⁰⁻³⁶¹ Chemical crosslinkers are affordable and provide excellent crosslinking efficiency; however, these chemical crosslinkers are cytotoxic and require prolonged wash steps to remove residual crosslinker.^{312, 361} Therefore, more recent crosslinking attempts have focused on alternative approaches, including electron beam^{357, 362} and UV irradiation techniques.²⁰²

Electron beam irradiation enables controlled, dose-dependent covalent crosslinking, allowing for a high degree of control over resultant material viscoelastic properties through the depth of the sample.³⁵⁷ However, electron beam irradiation is routinely used for sample sterilisation, resulting in substantial damage to DNA chains subsequently leading to cell death, and therefore is unsuitable for hydrogels containing encapsulated cells.³⁶³

Gelatin modification by methacrylic anhydride allows for the formation of GelMA,³⁶⁴ a biocompatible material which has seen extensive use in bioprinting applications.^{11, 365} In the presence of a photoinitiator, UV irradiated GelMA undergoes photoinitiated radical polymerisation; resulting in the formation of covalently crosslinked hydrogel networks. Specifically, upon exposure to UV irradiation, free radicals are generated from photoinitiators, initiating chain polymerisation of methacryloyl substitutions.³⁶⁶ Propagation ensues between methacryloyl groups on the same chain and methacryloyl groups on different chains; before finally, termination occurs between two propagating chains or between propagating chain and a second radical.³⁶⁶ Through control over crosslinking conditions, including source parameters (intensity, wavelength, and crosslinking duration) as well as careful consideration over photo-crosslinker (type and concentration), authors have achieved high viability, even when crosslinked in the presence of cells.^{194, 202}

GelMA offers high mechanical tunability through control over the DoF; with typical GelMA hydrogels ranging between 20% and 80% DoF.⁶⁵ Increasing DoF results in increased material stiffness, increases resistance to deformation, reduces material swelling, and reduces average material pore-size.³⁶⁷⁻³⁶⁸ However, highly functionalised GelMA may also restrict cellular spreading due to extensive crosslinks in the system.⁶⁵ GelMA mechanical properties are also heavily influenced by concentration, with higher concentrations yielding hydrogels of increased material stiffness and reduced swelling.³⁶⁸ However, controlling concentration alone is not ideal, as networks formed at high GelMA concentration may constrain biological functionality and nutrient exchange;³⁶⁹ while a concentration threshold limits networks formed at low concentration.²⁰³

While modulation of concentration and DoF has a clear influence on resultant mechanical properties, mechanisms of crosslinking are fundamentally different, and nanostructure organisational changes leading to macroscale mechanical differences are not well understood. Previously, SAXS has been used to observe nanostructured changes in electron-beam crosslinked gelatin hydrogels at various crosslinking doses and concentrations.³¹² However, to the best of our knowledge, this is the first time such analysis has been completed on GelMA hydrogels. Here, SAXS observations provide insight into local nanostructured differences between non-crosslinked and crosslinked hydrogels of differing

concentration and DoF. Nanostructured observations are further correlated to material viscoelastic properties as determined via rheology, and structure-function relationships are observed for a range of hydrogel parameters.

7.3 Results and Discussion

Understanding the structure-function relationships of biomaterials is a key requirement allowing for objective determination of the influence of functionalisation on material mechanical and subsequent biological properties. In this study, we investigate the relationship between engineered material variables (concentration, DoF) and resultant changes in the nanostructure. Firstly, nanostructural material properties are assessed via SAXS, allowing for observation of polymer network orientation and conformation. Specifically, SAXS is used to assess polymer conformation and network formation (mass fractal dimension), length between entanglements (correlation-length), and average mesh-size (**Figure 7-1A**). Secondly, we assess the effect concentration (**Figure 7-1B i**) or DoF (**Figure 7-1B ii**) has on the nanostructured organisation of these systems, and subsequently, determine how these properties alter material viscoelastic characteristics before and after crosslinking (**Figure 7-1B, C**). Finally, the effect of crosslinking on material nanostructure is determined (**Figure 7-1C i, ii**) and the subsequent outcome on material mechanical properties are measured via rheology.

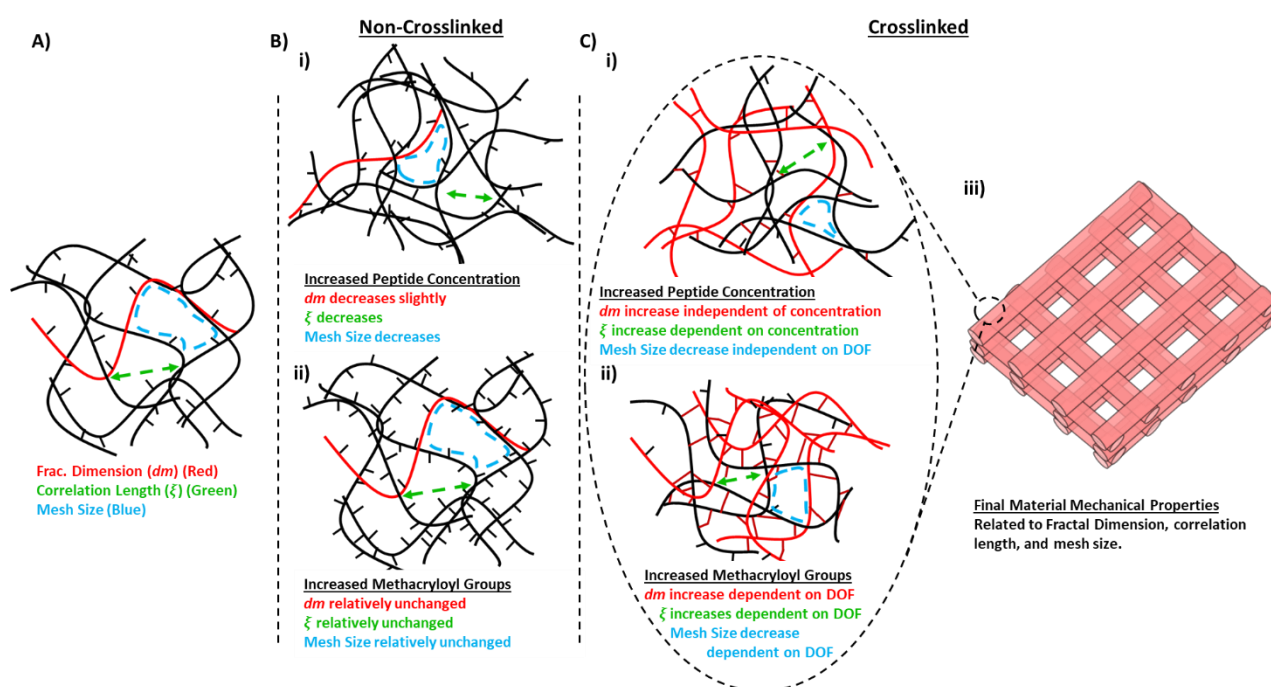


Figure 7-1 – Schematic showing Nanostructured properties as determined by SAXS. A) Polymer Network showing Frac. Dimension, Correlation Length, and Mesh size, B) Non-crosslinked nanostructure changes in relation to i) increased polymer concentration and ii) increased functionalisation, C) Nanostructural changes upon crosslinking and in relation to i) increased polymer concentration and ii) increased network functionalisation.

7.3.1 Non-crosslinked GelMA Trends

Non-crosslinked GelMA nanostructure was investigated using SAXS; following which, non-crosslinked viscoelastic properties were acquired via oscillatory rheology under temperature ramp conditions from 37°C to 4°C.

7.3.1.1 Small-Angle X-ray Scattering

SAXS analysis was employed to observe polymer conformational changes in response to concentration increase and alteration of peptide functionalisation. Scattering curves for 6% (w/v) (**Supplementary Figure S - 3A i**) and 10% (w/v) (**Supplementary Figure S - 3A ii**) samples were attained and analysed concerning polymer conformation, correlation length, and mesh-size. Fitting of models were performed over mid-low q ranges (**Supplementary Figure S - 4**).

Non-crosslinked Mass Fractal Dimension

The Porod region corresponds to a probed range smaller than the scattering objects, analysis of scattering in this region provides insight into polymer fractal dimension and subsequently, local polymer conformation.^{311, 313} A mass fractal dimension of 1 is indicative of a mathematical cylinder, while a mass fractal dimension of approximately 1.67 is associated with swollen polymer coils in a good solvent. Mass fractal dimensions between 2-3 are representative of branched polymers and are associated with network formation – particularly in chemically crosslinked systems.³¹¹⁻³¹² Fitting for mass fractal dimension can be described by **Equation 7-1**

$$I(q) = \frac{A}{q^{dm}}$$

Equation 7-1 – Fitting for Mass Fractal Dimension

Where A is a scaling factor, dm is the fractal dimension or power.

A similar mass fractal dimension was observed for all non-crosslinked, 6% (w/v) GelMA samples, ranging between 1.78 ($\pm <1\%$, 80% DoF) and 1.89 ($\pm <1\%$, 61% DoF) as is expected of a polymer in a good solvent. (**Figure 7-2A i**) Alternatively, 10% (w/v) GelMA samples demonstrated lower mass fractal dimensions overall, ranging from 1.60 ($\pm <1\%$, 18% DoF) to 1.75 ($\pm <1\%$, 61%

DoF), indicating a reduction in polymer conformation complexity with increased concentration (**Figure 7-2A i**). A similar trend was seen by Wisotski et al. wherein increasing gelatin concentration resulted in decreased mass fractal dimension.³¹² Importantly, mass fractal dimension in non-crosslinked samples does not appear to be a function of methacrylation percentage. These results are in accordance with correlation studies wherein a strong inverse correlation (-0.86) was observed between non-crosslinked mass fractal dimension and peptide concentration, while a negligible correlation (0.17) was observed between DoF and non-crosslinked mass fractal dimension.

Non-crosslinked Correlation Length

Analysis of correlation length provides insight into the distance between entanglements in semi-dilute systems and can be described by **Equation 7-2**.³¹¹⁻³¹²

$$I(q) = \left(\frac{C}{(1 + Q\xi)^m} \right) + bkg$$

Equation 7-2 - Fitting for Correlation Length

Where C is the Porod scaling factor relating to the intensity extrapolated at scattering vector $q=0$. Bkg accounts for background scattering; (m) is the Porod exponent and provides information relating to the local polymer structure, and ξ is the correlation length and provides an estimate of average entanglement length for semi-dilute solutions.³¹¹

In non-crosslinked, 6% (w/v) GelMA samples correlation length ranged between 3.9 nm (39.2 Å \pm 1.2%, 80% DoF) and 5.1 nm (50.6 Å \pm 1.6%, 46% DoF) (**Figure 7-2A ii**). Upon increase to 10% (w/v), samples demonstrated an overall decrease in correlation length as expected, ranging from 2.9 nm (29.1 Å \pm <1%, 18% DoF) to 3.4 nm (34.4 Å \pm <1%, 61% DoF) (**Figure 7-2A ii**). Once again, a strong inverse correlation (-0.90) was evident between non-crosslinked correlation length and peptide concentration, while negligible correlation (0.00) was observed between DoF and non-crosslinked correlation length. These results indicate an increase in GelMA concentration results in a decrease in distance between entanglements, as would be expected in a network of increased density; while increase in DoF does not appear to influence entanglement spacing.

Non-crosslinked Mesh Size

The intercept of two-powers in a log-log plot can be used to calculate the point of crossover (q_c), and subsequently, can be used to calculate the mesh characteristics of a polymer network, as described by

Equation 7-3.³¹¹⁻³¹²

$$Mesh\ Size = \frac{2\pi}{q_c}$$

Equation 7-3 - Fitting for Mesh Size

Calculation of average mesh size in 6% (w/v) samples finds no substantial variance over DoF, ranging between 14.2 nm ($142.0\ \text{\AA} \pm <1\%$) in 80% DoF hydrogels and 14.3 nm ($143.3\ \text{\AA} \pm <1\%$) in 46% DoF hydrogel samples (**Figure 7-2A iii**). Following an increase in peptide concentration to 10% (w/v), a decrease in mesh size is evident, ranging from 13.0 nm ($130.3\ \text{\AA} \pm <1\%$), 18% DoF to 13.6 nm ($136.1\ \text{\AA} \pm <1\%$, 61% DoF) (**Figure 7-2A iii**). Non-crosslinked mesh size is found to be inversely correlated (-0.93) to peptide concentration, while alteration of DoF does not affect non-crosslinked mesh size (0.00 correlation score).

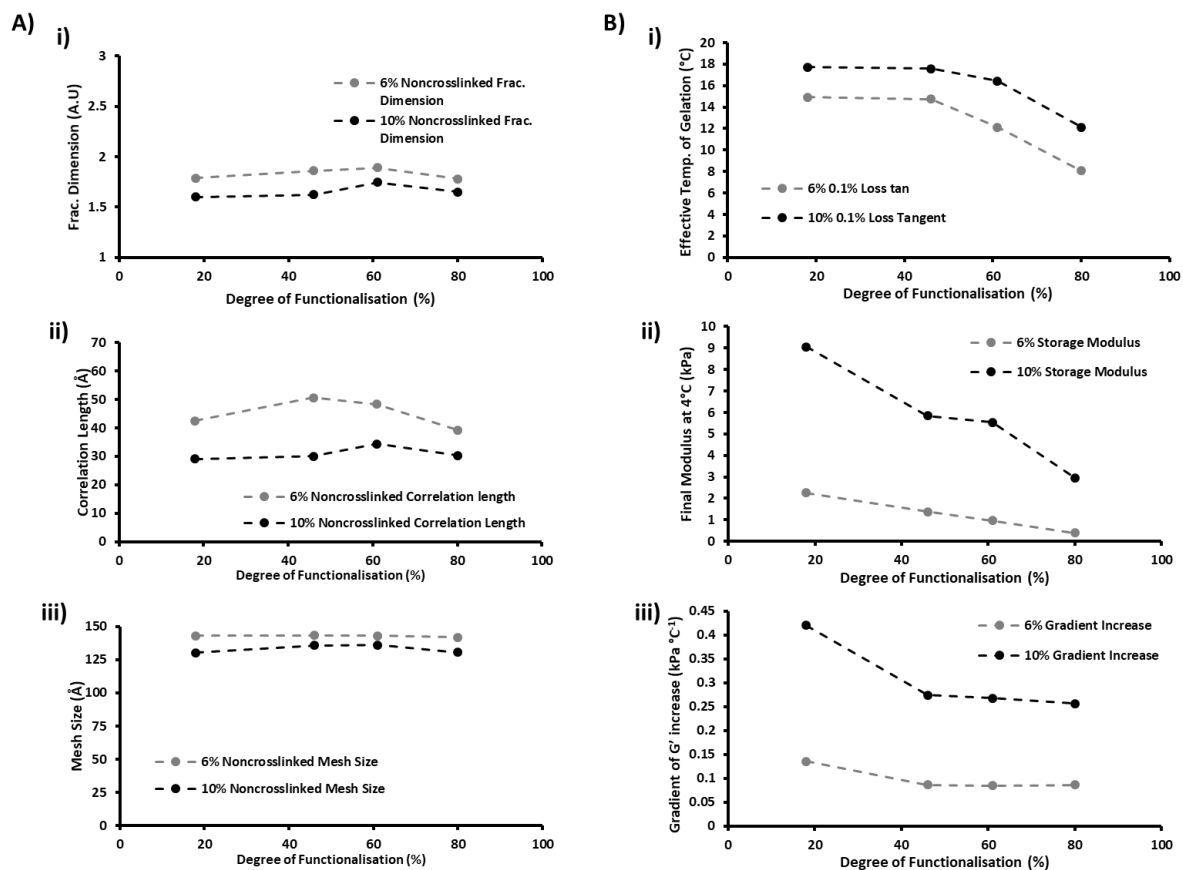


Figure 7-2 – Nanostructured and Viscoelastic properties of Non-crosslinked Gelma. A) nanostructured properties as determined through SAXS regarding i) mass fractal dimension, ii) correlation length, and iii) mesh size; B) Thermodependent viscoelastic properties including i) effective temperature of gel formation, ii) final modulus at 4°C, and iii) gradient of storage modulus increase.

7.3.1.2 Material Viscoelastic Properties

Rheological analysis was employed to investigate the effect of concentration and DoF on non-crosslinked material viscoelastic properties (**Supplementary Figure S - 7A**). Non-crosslinked hydrogels were analysed in respect to temperature dependences; specifically, temperature wherein loss tangent falls below 0.1, storage modulus at 4°C, and gradient of storage modulus increase.

Temperature of Stable Gel Formation

The point where loss tangent falls below 0.1 was selected in place of traditional point of gelation (where loss tangent falls below 1) as many samples did not display typical solution characteristics (Loss tangent > 1) prior to temperature decrease (**Supplementary Figure S - 5A**). Despite the altered value of measurement, calculation of temperature where loss tangent < 0.1 is strongly correlated (>0.99) to tan > 1 and provides a good estimate of stable gel formation (**Supplementary Table S - 1, 2**). From here on in, this value will be called effective temperature of gel formation.

6% (w/v) samples show a clear, inverse correlation to DoF, with effective temperature of gel formation ranging between 14.9°C (18% DoF) and 8.0°C (80% DoF) (**Figure 7-2B i**). Similarly, 10% (w/v) samples demonstrate a clear inverse correlation to DoF, with effective temperature of gel formation ranging from 17.7°C (18% DoF) to 12.1°C (80% DoF) (**Figure 7-2B i**). A good correlation (0.57) is evident between peptide concentration and effective temperature of gel formation, and DoF is found to be inversely correlated (-0.71) to effective temperature of gel formation. The inverse correlation between effective temperature of gel formation and DoF is likely a result of functional group interference in helix formation, as has previously been reported.³⁶⁴

Storage Modulus at 4°C

Storage modulus at 4°C was also assessed to further highlight correlations between material variables (DoF, and concentration) and functional properties. Here, storage modulus at 4°C was found to be dependent on both Gelma concentration and DoF. 6% (w/v) samples varied in storage modulus from 2.3 kPa (18% DoF) to 0.4 kPa (80% DoF) (**Figure 7-2B ii**). While 10% (w/v) samples ranged between 9.0kPa (18% DoF) and 3.0 kPa (80% DoF) (**Figure 7-2B ii**). A clear correlation (0.83) is evident

between storage modulus at 4°C and peptide concentration, while an inverse correlation (-0.5) is evident between storage modulus at 4°C and DoF. An inverse correlation between modulus after cooling and DoF has previously been observed, with authors finding physical structuring to be less pronounced as DoF increases; owing to interference in triple helix formation.³⁶⁴ 80% DoF samples had reduced molecular weights (62,688 Da) compared to 18% DoF samples (107,464 Da), (**Supplementary Table S - 3**) therefore, it is likely that DoF reduces molecular weight which would also affect GelMA viscosity.³⁷⁰ Unfortunately, molecular data for 46% and 61% DoF samples was unable to be acquired from supplier.

Gradient of Storage Modulus Increase

Finally, gradient of storage modulus increase as a function of temperature was used to further highlight correlations between material variables and outcome mechanical properties. Gradient of storage increase was assessed over 4°C following loss tangent < 0.1 to keep sample analysis consistent. The average gradient was determined as a means of demonstrating material kinetics, providing insight into the rate of storage modulus increase over a given temperature range, and subsequently, providing insight into the rate of entanglement formation. 6% (w/v) samples ranged in gradient of stiffness increase from 0.136 kPa °C⁻¹ (18% DoF) to 0.085 kPa °C⁻¹ (61% DoF) (**Figure 7-2B iii**); while 10% (w/v) samples demonstrated substantially greater gradients ranging between 0.420 kPa °C⁻¹ (18% DoF) and 0.257 kPa °C⁻¹ (80% DoF) (**Figure 7-2B iii**). A clear correlation (0.90) between concentration and gradient of stiffness increase is observed with 6% (w/v) samples demonstrating substantially slower rates compared to 10% (w/v) counterparts. Alternatively, despite a general reduction in gradient as DoF increases past 18%, no clear correlation (-0.34) is evident between DoF and gradient of stiffness increase.

7.3.1.3 Structure-Function Correlations.

Direct correlations between non-crosslinked nanostructured properties and observed viscoelastic trends are difficult to fully attain, as non-crosslinked SAXS data was collected at 37°C while viscoelastic trends generally only provided notable values below 18°C under these tested conditions. Nevertheless, 37°C was selected such that accurate comparisons could be made between crosslinked and non-crosslinked hydrogel nanostructure as observed via SAXS.

Despite the different temperature range, some strong correlations were observed. Moduli at 4°C demonstrated strong negative correlations with non-crosslinked mass fractal dimension (-0.79), correlation length (-0.75), and mesh-size (-0.77). Similarly, gradient of stiffness increase shared strong negative correlations with non-crosslinked mass fractal dimension (-0.89), correlation length (-0.86), and mesh size (-0.91). In both cases, concentration dependencies are likely the reason for strong correlations, as higher polymer concentrations yield networks of increased polymer densities, and subsequently, reduce mass fractal dimension, correlation length, and mesh size, yet increase modulus at 4°C and gradient of stiffness increase. The effect of temperature on these correlations, however, needs to be investigated further.

A full comparison of correlations can be found in supplementary data (**Supplementary Figure S - 6**).

7.3.2 Crosslinked GelMA Trends

To further investigate the effect of structural changes on functional properties, the structure-function relationship of Gelma is further assessed following photo-crosslinking. Again, GelMA nanostructure is investigated via SAXS; while viscoelastic properties are determined through oscillatory rheology.

7.3.2.1 Small-Angle X-ray Scattering

SAXS analysis is used to observe polymer conformation changes in response to photo-crosslinking. Scattering curves were acquired for GelMA samples at four DoF (18%, 46%, 61% and 80%) and at two concentrations (6% (w/v) and 10% (w/v)). SAXs trends were modelled with respect to polymer conformation (mass fractal dimension), distance between polymer entanglements (Correlation length), and average polymer mesh size.

Crosslinked Mass Fractal Dimension

Fitting SAXS curves to a mass fractal dimension model provides insight into polymer conformation.³¹¹
³¹³ Following crosslinking, all samples dramatically increased in mass fractal dimension compared to non-crosslinked counterparts (**Figure 7-2, Figure 7-3**), indicating a substantial increase in polymer complexity towards branched networks as is expected in covalently crosslinked systems.³¹¹⁻³¹² 6% (w/v) GelMA samples demonstrated a DoF-dependent increase in mass fractal dimension, ranging from 2.12 ($\pm <1\%$, 18% DoF) to 2.48 ($\pm <1\%$, 80% DoF)(**Figure 7-3A i**); while 10% (w/v) samples demonstrate a similar trend, ranging in mass fractal dimension from 2.17 ($\pm <1\%$, 18% DoF) to 2.61 ($\pm <1\%$, 61% DoF) (**Figure 7-3A i**). A clear correlation (0.89) is observed between DoF and crosslinked mass fractal dimension, indicating that GelMA samples of higher functionalisation result in the development of more complex polymer conformations following crosslinking. Alternatively, no significant correlation (0.2) is evident between concentration and crosslinked mass fractal dimension over the conditions tested. Results suggest that crosslinking of higher DoF samples results in greater polymer conformation complexity and branching, while concentration had a negligible effect on polymer complexity at these concentrations.

Crosslinked Correlation Length

Calculation of average correlation length provides a good estimate of distance between entanglements and subsequently allows for observation into local polymer network morphology.³¹¹ 6% (w/v) GelMA samples demonstrated a correlation length, which is inversely proportional to DoF, ranging from 6.6 nm ($66.3 \text{ \AA} \pm 2.0\%$) in 18% DoF samples to 4.0 nm ($40.5 \text{ \AA} \pm <1\%$) in 80% DoF samples (**Figure 7-3A ii**). Correlation lengths in 10% (w/v) samples followed a similar trend; however, correlation lengths presented shorter than 6% (w/v) counterparts (**Figure 7-3A ii**). 10% (w/v) GelMA samples ranged from 5.0 nm ($49.7 \text{ \AA} \pm 1\%$) in 46% DoF samples to 3.4 nm ($34.1 \text{ \AA} \pm <1\%$) in 80% DoF hydrogels. Despite 18% DoF, 10% (w/v) samples eliciting a lower correlation length than 46% DoF samples of the same concentration, a good inverse correlation (-0.65) was still observed between DoF and correlation length. As correlation length is reflective of all entanglements, it is likely that physical entanglements present during the crosslinking process remain post-crosslinking, resulting in 18% DoF samples demonstrating shorter correlation lengths compared to 46% DoF samples in higher concentration hydrogels;³¹² however, further research covering a range of crosslinking temperatures is required. An inverse correlation (-0.59) was also observed between GelMA concentration and crosslinked correlation length, as is expected in networks of increased density.

Crosslinked Mesh Size

Calculation of average mesh size provides further insight into network nano-morphology. A clear inverse relationship is observed between DoF and mesh size, with 6% (w/v) samples demonstrating a mesh size of 11.1 nm ($110.8 \text{ \AA} \pm 1.2\%$) for 18% DoF samples and 8.7 nm ($87.1 \text{ \AA} \pm <1\%$) for 80% DoF samples (**Figure 7-3A iii**). This trend is further highlighted in 10% (w/v) samples, wherein mesh size ranges between 11.9 nm ($119.5 \text{ \AA} \pm <1\%$) for 18% DoF samples and 8.3 nm ($82.6 \text{ \AA} \pm <1\%$) in 80% DoF hydrogels (**Figure 7-3A iii**). A notable inverse correlation (-0.93) is observed between DoF and crosslinked mesh size, as expected. These results indicate that as DoF increases, crosslinked mesh size decreases. As mesh size in similar covalently crosslinked systems largely reflect crosslinked mesh size and neglect physical entanglements,³¹² it is likely a result of reducing spacing between functional groups resulting in shorter spaces between polymer crosslinks and subsequently, reducing average polymer

mesh size. No significant correlation (0.05) is observed between peptide concentration and crosslinked mesh size at these tested concentrations.

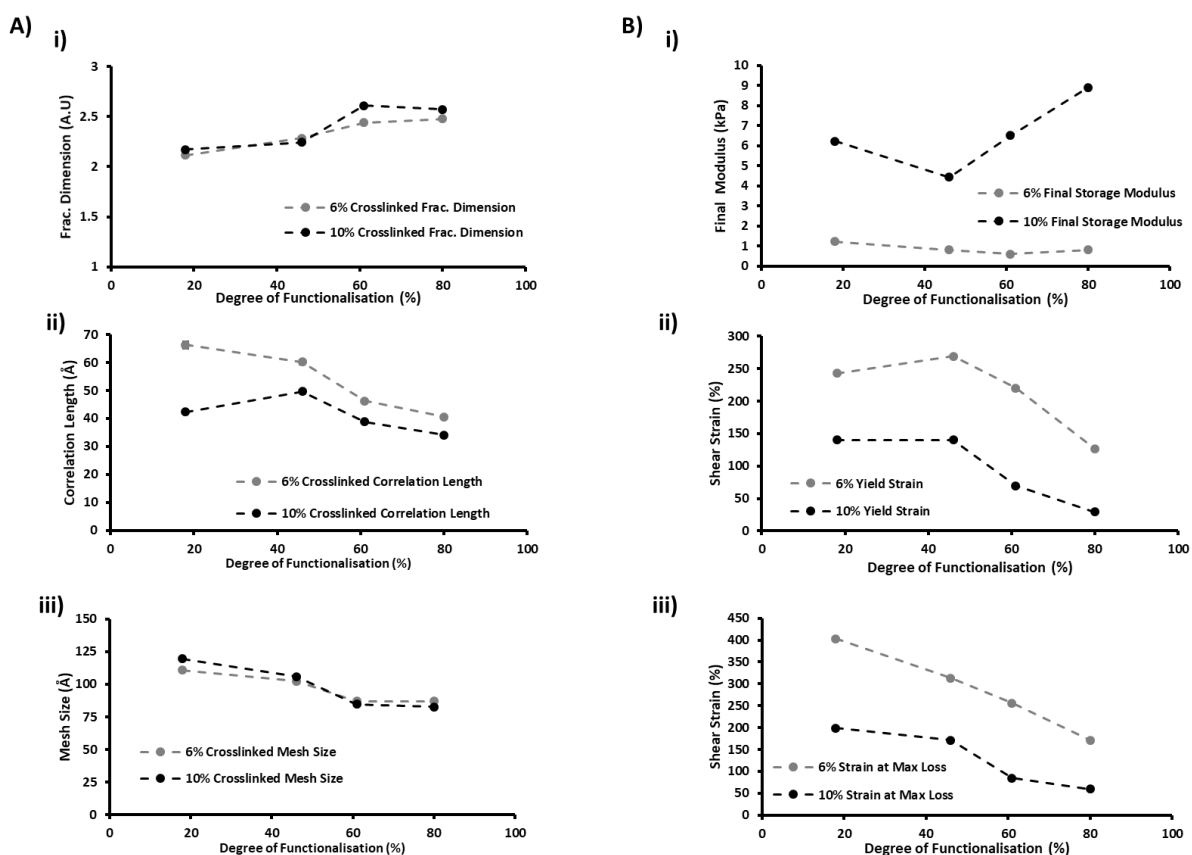


Figure 7-3 – Nanostructured and Viscoelastic properties of crosslinked GelMA. A) nanostructured properties as determined through SAXS regarding i) mass fractal dimension, ii) correlation length, and iii) mesh size; B) crosslinked viscoelastic properties including final modulus, yield strain, and strain at max loss modulus.

7.3.2.2 Material Viscoelastic Properties

Changes in material viscoelastic properties during crosslinking were observed via oscillatory rheology. Samples were photo-crosslinked *in situ* (365 nm, 4.5 mW cm⁻²), and changes in storage and loss modulus were recorded for 15 minutes. UV irradiation was applied at 1-minute and allowed to run for a further 14 minutes. Following crosslinking, a logarithmic amplitude sweep was applied to samples to test sample response to shear strain between 0.1% and 1000%. Dynamic response to shear-strain increase was plotted, and values of interest were selected for further investigation (**Supplementary Figure S - 7B, C**).

Crosslinked Storage Modulus

Following crosslinking completion (15 minutes testing), the final storage modulus of each sample was calculated. 6% (w/v) samples demonstrate relatively low final storage modulus', ranging between 1.2 kPa in 18% DoF samples and 0.6 kPa in 61% DoF samples (**Figure 7-3B i**). Alternatively, 10% (w/v) samples demonstrate substantially higher storage modulus, ranging between 4.4 kPa in 46% DoF samples and 8.9 kPa in 80% DoF samples (**Figure 7-3B i**).

Interestingly, observations made in 6% (w/v) samples challenge much of current literature, which finds increased DoF results in increased material stiffness following crosslinking.^{368 254} Here, we believe that these hydrogels at 6% are bordering on the concentration threshold for gel formation, limiting the number of crosslinks and subsequently, reducing the final storage modulus. Similarly, a discrepancy is evident in 10% (w/v) samples, wherein the 46% DoF hydrogel demonstrates a lower final modulus (4.4 kPa) than the 18% DoF sample (6.2 kPa). Here, it is possible that source variability and batch-batch differences is a leading cause for these inconsistencies. In both cases, however, further research is required over a greater range of concentration to adequately understand the underlying kinetics of these materials. Results may also benefit from analysis of material compressive moduli, allowing for more accurate comparison to literature. Despite no substantial correlation (0.13) between DoF and final modulus in this study, a clear correlation (0.93) was observed between GelMA concentration and final modulus.

Strain at Yield Point

Stress was plotted against shear-strain for 6% (w/v) (**Supplementary Figure S - 5B**) and 10% (w/v) (**Supplementary Figure S - 5C**) GelMA samples. Strain at stress peak was recorded for each sample and used as an indication of strain at the yield point. 6% (w/v) samples ranged in yield strain, from 269% in 46% DoF samples to 127% in 80% DoF samples (**Figure 7-3B ii**). Comparatively, 10% (w/v) samples were less tolerant to shear strain, with yield strains ranging between 140% in 18% DoF and 46% DoF samples, to 30% in 80% DoF samples (**Figure 7-3B ii**). A strong inverse correlation (-0.72) was evident between yield strain and DoF; while no notable correlation (0.09) was observed between concentration and yield strain. The lack of correlation is surprising, as higher concentration samples demonstrated substantially lower strain-tolerance compared to their 6% (w/v) counterparts, however, source variability may be masking trends. These results agree with current literature, which finds increased crosslinking density results in decreased ability to tolerate strain.³⁷¹

Strain Macro-Crack Formation

Strain at maximum loss modulus was used to measure material strain resistance. When an amplitude sweep is performed, the point of maximum loss modulus corresponds to the formation of a continuous macro-crack which runs the entire gap of the measuring system.³⁷² The strain at this point was recorded for each sample and used as a measure of material resistance to crack-formation. 6% (w/v) samples demonstrated an enhanced ability to resist macro-crack formation, requiring between 403% and 171% strain to reach macro-crack formation in 18% DoF and 80% DoF samples, respectively (**Figure 7-3B iii**). (w/v) samples demonstrate substantially less strain conformity, forming cracks after 199% and 60% for 18% DoF and 80% DoF respectively (**Figure 7-3B iii**). A strong inverse correlation (-0.74) is observed between GelMA concentration and strain at maximum loss modulus; while a strong inverse correlation (-0.65) is observed between DoF and strain at maximum loss modulus. As strain at maximum loss modulus shares strong correlations with both DoF and concentration, we suggest considering strain at maximum loss modulus in conjunction with yield strain for future studies of similar nature.

7.3.2.3 *Structure-Function Correlations.*

Various structure-function relationships are observed between crosslinked polymer network conformation and crosslinked hydrogel viscoelastic properties. Final storage modulus demonstrates a negative correlation (-0.66) with crosslinked correlation length; likely due to increased polymer density resulting in increased entanglement density. Strain at maximum loss modulus demonstrates a negative correlation (-0.75) with crosslinked mass fractal dimension, a strong positive correlation (0.93) with crosslinked correlation length, and a positive correlation (0.56) with crosslinked mesh size; here it is likely that high polymer complexity results in increased network rigidity and subsequently, less strain deformability prior to breaking. The direct correlation between correlation length and strain at maximum loss modulus is likely due to decreased entanglement density reducing network rigidity; likewise, an increase in mesh-size would reduce network rigidity, increasing strain tolerance. Similarly, yield strain demonstrated an inverse correlation (-0.64) with crosslinked mass fractal dimension, and a strong direct correlation (0.78) with crosslinked mesh size; these results strengthen observations made through analysis of strain at max loss modulus.

Interestingly, all crosslinked viscoelastic properties investigated also share strong correlations with non-crosslinked nanostructured properties. Specifically, final storage modulus shares strong negative correlations with non-crosslinked mass fractal dimension (-0.78), correlation length (-0.84) and non-crosslinked mesh size (-0.94); while strain at maximum loss modulus shares positive correlations to non-crosslinked mass fractal dimension (0.53), correlation length (0.79) and non-crosslinked mesh size (0.70). Again, this is likely an effect of concentration dependence, with increased concentration reducing non-crosslinked mass fractal dimension, correlation length, and mesh size yet once crosslinked, resulting in increased final modulus and decreased strain tolerance.

7.4 Conclusion

SAXS was used to observe GelMA polymer organisations; allowing otherwise unavailable monitoring of nanoscale structural changes in response to alteration of polymer concentration or DoF. Trends were observed and correlated to bulk material viscoelastic properties acquired through rheology. Polymer organisation was modelled in regard to mass fractal dimension, correlation length, and mesh size. For non-crosslinked samples, an increase in polymer concentration resulted in a decrease in non-crosslinked mass fractal dimension, correlation length, and mesh size, indicating an inverse relationship; whilst no substantial correlations were evident in response to an increase in DoF. Upon crosslinking, polymer mass fractal dimension substantially increased for all samples, indicating increased polymer morphological complexity. This increase was positively correlated with material DoF. Similarly, correlation length was found to increase upon crosslinking; however, magnitude of increase was inversely related to DoF. Mesh size decreased in response to crosslinking, with higher DoF samples experiencing the greatest decrease in mesh size. For crosslinked samples, an increase in polymer concentration only had a substantial effect on correlation length, resulting in an overall decrease in crosslinked correlation length. Alternatively, an increase in DoF was positively correlated with mass fractal dimension, and negatively correlated with correlation length and mesh size. Viscoelastic properties were determined via rheology. Clear positive correlations were evident between polymer concentration and resultant material stiffness, either in relation to cooling or photo-crosslinking. DoF was shown to be negatively correlated to temperature of stable gel formation, likely due to reduced molecular weights of these polymers. Despite an overall increase of final crosslinked modulus concerning DoF increase, no clear correlation was evident; here it is likely that source variability and concentration thresholds are masking trends. Finally, both DoF and polymer concentration showed strong inverse correlations to strain tolerance as measured through strain at maximum loss modulus.

Overall, these results highlight the structure-function relationships of GelMA and provide insight into nanostructured changes which result from control over GelMA concentration and DoF. Future investigations should focus on kinetics modelling of *in situ* structural changes during crosslinking, determining the dependence between threshold concentrations and DoF, and investigating

additional crosslinking temperatures. No substantial correlation was evident between source and trends, here it is likely that GelMA source variability was a contributing factor, as GelMA was sourced from two different suppliers (Sigma Aldrich and University of Wollongong) and methacrylation was performed on different gelatin batches. Subsequently, source variability may reduce clarity of observations; reiterating the need to move from natural proteins toward synthetic tissue analogues. Work outlined in this chapter will allow researchers to understand nanostructure organisations from rheological observations. From results in this chapter, 18% DOF at 6% (w/v) was selected for further bioink development in subsequent chapters, owing to its elevated gelation temperature and high strain tolerance.

Chapter Eight:

MUSCLE BIOINK

8.1 Preview

This chapter intends to further investigate the ability of Fmoc-SAPs to integrate with mechanically advantageous biomacromolecules; specifically, for the development of a preliminary bioink toolkit. Here, the extensively used functionalised macromolecule GelMA is combined with SAP fibrils constructed through coassembly of Fmoc-FRGDF and Fmoc-PHSRN, as described in **Chapter 4**. We hypothesise that fibril formation will be maintained in the presence of GelMA, allowing for the presentation of tuneable and functional biochemical signals within a bioprintable hydrogel bioink. We anticipate that the charged GelMA molecules will associate with the peptide fibrils, allowing for a high degree of control over hydrogel morphology, from nanoscale (through fibril formation) through to macroscale (through bioprinting). Hybrid material physical and mechanical properties are extensively investigated in respect to assembly mechanisms, nano/microarchitecture, viscoelastic properties, and ability to form 3D constructs through spatial and temporal control as facilitated through bioprinting. Fmoc-SAP fibril integration and its resultant effect on primary myoblast viability and differentiation are also investigated. Results show successful development of a hybrid bioink, resulting in a high degree of control over morphological properties, from nano- through to macroscale. Furthermore, the hybrid material demonstrates enhanced printability as assessed through thermoresponsive rheology and various printability tests. Here, printability is measured through calculation of loss tangent and ability to print a desired structure. Printed scaffolds remained stable over 4 weeks and supported high primary myoblast viability and early differentiation. This part of the work is a prerequisite for the development

of a modular bioink toolkit (**Chapter 9**), allowing for ease of customisation through Fmoc-SAP selection.

Contribution of the candidate:

- Concept development and experimental design
- Key contributor to protocol development
- Involved in the acquisition of all data, with substantial contributions in material analysis
- Primary researcher for acquisition and analysis of SAXS Data
- Prepared proposal, successful Funding for Synchrotron Experiments (ANSTO, AUS)
- First author of the manuscript.

Publications relevant to this chapter

Boyd-Moss, M., Firipis, K., Quigley, A., Cichocki, A., Dekiwadia, C., Long, B., Ngan, C., Witty, S., Nisbet, D., Kapsa, RMI., Williams, R (2019) '*Bioink Development using fmoc-SAP/Gelatin Methacrylate Blends*'. **Manuscript in preparation.**

Abstract:

The potential of bioprinting to deposit cells, structures and signals within a biomimetic, spatially defined, 3D construct provides substantial promise to current tissue engineering practices. The bottom-up approach of bioprinting allows for extensive control over biochemical and biomechanical cues, allowing for multi-material printing of functional regions. However, despite immense potential, bioprinting is still critically limited in bioink development, with most bioinks unable to simultaneously provide suitable biological functionality and material printability. Therefore, the development of a simple bioink toolkit which allows independent control over biochemical stimulation and mechanical properties would be of substantial advance to current tissue engineering applications. Fmoc-SAPs have shown considerable potential for use as artificial microenvironments, owing to their ease of biochemical modification and high structural similarity to the native ECM. Despite this, Fmoc-SAPs are limited in potential as they cannot form covalent bonds, and therefore are liable to dissociation in media. Alternatively, GelMA is a gelatin-derived biomaterial with extensive use in bioprinting applications owing to its favourable mechanical properties; however, GelMA is not without fault, as it is limited in biochemical functionalisation. Hence, this chapter focuses on the development of a novel bioink which has the potential for further development into a modular bioink toolkit through alteration of Fmoc-SAP sequence. Specifically, this chapter develops a hybrid bioink through the combination of Fmoc-FRGDF/Fmoc-PHSRN fibrils with Low Methacryloyl GelMA (LM-GelMA, 18% DoF). Results show enhanced bioprintability compared to LM-GelMA alone; and further demonstrates the efficacy of this approach as demonstrated through primary myoblast viability and differentiation.

8.2 Introduction

Tissue and organ engineering offers a substantial advance to current therapies for the replacement of damaged or diseased tissues; however, the regeneration of organs and higher order tissues is complex and requires control over spatial and temporal placement of cells and artificial tissue constructs.^{207, 373} Advances in additive manufacturing, materials science, and cell biotechnology have led to the development of bioprinting technologies, allowing the placement of cells, signals and artificial microenvironments within confined, 3D geometries.¹⁶⁰ This rapidly advancing technique allows for intricate control over scaffold micro- to macro properties, and facilitates multi-material printing, enabling the development of complex structures from multiple materials.^{189, 374} The ability to fabricate multi-material structures allows for gradient presentations of cells, signals and materials within a single 3D bioprinted construct.³⁷⁵ However, despite significant advance, current bioprinting approaches are substantially limited by the availability of effective bioinks, with many bioinks unable to demonstrate suitable biological properties whilst maintaining adequate mechanical characteristics demanded in bioprinting applications.¹¹

GelMA is a gelatin derived material which has been modified with methacryloyl groups, allowing for triggered covalent crosslinking upon exposure to UV irradiation.^{65, 366} GelMA demonstrates unique thermo-dependent viscoelastic properties allowing for precise control over material viscosity enabled through temperature control.³⁶⁹ These highly advantageous mechanical characteristics combined with GelMA's high bioactivity and biocompatibility has resulted in substantial use in bioprinting applications.²⁰³ However, despite GelMA being a gold standard for many tissue bioprinting applications, it is inherently restricted in its cell-signalling capacity; presenting only one (RGD) of two synergistic cell adhesion (RGD, PHSRN) epitopes.^{314, 366} Furthermore, GelMA is limited in morphology; with recent research aiming to introduce fibril-like structures through electrospinning.³⁷⁶ Current interest in GelMA use for soft tissue engineering has focused on altering the degree of methacryloyl, allowing for the development of materials of altered stiffness ideal for mechanotransduction.³⁷⁷⁻³⁷⁸ However, attempts to translate LM-GelMA into a bioprintable material have been disappointing, with LM-GelMA bioinks unable to maintain suitable shape fidelity.³⁶⁸

SAPSs are a unique class of synthetic peptide which spontaneously form highly biomimetic, hierarchical, structures that immobilise the surrounding solvent to form biocompatible hydrogels.²⁶ These materials allow for high structural and biochemical tunability, facilitating the formation of various structures, including ribbons, tapes, nanotubes, and fibrils.³⁷⁹ Furthermore, SAPs allow for substantial control over biochemical signalling, enabling targeted cell signalling facilitated through sequence selection.⁷ Aromatic Fmoc-SAPs are a promising subclass of SAPs, allowing for charge neutralised assembly facilitated through pH manipulation; resulting in the formation of large, highly biomimetic structures through π - π stacking of Fmoc groups and β -sheet formation between short peptide sequences (π - β assembly).⁸

Fmoc-FRGDF is a fibronectin-inspired SAP which has seen substantial success in tissue engineering applications both *in vitro*¹⁴³ and *in vivo*.^{141, 380} Recent research has combined this SAP with a similar, fibronectin-inspired sequence Fmoc-PHSRN, allowing for the formation of fibrillar structures decorated with synergistic fibronectin attachment motifs, RGD and PHSRN.³¹⁴ Further functionalisation of Fmoc-FRGDF has also been enabled through coassembly with macromolecules, as confirmed through network incorporation of fucoidan and versican.^{265, 337, 381} The ability of Fmoc-FRGDF to associate with charged molecules facilitates the development of novel hybrid artificial ECMs, increasing the versatility of this material. Despite the success of Fmoc-SAPs, hydrogels developed from this material demonstrate poor force endurance and some instability under physiological conditions; therefore, these materials would benefit from structural macromolecule incorporation.³⁸² To our knowledge, no previous work has been completed using Fmoc-SAPs as bioink components.

In this chapter, a hybrid material is developed through Fmoc-FRGDF/Fmoc-PHSRN coassembly in the presence of LM-GelMA; allowing for high mechanical tunability as offered through GelMA incorporation, and high biochemical tunability facilitated through Fmoc-SAP sequence selection. Specifically, we investigate the association between Fmoc-FRGDF/Fmoc-PHSRN fibrils and LM-GelMA, determining the mechanisms governing assembly. Hydrogel stiffness, printability, and network topology are also investigated, before subsequent investigations into material bioactivity and

ability to influence primary myoblast behaviour. The ultimate goal of this chapter is to investigate the potential of such hybrid systems as bioink toolkits, enabling ease of biochemical customisation through sequence engineering; and providing the foundation for further bioink development targeting alternate tissue types.

8.3 Results and Discussion

8.3.1 Formation of Bioinks

We have previously demonstrated the synergistic behaviour of hydrogels formed from fibronectin-inspired Fmoc-FRGDF and Fmoc-PHSRN (**Chapter 4**). In this study, we advance this hydrogel system into an effective bioink through the inclusion of LM-GelMA. Three peptide-based bioinks were developed. Firstly, a fibronectin-inspired Fmoc-SAP containing synergistic fibronectin attachment motifs, RGD and PHSRN, was self-assembled under physiological conditions (pH 7.4) using a well-characterised pH switch method.⁸ Here, Fmoc-FRGDF and Fmoc-PHSRN were coassembled in accordance with our previous study (**Figure 8-1A**), from here on this bioink will be termed coassembled.³¹⁴ A second bioink was developed through the low degree (18%) methacrylation of gelatin to form LM-GelMA which was dissolved in PBS such that the final concentration is 6% (w/v) (**Figure 8-1B**). LM-GelMA can undergo photo-crosslinking when subjected to UV irradiation in the presence of a photoinitiator, allowing for controlled and rapid gelation. A third bioink was assembled through a combination of Fmoc-FRGDF/Fmoc-PHSRN hydrogel (0.5% w/v) with LM-GelMA hydrogel (6% w/v) for a final concentration hybrid of 6.5% w/v (**Figure 8-1C**). Hereafter, this gel is termed FPG-Hybrid. Both the coassembled bioink and the FPG-Hybrid bioink were observed to present self-supporting gel-like morphologies at 20°C, remaining stable even once inverted (**Supplementary Figure S - 8**). Contrastingly, LM-GelMA did not demonstrate noticeable gel-like properties at this temperature and subsequently was found to flow to the bottom upon tube inversion (**Supplementary Figure S - 8**). All bioinks were observed to be clear upon assembly.

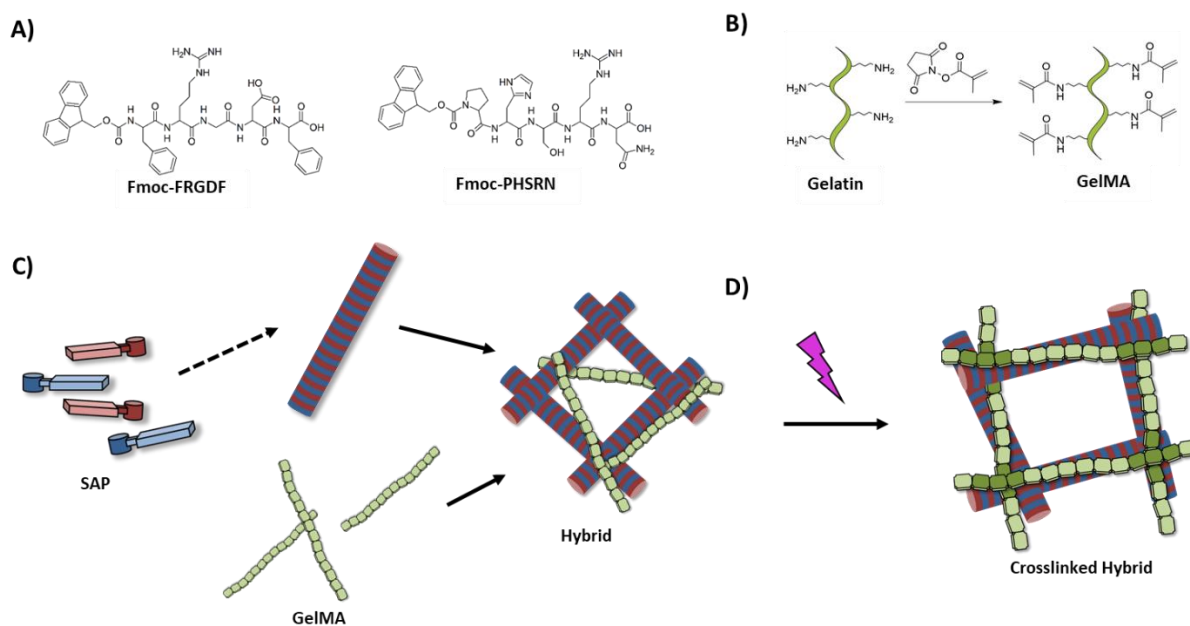


Figure 8-1 – Schematic showing hydrogel assembly (A) Chemical structure of Fmoc-FRGDF and Fmoc-PHSRN, (B) Schematic detailing gelatin modification with methacryloyl groups to produce gelatin methacryloyl. (C) Schematic representation of assembly mechanisms showing self-assembly of Fmoc-SAPs into fibrils in the presence of gelatin methacryloyl before subsequent photo-crosslinking of the network.

8.3.2 Visualisation of Assembled Structures and Network Architecture

Underlying structural and network morphologies of the developed bioinks were visualised using TEM, CryoSEM and SAXS.

8.3.2.1 *Transmission Electron Microscopy*

TEM provided insight into the nanoscale structures present in each bioinks (**Figure 8-2A-C**). The coassembled bioink was observed to possess fibrillar structures as is characteristic with this type of assembly.³¹⁴ These fibrillar structures were not evident in LM-GelMA samples, instead aggregates were observed. The hybrid bioink containing both Fmoc-FRGDF/Fmoc-PHSRN and LM-GelMA demonstrated fibrillar structures comparable to those seen in the coassembled sample alone. Fibril diameter was quantified using Image-J analysis for coassembled and hybrid samples. An average fibril diameter of 15.06 nm ($\sigma = 0.22$ nm) was observed for coassembled samples while the hybrid sample was shown to have slightly smaller fibrils of 13.12 nm ($\sigma = 1.00$). Despite a slight decrease in fibril diameter in hybrid samples, both were shown to maintain fibril formation.

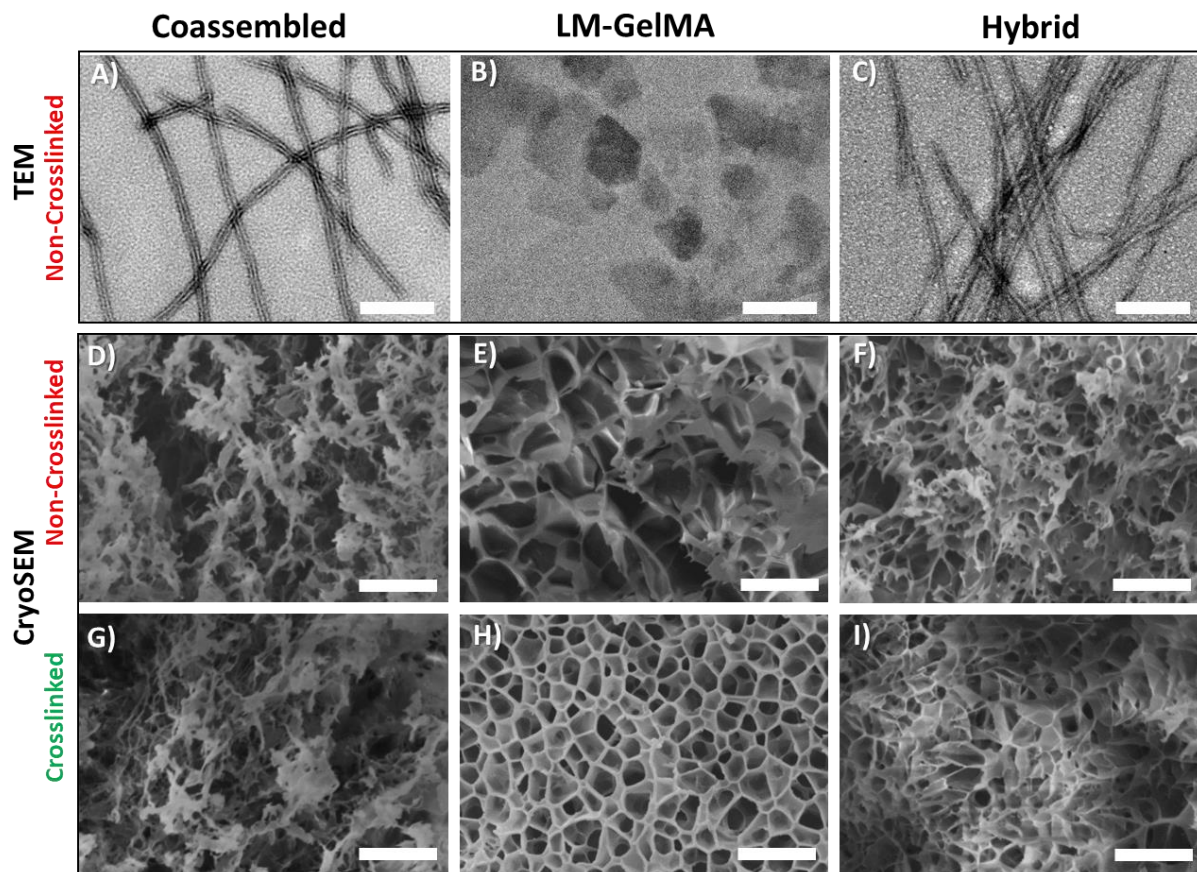


Figure 8-2 – Network Morphology (A-C) TEM analysis of material nanostructure Scale bar (200 nm), (D-F) CryoSEM Analysis of network microstructure before UV exposure, and (G-I) CryoSEM analysis of network microstructure following UV exposure. From left to right: Coassembled Fmoc-FRGDF/Fmoc-PHSRN, LM-GelMA, and FPG-Hybrid samples. Scale bar (100 μ m)

8.3.2.2 *Cryo-Scanning Electron Microscopy*

The investigation into network microstructure was observed through CryoSEM, allowing for sample network topology to be investigated with minimal compromise to structures. As ice templating effects could corrupt results, care was taken to avoid crystallised ice formation. Specifically, samples were plunge frozen in liquid nitrogen before being fractured and sublimated; this technique is routinely used within the RMMF labs. In each sample, network morphology was analysed before and after subjection to UV irradiation (**Figure 8-2D-I**). The coassembled bioink demonstrated a chaotic fibrillar architecture both before and after UV subjection with no significant change in structure (**Figure 8-2D, G**). Contrastingly, LM-GelMA was observed to present as a jagged network before UV subjection (**Figure 8-2E**) and transitions into a more ordered topology with a honeycomb-like structure following UV exposure (**Figure 8-2H**). Interestingly, the FPG-Hybrid sample appeared to contain both network morphologies before UV crosslinking, with nanofibrils and a jagged, LM-GelMA-like network both evident (**Figure 8-2F**). However, after UV exposure the network was found to become more ordered, following a similar trend to the crosslinked LM-GelMA sample (**Figure 8-2I**). These results suggest that the FPG-Hybrid sample possesses fibrillar structures owing to the presence of the SAP network and structural aspects relating to LM-GelMA addition. Importantly, the presence of LM-GelMA during self-assembly did not appear to influence fibril formation in the FPG-Hybrid. Furthermore, a significant structural change was evident in LM-GelMA containing samples upon subjection to UV irradiation, as generally observed in photo-crosslinkable samples.

8.3.3 Investigation of Assembled Structures and Mechanical Properties

8.3.3.1 Small-Angle X-ray Scattering

To verify structural observations made in TEM and CryoSEM analysis, SAXS was employed. Scattering curves were obtained for all samples and used to investigate nanostructural changes (**Figure 8-3A**). Coassembled Fmoc-FRGDF/Fmoc-PHSRN has previously been shown to form cylindrical structures, such as fibres, as indicated through q^{-4} shifting to a q^{-1} dependence at low q range and a comparable trend was observed in this instance.³¹⁴ Despite indications of fibrillar structures in FPG-Hybrid TEM analysis, LM-GelMA containing samples did not sufficiently satisfy a cylindrical model and therefore were fitted using shape independent models.

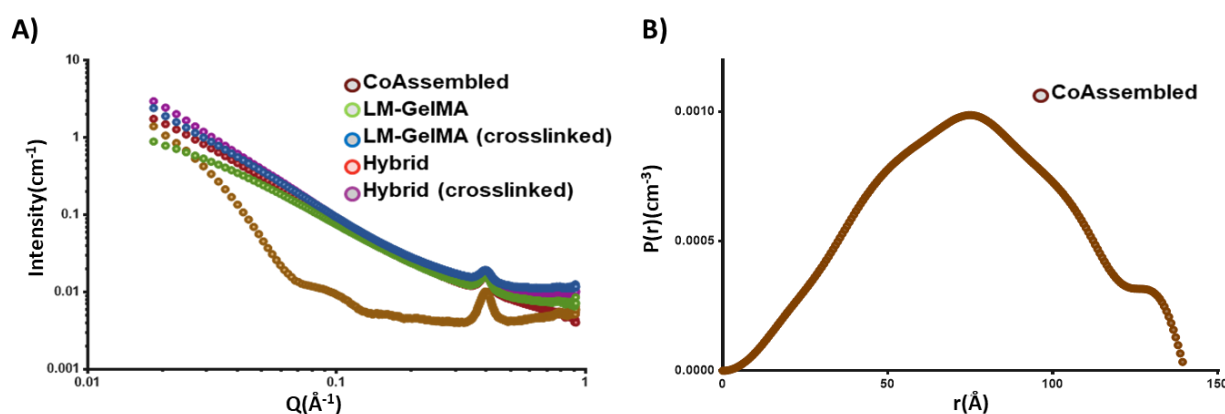


Figure 8-3 – Analysis of material nanostructure (A) SAXS curves of Fmoc-FRGDF/Fmoc-PHSRN, LM-GelMA, and FPG-Hybrid Samples (B) Resultant probability of average fibril radius modelled using P(r) function (SASView)

Calculation of Average Fibril Diameter

IFT analysis was performed on the coassembled sample to calculate average fibril radius via application of the P(r) function (SASview) (**Figure 8-3B**). TEM analysis indicated fibril length lies outside of the q range, and therefore, the value resulting in the maximum P(r) intensity was attributed to fibril radius. Analysis of P(r) fitting indicated average fibril diameter of 15.0 nm ($r = 75.2 \text{ Å}$) for the 5 mg/mL coassembled sample. Analysis of average fibril diameter was in agreement with previous studies³¹⁴ and observations made during TEM analysis.

Considering LM-GelMA containing samples did not sufficiently satisfy a cylinder model, shape independent analysis was performed on both crosslinked and non-crosslinked samples. Analysis of

scattering power or mass fractal dimension was calculated for each LM-GelMA containing sample before and after crosslinking (**Supplementary Figure S - 9**).

Determination of Mass Fractal Dimension

The linear region of scattering plots on a log-log scale was used to calculate mass fractal dimension, d_m , which quantifies self-similar organizations over a range of length scales, and consequently offered insight into polymer structure and conformation.³¹³ The mass fractal dimension can be described by **Equation 7-1**. (See Section 7.3.1 for more detail)

Analysis of mass fractal dimension for each LM-GelMA containing sample across mid q range ($0.05 - 0.2 \text{ nm}^{-1}$, **Supplementary Figure S - 9A**) revealed a relatively low value for non-crosslinked LM-GelMA of $1.797 (\pm <1\%)$. Upon subsection to UV irradiation, the mass fractal dimension is found to increase to $2.123 (\pm <1\%)$, as is expected with covalently crosslinked systems. In comparison, the FPG-Hybrid sample demonstrated an initial mass fractal dimension of $2.089 (\pm <1\%)$ before crosslinking, and this increased to $2.253 (\pm <1\%)$ following UV exposure. These results indicated that all systems demonstrate an increase in polymer conformation complexity toward branched systems as is characteristic of similar gelatin-based crosslinking systems.³¹² Importantly, polymers in the FPG-Hybrid system are initially branched to a greater degree, and upon UV subsection, retain their ability to crosslink further through the formation of covalent bonds, resulting in polymer conformations of greater complexity, likely due to the presence of nanostructured SAP fibrils.

Determination of Correlation Length

The correlation length of LM-GelMA and FPG-Hybrid samples was determined across the mid-low q range (**Supplementary Figure S - 9B**) using the correlation length model as described in **Equation 7-2**. (See Section 7.3.1 for more detail)

Correlation length provides a reasonable estimate of average entanglement length for semi-dilute polymer solutions.³¹¹ Non-crosslinked LM-GelMA demonstrates the lowest correlation length of all samples, exhibiting a correlation length (ξ) of $4.07 \text{ nm} (\pm <1\%)$. Upon photo-crosslinking of LM-GelMA, the correlation length was found to increase to $5.91 \text{ nm} (\pm 1\%)$. The FPG-Hybrid sample

demonstrated an initial correlation length of 8.31 nm ($\pm 1.9\%$) before crosslinking, and shifted to 7.52 nm ($\pm 1.9\%$) in crosslinked samples; interestingly, this trend appears to be in agreeance with similar gelatin-based crosslinking investigations, wherein correlation length was found to decrease upon crosslinking.³¹² This is likely due to increased network densification upon crosslinking, resulting in the formation of new junctions and subsequently, a decrease in correlation length.³⁸³ A possible explanation for the alternate trend experienced by LM-GelMA alone can be provided by Lindemann et al. wherein it was reported that more reactive crosslinkers increased correlation length.³⁸⁴ Despite both samples in this study using the same crosslinker and crosslinking concentration, LM-GelMA experienced a more considerable change in mass fractal dimension, and subsequently, demonstrated a greater structural change over the same crosslinking time.

The Porod exponent, m , provides insight into polymer conformational changes in a similar way to the mass fractal dimension. Here, the Porod Exponent ranged from 2.04 to 2.28, comparable with similar assemblies.³¹² Once again, Porod exponent was found to increase with covalent crosslinking, reinforcing observations made through mass fractal dimension calculation (**Supplementary Table S - 4**).

Determination of Mesh Size

Determination of mesh size provides insight into interpolymer relations (**Supplementary Figure S - 9C**). The determination of mesh size can be described by **Equation 7-3**. (*See Section 7.3.1 for more detail*)

Analysis of mesh size demonstrated a decrease upon crosslinking, from 13.64 nm ($\pm 1.2\%$) to 10.74 nm ($\pm <1\%$) in LM-GelMA samples, and from 10.34 nm ($\pm <1\%$) to 9.05 nm ($\pm 1.2\%$) in FPG-Hybrid samples (**Figure S3C**). These results are in agreeance with mass fractal dimension calculations and similar gelatin-based assemblies; wherein an increase in mass fractal dimension resulted in increased network formation and densification through the formation of covalent crosslinks. Consequently, this densification reduces the distance between polymers and results in reduced mesh size upon crosslinking.³¹²

Assembly mechanisms were further confirmed through CD, FT-IR, and fluorescence spectroscopy. Data demonstrated a maintenance of π - β assemblies in coassembled and FPG-Hybrid samples as are characteristic of Fmoc-systems, however spectra were heavily influenced by GelMA interactions (**Supplementary Figure S - 10**).

8.3.4 Mechanical Characteristics

8.3.4.1 Rheology - *In Situ* Crosslinking

Oscillatory rheology was used to determine mechanical changes during *in situ* photo-crosslinking (**Figure 8-4Ai**). The UV source (365 nm, 4.5 mW cm⁻¹) was turned on 1 minute after test commencement. As expected, the coassembled hydrogel demonstrated no significant change in modulus throughout UV exposure, exhibiting a storage modulus of ~20kPa. Contrastingly, a notable change in storage modulus was observed in both the FPG-Hybrid sample and in LM-GelMA alone, increasing significantly upon UV subjection. LM- GelMA demonstrated an initial G' of ~0.1Pa and this increased to 0.49 kPa. Similarly, the FPG-Hybrid sample increased substantially upon UV exposure, from G' 220 Pa to 5 kPa. Typical hydrogels demonstrate a storage modulus of greater magnitude than their corresponding loss modulus; as such, both SAP-containing samples were found to present as stable hydrogels before UV subjection in accordance with macroscopic observations. After UV subjection, all three samples were found to demonstrate typical hydrogel viscoelastic properties with storage modulus greater than loss modulus.

Analysis of G' rate of change can be used to indicate sufficient crosslinking (**Supplementary Figure S - 11A**). In this study, crosslinking completion was defined as the point where G' rate of change fell below 0.1% s⁻¹. LM-GelMA required the longest time to reach crosslinking completion, requiring ~8.4 minutes of UV subjection (9.4 minutes of testing). Alternatively, the FPG-Hybrid material required only 7 minutes of UV exposure (8 minutes of the test) to reach a similar rate. A possible explanation for LM-GelMA hydrogels requiring more crosslinking time to reach a similar rate may be attributed to the requirement for more significant polymer conformation change, as indicated through SAXS mass fractal dimension calculations. A further contributing factor could be the magnitude of change each sample experiences, with LM-GelMA samples experiencing a change of approximately three orders of magnitude compared to the FPG-Hybrid hydrogel which only experienced a change of one order of magnitude. For all subsequent tests, both samples were subject to UV crosslinking for 500 seconds to maintain consistency.

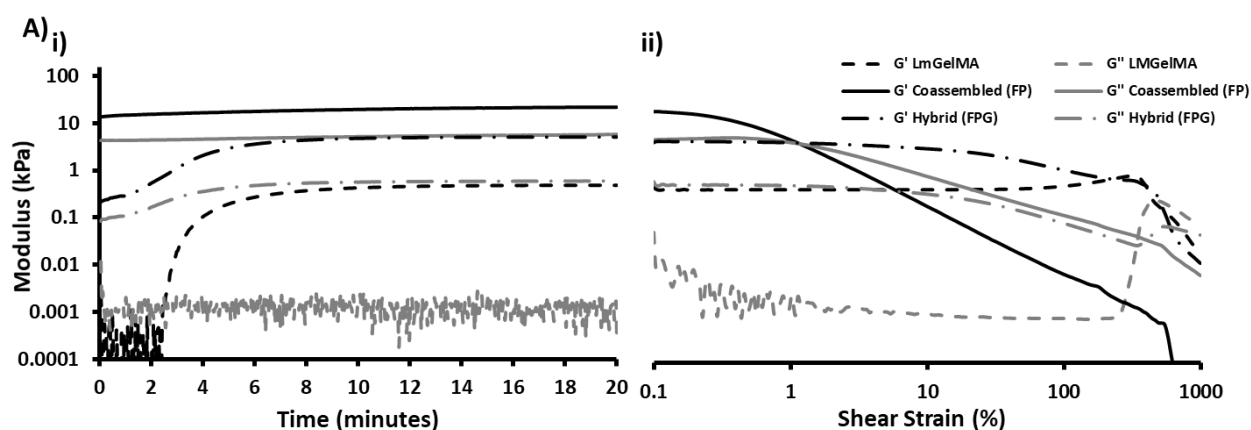


Figure 8-4 – **Analysis of material viscoelastic properties** (A) Rheological Analysis of i) *In situ* Crosslinking and ii) post-crosslinking material resistance to shear strain.

8.3.4.2 Rheology - Effect of Shear Strain

Fmoc-SAPs' propensity to swell coupled with their inability to undergo rapid gelation after shear thinning, resulting in poor shape fidelity, has rendered these peptides ineffective for bioink development to date (**Supplementary Figure S - 11C**). Therefore, SAP-incorporating bioinks which can withstand increased shear-strain post-printing would be of substantial benefit to bioprinting applications.

Oscillatory rheology was employed to investigate hydrogel response to shear-strain following UV exposure for all samples. Samples were subjected to an amplitude sweep from 0.1% shear strain to 1000% shear strain, and the point of modulus crossover (where G' falls below G'') was recorded (**Figure 8-4A ii**). As expected, the coassembled sample performed relatively poorly, undergoing a gel-sol transition at 1.15% shear strain. This relatively poor resistance to shear-strain is likely due to a lack of covalent bonds in this system. Alternatively, the LM-GelMA sample demonstrated significantly greater resistance to shear strain, with a crossover of modulus occurring around 450% shear-strain. Interestingly, the FPG-Hybrid system demonstrated the greatest resistance to shear strain, as indicated by a crossover of modulus occurring at approximately 605% shear-strain. The enhanced ability to resist shear strain in the FPG-Hybrid system indicates the hydrogel is acting as a composite system wherein the nanofibrils aid in resisting shear forces when placed in the environment of the well-ordered LM-GelMA network.

8.3.5 Investigation of Bioink Printability

Sample printability was investigated to determine the potential of formulated gels as bioink candidates. Initially, a temperature sweep was performed to determine temperatures which may provide suitable printability properties. Here, determination of suitable printability properties focused primarily on extrudability and shape integrity while maintaining relatively low-pressure printing conditions (> 69 kPa) which is necessary for cellular viability.³⁸⁵ The thermal dependence of material viscoelastic properties were assessed, and material printability was determined through the printing of a dual-layer grid of length 1cm, strut spacing 2.5 mm and 22G needle size (**Figure 8-5A**).

8.3.5.1 Viscoelastic Properties – Rheological Temperature Sweep

Oscillatory rheology was selected to investigate material thermo-dependent viscoelastic properties (**Figure 8-5B**). A temperature ramp was selected starting at 37°C and cooling to 4°C. Storage and loss moduli was again monitored for each material, and loss tangent ($\tan \delta$) was calculated as G''/G' (**Figure 8-5B, C**). Despite some increase in stiffness upon cooling, the loss tangent of the coassembled system remained constant at approximately 0.3. The coassembled sample demonstrated the stiffest storage moduli of ~ 87 kPa approaching 4°C. Contrastingly, LM-GelMA exhibited a significant decrease in loss tangent upon cooling, from < 1 to approximately 0.01, with an abrupt transition evident near 17°C. LM-GelMA also exhibited the lowest storage modulus ranging from < 1 Pa to approximately 2 kPa upon cooling to 4°C, with no noticeable change evident between 37°C and 18°C. Interestingly, the FPG-Hybrid was again found to be a compromise between LM-GelMA and the coassembled sample alone. A thermal dependence was evident with a notable sudden increase in material stiffness at approximately 17°C. FPG-Hybrid material storage modulus was found to increase from 650 Pa (37°C) to 24 kPa (4°C) following cooling. Interestingly, loss tangent was found to remain relatively constant ($\tan \delta = 0.4$) up until approximately 17°C, after which it decreases to 0.1 at 4°C. Recently, a study by Gao and colleagues found loss tangent to be a critical factor influencing material extrudability, extrusion uniformity, and structural integrity; ultimately finding loss-tangent as a suitable measure for indicating material printability.³⁸⁶ In their landmark study, the authors report a loss tangent between 0.25 and 0.45 provides an optimal printing window, allowing for suitable extrusion while maintaining good

uniformity and structural integrity.³⁸⁶ Importantly, the FPG-Hybrid material was found to exist within this range over a substantially large temperature range, from 37.0°C to 14.6°C. Contrastingly, LM-GelMA only exists in this window very briefly from 16.2°C to 16.0°C, during which the gradient was critically steep and as a result variance with temperature is significant. Therefore, we anticipated the FPG-Hybrid material would print best near 15°C, allowing for the most robust modulus while still existing within the range of desired loss tangent.

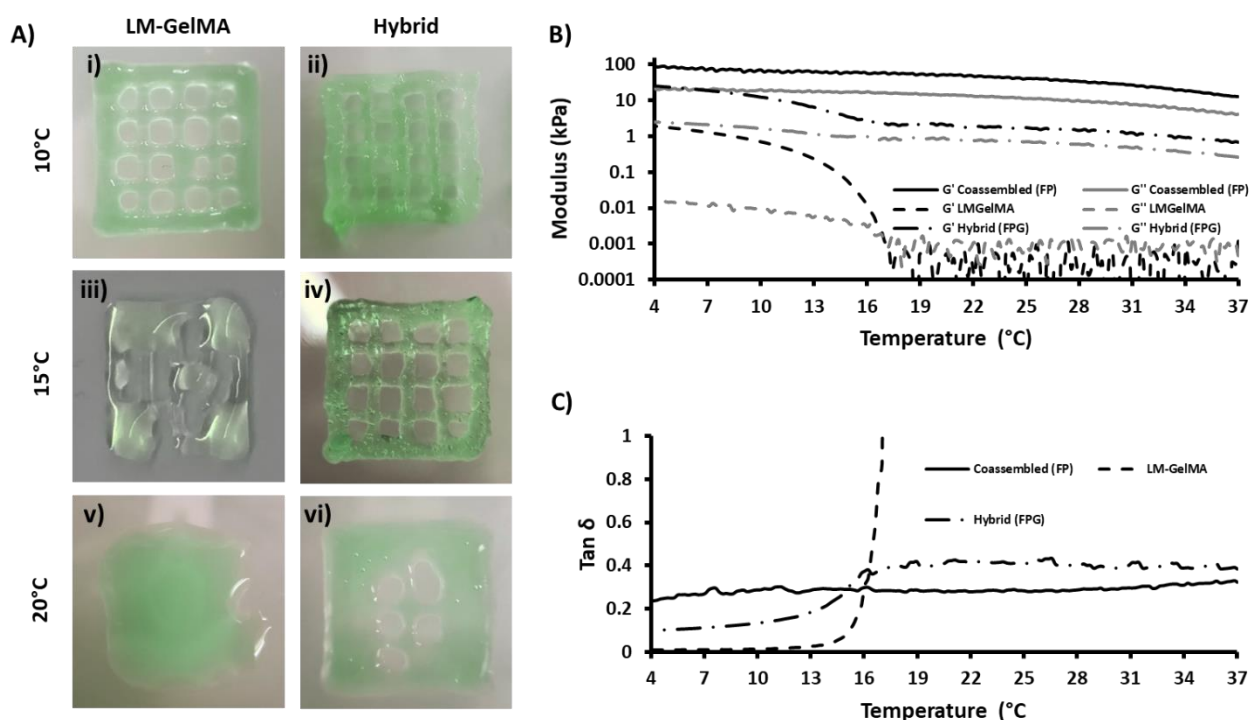


Figure 8-5 – Investigation into material printability (A) Images of LM-GelMA (left column) and Hybrid (right column) printability through printing of grid (1cm in length) at 10°C, 15°C and 20°C, (B) Thermoelastic properties of non-crosslinked materials acquired through oscillatory rheology, (C) Loss tangent as a function of temperature.

8.3.5.2 *Optimising Printability Through Temperature Control*

Printability tests were performed following characterisation of material thermo-responsive viscoelastic properties. All materials were printed at 10°C, 15°C, and 20°C to determine bioink potential (**Figure 8-5A**). Following printing, the coassembled material was unable to maintain shape fidelity under any of the tested conditions and therefore was excluded from all subsequent tests (**Supplementary Figure S - 11C**). Alternatively, LM-GelMA demonstrated relatively good prints at 10°C following which material printability reduced as temperature increased (**Figure 8-5A**). The FPG-Hybrid material was found to produce the best prints out of all the materials, with optimal printing occurring at 15°C (42 kPa) (**Figure 8-5A**). The FPG-Hybrid material-maintained printability at 10°C, however, prints were found to be less uniform and required greater pressure (66 kPa), while at 20°C the FPG-Hybrid was observed to be ineffective at maintaining printed geometry (**Figure 8-5A**). These results echo previous findings using similar gelatin inspired blends.³⁸⁶ Hydrogel network is likely to be disrupted during the printing process which may alter mechanical properties; however, care was taken to ensure sufficient recovery such that a self-supported network is maintained. Despite this possible mechanical disruption, hydrogels were found to remain stable past 4 weeks of simulated culture (PBS, 37°C, **Supplementary Figure S - 12**). Further investigation is required to comprehensively analyse the effect of printing on resultant mechanical characteristics.

8.3.6 *Investigation of Cytocompatibility*

Cytocompatibility of the developed bioink and associated bioprinting process was determined through bioprinting of Primary Myoblast-containing bioinks under predetermined optimal conditions (10°C, ~30 kPa for LM-GelMA, and 15°C, ~40 kPa for FPG-Hybrid). Grid-like structures were printed onto cooled plates and immediately crosslinked under UV light followed by immersion in proliferative media. Interestingly, the addition of cells was found to influence shape fidelity, with some grids demonstrating early erosion (**Supplementary Figure S - 13**). However, following initial erosion over ~1h, constructs remained stable and robust over the course of cell-culture experiments (2-weeks). This observation indicates that cells may be interfering with the crosslinking process and therefore warrants further investigation into cell seeding density and optimisation of printing processes, however this lies

outside the scope of this thesis. A 2D control was also prepared through seeding of primary myoblasts onto tissue culture plastic.

8.3.6.1 Viability

Following 24h and 72h culture, samples were stained with Calcein AM (green) and ethidium homodimer (red) to determine the proportion of live and dead cells respectively (**Figure 8-6A**). Cells were imaged using fluorescence microscopy, and the number of live and dead cells were determined through ImageJ analysis. Following 24h, the 2D control demonstrated the highest viability (97.3%) while printed LM-GelMA, and FPG-Hybrid samples demonstrated significantly lower viabilities of 86.7% ($p = 0.0056$) and 85.9% ($p = 0.0032$), respectively (**Figure 8-6B i**). However, following 72h culture, all samples demonstrated comparable viabilities (>98% viability for all samples) (**Figure 8-6B ii**), indicating that although the printing process results in an initial decrease of cell viability, both bioinks support cell proliferation following crosslinking. These results demonstrate the cytocompatible nature of both materials for myoblast bioprinting applications.

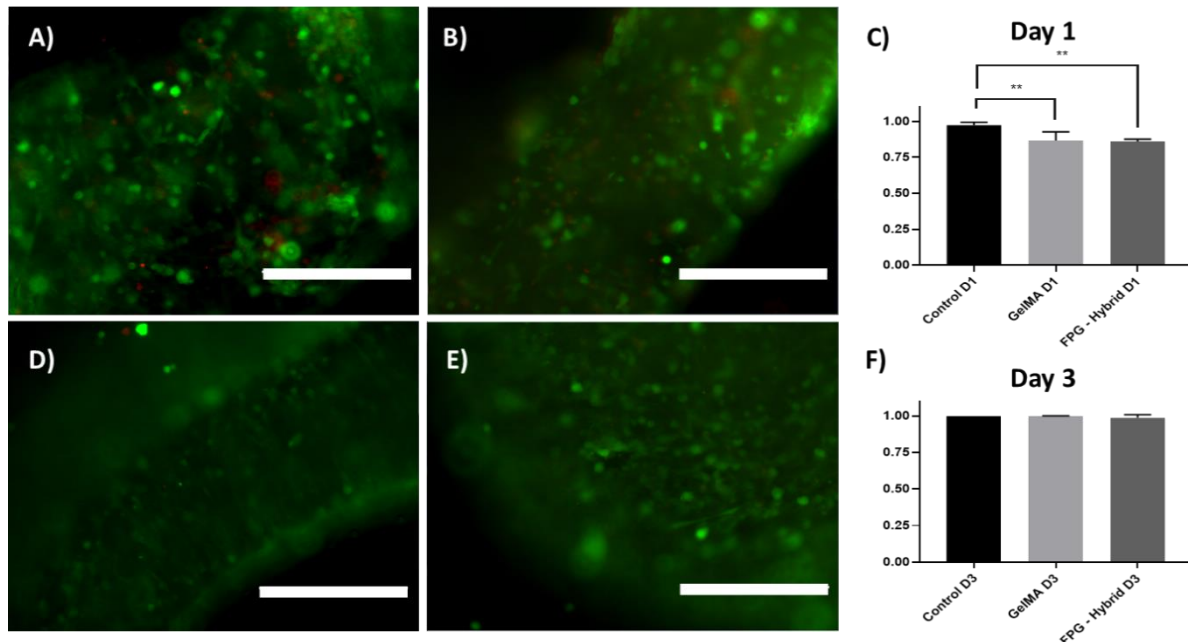


Figure 8-6 – Representative-images of Live/Dead stain (A) LM-GelMA 24 h (B) FPG-Hybrid 24 h (D) LM-GelMA 72 h (E) FPG-Hybrid 72 h. Viabilities of primary skeletal myoblasts on 2D control, or 3D-printed LM-GelMA and FPG-Hybrid at (C) 24h and (F) 72 h.

8.3.6.2 Differentiation

Following 7 days of differentiation, cells were observed to form aligned fibres. Cellular fusion was also observed resulting in the formation of multinucleated bundles. After 14 days of differentiation, most of the cells had migrated to the surface of the bioink (**Figure 8-7**) as seen in similar studies within our laboratories (unpublished data). Evidence of multinucleated myotube formation, combined with high cell viability, highlights the potential for mature muscle tissue formation using these bioinks.

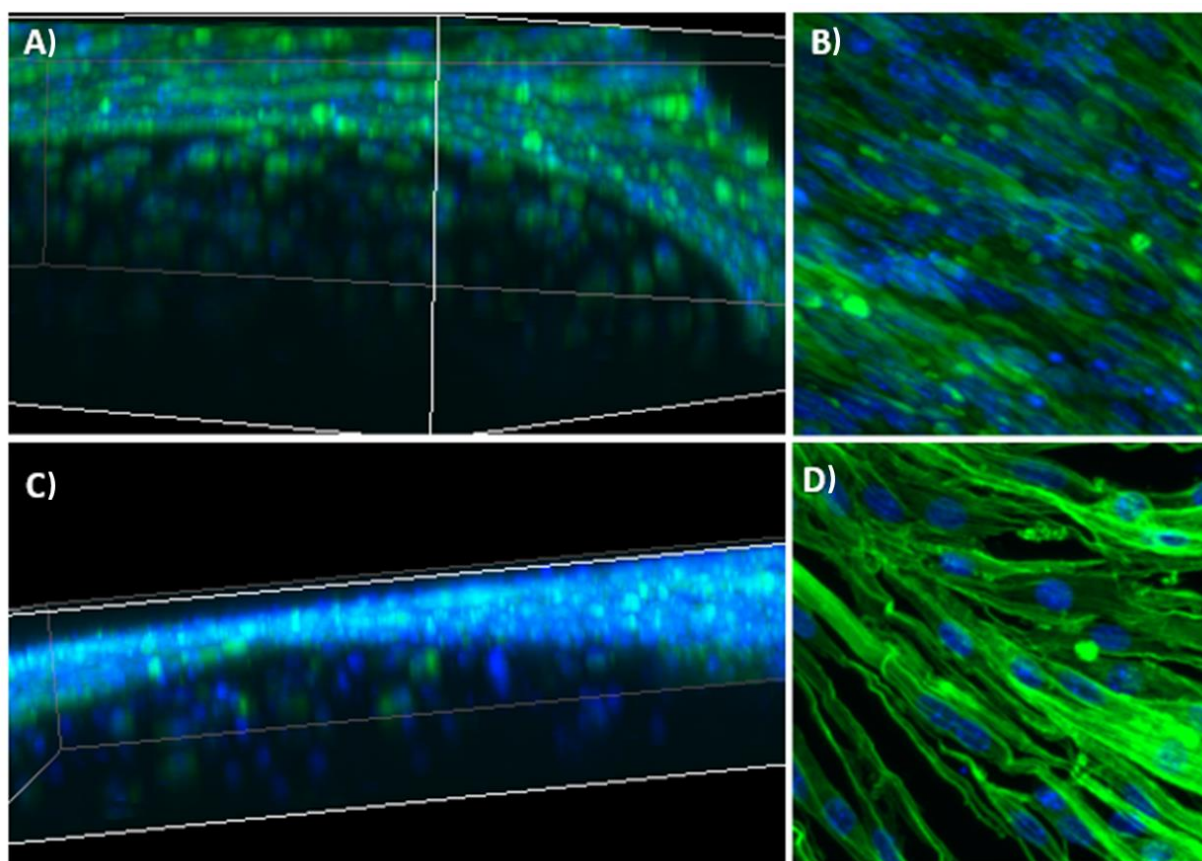


Figure 8-7 – Representative confocal images of 3D printed samples after 14 days of differentiation, majority of primary myoblasts are shown to migrate to sample surface and fuse to form multinucleated bundles. (A) LM-GelMA 3D Projection, (B) LM-GelMA surface, (C) FPG-Hybrid 3D Projection, (D) FPG-Hybrid surface.

Following confocal analysis, SEM analysis was performed to observe cell-material interactions. Grids were fixed with formalin and stained with osmium tetroxide, before being dried and gold-coated prior to analysis. Extensive myotube formation is evident in both samples (**Figure 8-8A, B**), moreover both samples support formation of myotube bundles (indicated by arrows) (**Figure 8-8C, D**), confirming the development of mature myotubes.

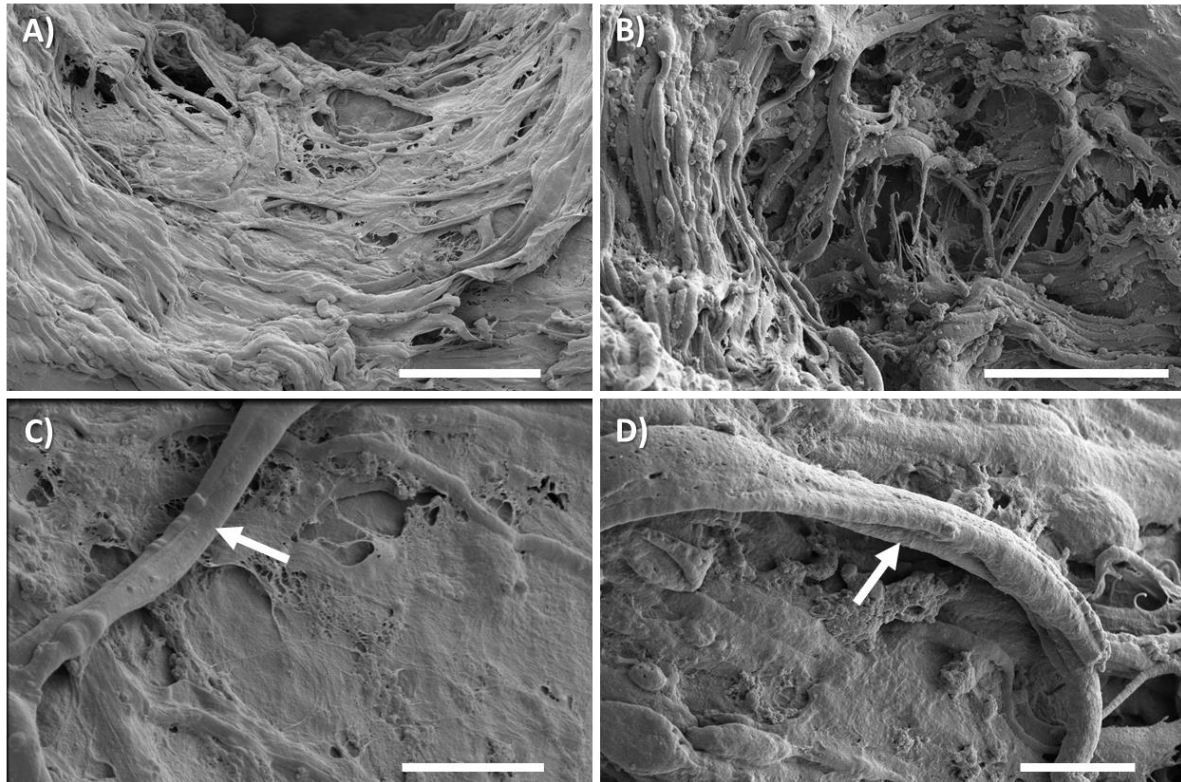


Figure 8-8 – SEM analysis of myotube formation on A) LM-GelMA bioink, B)FPG-Hybrid bioink, C)myotube bundle formation on LM-GelMA bioink, and D) Myotube bundle formation on FPG-Hybrid bioink. Arrows showing cell myotube formation. Scalebar: Top:50 μ m Bottom: 10 μ m

8.4 Conclusion

Advanced tissue development demands precise control over the deposition of cells and signals within a spatially defined 3D construct. However, currently, there is immense difficulty between recapitulating the biological complexities of the native ECM whilst simultaneously providing materials with mechanical properties required for cytocompatible printing (low temperature, physiological pH, low pressure). Precise control over the cell microenvironment is key for successful regulation of cell proliferation, differentiation, and migration, while high mechanical tunability allows for enhanced control over material printability and allows for control over mechanical cues experienced by cells. The design of specific cell attachment sites into SAPs and further incorporation into effective bioinks via melding with LM-GelMA is the focus of this chapter. Synergistic SAPs, Fmoc-FRGDF and Fmoc-PHSRN, were coassembled and combined with LM-GelMA. The coexistence of peptide and macromolecule provides nano- through macroscale features and proves to be of benefit through the enhancement of bioprintability. Encapsulated primary myoblast proliferation and differentiation were supported with high cell viability throughout printing and culture. Materials were extensively characterised to determine mechanisms of assembly, resultant structures, and effect on printability, with resultant hybrid bioinks demonstrating fibrous morphology (fibril diameter 15 nm), photo-curing (8 minutes), shape fidelity and longevity under culture conditions (over 4 weeks). GelMA-SAP hybrid bioinks demonstrate efficacy as a bioinks, future studies into the modularisation of GelMA-SAP hybrids to include alternative cell attachment motifs will be explored, as well as gene expression in differing materials.

Chapter Nine:

NEURAL BIOINK

9.1 Preview

This final experimental chapter intends to demonstrate the versatility and efficacy of the developed bioink toolkit. Explicitly, this chapter incorporates an alternate SAP sequence, Fmoc-DIKVAV, containing the laminin cell attachment motif IKVAV. Once again, this Fmoc-SAP sequence is incorporated within a LM-GelMA blend to develop an advanced hybrid bioink blend. We investigate the ability of this toolkit to support neural-cell growth and differentiation through seeding of rat cortical neurospheres. We hypothesise that the hybrid bioink containing the IKVAV-sequence will demonstrate unique mechanical properties, with trends similar to those observed in the previous chapter. We anticipate that the hybrid bioink will enhance neural cell viability and morphology, supporting early cell maturation. Material physical properties are extensively investigated through rheology, electron microscopy, small-angle X-ray scattering, and printability, while material bioactivity is assessed through analysis of cell viability and morphology. Results show highly similar mechanical properties to those observed in **Chapter 8**, while biologically, the material is found to promote rat cortical neurosphere viability, with noticeable differences in cell morphology between the hybrid material and the LM-GelMA control.

Contribution of the candidate:

- Concept development and experimental design
- Key contributor to protocol development
- Primary researcher for acquisition and analysis of all data
- Prepared proposal, successful Funding for Synchrotron Experiments (ANSTO, AUS)
- First Author of manuscript.

Publications relevant to this chapter

Boyd-Moss, M., N., Firipis, K., Quigley, A., Dekiwadia, C., Long, B., Cichocki, A., Kapsa, RMI., Nisbet, D., Williams, R. (2019) ‘SAP Inspired Hybrid Bioinks for Neural Tissue Engineering Applications’. **Manuscript in preparation.**

Abstract

The intrinsic limitation of the central nervous system to self-repair presents substantial difficulty in the field of tissue engineering. Bioprinting offers a potential avenue for enhanced tissue regeneration; however, the intricate balance between material printability and biological functionality has yielded few suitable bioinks. This balance is particularly precarious in neural tissue bioprinting applications, where cells necessitate soft biomaterials, yet extrusion printing processes generally benefit from materials of higher viscosity. Therefore, the development of a bioink which presents high mechanical tunability and is highly decorated with bioactive cell-specific motifs would be of substantial advance to the field. Fmoc-SAPs have been widely used in tissue engineering applications, with particular success in neural tissue engineering. However, these materials lack permanent bonds resulting in swelling and eventual dissociation in media. Alternatively, a gold-standard material in bioprinting applications, GelMA, is highly mechanically tuneable, yet lacks ease of biological tunability. Here, we combine these two materials to develop a hybrid bioink which draws on favourable properties from both materials, enabling high mechanical and biological tunability. Mechanical properties of bioinks are assessed regarding nano through to macromorphology, viscoelastic properties, and printability (as assessed through ability to print grid-like constructs); while biological properties are investigated through analysis of seeded and encapsulated rat cortical neurosphere viability and morphology. Results show enhanced printability and ability to support rat cortical neurospheres. Importantly, this chapter confirms the efficacy of the developed bioink toolkit and highlights its promise for bioprinting applications.

9.2 Introduction

Central Nervous System (CNS) repair presents a substantial challenge to tissue engineering applications owing to the inherently limited ability of self-repair in these tissues.³⁸⁷ Currently, disorders of the nervous system are estimated to affect over a billion people worldwide, with the prevalence only increasing owing in part to the increasing aging population.³⁸⁸⁻³⁸⁹ There are limited treatment options for many of these conditions, with some treatments only providing systematic relief.³⁹⁰ Cell therapy through the introduction of stem cells to damaged tissue has been proposed as a potential avenue for neural tissue regeneration,³⁹⁰ however cells alone do not provide an adequate environment conducive to functional tissue regeneration, with recent neural tissue engineering approaches focusing on the inclusion of biomimetic scaffolds to encapsulate cells and provide biochemical and mechanical cues required for controlling cell fate and driving tissue regeneration.³⁹¹ Despite this, the difficulty remains in controlling material architecture and developing printed constructs with a high degree of control over 3D shape.³⁹²

Bioprinting offers unique advantages to tissue engineering applications, allowing for the deposition of cells, structure and signals within a highly controlled 3D organisation.¹⁶⁰ Furthermore, effective bioinks used in bioprinting applications help shield cells from shear stress encountered in printing processes, and allow for cell migration, proliferation, differentiation and eventual tissue regeneration.^{11, 188} Despite the potential offered by bioprinting in neural tissue engineering applications, the field is still critically limited in ability to form soft, biocompatible bioinks which maintain good printability while providing signals to cells spatially and temporally.¹¹ Therefore, the development of new bioinks using novel materials would be of substantial benefit to neural tissue engineering applications.

GelMA-based bioinks have been extensively used in bioprinting applications and have seen substantial success in vasculature, muscular and cartilage engineering applications.^{68, 216, 393-396} Developed through the modification of gelatin with functional methacryloyl groups, GelMA presents unique advantageous over conventional gelatin for bioprinting applications.³⁵⁶ Particularly, GelMA allows control over DoF enabling a high degree of mechanical tunability both pre and post-crosslinking,

enabling enhanced mechanotransduction.³⁷⁷⁻³⁷⁸ Furthermore, GelMA retains collagens RGD attachment motif, allowing for cell attachment through integrin binding, and subsequently allowing for targeted cell adhesion.³⁶⁶ However, GelMA is restricted in its ability to target other cell domains; with recent bioprinting approaches incorporating additional biological functionalisation to drive neural cell differentiation with limited success.³⁹⁷ GelMA is also limited in ability to engineer specific nano-/microarchitectures, with recent efforts to engineer nanofibrous morphologies relying on the use of external deposition techniques such as electrospinning.³⁷⁶ Therefore, combining GelMA with a highly nanostructured and biologically tuneable material may promote the development of a truly advanced bioink.

Self-Assembled peptides have recently found substantial success in bioprinting applications.^{189-191, 200, 398-400} These materials are characteristic in their ability to form useful hierarchical structures from small building blocks and boast high water content (~99%), ease of sequence customisation, and high similarity to biological structures.^{7, 128} Fmoc-SAPs are a subclass of SAPs which take advantage of π - π stacking between aromatic Fmoc groups, allowing for the development of short, SAP building blocks of smaller length than conventional SAPs.⁸⁻⁹ This enables more straightforward modification of peptide sequence and ultimately facilitates easier mechanical and biological tuning.⁹ Fmoc-DIKVAV is an ECM inspired peptide which self-assembles through π - β assembly to form long biomimetic nanofibrils decorated with the laminin epitope IKVAV.¹⁴⁰ Despite Fmoc-DIKVAV's success in neural tissue engineering applications,^{141, 380} similar achievements have not yet been attained in neural bioprinting applications, owing in part to the poor shear resistance of Fmoc-SAPs (*See Section 8.3.4.2*). Therefore, the combination of this material with a covalently crosslinkable material may alleviate the associated shortcomings of this material; increasing SAP versatility in bioprinting applications.

In this chapter, a hybrid bioink is developed through the furthering of understandings gained in **Chapter 8**. Specifically, LM-GelMA is combined with Fmoc-DIKVAV during the assembly process to yield a hybrid material which draws from aspects of both bioinks. The hybrid material demonstrates enhanced printability as observed via rheology and printability tests with unique thermal dependent characteristics. Nanofibrils are present in the hybrid as observed via TEM and CryoSEM analysis.

Material conformational changes are also monitored via SAXS before cytocompatibility is investigated through seeding and bioprinting of rat cortical neurospheres. Our results show the efficacy of this bioink toolkit for neural tissue engineering applications and highlight the potential of this bioink system as a modular, tissue-specific toolkit.

9.3 Results and Discussion

9.3.1 Formation of Bioinks

Three peptide-based bioinks were developed. Firstly, a laminin-inspired Fmoc-SAP (Fmoc-DIKVAV), replete with a neurologically important attachment motif, IKVAV, was self-assembled under physiological conditions (pH 7.4) via a pH switch method.¹⁴⁰ A second bioink was developed through low-degree (18%) methacrylation of gelatin to LM-GelMA. LM-GelMA can undergo photo-crosslinking once subjected to UV irradiation in the presence of a photoinitiator, which allows for controlled and triggered gelation post-printing. A third bioink was developed through the incorporation of LM-GelMA during Fmoc-DIKVAV self-assembly. This hybrid material demonstrates properties owing to both materials, namely, the ability to present tuneable and biologically recognisable sequences (through peptide self-assembly); and the potential for photo-crosslinking via UV exposure. Here forth, we term this bioink DIKVAV-Hybrid.

Hydrogelation of Fmoc-DIKVAV resulted in the rapid (<2h) formation of an opaque gel which was stable following inversion (**Supplementary Figure S - 14**). Contrastingly, LM-GelMA resulted in the formation of a clear solution which presented as a gel at 4°C and as a fluidic solution at room temperature (23°C, **Supplementary Figure S - 14**). Finally, gelation of DIKVAV-Hybrid containing both Fmoc-DIKVAV and LM-GelMA resulted in the formation of an opaque gel at room temperature (**Supplementary Figure S - 14**).

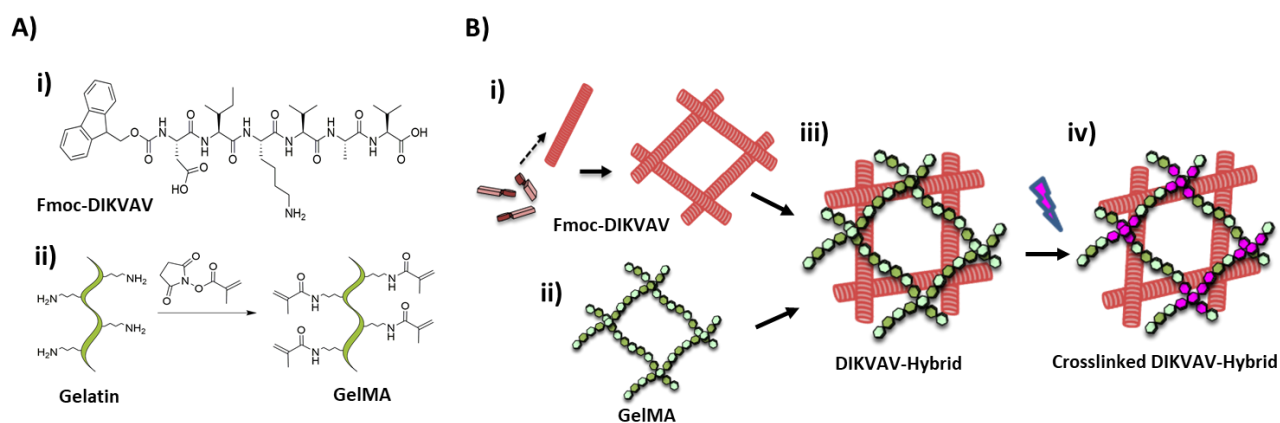


Figure 9-1 – Schematic of hydrogel assembly (A) Chemical structure of i) Fmoc-DIKVAV and ii) GelMA (B) Schematic representation of assembly mechanisms showing self-assembly of Fmoc-SAPs into fibrils in the presence of gelatin methacryloyl before subsequent photo-crosslinking of the network.

9.3.2 Investigation of bioink Micro-/nano-architecture

9.3.2.1 Fibril Topology Observed via TEM

To verify the structural morphology of the underlying assemblies and networks, a series of material characterisation techniques were performed. TEM showed the nanoscale structures formed for each material before photo-crosslinking (**Figure 9-2A-C**). The self-assembly of Fmoc-SAPs into nanofibers is found to be maintained in the Fmoc-DIKVAV sample (**Figure 9-2A**) with nanofiber morphology similar to previous investigations.¹⁴⁰ Alternatively, no fibrous morphology was evident in LM-GelMA samples (**Figure 9-2B**), rather material aggregates are observed throughout the sample. DIKVAV-Hybrid bioinks formed fibrous structures similar to those evident in Fmoc-DIKVAV samples alone. As these fibrils are not evident in LM-GelMA samples, they can be attributed to the self-assembly of Fmoc-DIKVAV within the LM-GelMA environment, demonstrating maintenance of self-organisation in the DIKVAV-Hybrid bioink (**Figure 9-2C**). Unfortunately, the requirement for TEM samples to be diluted before imaging limited their ability to image photo-crosslinked samples. ImageJ analysis of fibril diameter found 11.1 nm ($\sigma = 0.209$) and 11.0 nm ($\sigma = 0.213$) for Fmoc-DIKVAV alone and DIKVAV-Hybrid samples respectively.

9.3.2.2 Network Morphology Assessed via CryoSEM

CryoSEM shows the hydrated microscale structure of materials before and after subjection to UV irradiation (**Figure 9-2D-I**). Here, both photo-crosslinked and non-crosslinked samples are investigated in a hydrated state without dilution. CryoSEM analysis of Fmoc-DIKVAV bioinks shows a highly fibrous network both before and after subjection to UV irradiation (**Figure 9-2D, G**). LM-GelMA is found to have a highly porous structure before UV exposure (**Figure 9-2E**); this structure is generally maintained after photo-crosslinking, with some slight observable differences in perceived pore size and network order (**Figure 9-2H**). DIKVAV-Hybrid demonstrates a network morphology which is highly similar to that of LM-GelMA both before and after UV exposure (**Figure 9-2F, I**). Fibre-like structures are observed within pores in both LM-GelMA and DIKVAV-Hybrid samples, however, despite a perceived increase in fibre number within the DIKVAV-Hybrid bioink; this cannot be solely attributed to the presence of Fmoc-DIKVAV without further quantification. Interestingly in respect to the

DIKVAV-Hybrid, the overarching nanoscale structure as observed in TEM analysis can be attributed to the presence of Fmoc-DIKVAV, while through CryoSEM analysis, the predominant microarchitecture and network orientation are reminiscent of that seen in LM-GelMA.

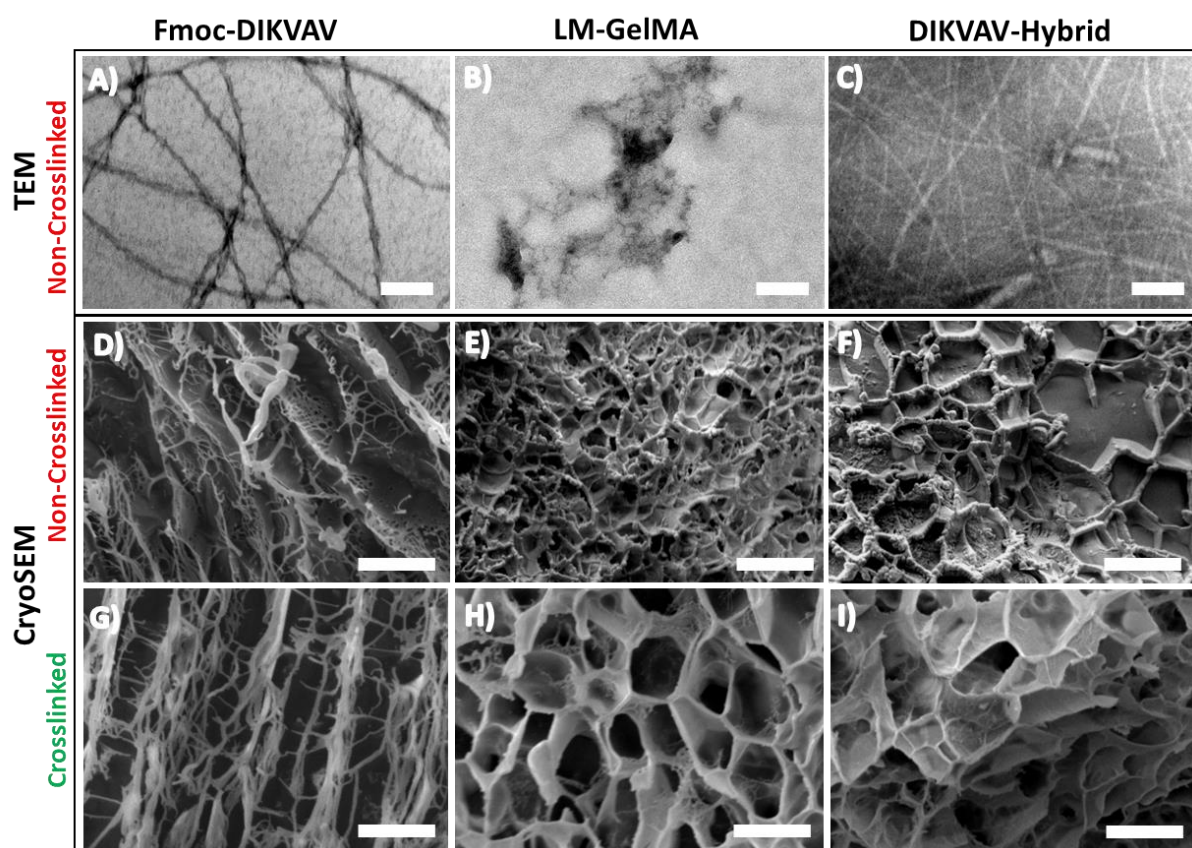


Figure 9-2 – Observation of hydrogel network morphology (A-C) TEM analysis of material nanostructure Scale bar (100 nm), (D-F) CryoSEM Analysis of network microstructure before UV exposure, and (G-I) CryoSEM analysis of network microstructure following UV exposure. From left to right: Coassembled Fmoc - FRGDF/Fmoc-PHSRN, LM-GelMA, and FPG-Hybrid samples. Scale bar (10 μ m)

SAXS curves were obtained for all samples and used to assess nanostructural differences between bioink samples. Fmoc-DIKVAV curves supported the cylindrical nature of the nanofibrils as scattering curves provided a q^{-1} dependence at low q indicating elongated cylindrical structures (**Figure 9-3A**). Alternatively, crosslinked and non-crosslinked LM-GelMA and LM-GelMA/DIKVAV bioinks did not sufficiently satisfy the cylindrical model; therefore, these samples were fitted to shape independent models.

IFT analysis was performed on Fmoc-DIKVAV scattering curves to determine probable radius through the implementation of the $P(r)$ function (SASview) (**Figure 9-3B**). TEM observations showed fibril length was outside the q range of SAXS analysis and therefore our focus was attuned to the determination of average fibril radius. As the fibrillar nature of Fmoc-DIKVAV bioinks has been confirmed via TEM and CryoSEM analysis, the maximum $P(r)$ value acquired during IFT calculations was attributed to an average fibril radius. These calculations indicate average fibril diameters of 11.1 nm ($r = 55.7 \text{ \AA}$) for 5 mg/mL Fmoc-DIKAV, supporting observations gained through similar assemblies of higher concentration.¹⁴⁰ SAXS analysis of nanofibrous Fmoc-DIKAV radius is in accordance with TEM observations.

Crosslinked and non-crosslinked conditions were investigated for LM-GelMA and DIKVAV-hybrid bioinks. As scattering curves did not adequately fit a cylindrical model, curves were fitted to shape independent models. Bioinks were analysed with respect to mass fractal dimension (**Figure 9-3C**); providing insight into local polymer configuration³¹³. The mass fractal dimension was determined for LM-GelMA and DIKVAV-Hybrid bioinks over a mid q range (**Figure 9-3C**) and is described by **Equation 7-1**. (*See Section 7.3.1 for more detail*)

Calculation of mass fractal dimension for LM-GelMA and DIKVAV-Hybrid samples revealed a low value of 1.74 ($\pm <1\%$) for LM-GelMA prior to crosslinking, increasing to 2.01 ($\pm <1\%$) for crosslinked LM-GelMA. Similarly, DIKVAV-Hybrid demonstrated a comparable trend, demonstrating a d_m of 2.02 ($\pm <1\%$) and 2.21 ($\pm <1\%$) for non-crosslinked and crosslinked conditions respectively.

Assembly mechanisms were also investigated via CD and FT-IR spectroscopy, however, in both cases, material proprieties were dominated by GelMA related peaks (Supplementary Figure S - 15).

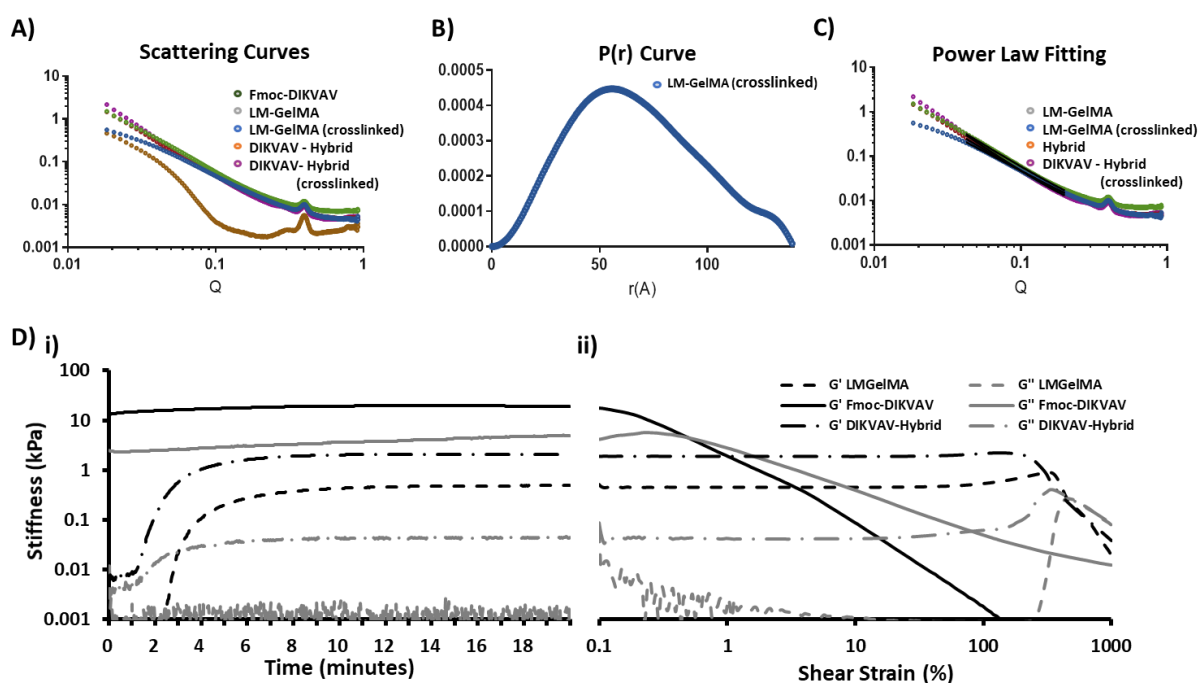


Figure 9-3 – Investigation of hydrogel nanostructure and viscoelastic properties (A) SAXS curves of Fmoc-DIKVAV, LM-GelMA, and DIKVAV-Hybrid Samples (B) Resultant probability of average fibril radius modelled using $P(r)$ function (SASView), (C) Fitting through power law model (SASVIEW) (D) Rheological Analysis of i) *In situ* Crosslinking and ii) post-crosslinking material resistance to shear strain.

Rheological analysis provides insight into material viscoelastic properties. **(Figure 9-3D)** Parallel-plate oscillatory rheology was employed to analyse change in material viscoelastic properties during *in situ* crosslinking. Briefly, materials were loaded into the rheometer (37°C) and analysed for 1 minute at a constant shear rate (0.1%) before UV activation; this allowed materials to reach stable viscoelastic characteristics before subjection to crosslinking. After 1 minute, UV radiation was activated at 4.5 mW/cm² and remained activated until completion of analysis (10 minutes). As expected, Fmoc-DIKVAV demonstrated a storage modulus of ~20kPa and did not demonstrate any significant increase in stiffness after UV exposure. Alternatively, LM-GelMA bioinks demonstrated a significant increase upon UV exposure, with storage modulus increasing from ~0.04 kPa to ~1 kPa. DIKVAV-Hybrid samples increased in storage modulus by an order of magnitude upon UV exposure, from an initial storage modulus of ~0.8 kPa before UV exposure to ~10 kPa post-crosslinking. This increase in stiffness confirms maintenance of photo-crosslinking in the DIKVAV-Hybrid sample.

Analysis of G' rate of change was once again used to determine the point of crosslinking completion and was defined as the point where G' rate of change dropped below 0.1% s⁻¹. Similar to observations made in FPG-Hybrid analysis, LM-GelMA required the longest time to reach crosslinking completion, requiring approximately 8.2 minutes of crosslinking (9.2 minutes into testing). Alternatively, DIKVAV-Hybrid required approximately 6.7 minutes of crosslinking to reach completion (7.7 minutes into testing). To maintain consistency between bioink toolkits, 500 seconds (8.33 minutes) at 4.5 mW cm⁻² was once again selected for all samples in subsequent crosslinked experiments **(Supplementary Figure S - 16A).**

9.3.3 Material Printability and Thermoresponsive Viscoelasticity

Thermoresponsive viscoelastic properties were tested for each bioink using parallel-plate rheology (**Figure 9-4A**). Here, a temperature sweep was performed on samples starting at an initial temperature of 37°C and sweeping at a constant rate to 4°C. Fmoc-DIKVAV did not demonstrate a significant increase in viscosity upon temperature change. Alternatively, LM-GelMA demonstrated a significant increase in viscosity as temperature decreased. DIKVAV-Hybrid samples presented as a hydrogel at all tested temperatures, as indicated by a storage modulus of greater magnitude than loss modulus; and demonstrated a more gradual and controlled increase in stiffness as temperature decreased. The stiffness of DIKVAV-Hybrid samples (5.7 kPa at 4°C) was also observed to be greater than that of LM-GelMA alone (~1.9 kPa at 4°C), here it is likely that the peptide fibrils act as a composite system, exaggerating entanglements and resulting in enhanced stiffness increase.

The loss tangent can be calculated as G''/G' and provides insight into material state. Recently, a landmark study by Gao et al. found that a loss tangent within the window of 0.25 and 0.45 provides optimal printability.³⁸⁶ The loss tangent was determined for each material between 4°C and 37°C (**Figure 9-4B**). Despite Fmoc-DIKVAV eliciting a loss tangent bordering this window ($\delta \approx 0.25$) for all tested temperatures, printability is likely to be reduced as demonstrated in the previous chapter (**Chapter 8**), as Fmoc-DIKVAV alone provides very little resistance to shear stress (**Figure 9-3D**). Contrastingly, LM-GelMA bioinks elicit a very steep change in loss tangent at the point of sol/gel transition; as a result, this bioink would be difficult to maintain within this window, with slight temperature fluctuations greatly effecting material printability and required printing pressures. DIKVAV-Hybrid bioinks provide a compromise between both bioink samples, and as a result, provide a flatter slope compared to LM-GelMA alone. This DIKVAV-Hybrid bioink remains in this window from approximately 17°C to 20°C, and therefore, provides a larger temperature range to maintain good printability. This coupled with the bioinks ability to form covalent crosslinks and resist strain forces highlights its efficacy in bioprinting applications.

To further investigate material printability, all three bioinks (Fmoc-DIKVAV, LM-GelMA, and DIKVAV-Hybrid) were placed into 3 mL cartridges for printability tests. Three temperatures were

investigated for bioprinting as determined most suitable from analysis of thermodependent viscoelastic trends. Specifically, 10°C, 15°C and 23°C (room temp) were selected as printing temperatures and cartridge temperature was verified using a thermal imaging infrared camera (FLIR, Extech*). Fmoc-DIKVAV alone was unable to hold its shape after printing, even at the lowest temperature, resulting in the formation of large ‘pools’ of solution (**Figure 9-4C i**), and therefore, was excluded from further printability tests. Alternatively, LM-GelMA demonstrated good printability at 10°C (**Figure 9-4C ii**) in accordance to findings in the previous chapter (**Chapter 8**), Material printability was substantially worse in the 15°C LM-GelMA and 23°C LM-GelMA samples (**Supplementary Figure S - 16C**). This observation is in agreeance with rheological data, which indicates a steep and rapid increase in loss tangent coupled with decreasing viscosity at these temperatures (**Figure 9-3D**). The DIKVAV-Hybrid bioink maintained the potential to print at 10°C; however, the print demonstrated relatively poor shape fidelity (**Supplementary Figure S - 16D**). Upon increasing the temperature to 15°C, the material demonstrated optimal printing conditions, resulting in the greatest maintenance of shape fidelity out of all the samples (**Figure 9-4C iii**). Further increasing the temperature to 20°C drastically reduced the materials ability to maintain suitable shape fidelity, likely due to diminishing storage moduli at this temperature (**Supplementary Figure S - 16C**). Constructs printed at optimal temperatures for each bioink are displayed in (**Figure 9-4C**). DIKVAV-Hybrid at 15°C demonstrated enhanced printability compared to both LM-GelMA and Fmoc-DIKVAV, however, required slightly increased pressure (~50kPa). Both LM-GelMA and DIKVAV-Hybrid demonstrated the ability to form 3D grids consisting of multiple layers with both bioinks capable of holding consistent shape fidelity during printing and following crosslinking. Our results echo the findings of Gao et al.,³⁸⁶ and further reinforce observations gained in the previous chapter (**Chapter 8**) where similar hybrid assemblies containing LM-GelMA demonstrated optimal printability at 15°C, while LM-GelMA alone printed best at 10°C.

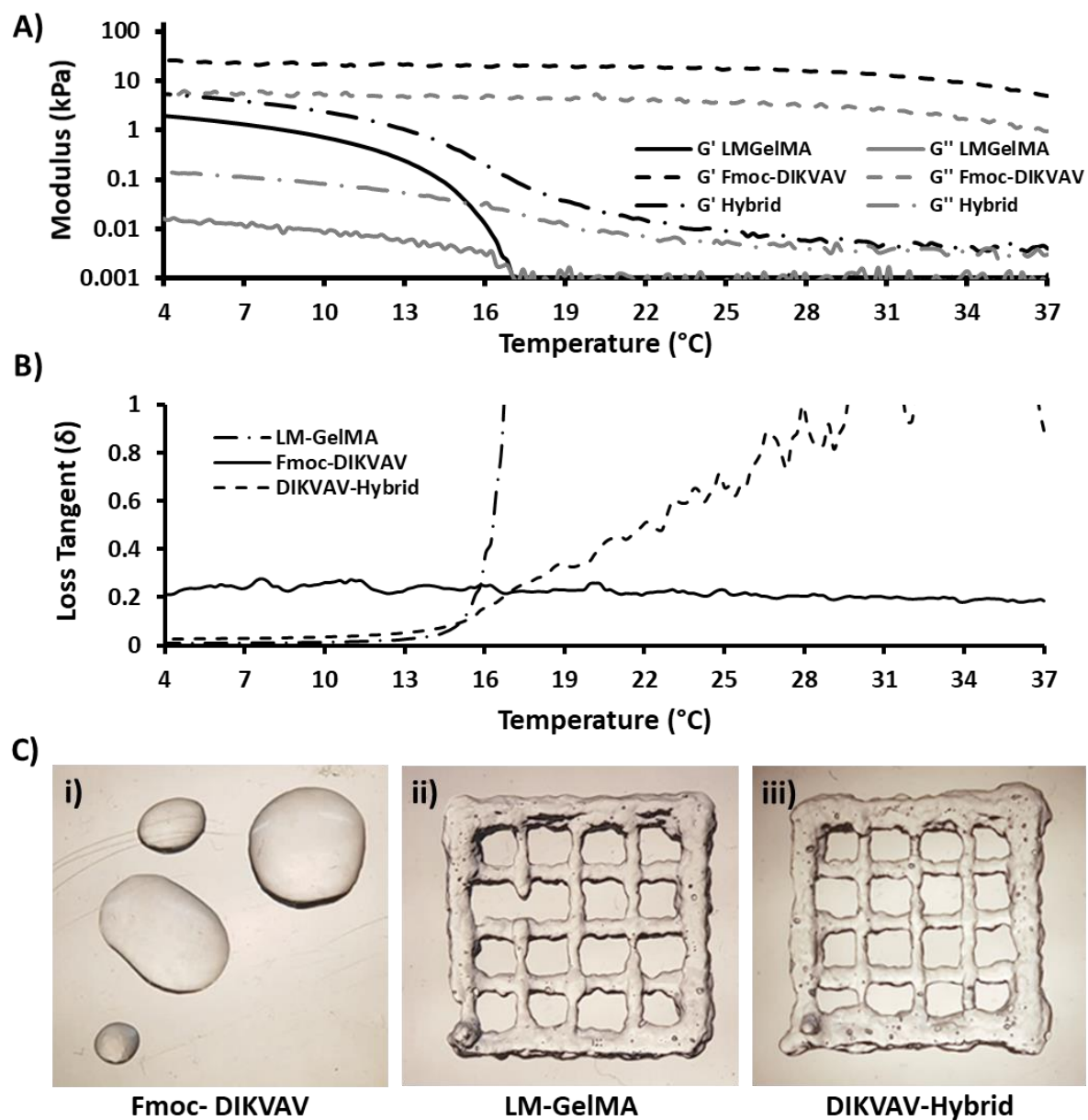


Figure 9-4 – Investigation into material printability (A) Thermoelastic properties of non-crosslinked materials acquired through oscillatory rheology, (B) Loss tangent as a function of temperature, (C) Images of Optimal material printability through printing of i) Fmoc-DIKVAV (10°C), ii) LM-GelMA (10°C), and iii) DIKVAV Hybrid (15°C).

Print geometries of differing strut spacings were designed to test the ability of the developed bioink further. Here, three grids are designed; the first incorporates 2.5 mm strut spacing, the second reduces this to 1.5 mm, and finally, the third reduces this distance further to 1 mm. (**Figure 9-5**) The reduction in gap allows for analysis of material regularity as a further test of material printability. Here a 25G (260 μm) nozzle was used. To investigate the effectiveness of geometry alteration, grid types are printed and crosslinked for 500 seconds before being cultured under simulated conditions (PBS, 37°C incubation) for 4 weeks. In all cases, the DIKVAV-Hybrid material printed well, producing complete multi-layer grids with consistent strut spacing and thickness (**Figure 9-5**). Furthermore, all geometries were found to swell following 10 minutes of simulated culture, resulting in a core region and a feathered fibrous outer region.

Despite some loss of the feathered region following 9h culture, DIKVAV-Hybrid bioinks were found to remain stable over 4 weeks (**Supplementary Figure S - 17**), with the majority of swelling occurring in the first 10 minutes and no significant swelling evident at later time points.

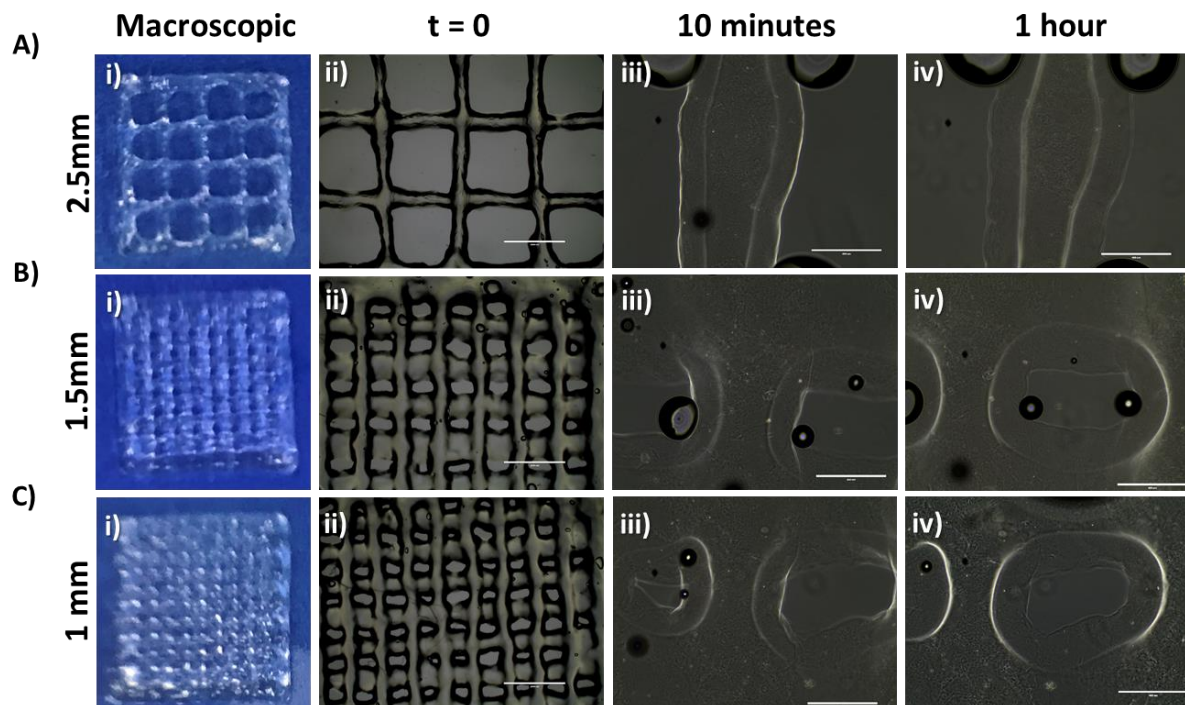


Figure 9-5 – Images of Print Geometries (i) before PBS addition, (ii) immediately following PBS addition, (iii) 10 minutes following PBS addition, and (iv) 1 hour following PBS addition for prints of (A) 2.5 mm strut spacings, (B) 1.5 mm Strut Spacings, and (C) 1 mm strut spacings. Scalebar 2000 μm (ii) and 400 μm (iii, iv)

Further analysis was completed to determine the nature of the feathered and core region. FITC fluorescently-labelled GelMA was added during bioink synthesis to distinguish GelMA regions. Gels were once again printed as before, and strut morphology analysed under fluorescence microscopy. Here, a clear localisation of GelMA to printed strut-cores was observed. Therefore, the feathered region is likely to be SAP fibrils presented on the surface, as is confirmed through GelMA isolation in strut core. **(Figure 9-6)**

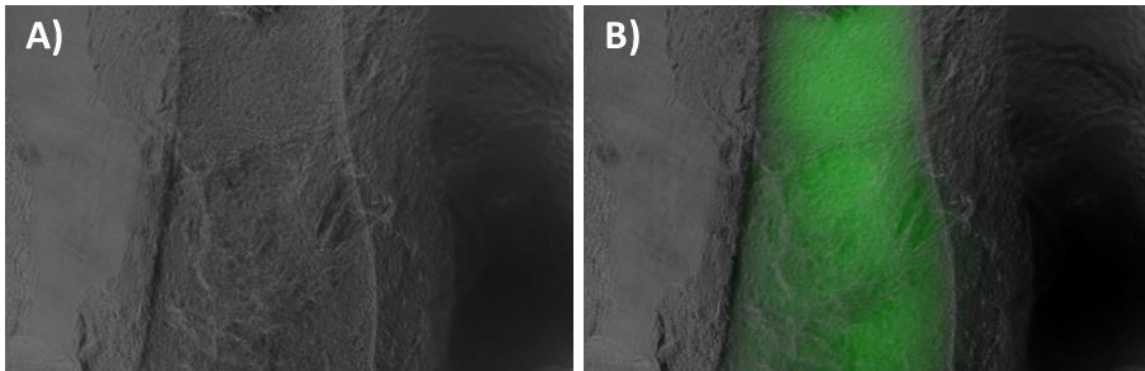


Figure 9-6 – Analysis of GelMA regions within DIKVAV-Hybrid bioink A) Image centred on printed strut i) Brightfield image, ii) Fluorescence overlayed on brightfield; B) Image centred on printed gap showing bioink feathered region i) Brightfield image, ii) Fluorescence overlayed on brightfield.

9.3.4 *In Vitro* Analysis of Developed Bioinks using Rat Cortical Neurospheres

Material cytocompatibility was investigated *in vitro* using rat cortical neurospheres (**Figure 9-7**). Initially, cytocompatibility was investigated through seeding of dissociated rat cortical neurospheres on cast DIKVAV-Hybrid samples and viability was compared to cells seeded on laminin, Fmoc-DIKVAV, and LM-GelMA samples (**Figure 9-7A**). Following 24h culture, all samples demonstrated similar cell viability, with no significant difference evident between samples (**Figure 9-7C i**). However, following 48h culture, significantly lower cell viability (40.4%, $p = 0.0022$) is evident in Fmoc-DIKVAV compared to the laminin control (**Figure 9-7C ii**). This is likely a result of material dissociation due in part to the low peptide concentration. Following 72h culture, the SAP Fmoc-DIKVAV shows significantly lower cell viability compared to the laminin control (51.5%, $p = 0.0076$) (**Figure 9-7C iii**). No significant difference is evident between laminin, GelMA, and DIKVAV-Hybrid samples. Cells seeded onto the laminin control demonstrated a significant increase in viability over 3 day's in culture (**Figure 9-7B**). Despite there being no significant difference in cell viability between GelMA and DIKVAV-Hybrid samples, there is a difference in morphology; dissociated neurospheres formed clusters when placed onto the GelMA bioink (**Figure 9-7A i**), whilst dissociated neurospheres cultured on DIKVAV-Hybrid scaffolds produced cell extensions (indicated by arrows) and generally avoided clustering (**Figure 9-7A ii**).

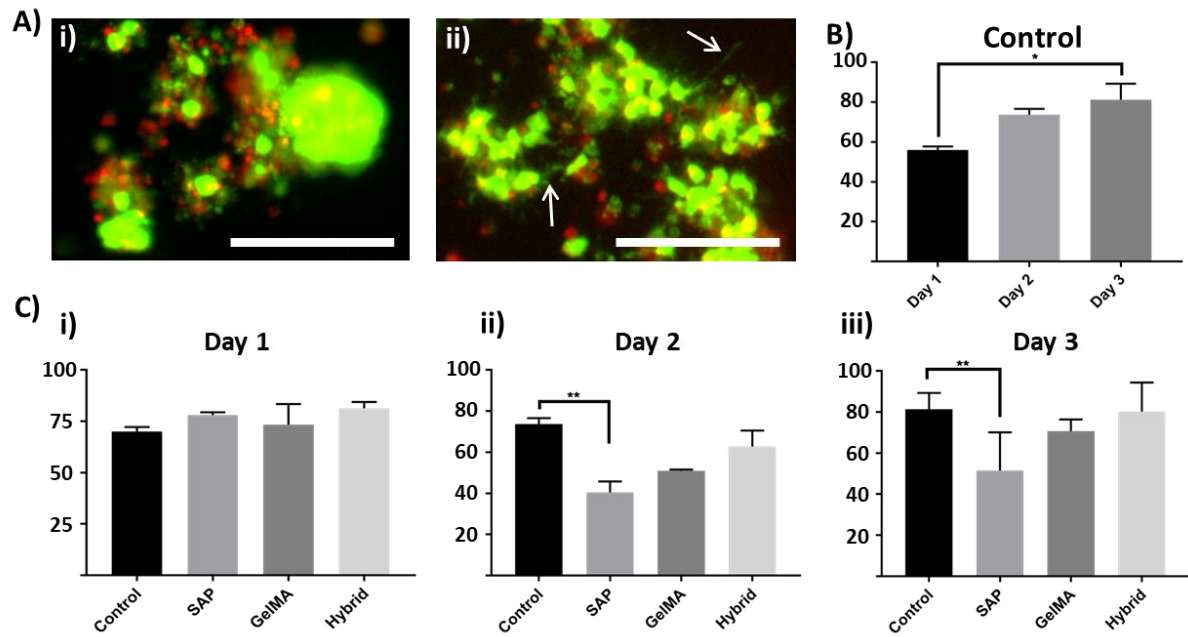


Figure 9-7 – Preliminary hydrogel cytotoxicity tests (a) Neurosphere morphology following 48h culture on (i) LM-GelMA, and (ii) DIKVAV-Hybrid (arrows show cell extensions) , (B) Viability of cells seeded onto laminin control, (C) Cell viability of seeded neurospheres at (i) 24h, (ii) 48h, (iii) 72h culture, and (D) viability of encapsulated neurospheres following (i) 24h, (ii) 48h, and (iii) 72h culture.

9.3.5 *In Vitro* Analysis of Printed Constructs.

Cytocompatibility is the most imperative factor to consider for neural bioprinting applications, especially considering neural cells tend to be less tolerant to environmental stresses than many other cells types.⁴⁰¹ Therefore, bioprinting approaches which promote high cell viability are of particular promise to neural regeneration applications. Cytocompatibility of the DIKVAV-Hybrid bioink and associated bioprinting process was determined via bioprinting of rat cortical neurosphere-containing bioinks under predetermined optimal conditions (10°C, ~30 kPa for LM-GelMA, and 15°C, ~ 40 kPa for DIKVAV-Hybrid). Grid-like structures were printed onto cooled plates and immediately crosslinked under UV light. A 2D control was also prepared through seeding of rat cortical neurospheres onto laminin-coated tissue culture plastic.

9.3.5.1 *Cell Viability*

Following 24h and 72h culture, cell viability of printed rat cortical neurospheres was assessed for each material and compared to the laminin control (**Figure 9-8A**). Cell viability was quantified through staining with Calcein AM (green) and ethidium homodimer (red) to determine the relative proportion of live and dead cell respectively. Cells were imaged using fluorescence microscopy, and the number of live and dead cells were determined through ImageJ analysis. Following 24h, no significant viability was observed between the 2D control (83.4%) and either of the printed bioinks; however, a significant difference ($p = 0.0201$) was evident between GelMA and the DIKVAV Hybrid bioink, demonstrating viabilities of 70.6% and 87.3%, respectively. Following 72h culture, significant viability differences were observed between the control (91.8%) and printed samples. Specifically, GelMA demonstrated a significantly lower viability ($p = 0.0001$) of 60.6% compared to the 2D control, while DIKVAV-hybrid samples demonstrated significantly lower viabilities ($p = 0.0156$) of 74.5% compared to the control. Despite DIKVAV-hybrid bioink samples demonstrating superior viability to GelMA bioink samples, the difference was not significant. This is likely due to increased variance from refracted fluorescent light in these 3D bioprinted samples; however, despite lack of a significant difference in 72h viability, both printed constructs were shown to support sufficient cell viability.

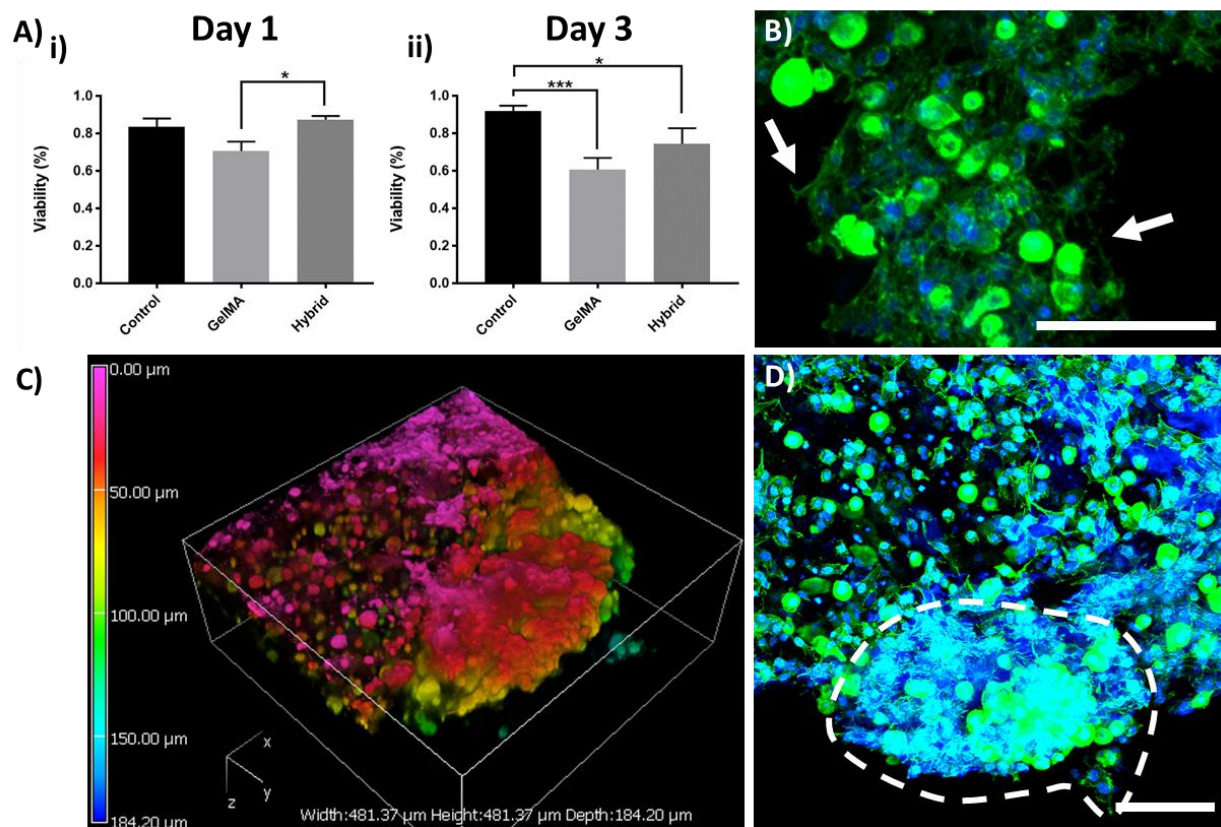


Figure 9-8 – Biological response to scaffolds A) Cell viability following i) 24h and ii) 72H proliferative culture. B) Morphology of cells printed within DIKVAV-Hybrid bioinks (arrows show cellular extensions), C) Depth coding of cells within DIKVAV-Hybrid bioinks, and D) cell morphology within DIKVAV-Hybrid bioinks showing increased density within feathered region. Scalebar: 100 μ m

Cell Morphology following 72h proliferative culture was also assessed for DIKVAV-Hybrid samples (**Figure 9-8B-D**). Samples were stained with phalloidin and DAPI to observe actin filaments and cell nuclei, respectively. Confocal analysis was completed to verify cell morphology. Clear cell extensions are visible in DIKVAV-Hybrid samples with extensive networking evident (indicated by arrows) (**Figure 9-8B**). Furthermore, through depth coding, cells are shown to exist through the sample to a depth of 180 μm (**Figure 9-8C**). Interestingly, confocal staining also showed a greater density of cells within the feathered region previously observed (indicated by dashed region) (**Figure 9-8D**). The increase of cell density in this region may be a result of heterogeneity in the printing process; however, the altered morphology of these cells warrants future investigation, and potentially allows for the development of advanced scaffolds with regions of altered biological response.

Interactions between cell extensions and bioinks were observed via SEM (**Figure 9-9**) following 3 days in proliferative culture. Despite cell-shrinking during the drying processes, cell extensions were clearly evident in both cases, indicating good cell-material integration.

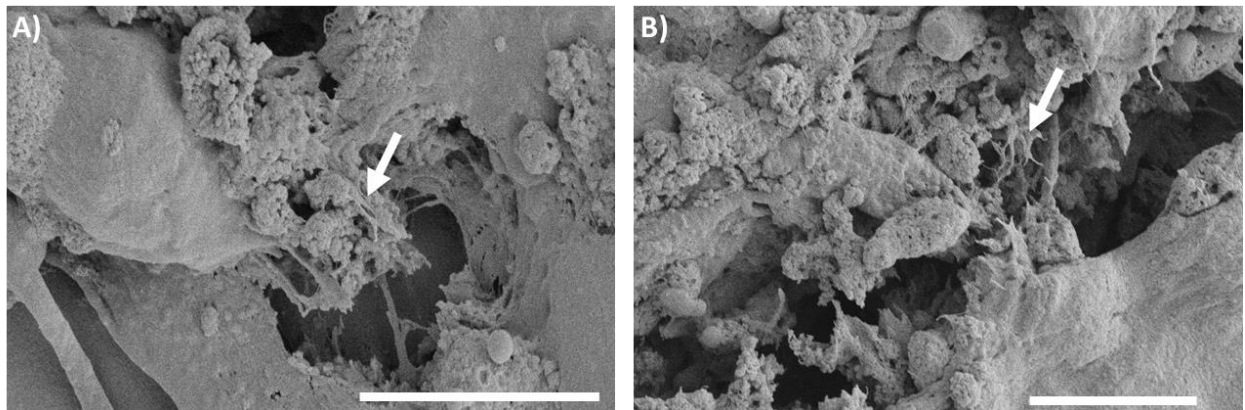


Figure 9-9 – SEM analysis of cells in A) GelMA and B) DIKVAV-Hybrid, Arrows showing cell extensions, Scale bar = 100 μm

Following 7-days of culture, proliferative media was removed and replaced with differentiation media. Confocal analysis was employed to observe morphological response as an indication of differentiation following 14 days in differentiation culture (21 days total culture) (**Figure 9-10**). Depth-coding of LM-GelMA constructs revealed cell migration to the surface of the construct, with extensive cell spreading (**Figure 9-10A**). Depth-coding of DIKVAV-Hybrid samples demonstrate some migration to the surface, with more cells distributed through the construct, however encapsulated cells demonstrated poor cell spreading (**Figure 9-10C**). Cells in LM-GelMA demonstrate extensive actin spreading (green) along the surface of the sample, while cells on the surfaces of DIKVAV-Hybrid printed structures show limited spreading (**Figure 9-10B, D**).

Despite the poor differentiation of dissociated rat cortical neurospheres in the DIKVAV-Hybrid constructs, this material is still found to maintain high viability at high cell density, thus meeting the design requirements highlighted in **section 2.2**. Furthermore, we have verified the efficacy of this modular bioink approach for tissue engineering applications, with high cell viability evident following printing in the neural-specific DIKVAV-Hybrid bioink, despite the increased sensitivity of neural cells to external stresses.⁴⁰¹ In this study, we have successfully developed a bioink approach for the printing of dissociated rat-cortical neurosphere cells, however further optimisation in bioprinting techniques and cell culturing would likely lead to improved cell response. In particular, the culturing of constructs within a bioreactor may lead to improved cell response, however this lies outside the scope of this thesis and should be a future research focus.⁴⁹

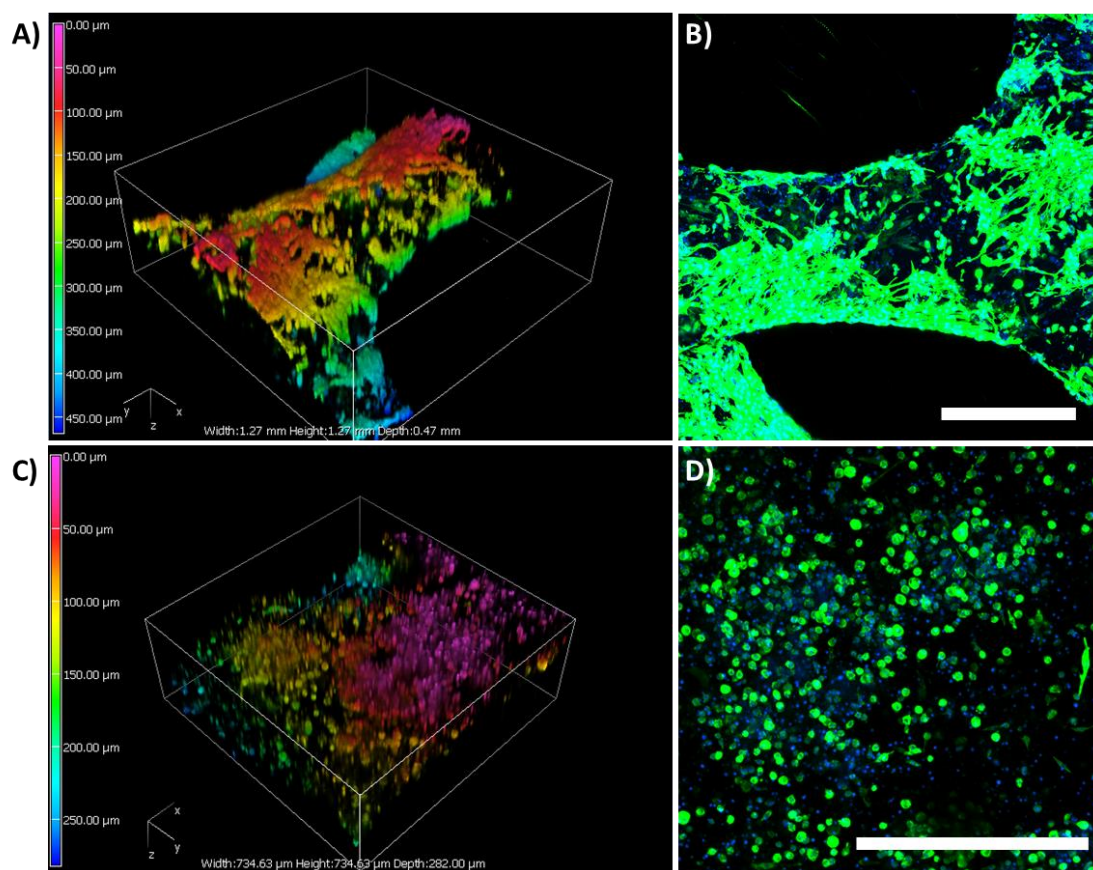


Figure 9-10 – Analysis of cell morphology, migration and spreading following 14 days differentiation in LM-GelMA (Top) and DIKVAV-Hybrid (Bottom). A) Depth-coding of cells within LM-GelMA constructs, B) Flattened confocal stack showing cell morphology through actin (green) and nuclei (blue) staining in LM-GelMA samples. C) Depth-coding of cells within DIKVAV-Hybrid constructs, D) Flattened confocal stack showing cell morphology through actin (green) and nuclei (blue) staining in DIKVAV-Hybrid samples. (scalebars: 400 μm)

9.4 Conclusion

Central nervous system repair is particularly complex owing to the bodies innate inability for self-repair. Bioprinting offers a potential resolve, allowing for the controlled spatial deposition of cells, signals, and factors within a highly engineered artificial tissue construct. However, currently, few bioinks can provide mechanical properties necessitated by cytocompatible bioprinting processes while maintaining suitable biological properties to support desired cell behaviour. The design of advanced bioinks allowing for high mechanical and biological tunability is investigated in this chapter. Here, LM-GelMA is combined with Fmoc-DIKVAV to form an advanced bioink for neural tissue repair. The DIKVAV-hybrid bioink demonstrates high mechanical tunability owing to LM-GelMA's unique thermodependent viscosity, while biological tunability is facilitated through Fmoc-DIKVAV incorporation. Furthermore, the hybrid bioink is shown to maintain the propensity to form covalent crosslinks when subject to UV irradiation, allowing for greater resistance to shear strain and a maintenance of shape fidelity even after 4 weeks in simulated culture ($1\times$ PBS, 37°C). Conservation of nanofibril formation is also observed in DIKVAV-Hybrid samples, confirming successful engineering of nano through to macro architectures. DIKVAV-hybrid bioinks show comparable viability of seeded and printed rat cortical neurospheres to the gold-standard LM-GelMA control, with seeded rat cortical neurospheres also demonstrating enhanced cell morphology in DIKVAV-Hybrid samples compared to the LM-GelMA control. Results from this study emphasis the need for future optimisation of cell culture practices for 3D applications and provide fundamentals for further material optimisation. Importantly, this chapter highlights the versatility of this modular bioink toolkit and provides foundations for further comprehensive biological analysis.

Chapter Ten:

CONCLUSIONS

The research performed in this thesis has detailed the design, development, and use of advanced self-assembling peptide-based scaffolds for tissue engineering applications. In each chapter, materials have been rigorously characterised and investigated regarding mechanical properties and/or biological influence on cells. Our results demonstrate a systematic approach for the development of advanced biomaterials containing Fmoc-based SAPs, with focus on achieving a modular bioink toolkit. In this thesis, we engineered hydrogels containing ECM-inspired motifs, including fibronectin's RGD and PHSRN synergistic attachment motifs, and laminin's IKVAV motif. In all cases, Fmoc-SAP assembly was triggered via charge neutralisation as enabled through a pH switch method, resulting in the formation of long nanofibrils through π - β assembly as facilitated through hierarchical self-organisation of short, Fmoc-based peptides.

The ultimate aim of this project was to develop advanced fmoc-SAP based hydrogel systems for tissue engineering applications, with a focus on the formation of fmoc-SAP containing bioinks for soft-tissue engineering applications. These aims were achieved through sequential development of Fmoc-based self-assembling peptide systems. The research detailed in this thesis progressed from material functionalisation through sequence alteration, to structural and biological modification through macromolecule incorporation. Key understandings acquired during material functionalisation chapters were then applied for the development of Fmoc-based SAP-containing bioinks.

Specifically, early material development focused on the potential of multisequence functionalisation through control over the assembly mechanism. The incorporation of two fibronectin derived synergistic epitopes, RGD and PHSRN were investigated in ability to enhance HMFCs viability, proliferation, and spreading. Here, the effect of assembly mechanism was also investigated with peptide coassembly compared to sequence concatenation, or either sequence alone. Coassembly resulted in improved adhesion, proliferation, and spreading compared to the concatenated version or either sequence alone. The ability of these peptides to form coassembled, multisequence hydrogels was further observed through coassembly of a Fmoc-SAP containing fibronectin's RGD motif, and a second Fmoc-SAP containing laminin's IKVAV sequence. The utility of this material was investigated for use as an advanced cancer model, with comprehensive analysis comparing the effect of the cell environment regarding both cell-cell and cell-ECM communication. Results found that co-cultured spheroids containing both NOR-10 fibroblasts and Lewis lung cancer cells demonstrated greater cancer-like properties when encapsulated within the coassembled microenvironment containing RGD and IKVAV compared to an agarose control. Specifically, NOR-10 and LLC cells co-cultures encapsulated in Fmoc-DIKVAV/Fmoc-FRGDF hydrogels demonstrated enhanced motility, and metabolic activity, with a higher degree of NOR-10 differentiation into CAF.

We further investigated hydrogel functionalisation through the incorporation of developmentally and structurally important macromolecules. Here, fucoidan and versican were incorporated during Fmoc-SAP assembly, resulting in the formation of a multicomponent hydrogel. Influence of macromolecule incorporation on resultant assembly, structure, and mechanical properties were extensively evaluated. The coassembly of fucoidan and Fmoc-FRGDF resulted in increased fibre bundling proportional to fucoidan concentration. Subsequently, Fmoc-FRGDF/fucoidan coassembly demonstrated enhanced stiffness as assessed through rheology. Biologically, fucoidan addition did not affect myoblast (C2C12) proliferation and viability, but strongly influenced cell morphology, resulting in reduced cell surface area and an overall reduction of multinucleated syncytia. Similarly, versican addition had no significant effect on C2C12 proliferation and viability; however, morphology was greatly affected, with smaller cells evident at 24h compared to the empty vector control. After 72h

however, cells demonstrated similar morphologies to the empty vector control, and number of multinucleated syncytia was unaffected.

Next, we demonstrated the ability Fmoc-SAPs to form hybrid bioinks through the incorporation of charged photo-crosslinkable materials. Specifically, GelMA was incorporated with Fmoc-FRGDF and Fmoc-PHSRN during assembly to form a hybrid material which elicits desirable mechanical and biological properties. Initially, the DoF of GelMA hydrogels was investigated regarding nanostructure and viscoelastic properties through SAXS and rheology respectively. Here, unique trends were observed tying nanostructure organisation to their associated effect on material viscoelasticity. Low-Methacryloyl GelMA (18% DoF) was selected for hybrid bioink development owing to its heightened gel/sol transition temperature and excellent resistance to shear strain. We further extended this research into the development of a hybrid LM-GelMA/Fmoc-FRGDF/Fmoc-PHSRN bioink (FPG-Hybrid). Analysis of FPG-Hybrid bioink nanostructure found the preservation of nanofibrils, indicating a maintenance of nanofiber formation despite the presence of GelMA. Conformational changes of the bioinks were investigated through SAXS, wherein mass fractal dimension (power) increased upon crosslinking for both LM-GelMA and FPG-Hybrid, indicating the formation of chemically crosslinked, branched networks. Importantly, the FPG-Hybrid demonstrated enhanced printability, with optimal printing conditions existing at $\sim 15^{\circ}\text{C}$ compared to $\sim 10^{\circ}\text{C}$ in LM-GelMA samples. FPG-Hybrid bioinks maintained high cell viability following 72h culture ($>98\%$ viability) and facilitated early differentiation as assessed by multinucleated myotube formation.

Finally, the utility of the hybrid bioink model for use as a bioink toolkit was investigated through substitution of Fmoc-FRGDF/Fmoc-PHSRN nanofibers for Fmoc-DIKVAV nanofibers, allowing for the targeting of neuronal tissue types. DIKVAV-Hybrid bioinks were assembled as FPG-Hybrids; however, prior to assembly Fmoc-FRGDF/Fmoc-PHSRN was substituted with Fmoc-DIKVAV. DIKVAV-Hybrids demonstrated highly similar mechanical properties to FPG-Hybrid bioinks, highlighting the ease of biological tunability in these systems. DIKVAV-Hybrid bioinks, however, elicit unique swelling characteristics, with the formation of a feathered border following 10 minutes culture. DIKVAV-Hybrids supported enhanced seeded rat cortical neurosphere viability and

facilitated neuronal extensions, while cells seeded on LM-GelMA constructs presented with more clustered morphologies; furthermore, printed rat cortical neurospheres within DIKVAV-Hybrid bioinks demonstrated high viability (87.3%) following 72h culture. These results highlight the potential of Fmoc-SAPs/GelMA systems as modular bioink toolkits for advanced tissue engineering applications and warrant further biological investigation and optimisation.

In conclusion, we successfully achieved the aims set out within this project, resulting in the development of a modular Fmoc-SAP-based bioink toolkit for cytocompatible bioprinting allowing for the controlled deposition of cells, structures, and signals within predefined geometries. Bioinks developed through this approach boast ease of mechanical and biological tunability, allowing for tissue-specific signalling and nano- through to macro control over bioink architecture.

Chapter Eleven:

FUTURE DIRECTIONS

In this thesis, we described the development of advanced Fmoc-SAP-based strategies to improve current tissue engineering applications and allow for the development of a functionalised, modular bioink toolkit. The results of this thesis demonstrate the versatility of Fmoc-SAPs for tissue engineering applications and establish the potential for biological functionalisation and mechanical tunability. Ultimately, this thesis establishes Fmoc-SAPs as a platform for the modification and development of advanced bioink toolkits through assembly with favourable macromolecules for use with a range of tissues. The potential use of Fmoc-SAP-based bioinks, however, can be further explored through extension in several directions.

Firstly, as a furthering of work in **Chapter 5**, the utility of the cancer model containing spheroids encapsulated in Fmoc-FRGDF/Fmoc-DIKVAV could be further investigated through testing of anti-cancer drugs on encapsulated hydrogels, comparing their response to drug-free samples. Here, the anti-inflammatory polysaccharide fucoidan could be investigated, as previous use has indicated anti-cancer properties and its integration within Fmoc-SAP hydrogels is well known. Similarly, as a furthering of **Chapter 6**, further research could be placed into assessing the mechanisms of surface versican degradation, resulting in attenuation of cell spreading.

Secondly, as a continuation of work performed in **Chapter 7**, future works should focus on kinetics modelling of GelMA's structure-function relationships through the pairing of *in situ* SAXS and rheological data to gain a deeper understanding of structure-function dependencies. Threshold

concentrations should also be investigated further, particularly in relation to DoF, as there are preliminary indications of DoF-related concentration dependencies within our data. Effect of increased DoF on molecular weight should also be investigated, as preliminary results indicate an inverse relationship. Crosslinking temperature and subsequent effect on nanostructured properties should also be investigated to gain a more robust understanding of mechanical synergies resulting from the interplay between physical and chemical crosslinks.

Thirdly, as a furthering of work performed in **Chapter 7** and **Chapter 8**, the potential for mechanical tunability of Fmoc-SAP Hybrid bioinks could be further investigated through control of DoF. Specifically, hybrid bioinks could be developed using differing degrees of methacrylation to alter final modulus, shear resistance, thermodependent viscoelasticity, and nano-/microarchitectures.

Fourthly, as an extension of **Chapter 9**, other peptide nanofibers or macromolecules could be incorporated into the hybrid bioink system, allowing for tailored and targeted cell signalling, resulting in tissue-specific bioink development while maintaining the modular nature of the developed bioink toolkit. The developed DIKVAV-Hybrid bioink could potentially be expanded for the development of neuromuscular junctions, with neural cells existing within the feathered, Fmoc-DIKVAV, region of the hydrogel, and muscle fibres forming on the surface of the GelMA core. However, research first needs to be placed into increasing and enhancing the longevity of this feathered region.

Fifthly, as a continuation of work in **Chapter 8** and **Chapter 9**, further cell analysis through molecular biology could be completed to comprehensively and systematically assess any differences between cells cultured on the hybrid materials compared to the control. In particular, further cell analysis should quantify differentiation and cell maturity. Investigation into optimal cell seeding density within these materials would also be of substantial benefit, as cell seeding density influences cell behaviour and material longevity.

Further research in this area will require a multidisciplinary approach that encompasses the knowledge and understandings acquired in materials science, advanced manufacturing, and biology. Building on the foundations presented in this thesis, future research and development could

substantially advance current bioink and 3D scaffold technologies, yielding new treatment prospects for the regeneration and repair of once damaged, diseased, or lost tissue.

REFERENCES

1. Frantz, C.; Stewart, K. M.; Weaver, V. M., The extracellular matrix at a glance. *Journal of cell science* **2010**, *123* (24), 4195-4200.
2. Tang, W.; Lin, D.; Yu, Y.; Niu, H.; Guo, H.; Yuan, Y.; Liu, C., Bioinspired trimodal macro/micro/nano-porous scaffolds loading rhBMP-2 for complete regeneration of critical size bone defect. *Acta biomaterialia* **2016**, *32*, 309-323.
3. Coutu, D. L.; Cuerquis, J.; El Ayoubi, R.; Forner, K.-A.; Roy, R.; François, M.; Griffith, M.; Lillicrap, D.; Yousefi, A.-M.; Blostein, M. D., Hierarchical scaffold design for mesenchymal stem cell-based gene therapy of hemophilia B. *Biomaterials* **2011**, *32* (1), 295-305.
4. Drury, J. L.; Mooney, D. J., Hydrogels for tissue engineering: scaffold design variables and applications. *Biomaterials* **2003**, *24* (24), 4337-4351.
5. Lee, K. Y.; Mooney, D. J., Hydrogels for tissue engineering. *Chemical reviews* **2001**, *101* (7), 1869-1880.
6. Tibbitt, M. W.; Anseth, K. S., Hydrogels as extracellular matrix mimics for 3D cell culture. *Biotechnology and bioengineering* **2009**, *103* (4), 655-663.
7. Li, R.; Rodriguez, A.; Nisbet, D. R.; Barrow, C. J.; Williams, R. J., Chapter 3 - Self-Assembled Peptide Nanostructures for the Fabrication of Cell Scaffolds A2 - Castillo-León, Jaime. In *Micro and Nanofabrication Using Self-Assembled Biological Nanostructures*, Svendsen, W. E., Ed. William Andrew Publishing: Oxford, 2015; pp 33-61.
8. Smith, A. M.; Williams, R. J.; Tang, C.; Coppo, P.; Collins, R. F.; Turner, M. L.; Saiani, A.; Ulijn, R. V., Fmoc-Diphenylalanine Self Assembles to a Hydrogel via a Novel Architecture Based on Π - π Interlocked β -Sheets. *Advanced Materials* **2008**, *20* (1), 37-41.
9. Fleming, S.; Ulijn, R. V., Design of nanostructures based on aromatic peptide amphiphiles. *Chemical Society Reviews* **2014**, *43* (23), 8150-8177.
10. Zhang, S.; Zhao, X., Design of molecular biological materials using peptide motifs. *Journal of Materials Chemistry* **2004**, *14* (14), 2082-2086.
11. Boyd-Moss, M.; Fox, K.; Brandt, M.; Nisbet, D.; Williams, R., Bioprinting and Biofabrication with Peptide and Protein Biomaterials. In *Peptides and Peptide-based Biomaterials and their Biomedical Applications*, Springer: 2017; pp 95-129.
12. Thies, R. S.; Murry, C. E., The advancement of human pluripotent stem cell-derived therapies into the clinic. *Development* **2015**, *142* (18), 3077-3084.
13. Freitag, J.; Bates, D.; Boyd, R.; Shah, K.; Barnard, A.; Huguenin, L.; Tenen, A., Mesenchymal stem cell therapy in the treatment of osteoarthritis: reparative pathways, safety and efficacy—a review. *BMC musculoskeletal disorders* **2016**, *17* (1), 230.
14. Kim, S. U.; De Vellis, J., Stem cell-based cell therapy in neurological diseases: a review. *Journal of neuroscience research* **2009**, *87* (10), 2183-2200.
15. Cheng, A.; Hardingham, T. E.; Kimber, S. J., Generating cartilage repair from pluripotent stem cells. *Tissue Engineering Part B: Reviews* **2013**, *20* (4), 257-266.
16. Muir, L. A.; Chamberlain, J. S., Emerging strategies for cell and gene therapy of the muscular dystrophies. *Expert reviews in molecular medicine* **2009**, *11*.
17. Strauer, B. E.; Brehm, M.; Zeus, T.; Köstering, M.; Hernandez, A.; Sorg, R. d. V.; Kögler, G.; Wernet, P., Repair of infarcted myocardium by autologous intracoronary mononuclear bone marrow cell transplantation in humans. *Circulation* **2002**, *106* (15), 1913-1918.
18. Weiss, D. J.; Bertoncello, I.; Borok, Z.; Kim, C.; Panoskaltsis-Mortari, A.; Reynolds, S.; Rojas, M.; Stripp, B.; Warburton, D.; Prockop, D. J., Stem cells and cell therapies in lung biology and lung diseases. *Proceedings of the American Thoracic Society* **2011**, *8* (3), 223-272.
19. Branski, L. K.; Gauglitz, G. G.; Herndon, D. N.; Jeschke, M. G., A review of gene and stem cell therapy in cutaneous wound healing. *Burns* **2009**, *35* (2), 171-180.
20. Neirinckx, V.; Coste, C.; Rogister, B.; Wislet-Gendebien, S., Concise review: adult mesenchymal stem cells, adult neural crest stem cells, and therapy of neurological pathologies: a state of play. *Stem cells translational medicine* **2013**, *2* (4), 284-296.

21. Toh, W. S.; Loh, X. J., Advances in hydrogel delivery systems for tissue regeneration. *Materials Science and Engineering: C* **2014**, *45*, 690-697.
22. Sadtler, K.; Singh, A.; Wolf, M. T.; Wang, X.; Pardoll, D. M.; Elisseeff, J. H., Design, clinical translation and immunological response of biomaterials in regenerative medicine. *Nature Reviews Materials* **2016**, *1*, 16040.
23. Chen, F.-M.; Liu, X., Advancing biomaterials of human origin for tissue engineering. *Progress in polymer science* **2016**, *53*, 86-168.
24. Novosel, E. C.; Kleinhans, C.; Kluger, P. J., Vascularization is the key challenge in tissue engineering. *Advanced drug delivery reviews* **2011**, *63* (4), 300-311.
25. Fortunato, T. M.; Beltrami, C.; Emanuelli, C.; De Bank, P. A.; Pula, G., Platelet lysate gel and endothelial progenitors stimulate microvascular network formation in vitro: tissue engineering implications. *Scientific reports* **2016**, *6*.
26. Horgan, C. C.; Rodriguez, A. L.; Li, R.; Bruggeman, K. F.; Stupka, N.; Raynes, J. K.; Day, L.; White, J. W.; Williams, R. J.; Nisbet, D. R., Characterisation of minimalist co-assembled fluorenylmethyloxycarbonyl self-assembling peptide systems for presentation of multiple bioactive peptides. *Acta biomaterialia* **2016**, *38*, 11-22.
27. Bogdani, M.; Korpos, E.; Simeonovic, C. J.; Parish, C. R.; Sorokin, L.; Wight, T. N., Extracellular matrix components in the pathogenesis of type 1 diabetes. *Current diabetes reports* **2014**, *14* (12), 1-11.
28. Lutolf, M.; Hubbell, J., Synthetic biomaterials as instructive extracellular microenvironments for morphogenesis in tissue engineering. *Nature biotechnology* **2005**, *23* (1), 47-55.
29. Taubenberger, A. V.; Woodruff, M. A.; Bai, H.; Muller, D. J.; Hutmacher, D. W., The effect of unlocking RGD-motifs in collagen I on pre-osteoblast adhesion and differentiation. *Biomaterials* **2010**, *31* (10), 2827-2835.
30. Kim, S.-H.; Turnbull, J.; Guimond, S., Extracellular matrix and cell signalling: the dynamic cooperation of integrin, proteoglycan and growth factor receptor. *Journal of Endocrinology* **2011**, *209* (2), 139-151.
31. Kielty, C. M.; Sherratt, M. J.; Shuttleworth, C. A., Elastic fibres. *Journal of cell science* **2002**, *115* (14), 2817-2828.
32. Pavelka, M.; Roth, J., Connective Tissue. In *Functional Ultrastructure*, Springer: 2015; pp 314-329.
33. Halper, J.; Kjaer, M., Basic components of connective tissues and extracellular matrix: elastin, fibrillin, fibulins, fibrinogen, fibronectin, laminin, tenascins and thrombospondins. In *Progress in Heritable Soft Connective Tissue Diseases*, Springer: 2014; pp 31-47.
34. Kleinman, H. K.; Philp, D.; Hoffman, M. P., Role of the extracellular matrix in morphogenesis. *Current opinion in biotechnology* **2003**, *14* (5), 526-532.
35. Pulido, D.; Hussain, S.-A.; Hohenester, E., Crystal structure of the heterotrimeric integrin-binding region of laminin-111. *Structure* **2017**, *25* (3), 530-535.
36. Sun, W.; Incitti, T.; Migliaresi, C.; Quattrone, A.; Casarosa, S.; Motta, A., Viability and neuronal differentiation of neural stem cells encapsulated in silk fibroin hydrogel functionalized with an IKVAV peptide. *Journal of tissue engineering and regenerative medicine* **2015**.
37. Smith, M. L.; Gourdon, D.; Little, W. C.; Kubow, K. E.; Eguiluz, R. A.; Luna-Morris, S.; Vogel, V., Force-induced unfolding of fibronectin in the extracellular matrix of living cells. *PLoS Biol* **2007**, *5* (10), e268.
38. Reed, R. K.; Rubin, K., Transcapillary exchange: role and importance of the interstitial fluid pressure and the extracellular matrix. *Cardiovascular research* **2010**, *87* (2), 211-217.
39. Stylianopoulos, T.; Martin, J. D.; Chauhan, V. P.; Jain, S. R.; Diop-Frimpong, B.; Bardeesy, N.; Smith, B. L.; Ferrone, C. R.; Hornicek, F. J.; Boucher, Y., Causes, consequences, and remedies for growth-induced solid stress in murine and human tumors. *Proceedings of the National Academy of Sciences* **2012**, 201213353.
40. Rosso, F.; Giordano, A.; Barbarisi, M.; Barbarisi, A., From cell-ECM interactions to tissue engineering. *Journal of cellular physiology* **2004**, *199* (2), 174-180.
41. Wilson, H. K.; Canfield, S. G.; Hjortness, M. K.; Palecek, S. P.; Shusta, E. V., Exploring the effects of cell seeding density on the differentiation of human pluripotent stem cells to brain microvascular endothelial cells. *Fluids and Barriers of the CNS* **2015**, *12* (1), 13.

42. Mao, A. S.; Shin, J.-W.; Mooney, D. J., Effects of substrate stiffness and cell-cell contact on mesenchymal stem cell differentiation. *Biomaterials* **2016**, 98, 184-191.
43. Yassin, M. A.; Leknes, K. N.; Pedersen, T. O.; Xing, Z.; Sun, Y.; Lie, S. A.; Finne-Wistrand, A.; Mustafa, K., Cell seeding density is a critical determinant for copolymer scaffolds-induced bone regeneration. *Journal of Biomedical Materials Research Part A* **2015**, 103 (11), 3649-3658.
44. Madl, C. M.; Heilshorn, S. C.; Blau, H. M., Bioengineering strategies to accelerate stem cell therapeutics. *Nature* **2018**, 557 (7705), 335.
45. Del Amo, C.; Olivares, V.; Córdor, M.; Blanco, A.; Santolaria, J.; Asín, J.; Borau, C.; García-Aznar, J. M., Matrix architecture plays a pivotal role in 3D osteoblast migration: The effect of interstitial fluid flow. *Journal of the mechanical behavior of biomedical materials* **2018**, 83, 52-62.
46. Gage, F. H., Cell therapy. *NATURE-LONDON* **1998**, 18-24.
47. Liu, S.; Zhou, J.; Zhang, X.; Liu, Y.; Chen, J.; Hu, B.; Song, J.; Zhang, Y., Strategies to optimize adult stem cell therapy for tissue regeneration. *International journal of molecular sciences* **2016**, 17 (6), 982.
48. Gouadon, E.; Moore-Morris, T.; Smit, N. W.; Chatenoud, L.; Coronel, R.; Harding, S. E.; Jourdon, P.; Lambert, V.; Rucker-Martin, C.; Pucéat, M., Concise Review: Pluripotent Stem Cell-Derived Cardiac Cells, A Promising Cell Source for Therapy of Heart Failure: Where Do We Stand? *Stem cells* **2016**, 34 (1), 34-43.
49. Antoni, D.; Burckel, H.; Josset, E.; Noel, G., Three-dimensional cell culture: a breakthrough in vivo. *International journal of molecular sciences* **2015**, 16 (3), 5517-5527.
50. Hunt, J. A.; Chen, R.; van Veen, T.; Bryan, N., Hydrogels for tissue engineering and regenerative medicine. *Journal of Materials Chemistry B* **2014**, 2 (33), 5319-5338.
51. Guo, B.; Ma, P. X., Synthetic biodegradable functional polymers for tissue engineering: a brief review. *Science China Chemistry* **2014**, 57 (4), 490-500.
52. Nilasaroya, A.; Poole-Warren, L. A.; Whitelock, J. M.; Martens, P. J., Structural and functional characterisation of poly (vinyl alcohol) and heparin hydrogels. *Biomaterials* **2008**, 29 (35), 4658-4664.
53. Pati, F.; Jang, J.; Ha, D.-H.; Kim, S. W.; Rhie, J.-W.; Shim, J.-H.; Kim, D.-H.; Cho, D.-W., Printing three-dimensional tissue analogues with decellularized extracellular matrix bioink. *Nature Communications* **2014**, 5.
54. Jang, J.; Kim, T. G.; Kim, B. S.; Kim, S.-W.; Kwon, S.-M.; Cho, D.-W., Tailoring mechanical properties of decellularized extracellular matrix bioink by vitamin B2-induced photo-crosslinking. *Acta biomaterialia* **2016**, 33, 88-95.
55. Gilbert, T. W.; Sellaro, T. L.; Badylak, S. F., Decellularization of tissues and organs. *Biomaterials* **2006**, 27 (19), 3675-3683.
56. Crapo, P. M.; Gilbert, T. W.; Badylak, S. F., An overview of tissue and whole organ decellularization processes. *Biomaterials* **2011**, 32 (12), 3233-3243.
57. Ahmed, E. M., Hydrogel: Preparation, characterization, and applications: A review. *Journal of advanced research* **2015**, 6 (2), 105-121.
58. Crapo, P. M.; Tottey, S.; Slivka, P. F.; Badylak, S. F., Effects of biologic scaffolds on human stem cells and implications for CNS tissue engineering. *Tissue Engineering Part A* **2013**, 20 (1-2), 313-323.
59. Viswanath, A.; Vanacker, J.; Germain, L.; Leprince, J. G.; Diogenes, A.; Shakesheff, K. M.; White, L. J.; des Rieux, A., Extracellular matrix-derived hydrogels for dental stem cell delivery. *Journal of Biomedical Materials Research Part A* **2017**, 105 (1), 319-328.
60. Lynn, A.; Yannas, I.; Bonfield, W., Antigenicity and immunogenicity of collagen. *Journal of Biomedical Materials Research Part B: Applied Biomaterials* **2004**, 71 (2), 343-354.
61. Rice, J. J.; Martino, M. M.; De Laporte, L.; Tortelli, F.; Briquez, P. S.; Hubbell, J. A., Engineering the regenerative microenvironment with biomaterials. *Advanced healthcare materials* **2013**, 2 (1), 57-71.
62. Glowacki, J.; Mizuno, S., Collagen scaffolds for tissue engineering. *Biopolymers: Original Research on Biomolecules* **2008**, 89 (5), 338-344.
63. Lee, C. H.; Singla, A.; Lee, Y., Biomedical applications of collagen. *International journal of pharmaceutics* **2001**, 221 (1), 1-22.
64. Ratner, B. D.; Hoffman, A. S.; Schoen, F. J.; Lemons, J. E., *Biomaterials science: an introduction to materials in medicine*. Elsevier: 2004.

65. Klotz, B. J.; Gawlitta, D.; Rosenberg, A. J.; Malda, J.; Melchels, F. P., Gelatin-methacryloyl hydrogels: towards biofabrication-based tissue repair. *Trends in biotechnology* **2016**, *34* (5), 394-407.
66. Nguyen, K. T.; West, J. L., Photopolymerizable hydrogels for tissue engineering applications. *Biomaterials* **2002**, *23* (22), 4307-4314.
67. Heo, D. N.; Ko, W.-K.; Bae, M. S.; Lee, J. B.; Lee, D.-W.; Byun, W.; Lee, C. H.; Kim, E.-C.; Jung, B.-Y.; Kwon, I. K., Enhanced bone regeneration with a gold nanoparticle-hydrogel complex. *Journal of Materials Chemistry B* **2014**, *2* (11), 1584-1593.
68. Di Bella, C.; Duchi, S.; O'Connell, C. D.; Blanchard, R.; Augustine, C.; Yue, Z.; Thompson, F.; Richards, C.; Beirne, S.; Onofrillo, C., In situ handheld three-dimensional bioprinting for cartilage regeneration. *Journal of tissue engineering and regenerative medicine* **2018**, *12* (3), 611-621.
69. Hosseini, V.; Ahadian, S.; Ostrovidov, S.; Camci-Unal, G.; Chen, S.; Kaji, H.; Ramalingam, M.; Khademhosseini, A., Engineered contractile skeletal muscle tissue on a microgrooved methacrylated gelatin substrate. *Tissue Engineering Part A* **2012**, *18* (23-24), 2453-2465.
70. Kolesky, D. B.; Truby, R. L.; Gladman, A.; Busbee, T. A.; Homan, K. A.; Lewis, J. A., 3D bioprinting of vascularized, heterogeneous cell-laden tissue constructs. *Advanced materials* **2014**, *26* (19), 3124-3130.
71. Laurent, T. C.; Fraser, J., Hyaluronan. *The FASEB journal* **1992**, *6* (7), 2397-2404.
72. Mero, A.; Campisi, M., Hyaluronic acid bioconjugates for the delivery of bioactive molecules. *Polymers* **2014**, *6* (2), 346-369.
73. Camci-Unal, G.; Cuttica, D.; Annabi, N.; Demarchi, D.; Khademhosseini, A., Synthesis and characterization of hybrid hyaluronic acid-gelatin hydrogels. *Biomacromolecules* **2013**, *14* (4), 1085-1092.
74. Doolittle, R. F., Fibrinogen and fibrin. *eLS* **2001**.
75. Thiagarajan, P.; Narayanan, A., Thrombin. *eLS* **2001**.
76. Hsieh, J. Y.; Smith, T. D.; Meli, V. S.; Tran, T. N.; Botvinick, E. L.; Liu, W. F., Differential regulation of macrophage inflammatory activation by fibrin and fibrinogen. *Acta Biomaterialia* **2017**, *47*, 14-24.
77. de la Puente, P.; Ludeña, D., Cell culture in autologous fibrin scaffolds for applications in tissue engineering. *Experimental cell research* **2014**, *322* (1), 1-11.
78. Whelan, D.; Caplice, N.; Clover, A., Fibrin as a delivery system in wound healing tissue engineering applications. *Journal of Controlled Release* **2014**, *196*, 1-8.
79. Spotnitz, W. D., Fibrin sealant: past, present, and future: a brief review. *World journal of surgery* **2010**, *34* (4), 632-634.
80. Brown, A. C.; Barker, T. H., Fibrin-based biomaterials: modulation of macroscopic properties through rational design at the molecular level. *Acta biomaterialia* **2014**, *10* (4), 1502-1514.
81. Kundu, B.; Rajkhowa, R.; Kundu, S. C.; Wang, X., Silk fibroin biomaterials for tissue regenerations. *Advanced drug delivery reviews* **2013**, *65* (4), 457-470.
82. Tanaka, K.; Inoue, S.; Mizuno, S., Hydrophobic interaction of P25, containing Asn-linked oligosaccharide chains, with the HL complex of silk fibroin produced by *Bombyx mori*. *Insect biochemistry and molecular biology* **1999**, *29* (3), 269-276.
83. Sehnal, F.; Zúrovec, M., Construction of silk fiber core in Lepidoptera. *Biomacromolecules* **2004**, *5* (3), 666-674.
84. Li, C.; Vepari, C.; Jin, H.-J.; Kim, H. J.; Kaplan, D. L., Electrospun silk-BMP-2 scaffolds for bone tissue engineering. *Biomaterials* **2006**, *27* (16), 3115-3124.
85. Jin, H.-J.; Chen, J.; Karageorgiou, V.; Altman, G. H.; Kaplan, D. L., Human bone marrow stromal cell responses on electrospun silk fibroin mats. *Biomaterials* **2004**, *25* (6), 1039-1047.
86. Sahoo, S.; Toh, S. L.; Goh, J. C., A bFGF-releasing silk/PLGA-based biohybrid scaffold for ligament/tendon tissue engineering using mesenchymal progenitor cells. *Biomaterials* **2010**, *31* (11), 2990-2998.
87. Fang, Q.; Chen, D.; Yang, Z.; Li, M., In vitro and in vivo research on using *Antheraea pernyi* silk fibroin as tissue engineering tendon scaffolds. *Materials Science and Engineering: C* **2009**, *29* (5), 1527-1534.
88. Kasoju, N.; Bora, U., Silk fibroin in tissue engineering. *Advanced healthcare materials* **2012**, *1* (4), 393-412.

89. Yan, L.-P.; Oliveira, J. M.; Oliveira, A. L.; Caridade, S. G.; Mano, J. F.; Reis, R. L., Macro/microporous silk fibroin scaffolds with potential for articular cartilage and meniscus tissue engineering applications. *Acta biomaterialia* **2012**, 8 (1), 289-301.
90. Wang, Y.; Blasioli, D. J.; Kim, H.-J.; Kim, H. S.; Kaplan, D. L., Cartilage tissue engineering with silk scaffolds and human articular chondrocytes. *Biomaterials* **2006**, 27 (25), 4434-4442.
91. Ding, F.; Deng, H.; Du, Y.; Shi, X.; Wang, Q., Emerging chitin and chitosan nanofibrous materials for biomedical applications. *Nanoscale* **2014**, 6 (16), 9477-9493.
92. Bhattarai, N.; Gunn, J.; Zhang, M., Chitosan-based hydrogels for controlled, localized drug delivery. *Advanced drug delivery reviews* **2010**, 62 (1), 83-99.
93. Zarrintaj, P.; Manouchehri, S.; Ahmadi, Z.; Saeb, M. R.; Urbanska, A. M.; Kaplan, D. L.; Mozafari, M., Agarose-based biomaterials for tissue engineering. *Carbohydrate polymers* **2018**.
94. Sánchez-Salcedo, S.; Nieto, A.; Vallet-Regí, M., Hydroxyapatite/ β -tricalcium phosphate/agarose macroporous scaffolds for bone tissue engineering. *Chemical engineering journal* **2008**, 137 (1), 62-71.
95. Gasperini, L.; Mano, J. F.; Reis, R. L., Natural polymers for the microencapsulation of cells. *Journal of the Royal Society Interface* **2014**, 11 (100), 20140817.
96. Augst, A. D.; Kong, H. J.; Mooney, D. J., Alginate hydrogels as biomaterials. *Macromolecular bioscience* **2006**, 6 (8), 623-633.
97. Rowley, J. A.; Madlambayan, G.; Mooney, D. J., Alginate hydrogels as synthetic extracellular matrix materials. *Biomaterials* **1999**, 20 (1), 45-53.
98. Rowley, J. A.; Mooney, D. J., Alginate type and RGD density control myoblast phenotype. *Journal of Biomedical Materials Research: An Official Journal of The Society for Biomaterials, The Japanese Society for Biomaterials, and The Australian Society for Biomaterials and the Korean Society for Biomaterials* **2002**, 60 (2), 217-223.
99. Panwar, A.; Tan, L., Current status of bioinks for micro-extrusion-based 3D bioprinting. *Molecules* **2016**, 21 (6), 685.
100. Fu, Y.; Fan, X.; Tian, C.; Luo, J.; Zhang, Y.; Deng, L.; Qin, T.; Lv, Q., Decellularization of porcine skeletal muscle extracellular matrix for the formulation of a matrix hydrogel: a preliminary study. *Journal of cellular and molecular medicine* **2016**, 20 (4), 740-749.
101. Sharifi, E.; Azami, M.; Kajbafzadeh, A.-M.; Moztarzadeh, F.; Faridi-Majidi, R.; Shamousi, A.; Karimi, R.; Ai, J., Preparation of a biomimetic composite scaffold from gelatin/collagen and bioactive glass fibers for bone tissue engineering. *Materials Science and Engineering: C* **2016**, 59, 533-541.
102. Santana, B. P.; Nedel, F.; Perelló Ferrúa, C.; e Silva, R. M.; da Silva, A. F.; Demarco, F. F.; Lenin Villarreal Carreño, N., Comparing different methods to fix and to dehydrate cells on alginate hydrogel scaffolds using scanning electron microscopy. *Microscopy research and technique* **2015**, 78 (7), 553-561.
103. Naahidi, S.; Jafari, M.; Logan, M.; Wang, Y.; Yuan, Y.; Bae, H.; Dixon, B.; Chen, P., Biocompatibility of hydrogel-based scaffolds for tissue engineering applications. *Biotechnology advances* **2017**, 35 (5), 530-544.
104. Totaro, A.; Salerno, A.; Imparato, G.; Domingo, C.; Urciuolo, F.; Netti, P. A., PCL-HA microscaffolds for in vitro modular bone tissue engineering. *Journal of tissue engineering and regenerative medicine* **2017**, 11 (6), 1865-1875.
105. Khoshroo, K.; Kashi, T. S. J.; Moztarzadeh, F.; Tahriri, M.; Jazayeri, H. E.; Tayebi, L., Development of 3D PCL microsphere/TiO₂ nanotube composite scaffolds for bone tissue engineering. *Materials Science and Engineering: C* **2017**, 70, 586-598.
106. Bal, T.; Kepsutlu, B.; Kizilel, S., Characterization of protein release from poly (ethylene glycol) hydrogels with crosslink density gradients. *Journal of Biomedical Materials Research Part A: An Official Journal of The Society for Biomaterials, The Japanese Society for Biomaterials, and The Australian Society for Biomaterials and the Korean Society for Biomaterials* **2014**, 102 (2), 487-495.
107. Skaalure, S. C.; Dimson, S. O.; Pennington, A. M.; Bryant, S. J., Semi-interpenetrating networks of hyaluronic acid in degradable PEG hydrogels for cartilage tissue engineering. *Acta biomaterialia* **2014**, 10 (8), 3409-3420.
108. Magnusson, J. P.; Saeed, A. O.; Fernández-Trillo, F.; Alexander, C., Synthetic polymers for biopharmaceutical delivery. *Polymer Chemistry* **2011**, 2 (1), 48-59.

109. Schmedlen, R. H.; Masters, K. S.; West, J. L., Photocrosslinkable polyvinyl alcohol hydrogels that can be modified with cell adhesion peptides for use in tissue engineering. *Biomaterials* **2002**, 23 (22), 4325-4332.
110. Holloway, J. L.; Lowman, A. M.; Palmese, G. R., Mechanical evaluation of poly (vinyl alcohol)-based fibrous composites as biomaterials for meniscal tissue replacement. *Acta biomaterialia* **2010**, 6 (12), 4716-4724.
111. Gupta, S.; Webster, T. J.; Sinha, A., Evolution of PVA gels prepared without crosslinking agents as a cell adhesive surface. *Journal of Materials Science: Materials in Medicine* **2011**, 22 (7), 1763-1772.
112. Nuttelman, C. R.; Mortisen, D. J.; Henry, S. M.; Anseth, K. S., Attachment of fibronectin to poly (vinyl alcohol) hydrogels promotes NIH3T3 cell adhesion, proliferation, and migration. *Journal of Biomedical Materials Research: An Official Journal of The Society for Biomaterials, The Japanese Society for Biomaterials, and The Australian Society for Biomaterials and the Korean Society for Biomaterials* **2001**, 57 (2), 217-223.
113. Nuttelman, C. R.; Henry, S. M.; Anseth, K. S., Synthesis and characterization of photocrosslinkable, degradable poly (vinyl alcohol)-based tissue engineering scaffolds. *Biomaterials* **2002**, 23 (17), 3617-3626.
114. Gümüşderelioğlu, M.; Karakeçili, A. G., Uses of thermoresponsive and RGD/insulin-modified poly (vinyl ether)-based hydrogels in cell cultures. *Journal of Biomaterials Science, Polymer Edition* **2003**, 14 (3), 199-211.
115. Krishna, L.; Jayabalan, M., Synthesis and characterization of biodegradable poly (ethylene glycol) and poly (caprolactone diol) end capped poly (propylene fumarate) cross linked amphiphilic hydrogel as tissue engineering scaffold material. *Journal of Materials Science: Materials in Medicine* **2009**, 20 (1), 115.
116. Finosh, G.; Jayabalan, M.; Vandana, S.; Raghu, K., Hybrid alginate-polyester bimodal network hydrogel for tissue engineering—Influence of structured water on long-term cellular growth. *Colloids and Surfaces B: Biointerfaces* **2015**, 135, 855-864.
117. Suggs, L. J.; Payne, R. G.; Yaszemski, M. J.; Alemany, L. B.; Mikos, A. G., Synthesis and characterization of a block copolymer consisting of poly (propylene fumarate) and poly (ethylene glycol). *Macromolecules* **1997**, 30 (15), 4318-4323.
118. Behraves, E.; Shung, A. K.; Jo, S.; Mikos, A. G., Synthesis and characterization of triblock copolymers of methoxy poly (ethylene glycol) and poly (propylene fumarate). *Biomacromolecules* **2002**, 3 (1), 153-158.
119. Wang, K.; Cai, L.; Wang, S., Methacryl-polyhedral oligomeric silsesquioxane as a crosslinker for expediting photo-crosslinking of Poly (propylene fumarate): Material properties and bone cell behavior. *Polymer* **2011**, 52 (13), 2827-2839.
120. Fisher, J. P.; Lalani, Z.; Bossano, C. M.; Brey, E. M.; Demian, N.; Johnston, C. M.; Dean, D.; Jansen, J. A.; Wong, M. E.; Mikos, A. G., Effect of biomaterial properties on bone healing in a rabbit tooth extraction socket model. *Journal of Biomedical Materials Research Part A: An Official Journal of The Society for Biomaterials, The Japanese Society for Biomaterials, and The Australian Society for Biomaterials and the Korean Society for Biomaterials* **2004**, 68 (3), 428-438.
121. Fisher, J. P.; Dean, D.; Mikos, A. G., Photocrosslinking characteristics and mechanical properties of diethyl fumarate/poly (propylene fumarate) biomaterials. *Biomaterials* **2002**, 23 (22), 4333-4343.
122. Thankam, F. G.; Muthu, J., Alginate based hybrid copolymer hydrogels—Influence of pore morphology on cell-material interaction. *Carbohydrate polymers* **2014**, 112, 235-244.
123. Li, Z.; Li, J., Control of hyperbranched structure of polycaprolactone/poly (ethylene glycol) polyurethane block copolymers by glycerol and their hydrogels for potential cell delivery. *The Journal of Physical Chemistry B* **2013**, 117 (47), 14763-14774.
124. Díez-Pascual, A. M.; Díez-Vicente, A. L., Poly (propylene fumarate)/polyethylene glycol-modified graphene oxide nanocomposites for tissue engineering. *ACS applied materials & interfaces* **2016**, 8 (28), 17902-17914.
125. Castro-Aguirre, E.; Iñiguez-Franco, F.; Samsudin, H.; Fang, X.; Auras, R., Poly (lactic acid)—Mass production, processing, industrial applications, and end of life. *Advanced Drug Delivery Reviews* **2016**, 107, 333-366.

126. DeMerlis, C.; Schoneker, D., Review of the oral toxicity of polyvinyl alcohol (PVA). *Food and chemical Toxicology* **2003**, *41* (3), 319-326.
127. Yang, S.-l.; Wu, Z.-H.; Yang, W.; Yang, M.-B., Thermal and mechanical properties of chemical crosslinked polylactide (PLA). *Polymer Testing* **2008**, *27* (8), 957-963.
128. Nisbet, D. R.; Williams, R. J., Self-assembled peptides: characterisation and in vivo response. *Biointerphases* **2012**, *7* (1), 2.
129. Bruggeman, K. F.; Rodriguez, A. L.; Parish, C. L.; Williams, R. J.; Nisbet, D. R., Temporally controlled release of multiple growth factors from a self-assembling peptide hydrogel. *Nanotechnology* **2016**, *27* (38), 385102.
130. Paramonov, S. E.; Jun, H.-W.; Hartgerink, J. D., Self-assembly of peptide– amphiphile nanofibers: the roles of hydrogen bonding and amphiphilic packing. *Journal of the American Chemical Society* **2006**, *128* (22), 7291-7298.
131. Aggeli, A.; Nyrkova, I. A.; Bell, M.; Harding, R.; Carrick, L.; McLeish, T. C.; Semenov, A. N.; Boden, N., Hierarchical self-assembly of chiral rod-like molecules as a model for peptide β -sheet tapes, ribbons, fibrils, and fibers. *Proceedings of the National Academy of Sciences* **2001**, *98* (21), 11857-11862.
132. Matsumura, S.; Uemura, S.; Mihara, H., Fabrication of Nanofibers with Uniform Morphology by Self-Assembly of Designed Peptides. *Chemistry–A European Journal* **2004**, *10* (11), 2789-2794.
133. Sargeant, T. D.; Aparicio, C.; Goldberger, J. E.; Cui, H.; Stupp, S. I., Mineralization of peptide amphiphile nanofibers and its effect on the differentiation of human mesenchymal stem cells. *Acta biomaterialia* **2012**, *8* (7), 2456-2465.
134. Marini, D. M.; Hwang, W.; Lauffenburger, D. A.; Zhang, S.; Kamm, R. D., Left-handed helical ribbon intermediates in the self-assembly of a β -sheet peptide. *Nano Letters* **2002**, *2* (4), 295-299.
135. Acar, H.; Srivastava, S.; Chung, E. J.; Schnorenberg, M. R.; Barrett, J. C.; LaBelle, J. L.; Tirrell, M., Self-assembling peptide-based building blocks in medical applications. *Advanced drug delivery reviews* **2017**, *110*, 65-79.
136. Borges, J.; Sousa, M. P.; Cinar, G.; Caridade, S. G.; Guler, M. O.; Mano, J. F., Nanoengineering Hybrid Supramolecular Multilayered Biomaterials Using Polysaccharides and Self-Assembling Peptide Amphiphiles. *Advanced Functional Materials* **2017**, *27* (17), 1605122.
137. Tang, C.; Smith, A. M.; Collins, R. F.; Ulijn, R. V.; Saiani, A., Fmoc-diphenylalanine self-assembly mechanism induces apparent pK_a shifts. *Langmuir* **2009**, *25* (16), 9447-9453.
138. Reches, M.; Gazit, E., Casting metal nanowires within discrete self-assembled peptide nanotubes. *Science* **2003**, *300* (5619), 625-627.
139. Toledano, S.; Williams, R. J.; Jayawarna, V.; Ulijn, R. V., Enzyme-triggered self-assembly of peptide hydrogels via reversed hydrolysis. *Journal of the American Chemical Society* **2006**, *128* (4), 1070-1071.
140. Rodriguez, A. L.; Parish, C. L.; Nisbet, D. R.; Williams, R. J., Tuning the amino acid sequence of minimalist peptides to present biological signals via charge neutralised self assembly. *Soft matter* **2013**, *9* (15), 3915-3919.
141. Rodriguez, A.; Wang, T.-Y.; Bruggeman, K.; Horgan, C.; Li, R.; Williams, R. J.; Parish, C. L.; Nisbet, D., In vivo assessment of grafted cortical neural progenitor cells and host response to functionalized self-assembling peptide hydrogels and the implications for tissue repair. *Journal of Materials Chemistry B* **2014**, *2* (44), 7771-7778.
142. Xing, R.; Yuan, C.; Li, S.; Song, J.; Li, J.; Yan, X., Charge-Induced Secondary Structure Transformation of Amyloid-Derived Dipeptide Assemblies from β -Sheet to α -Helix. *Angewandte Chemie International Edition* **2018**, *57* (6), 1537-1542.
143. Modepalli, V. N.; Rodriguez, A. L.; Li, R.; Pavuluri, S.; Nicholas, K. R.; Barrow, C. J.; Nisbet, D. R.; Williams, R. J., In vitro response to functionalized self-assembled peptide scaffolds for three-dimensional cell culture. *Peptide Science* **2014**, *102* (2), 197-205.
144. Fry, H. C.; Garcia, J. M.; Medina, M. J.; Ricoy, U. M.; Gosztola, D. J.; Nikiforov, M. P.; Palmer, L. C.; Stupp, S. I., Self-assembly of highly ordered peptide amphiphile metalloporphyrin arrays. *Journal of the American Chemical Society* **2012**, *134* (36), 14646-14649.
145. Zhang, Y.; Yu, Y.; Akkouch, A.; Dababneh, A.; Dolati, F.; Ozbolat, I. T., In vitro study of directly bioprinted perfusable vasculature conduits. *Biomaterials science* **2015**, *3* (1), 134-143.

146. Calikoglu Koyuncu, A.; Gurel Pekozer, G.; Ramazanoglu, M.; Torun Kose, G.; Hasirci, V., Cartilage tissue engineering on macroporous scaffolds using human tooth germ stem cells. *Journal of tissue engineering and regenerative medicine* **2017**, *11* (3), 765-777.
147. Kondiah, P.; Choonara, Y.; Kondiah, P.; Marimuthu, T.; Kumar, P.; du Toit, L.; Pillay, V., A review of injectable polymeric hydrogel systems for application in bone tissue engineering. *Molecules* **2016**, *21* (11), 1580.
148. Stathopoulos, N.; Hellums, J., Shear stress effects on human embryonic kidney cells in vitro. *Biotechnology and Bioengineering* **1985**, *27* (7), 1021-1026.
149. Yang, G.; Li, X.; He, Y.; Ma, J.; Ni, G.; Zhou, S., From nano to micro to macro: Electrospun hierarchically structured polymeric fibers for biomedical applications. *Progress in Polymer Science* **2017**.
150. Doshi, J.; Reneker, D. H., Electrospinning process and applications of electrospun fibers. *Journal of electrostatics* **1995**, *35* (2-3), 151-160.
151. Kitsara, M.; Agbulut, O.; Kontziampasis, D.; Chen, Y.; Menasché, P., Fibers for hearts: A critical review on electrospinning for cardiac tissue engineering. *Acta biomaterialia* **2017**, *48*, 20-40.
152. Gandhimathi, C.; Venugopal, J. R.; Ramakrishna, S.; Srinivasan, D. K., Electrospun-electrosprayed hydroxyapatite nanostructured composites for bone tissue regeneration. *Journal of Applied Polymer Science* **2018**, 46756.
153. Masaeli, E.; Karamali, F.; Loghmani, S.; Eslaminejad, M. B.; Nasr-Esfahani, M. H., Bio-engineered electrospun nanofibrous membranes using cartilage extracellular matrix particles. *Journal of Materials Chemistry B* **2017**, *5* (4), 765-776.
154. Agheb, M.; Dinari, M.; Rafienia, M.; Salehi, H., Novel electrospun nanofibers of modified gelatin-tyrosine in cartilage tissue engineering. *Materials Science and Engineering: C* **2017**, *71*, 240-251.
155. Soliman, E.; Bianchi, F.; Sleight, J. N.; George, J. H.; Cader, M. Z.; Cui, Z.; Ye, H., Engineered method for directional growth of muscle sheets on electrospun fibers. *Journal of Biomedical Materials Research Part A* **2018**, *106* (5), 1165-1176.
156. Schoen, B.; Avrahami, R.; Baruch, L.; Efraim, Y.; Goldfracht, I.; Elul, O.; Davidov, T.; Gepstein, L.; Zussman, E.; Machluf, M., Electrospun Extracellular Matrix: Paving the Way to Tailor-Made Natural Scaffolds for Cardiac Tissue Regeneration. *Advanced Functional Materials* **2017**, *27* (34), 1700427.
157. Hu, J.; Kai, D.; Ye, H.; Tian, L.; Ding, X.; Ramakrishna, S.; Loh, X. J., Electrospinning of poly (glycerol sebacate)-based nanofibers for nerve tissue engineering. *Materials Science and Engineering: C* **2017**, *70*, 1089-1094.
158. Wang, W.; Itoh, S.; Konno, K.; Kikkawa, T.; Ichinose, S.; Sakai, K.; Ohkuma, T.; Watabe, K., Effects of Schwann cell alignment along the oriented electrospun chitosan nanofibers on nerve regeneration. *Journal of Biomedical Materials Research Part A: An Official Journal of The Society for Biomaterials, The Japanese Society for Biomaterials, and The Australian Society for Biomaterials and the Korean Society for Biomaterials* **2009**, *91* (4), 994-1005.
159. Bruggeman, K. F.; Wang, Y.; Maclean, F. L.; Parish, C. L.; Williams, R. J.; Nisbet, D. R., Temporally controlled growth factor delivery from a self-assembling peptide hydrogel and electrospun nanofibre composite scaffold. *Nanoscale* **2017**, *9* (36), 13661-13669.
160. Murphy, S. V.; Atala, A., 3D bioprinting of tissues and organs. *Nature biotechnology* **2014**, *32* (8), 773-785.
161. Richards, D.; Jia, J.; Yost, M.; Markwald, R.; Mei, Y., 3D Bioprinting for Vascularized Tissue Fabrication. *Annals of biomedical engineering* **2016**, 1-16.
162. Wang, Z.; Abdulla, R.; Parker, B.; Samanipour, R.; Ghosh, S.; Kim, K., A simple and high-resolution stereolithography-based 3D bioprinting system using visible light crosslinkable bioinks. *Biofabrication* **2015**, *7* (4), 045009.
163. Skardal, A.; Atala, A., Biomaterials for integration with 3-D bioprinting. *Annals of Biomedical Engineering* **2015**, *43* (3), 730-746.
164. Huang, S. H.; Liu, P.; Mokasdar, A.; Hou, L., Additive manufacturing and its societal impact: a literature review. *The International Journal of Advanced Manufacturing Technology* **2013**, *67* (5-8), 1191-1203.

165. Tang, D.; Tare, R. S.; Yang, L.-Y.; Williams, D. F.; Ou, K.-L.; Oreffo, R. O., Biofabrication of bone tissue: approaches, challenges and translation for bone regeneration. *Biomaterials* **2016**, 83, 363-382.
166. Vaezi, M.; Seitz, H.; Yang, S., A review on 3D micro-additive manufacturing technologies. *The International Journal of Advanced Manufacturing Technology* **2013**, 67 (5-8), 1721-1754.
167. Kamisuki, S.; Hagata, T.; Tezuka, C.; Nose, Y.; Fujii, M.; Atobe, M. In *A low power, small, electrostatically-driven commercial inkjet head*, Micro Electro Mechanical Systems, 1998. MEMS 98. Proceedings., The Eleventh Annual International Workshop on, IEEE: 1998; pp 63-68.
168. Nishiyama, Y.; Henmi, C.; Iwanaga, S.; Nakagawa, H.; Yamaguchi, K.; Akita, K.; Mochizuki, S.; Takiura, K.; Nakamura, M., Ink jet three-dimensional digital fabrication for biological tissue manufacturing: analysis of alginate microgel beads produced by ink jet droplets for three dimensional tissue fabrication. *Journal of Imaging Science and Technology* **2008**, 52 (6), 60201-1-60201-6.
169. Ozbolat, I. T.; Hospodiuk, M., Current advances and future perspectives in extrusion-based bioprinting. *Biomaterials* **2016**, 76, 321-343.
170. Bammesberger, S. B.; Kartmann, S.; Tanguy, L.; Liang, D.; Mutschler, K.; Ernst, A.; Zengerle, R.; Koltay, P., A Low-Cost, Normally Closed, Solenoid Valve for Non-Contact Dispensing in the Sub- μ L Range. *Micromachines* **2013**, 4 (1), 9-21.
171. Ozbolat, I. T.; Moncal, K. K.; Gudapati, H., Evaluation of bioprinter technologies. *Additive Manufacturing* **2017**, 13, 179-200.
172. Odde, D. J.; Renn, M. J., Laser-guided direct writing for applications in biotechnology. *Trends in biotechnology* **1999**, 17 (10), 385-389.
173. Odde, D. J.; Renn, M. J., Laser-guided direct writing of living cells. *Biotechnology and bioengineering* **2000**, 67 (3), 312-318.
174. Ferris, C. J.; Gilmore, K. G.; Wallace, G. G., Biofabrication: an overview of the approaches used for printing of living cells. *Applied microbiology and biotechnology* **2013**, 97 (10), 4243-4258.
175. Schiele, N. R.; Corr, D. T.; Huang, Y.; Raof, N. A.; Xie, Y.; Chrisey, D. B., Laser-based direct-write techniques for cell printing. *Biofabrication* **2010**, 2 (3), 032001.
176. Guillemot, F.; Guillotin, B.; Fontaine, A.; Ali, M.; Catros, S.; Kériquel, V.; Fricain, J.-C.; Rémy, M.; Bareille, R.; Amédée-Vilamitjana, J., Laser-assisted bioprinting to deal with tissue complexity in regenerative medicine. *MRS bulletin* **2011**, 36 (12), 1015-1019.
177. Cui, H.; Nowicki, M.; Fisher, J. P.; Zhang, L. G., 3D Bioprinting for Organ Regeneration. *Advanced Healthcare Materials* **2016**.
178. Hölzl, K.; Lin, S.; Tytgat, L.; Van Vlierberghe, S.; Gu, L.; Ovsianikov, A., Bioink properties before, during and after 3D bioprinting. *Biofabrication* **2016**, 8 (3), 032002.
179. Loo, Y.; Lakshmanan, A.; Ni, M.; Toh, L. L.; Wang, S.; Hauser, C. A., Peptide bioink: self-assembling nanofibrous scaffolds for three-dimensional organotypic cultures. *Nano letters* **2015**, 15 (10), 6919-6925.
180. Chimene, D.; Lennox, K. K.; Kaunas, R. R.; Gaharwar, A. K., Advanced Bioinks for 3D Printing: A Materials Science Perspective. *Annals of biomedical engineering* **2016**, 1-13.
181. Park, J. Y.; Gao, G.; Jang, J.; Cho, D.-W., 3D printed structures for delivery of biomolecules and cells: tissue repair and regeneration. *Journal of Materials Chemistry B* **2016**, 4 (47), 7521-7539.
182. Gao, G.; Cui, X., Three-dimensional bioprinting in tissue engineering and regenerative medicine. *Biotechnology letters* **2016**, 38 (2), 203-211.
183. Collins, M. N.; Birkinshaw, C., Hyaluronic acid based scaffolds for tissue engineering—A review. *Carbohydrate polymers* **2013**, 92 (2), 1262-1279.
184. Lau, H. K.; Kiick, K. L., Opportunities for multicomponent hybrid hydrogels in biomedical applications. *Biomacromolecules* **2014**, 16 (1), 28-42.
185. Guvendiren, M.; Burdick, J. A., Engineering synthetic hydrogel microenvironments to instruct stem cells. *Current opinion in biotechnology* **2013**, 24 (5), 841-846.
186. Buenger, D.; Topuz, F.; Groll, J., Hydrogels in sensing applications. *Progress in Polymer Science* **2012**, 37 (12), 1678-1719.
187. Jungst, T.; Smolan, W.; Schacht, K.; Scheibel, T.; Groll, J. r., Strategies and molecular design criteria for 3D printable hydrogels. *Chemical reviews* **2015**, 116 (3), 1496-1539.

188. Dubbin, K.; Hori, Y.; Lewis, K. K.; Heilshorn, S. C., Dual-Stage Crosslinking of a Gel-Phase Bioink Improves Cell Viability and Homogeneity for 3D Bioprinting. *Advanced healthcare materials* **2016**, 5 (19), 2488-2492.
189. Hedegaard, C. L.; Collin, E. C.; Redondo-Gómez, C.; Nguyen, L. T.; Ng, K. W.; Castrejón-Pita, A. A.; Castrejón-Pita, J. R.; Mata, A., Hydrodynamically Guided Hierarchical Self-Assembly of Peptide-Protein Bioinks. *Advanced Functional Materials* **2018**, 28 (16), 1703716.
190. Raphael, B.; Khalil, T.; Workman, V. L.; Smith, A.; Brown, C. P.; Streuli, C.; Saiani, A.; Domingos, M., 3D cell bioprinting of self-assembling peptide-based hydrogels. *Materials Letters* **2017**, 190, 103-106.
191. Hart, L. R.; Harries, J. L.; Greenland, B. W.; Colquhoun, H. M.; Hayes, W., Supramolecular approach to new inkjet printing inks. *ACS applied materials & interfaces* **2015**, 7 (16), 8906-8914.
192. Sargeant, T. D.; Desai, A. P.; Banerjee, S.; Agawu, A.; Stopek, J. B., An in situ forming collagen-PEG hydrogel for tissue regeneration. *Acta biomaterialia* **2012**, 8 (1), 124-132.
193. Dikovsky, D.; Bianco-Peled, H.; Seliktar, D., The effect of structural alterations of PEG-fibrinogen hydrogel scaffolds on 3-D cellular morphology and cellular migration. *Biomaterials* **2006**, 27 (8), 1496-1506.
194. Lim, K. S.; Schon, B. S.; Mekhileri, N. V.; Brown, G. C.; Chia, C. M.; Prabakar, S.; Hooper, G. J.; Woodfield, T. B., New Visible-Light Photoinitiating System for Improved Print Fidelity in Gelatin-Based Bioinks. *ACS Biomaterials Science & Engineering* **2016**, 2 (10), 1752-1762.
195. Lee, H. J.; Kim, Y. B.; Ahn, S. H.; Lee, J. S.; Jang, C. H.; Yoon, H.; Chun, W.; Kim, G. H., A New Approach for Fabricating Collagen/ECM-Based Bioinks Using Preosteoblasts and Human Adipose Stem Cells. *Advanced healthcare materials* **2015**, 4 (9), 1359-1368.
196. Kim, Y. B.; Lee, H.; Kim, G. H., Strategy to Achieve Highly Porous/Biocompatible Macroscale Cell Blocks, Using a Collagen/Genipin-bioink and an Optimal 3D Printing Process. *ACS Applied Materials & Interfaces* **2016**, 8 (47), 32230-32240.
197. Irvine, S. A.; Agrawal, A.; Lee, B. H.; Chua, H. Y.; Low, K. Y.; Lau, B. C.; Machluf, M.; Venkatraman, S., Printing cell-laden gelatin constructs by free-form fabrication and enzymatic protein crosslinking. *Biomedical microdevices* **2015**, 17 (1), 1-8.
198. Cui, X.; Boland, T., Human microvasculature fabrication using thermal inkjet printing technology. *Biomaterials* **2009**, 30 (31), 6221-6227.
199. Das, S.; Pati, F.; Choi, Y.-J.; Rijal, G.; Shim, J.-H.; Kim, S. W.; Ray, A. R.; Cho, D.-W.; Ghosh, S., Bioprintable, cell-laden silk fibroin-gelatin hydrogel supporting multilineage differentiation of stem cells for fabrication of three-dimensional tissue constructs. *Acta biomaterialia* **2015**, 11, 233-246.
200. Yan, M.; Lewis, P.; Shah, R., Tailoring nanostructure and bioactivity of 3D-printable hydrogels with self-assemble peptides amphiphile (PA) for promoting bile duct formation. *Biofabrication* **2018**, 10 (3), 035010.
201. Skardal, A.; Devarasetty, M.; Kang, H.-W.; Mead, I.; Bishop, C.; Shupe, T.; Lee, S. J.; Jackson, J.; Yoo, J.; Soker, S.; Atala, A., A hydrogel bioink toolkit for mimicking native tissue biochemical and mechanical properties in bioprinted tissue constructs. *Acta biomaterialia* **2015**, 25, 24-34.
202. O'Connell, C. D.; Zhang, B.; Onofrillo, C.; Duchi, S.; Blanchard, R.; Quigley, A.; Bourke, J.; Gambhir, S.; Kapsa, R.; Di Bella, C., Tailoring the mechanical properties of gelatin methacryloyl hydrogels through manipulation of the photocrosslinking conditions. *Soft matter* **2018**, 14 (11), 2142-2151.
203. Liu, W.; Heinrich, M. A.; Zhou, Y.; Akpek, A.; Hu, N.; Liu, X.; Guan, X.; Zhong, Z.; Jin, X.; Khademhosseini, A., Extrusion Bioprinting of Shear-Thinning Gelatin Methacryloyl Bioinks. *Advanced healthcare materials* **2017**, 6 (12), 1601451.
204. Xu, T.; Gregory, C. A.; Molnar, P.; Cui, X.; Jalota, S.; Bhaduri, S. B.; Boland, T., Viability and electrophysiology of neural cell structures generated by the inkjet printing method. *Biomaterials* **2006**, 27 (19), 3580-3588.
205. Prince, E.; Kumacheva, E., Design and applications of man-made biomimetic fibrillar hydrogels. *Nature Reviews Materials* **2019**, 1.
206. Almany, L.; Seliktar, D., Biosynthetic hydrogel scaffolds made from fibrinogen and polyethylene glycol for 3D cell cultures. *Biomaterials* **2005**, 26 (15), 2467-2477.
207. Zhang, X.; Zhang, Y., Tissue engineering applications of three-dimensional bioprinting. *Cell biochemistry and biophysics* **2015**, 72 (3), 777-782.

208. Gao, G.; Schilling, A. F.; Hubbell, K.; Yonezawa, T.; Truong, D.; Hong, Y.; Dai, G.; Cui, X., Improved properties of bone and cartilage tissue from 3D inkjet-bioprinted human mesenchymal stem cells by simultaneous deposition and photocrosslinking in PEG-GelMA. *Biotechnology letters* **2015**, *37* (11), 2349-2355.
209. Ren, X.; Wang, F.; Chen, C.; Gong, X.; Yin, L.; Yang, L., Engineering zonal cartilage through bioprinting collagen type II hydrogel constructs with biomimetic chondrocyte density gradient. *BMC Musculoskeletal Disorders* **2016**, *17* (1), 301.
210. Wüst, S.; Godla, M. E.; Müller, R.; Hofmann, S., Tunable hydrogel composite with two-step processing in combination with innovative hardware upgrade for cell-based three-dimensional bioprinting. *Acta biomaterialia* **2014**, *10* (2), 630-640.
211. Levato, R.; Visser, J.; Planell, J. A.; Engel, E.; Malda, J.; Mateos-Timoneda, M. A., Biofabrication of tissue constructs by 3D bioprinting of cell-laden microcarriers. *Biofabrication* **2014**, *6* (3), 035020.
212. Duarte Campos, D. F.; Blaeser, A.; Buellesbach, K.; Sen, K. S.; Xun, W.; Tillmann, W.; Fischer, H., Bioprinting Organotypic Hydrogels with Improved Mesenchymal Stem Cell Remodeling and Mineralization Properties for Bone Tissue Engineering. *Advanced healthcare materials* **2016**, *5* (11), 1336-1345.
213. Shim, J.-H.; Jang, K.-M.; Hahn, S. K.; Park, J. Y.; Jung, H.; Oh, K.; Park, K. M.; Yeom, J.; Park, S. H.; Kim, S. W., Three-dimensional bioprinting of multilayered constructs containing human mesenchymal stromal cells for osteochondral tissue regeneration in the rabbit knee joint. *Biofabrication* **2016**, *8* (1), 014102.
214. Daly, A. C.; Critchley, S. E.; Rencsok, E. M.; Kelly, D. J., A comparison of different bioinks for 3D bioprinting of fibrocartilage and hyaline cartilage. *Biofabrication* **2016**, *8* (4), 045002.
215. Gurkan, U. A.; El Assal, R.; Yildiz, S. E.; Sung, Y.; Trachtenberg, A. J.; Kuo, W. P.; Demirci, U., Engineering anisotropic biomimetic fibrocartilage microenvironment by bioprinting mesenchymal stem cells in nanoliter gel droplets. *Molecular pharmaceutics* **2014**, *11* (7), 2151-2159.
216. Jia, W.; Gungor-Ozkerim, P. S.; Zhang, Y. S.; Yue, K.; Zhu, K.; Liu, W.; Pi, Q.; Byambaa, B.; Dokmeci, M. R.; Shin, S. R.; Khademhosseini, A., Direct 3D bioprinting of perfusable vascular constructs using a blend bioink. *Biomaterials* **2016**, *106*, 58-68.
217. Guillotin, B.; Souquet, A.; Catros, S.; Duocastella, M.; Pippenger, B.; Bellance, S.; Bareille, R.; Rémy, M.; Bordenave, L.; Amédée, J.; Guillemot, F., Laser assisted bioprinting of engineered tissue with high cell density and microscale organization. *Biomaterials* **2010**, *31* (28), 7250-7256.
218. Choi, Y. J.; Kim, T. G.; Jeong, J.; Yi, H. G.; Park, J. W.; Hwang, W.; Cho, D. W., 3D Cell Printing of Functional Skeletal Muscle Constructs Using Skeletal Muscle-Derived Bioink. *Advanced healthcare materials* **2016**, *5* (20), 2636-2645.
219. England, S.; Rajaram, A.; Schreyer, D. J.; Chen, X., Bioprinted fibrin-factor XIII-hyaluronate hydrogel scaffolds with encapsulated Schwann cells and their in vitro characterization for use in nerve regeneration. *Bioprinting* **2016**.
220. Jang, J.; Park, H.-J.; Kim, S.-W.; Kim, H.; Park, J. Y.; Na, S. J.; Kim, H. J.; Park, M. N.; Choi, S. H.; Park, S. H.; Kim, S. W.; Kwon, S.-M.; Kim, P.-J.; Cho, D.-W., 3D printed complex tissue construct using stem cell-laden decellularized extracellular matrix bioinks for cardiac repair. *Biomaterials* **2017**, *112*, 264-274.
221. Zhang, Y. S.; Arneri, A.; Bersini, S.; Shin, S.-R.; Zhu, K.; Goli-Malekabadi, Z.; Aleman, J.; Colosi, C.; Busignani, F.; Dell'Erba, V.; Bishop, C.; Shupe, T.; Demarchi, D.; Moretti, M.; Rasponi, M.; Dokmeci, M. R.; Atala, A.; Khademhosseini, A., Bioprinting 3D microfibrous scaffolds for engineering endothelialized myocardium and heart-on-a-chip. *Biomaterials* **2016**, *110*, 45-59.
222. Duan, B.; Hockaday, L. A.; Kang, K. H.; Butcher, J. T., 3D bioprinting of heterogeneous aortic valve conduits with alginate/gelatin hydrogels. *Journal of biomedical materials research Part A* **2013**, *101* (5), 1255-1264.
223. Duan, B.; Kapetanovic, E.; Hockaday, L. A.; Butcher, J. T., Three-dimensional printed trileaflet valve conduits using biological hydrogels and human valve interstitial cells. *Acta biomaterialia* **2014**, *10* (5), 1836-1846.
224. Li, S.; Xiong, Z.; Wang, X.; Yan, Y.; Liu, H.; Zhang, R., Direct fabrication of a hybrid cell/hydrogel construct by a double-nozzle assembling technology. *Journal of Bioactive and Compatible Polymers* **2009**, *24* (3), 249-265.

225. Bhise, N. S.; Manoharan, V.; Massa, S.; Tamayol, A.; Ghaderi, M.; Miscuglio, M.; Lang, Q.; Zhang, Y. S.; Shin, S. R.; Calzone, G., A liver-on-a-chip platform with bioprinted hepatic spheroids. *Biofabrication* **2016**, 8 (1), 014101.
226. Cubo, N.; Garcia, M.; del Cañizo, J. F.; Velasco, D.; Jorcano, J. L., 3D bioprinting of functional human skin: production and in vivo analysis. *Biofabrication* **2016**, 9 (1), 015006.
227. Olszta, M. J.; Cheng, X.; Jee, S. S.; Kumar, R.; Kim, Y.-Y.; Kaufman, M. J.; Douglas, E. P.; Gower, L. B., Bone structure and formation: a new perspective. *Materials Science and Engineering: R: Reports* **2007**, 58 (3), 77-116.
228. Weiner, S.; Wagner, H. D., The material bone: structure-mechanical function relations. *Annual Review of Materials Science* **1998**, 28 (1), 271-298.
229. Burg, K. J.; Porter, S.; Kellam, J. F., Biomaterial developments for bone tissue engineering. *Biomaterials* **2000**, 21 (23), 2347-2359.
230. Nukavarapu, S. P.; Dorcenus, D. L., Osteochondral tissue engineering: Current strategies and challenges. *Biotechnology Advances* **2013**, 31 (5), 706-721.
231. Karlsen, T. A.; Jakobsen, R. B.; Brinchmann, J. E., Early molecular events during in vitro chondrogenesis. *The Biology and Therapeutic Application of Mesenchymal Cells* **2017**, 167-190.
232. García-Martínez, L.; Campos, F.; Godoy-Guzmán, C.; del Carmen Sánchez-Quevedo, M.; Garzón, I.; Alaminos, M.; Campos, A.; Carriel, V., Encapsulation of human elastic cartilage-derived chondrocytes in nanostructured fibrin-agarose hydrogels. *Histochemistry and Cell Biology* **2017**, 147 (1), 83-95.
233. Bhosale, A. M.; Richardson, J. B., Articular cartilage: structure, injuries and review of management. *British medical bulletin* **2008**, 87 (1), 77-95.
234. Nerem, R. M.; Seliktar, D., Vascular tissue engineering. *Annual review of biomedical engineering* **2001**, 3 (1), 225-243.
235. Pugsley, M. K.; Tabrizchi, R., The vascular system: An overview of structure and function. *Journal of Pharmacological and Toxicological Methods* **2000**, 44 (2), 333-340.
236. Lewis, M. P.; Mudera, V.; Cheema, U.; Shah, R., Muscle tissue engineering. In *Fundamentals of Tissue Engineering and Regenerative Medicine*, Springer: 2009; pp 243-253.
237. Schiaffino, S.; Reggiani, C., Fiber types in mammalian skeletal muscles. *Physiological reviews* **2011**, 91 (4), 1447-1531.
238. Winter, J. O.; Schmidt, C. E., Biomimetic strategies and applications in the nervous system. *Biomimetic materials and design* **2002**, 375-415.
239. Schmidt, C. E.; Leach, J. B., Neural tissue engineering: strategies for repair and regeneration. *Annual review of biomedical engineering* **2003**, 5 (1), 293-347.
240. Zimmermann, W.-H.; Melnychenko, I.; Eschenhagen, T., Engineered heart tissue for regeneration of diseased hearts. *Biomaterials* **2004**, 25 (9), 1639-1647.
241. Böttcher-Haberzeth, S.; Biedermann, T.; Reichmann, E., Tissue engineering of skin. *Burns* **2010**, 36 (4), 450-460.
242. MacNeil, S., Progress and opportunities for tissue-engineered skin. *Nature* **2007**, 445 (7130), 874-880.
243. Li, R.; Horgan, C. C.; Long, B.; Rodriguez, A. L.; Mather, L.; Barrow, C. J.; Nisbet, D. R.; Williams, R. J., Tuning the mechanical and morphological properties of self-assembled peptide hydrogels via control over the gelation mechanism through regulation of ionic strength and the rate of pH change. *RSC advances* **2015**, 5 (1), 301-307.
244. Stupka, N.; Kintakas, C.; White, J. D.; Fraser, F. W.; Hanciu, M.; Aramaki-Hattori, N.; Martin, S.; Coles, C.; Collier, F.; Ward, A. C., Versican processing by a disintegrin-like and metalloproteinase domain with thrombospondin-1 repeats proteinases-5 and-15 facilitates myoblast fusion. *Journal of Biological Chemistry* **2013**, 288 (3), 1907-1917.
245. McCulloch, D. R.; Nelson, C. M.; Dixon, L. J.; Silver, D. L.; Wylie, J. D.; Lindner, V.; Sasaki, T.; Cooley, M. A.; Argraves, W. S.; Apte, S. S., ADAMTS metalloproteinases generate active versican fragments that regulate interdigital web regression. *Developmental cell* **2009**, 17 (5), 687-698.
246. Langer, R.; Vacanti, J., Advances in tissue engineering. *Journal of pediatric surgery* **2016**, 51 (1), 8-12.

247. Miserez, A.; Weaver, J. C.; Chaudhuri, O., Biological materials and molecular biomimetics—filling up the empty soft materials space for tissue engineering applications. *Journal of Materials Chemistry B* **2015**, 3 (1), 13-24.
248. Sheikhpour, M.; Barani, L.; Kasaeian, A., Biomimetics in drug delivery systems: A critical review. *Journal of Controlled Release* **2017**, 253, 97-109.
249. Pankov, R.; Yamada, K. M., Fibronectin at a glance. *Journal of cell science* **2002**, 115 (20), 3861-3863.
250. Hersel, U.; Dahmen, C.; Kessler, H., RGD modified polymers: biomaterials for stimulated cell adhesion and beyond. *Biomaterials* **2003**, 24 (24), 4385-4415.
251. Altroff, H.; Van der Walle, C. F.; Asselin, J.; Fairless, R.; Campbell, I. D.; Mardon, H. J., The eighth FIII domain of human fibronectin promotes integrin $\alpha 5 \beta 1$ binding via stabilization of the ninth FIII domain. *Journal of Biological Chemistry* **2001**.
252. Kao, W. J.; Lee, D.; Schense, J. C.; Hubbell, J. A., Fibronectin modulates macrophage adhesion and FBGC formation: the role of RGD, PHSRN, and PRRARV domains. *Journal of biomedical materials research* **2001**, 55 (1), 79-88.
253. Engler, A. J.; Sen, S.; Sweeney, H. L.; Discher, D. E., Matrix elasticity directs stem cell lineage specification. *Cell* **2006**, 126 (4), 677-689.
254. Li, X.; Chen, S.; Li, J.; Wang, X.; Zhang, J.; Kawazoe, N.; Chen, G., 3D culture of chondrocytes in gelatin hydrogels with different stiffness. *Polymers* **2016**, 8 (8), 269.
255. Levental, I.; Georges, P. C.; Janmey, P. A., Soft biological materials and their impact on cell function. *Soft Matter* **2007**, 3 (3), 299-306.
256. Wang, J.; Wang, Z.; Gao, J.; Wang, L.; Yang, Z.; Kong, D.; Yang, Z., Incorporation of supramolecular hydrogels into agarose hydrogels—a potential drug delivery carrier. *Journal of Materials Chemistry* **2009**, 19 (42), 7892-7896.
257. Kloareg, B.; Demarty, M.; Mabeau, S., Polyanionic characteristics of purified sulphated homofucans from brown algae. *International Journal of Biological Macromolecules* **1986**, 8 (6), 380-386.
258. Wang, J.; Zhang, Q.; Zhang, Z.; Song, H.; Li, P., Potential antioxidant and anticoagulant capacity of low molecular weight fucoidan fractions extracted from *Laminaria japonica*. *International journal of biological macromolecules* **2010**, 46 (1), 6-12.
259. Li, B.; Lu, F.; Wei, X.; Zhao, R., Fucoidan: structure and bioactivity. *Molecules* **2008**, 13 (8), 1671-1695.
260. Irhimeh, M. R.; Fitton, J. H.; Ko, K.-H.; Lowenthal, R. M.; Nordon, R. E., Formation of an adherent hematopoietic expansion culture using fucoidan. *Annals of hematology* **2011**, 90 (9), 1005-1015.
261. Murakami, K.; Aoki, H.; Nakamura, S.; Nakamura, S.-i.; Takikawa, M.; Hanzawa, M.; Kishimoto, S.; Hattori, H.; Tanaka, Y.; Kiyosawa, T., Hydrogel blends of chitin/chitosan, fucoidan and alginate as healing-impaired wound dressings. *Biomaterials* **2010**, 31 (1), 83-90.
262. Sezer, A. D.; Cevher, E.; Hatipoğlu, F.; Oğurtan, Z.; Baş, A. L.; Akbuğa, J., Preparation of fucoidan-chitosan hydrogel and its application as burn healing accelerator on rabbits. *Biological and Pharmaceutical Bulletin* **2008**, 31 (12), 2326-2333.
263. Nakamura, S.; Nambu, M.; Ishizuka, T.; Hattori, H.; Kanatani, Y.; Takase, B.; Kishimoto, S.; Amano, Y.; Aoki, H.; Kiyosawa, T., Effect of controlled release of fibroblast growth factor-2 from chitosan/fucoidan micro complex-hydrogel on in vitro and in vivo vascularization. *Journal of Biomedical Materials Research Part A: An Official Journal of The Society for Biomaterials, The Japanese Society for Biomaterials, and The Australian Society for Biomaterials and the Korean Society for Biomaterials* **2008**, 85 (3), 619-627.
264. Belford, D. A.; Hendry, I. A.; Parish, C. R., Investigation of the ability of several naturally occurring and synthetic polyanions to bind to and potentiate the biological activity of acidic fibroblast growth factor. *Journal of cellular physiology* **1993**, 157 (1), 184-189.
265. Li, R.; Pavuluri, S.; Bruggeman, K.; Long, B. M.; Parnell, A. J.; Martel, A.; Parnell, S. R.; Pfeffer, F. M.; Dennison, A. J.; Nicholas, K. R., Coassembled nanostructured bioscaffold reduces the expression of proinflammatory cytokines to induce apoptosis in epithelial cancer cells. *Nanomedicine: Nanotechnology, Biology and Medicine* **2016**, 12 (5), 1397-1407.

266. Ulijn, R. V.; Smith, A. M., Designing peptide based nanomaterials. *Chemical Society Reviews* **2008**, 37 (4), 664-675.
267. Partlow, B. P.; Hanna, C. W.; Rnjak-Kovacina, J.; Moreau, J. E.; Applegate, M. B.; Burke, K. A.; Marelli, B.; Mitropoulos, A. N.; Omenetto, F. G.; Kaplan, D. L., Highly tunable elastomeric silk biomaterials. *Advanced functional materials* **2014**, 24 (29), 4615-4624.
268. Zhu, Y.; Jiang, H.; Ye, S.-H.; Yoshizumi, T.; Wagner, W. R., Tailoring the degradation rates of thermally responsive hydrogels designed for soft tissue injection by varying the autocatalytic potential. *Biomaterials* **2015**, 53, 484-493.
269. MacArthur, M. W.; Thornton, J. M., Influence of proline residues on protein conformation. *Journal of molecular biology* **1991**, 218 (2), 397-412.
270. Bhattacharyya, R.; Chakrabarti, P., Stereospecific interactions of proline residues in protein structures and complexes. *Journal of molecular biology* **2003**, 331 (4), 925-940.
271. Zanuy, D.; Poater, J.; Sola, M.; Hamley, I. W.; Alemán, C., Fmoc-RGDS based fibrils: atomistic details of their hierarchical assembly. *Physical Chemistry Chemical Physics* **2016**, 18 (2), 1265-1278.
272. Kubelka, J.; Keiderling, T. A., Differentiation of β -sheet-forming structures: Ab initio-based simulations of IR absorption and vibrational CD for model peptide and protein β -sheets. *Journal of the American Chemical Society* **2001**, 123 (48), 12048-12058.
273. Dong, A.; Huang, P.; Caughey, W. S., Protein secondary structures in water from second-derivative amide I infrared spectra. *Biochemistry* **1990**, 29 (13), 3303-3308.
274. Kelly, S. M.; Jess, T. J.; Price, N. C., How to study proteins by circular dichroism. *Biochimica et Biophysica Acta (BBA)-Proteins and Proteomics* **2005**, 1751 (2), 119-139.
275. Nasipuri, D., *Stereochemistry of organic compounds: principles and applications*. New Age International: 1994.
276. Mu, X.; Eckes, K. M.; Nguyen, M. M.; Suggs, L. J.; Ren, P., Experimental and computational studies reveal an alternative supramolecular structure for Fmoc-dipeptide self-assembly. *Biomacromolecules* **2012**, 13 (11), 3562-3571.
277. Banerji, B.; Pramanik, S. K.; Pal, U.; Maiti, N. C., Conformation and cytotoxicity of a tetrapeptide constellated with alternative D-and L-proline. *Rsc Advances* **2012**, 2 (17), 6744-6747.
278. Rucker, A. L.; Creamer, T. P., Polyproline II helical structure in protein unfolded states: lysine peptides revisited. *Protein science* **2002**, 11 (4), 980-985.
279. Hirst, A. R.; Roy, S.; Arora, M.; Das, A. K.; Hodson, N.; Murray, P.; Marshall, S.; Javid, N.; Sefcik, J.; Boekhoven, J., Biocatalytic induction of supramolecular order. *Nature chemistry* **2010**, 2 (12), 1089.
280. Williams, R. J.; Smith, A. M.; Collins, R.; Hodson, N.; Das, A. K.; Ulijn, R. V., Enzyme-assisted self-assembly under thermodynamic control. *Nature nanotechnology* **2009**, 4 (1), 19.
281. Mardilovich, A.; Craig, J. A.; McCammon, M. Q.; Garg, A.; Kokkoli, E., Design of a novel fibronectin-mimetic peptide– amphiphile for functionalized biomaterials. *Langmuir* **2006**, 22 (7), 3259-3264.
282. Leahy, D. J.; Aukhil, I.; Erickson, H. P., 2.0 Å crystal structure of a four-domain segment of human fibronectin encompassing the RGD loop and synergy region. *Cell* **1996**, 84 (1), 155-164.
283. Williams, R. J.; Gardiner, J.; Sorensen, A. B.; Marchesan, S.; Mulder, R. J.; McLean, K. M.; Hartley, P. G., Monitoring the early stage self-assembly of enzyme-assisted peptide hydrogels. *Australian Journal of Chemistry* **2013**, 66 (5), 572-578.
284. Chen, L.; Revel, S.; Morris, K.; Spiller, D. G.; Serpell, L. C.; Adams, D. J., Low molecular weight gelator–dextran composites. *Chemical Communications* **2010**, 46 (36), 6738-6740.
285. Das, A. K.; Hirst, A. R.; Ulijn, R. V., Evolving nanomaterials using enzyme-driven dynamic peptide libraries (eDPL). *Faraday discussions* **2009**, 143, 293-303.
286. Ermi, B. D.; Amis, E. J., Domain structures in low ionic strength polyelectrolyte solutions. *Macromolecules* **1998**, 31 (21), 7378-7384.
287. Nierlich, M.; Williams, C.; Boue, F.; Cotton, J.; Daoud, M.; Famoux, B.; Jannink, G.; Picot, C.; Moan, M.; Wolff, C., Small angle neutron scattering by semi-dilute solutions of polyelectrolyte. *Journal de Physique* **1979**, 40 (7), 701-704.
288. Saffer, E. M.; Lackey, M. A.; Griffin, D. M.; Kishore, S.; Tew, G. N.; Bhatia, S. R., SANS study of highly resilient poly (ethylene glycol) hydrogels. *Soft Matter* **2014**, 10 (12), 1905-1916.

289. Chang, Y.; Hu, Y.; Yu, L.; McClements, D. J.; Xu, X.; Liu, G.; Xue, C., Primary structure and chain conformation of fucoidan extracted from sea cucumber *Holothuria tubulosa*. *Carbohydrate polymers* **2016**, *136*, 1091-1097.
290. Williams, R. J.; Hall, T. E.; Glattauer, V.; White, J.; Pasic, P. J.; Sorensen, A. B.; Waddington, L.; McLean, K. M.; Currie, P. D.; Hartley, P. G., The in vivo performance of an enzyme-assisted self-assembled peptide/protein hydrogel. *Biomaterials* **2011**, *32* (22), 5304-5310.
291. Gottarelli, G.; Lena, S.; Masiero, S.; Pieraccini, S.; Spada, G. P., The use of circular dichroism spectroscopy for studying the chiral molecular self-assembly: an overview. *Chirality: The Pharmacological, Biological, and Chemical Consequences of Molecular Asymmetry* **2008**, *20* (3-4), 471-485.
292. Cheng, G.; Castelletto, V.; Moulton, C.; Newby, G.; Hamley, I., Hydrogelation and self-assembly of Fmoc-tripeptides: unexpected influence of sequence on self-assembled fibril structure, and hydrogel modulus and anisotropy. *Langmuir* **2010**, *26* (7), 4990-4998.
293. Xu, X.; Farach-Carson, M. C.; Jia, X., Three-dimensional in vitro tumor models for cancer research and drug evaluation. *Biotechnology advances* **2014**, *32* (7), 1256-1268.
294. Jaganathan, H.; Gage, J.; Leonard, F.; Srinivasan, S.; Souza, G. R.; Dave, B.; Godin, B., Three-dimensional in vitro co-culture model of breast tumor using magnetic levitation. *Scientific reports* **2014**, *4*, 6468.
295. Egeblad, M.; Rasch, M. G.; Weaver, V. M., Dynamic interplay between the collagen scaffold and tumor evolution. *Current opinion in cell biology* **2010**, *22* (5), 697-706.
296. Clark, A. G.; Vignjevic, D. M., Modes of cancer cell invasion and the role of the microenvironment. *Current opinion in cell biology* **2015**, *36*, 13-22.
297. Conklin, M. W.; Eickhoff, J. C.; Riching, K. M.; Pehlke, C. A.; Eliceiri, K. W.; Provenzano, P. P.; Friedl, A.; Keely, P. J., Aligned collagen is a prognostic signature for survival in human breast carcinoma. *The American journal of pathology* **2011**, *178* (3), 1221-1232.
298. Cox, T. R.; Bird, D.; Baker, A.-M.; Barker, H. E.; Ho, M. W.; Lang, G.; Erler, J. T., LOX-mediated collagen crosslinking is responsible for fibrosis-enhanced metastasis. *Cancer research* **2013**, *73* (6), 1721-1732.
299. Charoen, K. M.; Fallica, B.; Colson, Y. L.; Zaman, M. H.; Grinstaff, M. W., Embedded multicellular spheroids as a biomimetic 3D cancer model for evaluating drug and drug-device combinations. *Biomaterials* **2014**, *35* (7), 2264-2271.
300. Yip, D.; Cho, C. H., A multicellular 3D heterospheroid model of liver tumor and stromal cells in collagen gel for anti-cancer drug testing. *Biochemical and biophysical research communications* **2013**, *433* (3), 327-332.
301. Finnberg, N. K.; Gokare, P.; Lev, A.; Grivennikov, S. I.; MacFarlane IV, A. W.; Campbell, K. S.; Winters, R. M.; Kaputa, K.; Farma, J. M.; Abbas, A. E.-S., Application of 3D tumoroid systems to define immune and cytotoxic therapeutic responses based on tumoroid and tissue slice culture molecular signatures. *Oncotarget* **2017**, *8* (40), 66747.
302. Fang, Y.; Eglen, R. M., Three-dimensional cell cultures in drug discovery and development. *SLAS DISCOVERY: Advancing Life Sciences R&D* **2017**, *22* (5), 456-472.
303. Lee, K. Y.; Mooney, D. J., Alginate: properties and biomedical applications. *Progress in polymer science* **2012**, *37* (1), 106-126.
304. Zhou, M.; Smith, A. M.; Das, A. K.; Hodson, N. W.; Collins, R. F.; Ulijn, R. V.; Gough, J. E., Self-assembled peptide-based hydrogels as scaffolds for anchorage-dependent cells. *Biomaterials* **2009**, *30* (13), 2523-2530.
305. Jahan-Abad, A. J.; Negah, S. S.; Ravandi, H. H.; Ghasemi, S.; Borhani-Haghighi, M.; Stummer, W.; Gorji, A.; Ghadiri, M. K., Human Neural Stem/Progenitor Cells Derived From Epileptic Human Brain in a Self-Assembling Peptide Nanoscaffold Improve Traumatic Brain Injury in Rats. *Molecular neurobiology* **2018**, *55* (12), 9122-9138.
306. Wu, G.; Pan, M.; Wang, X.; Wen, J.; Cao, S.; Li, Z.; Li, Y.; Qian, C.; Liu, Z.; Wu, W., Osteogenesis of peripheral blood mesenchymal stem cells in self assembling peptide nanofiber for healing critical size calvarial bony defect. *Scientific reports* **2015**, *5*, 16681.
307. Ando, K.; Imagama, S.; Kobayashi, K.; Ito, K.; Tsushima, M.; Morozumi, M.; Tanaka, S.; Machino, M.; Ota, K.; Nishida, K., Feasibility and effects of a self-assembling peptide as a scaffold in

bone healing: An in vivo study in rabbit lumbar posterolateral fusion and tibial intramedullary models. *Journal of Orthopaedic Research®* **2018**, 36 (12), 3285-3293.

308. Yang, Z.; Zhao, X., A 3D model of ovarian cancer cell lines on peptide nanofiber scaffold to explore the cell-scaffold interaction and chemotherapeutic resistance of anticancer drugs. *International journal of nanomedicine* **2011**, 6, 303.

309. Nath, S.; Devi, G. R., Three-dimensional culture systems in cancer research: Focus on tumor spheroid model. *Pharmacology & therapeutics* **2016**, 163, 94-108.

310. Hur, J.; Park, H. G.; Kim, M. I., Reagentless colorimetric biosensing platform based on nanoceria within an agarose gel matrix. *Biosensors and Bioelectronics* **2017**, 93, 226-233.

311. Hammouda, B., Probing nanoscale structures-the sans toolbox. *National Institute of Standards and Technology* **2008**, 1-717.

312. Wisotzki, E. I.; Tempesti, P.; Fratini, E.; Mayr, S. G., Influence of high energy electron irradiation on the network structure of gelatin hydrogels as investigated by small-angle X-ray scattering (SAXS). *Physical Chemistry Chemical Physics* **2017**, 19 (19), 12064-12074.

313. Schmidt, P. W., Small-angle scattering studies of disordered, porous and fractal systems. *Journal of Applied Crystallography* **1991**, 24 (5), 414-435.

314. Aye, S.-S.; Li, R.; Boyd-Moss, M.; Long, B.; Pavuluri, S.; Bruggeman, K.; Wang, Y.; Barrow, C.; Nisbet, D.; Williams, R., Scaffolds formed via the non-equilibrium supramolecular assembly of the synergistic ECM peptides RGD and PHSRN demonstrate improved cell attachment in 3D. *Polymers* **2018**, 10 (7), 690.

315. Bays, J. L.; DeMali, K. A., Vinculin in cell-cell and cell-matrix adhesions. *Cellular and Molecular Life Sciences* **2017**, 74 (16), 2999-3009.

316. Li, T.; Guo, H.; Song, Y.; Zhao, X.; Shi, Y.; Lu, Y.; Hu, S.; Nie, Y.; Fan, D.; Wu, K., Loss of vinculin and membrane-bound β -catenin promotes metastasis and predicts poor prognosis in colorectal cancer. *Molecular cancer* **2014**, 13 (1), 263.

317. Toma-Jonik, A.; Widlak, W.; Korfanty, J.; Cichon, T.; Smolarczyk, R.; Gogler-Pigłowska, A.; Widlak, P.; Vydra, N., Active heat shock transcription factor 1 supports migration of the melanoma cells via vinculin down-regulation. *Cellular signalling* **2015**, 27 (2), 394-401.

318. Hellman, K.; Alaiya, A. A.; Becker, S.; Lomnytska, M.; Schedvins, K.; Steinberg, W.; Hellström, A.-C.; Andersson, S.; Hellman, U.; Auer, G., Differential tissue-specific protein markers of vaginal carcinoma. *British journal of cancer* **2009**, 100 (8), 1303.

319. Théry, M., Micropatterning as a tool to decipher cell morphogenesis and functions. *J Cell Sci* **2010**, 123 (24), 4201-4213.

320. Zhou, Y.; Chen, H.; Li, H.; Wu, Y., 3D culture increases pluripotent gene expression in mesenchymal stem cells through relaxation of cytoskeleton tension. *Journal of cellular and molecular medicine* **2017**, 21 (6), 1073-1084.

321. Kalluri, R.; Weinberg, R. A., The basics of epithelial-mesenchymal transition. *The Journal of clinical investigation* **2009**, 119 (6), 1420-1428.

322. Yamashita, M.; Ogawa, T.; Zhang, X.; Hanamura, N.; Kashikura, Y.; Takamura, M.; Yoneda, M.; Shiraishi, T., Role of stromal myofibroblasts in invasive breast cancer: stromal expression of alpha-smooth muscle actin correlates with worse clinical outcome. *Breast cancer* **2012**, 19 (2), 170-176.

323. Ulrich, T. A.; Jain, A.; Tanner, K.; MacKay, J. L.; Kumar, S., Probing cellular mechanobiology in three-dimensional culture with collagen-agarose matrices. *Biomaterials* **2010**, 31 (7), 1875-1884.

324. Hynes, R. O., The extracellular matrix: not just pretty fibrils. *Science* **2009**, 326 (5957), 1216-1219.

325. Schenk, V.; Rossegger, E.; Ebner, C.; Bangerl, F.; Reichmann, K.; Hoffmann, B.; Höpfner, M.; Wiesbrock, F., RGD-functionalization of poly (2-oxazoline)-based networks for enhanced adhesion to cancer cells. *Polymers* **2014**, 6 (2), 264-279.

326. Fan, X.; Zhang, W.; Hu, Z.; Li, Z., Facile synthesis of RGD-conjugated unimolecular micelles based on a polyester dendrimer for targeting drug delivery. *Journal of Materials Chemistry B* **2017**, 5 (5), 1062-1072.

327. Gribova, V.; Gauthier-Rouvière, C.; Albigès-Rizo, C.; Auzely-Velty, R.; Picart, C., Effect of RGD functionalization and stiffness modulation of polyelectrolyte multilayer films on muscle cell differentiation. *Acta biomaterialia* **2013**, 9 (5), 6468-6480.

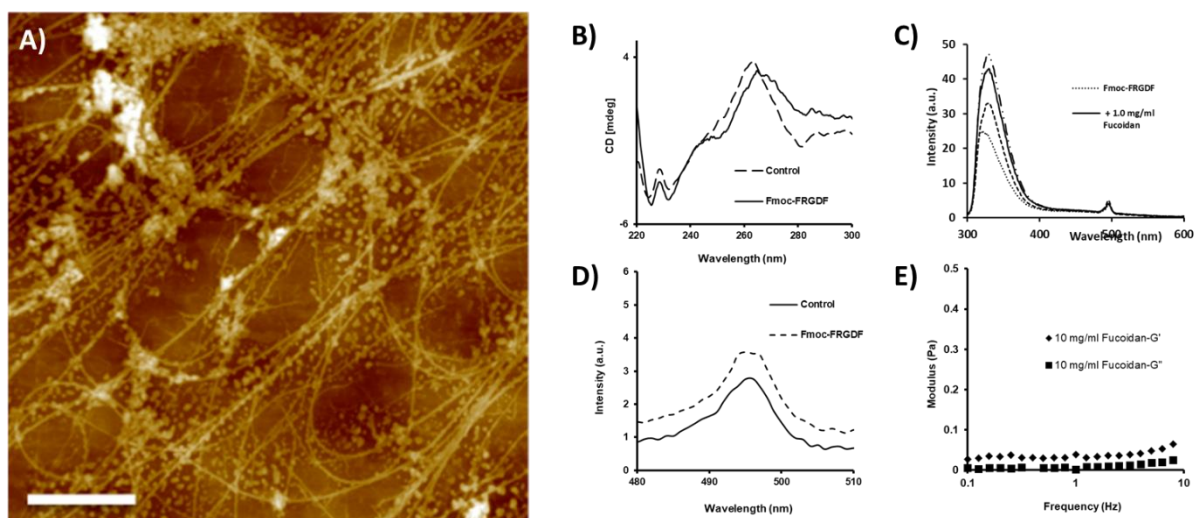
328. Mauri, E.; Sacchetti, A.; Vicario, N.; Peruzzotti-Jametti, L.; Rossi, F.; Pluchino, S., Evaluation of RGD functionalization in hybrid hydrogels as 3D neural stem cell culture systems. *Biomaterials science* **2018**, 6 (3), 501-510.
329. Kudva, A. K.; Luyten, F. P.; Patterson, J., RGD-functionalized polyethylene glycol hydrogels support proliferation and in vitro chondrogenesis of human periosteum-derived cells. *Journal of Biomedical Materials Research Part A* **2018**, 106 (1), 33-42.
330. Gan, D.; Liu, M.; Xu, T.; Wang, K.; Tan, H.; LU, X., Chitosan/biphasic calcium phosphate scaffolds functionalized with BMP-2-encapsulated Nanoparticles and RGD for Bone Regeneration. *Journal of Biomedical Materials Research Part A* **2018**.
331. Hunt, N. C.; Hallam, D.; Karimi, A.; Mellough, C. B.; Chen, J.; Steel, D. H.; Lako, M., 3D culture of human pluripotent stem cells in RGD-alginate hydrogel improves retinal tissue development. *Acta biomaterialia* **2017**, 49, 329-343.
332. Cunha, C.; Panseri, S.; Villa, O.; Silva, D.; Gelain, F., 3D culture of adult mouse neural stem cells within functionalized self-assembling peptide scaffolds. *International journal of nanomedicine* **2011**, 6, 943.
333. Hoglebe, N. J.; Reinhardt, J. W.; Tram, N. K.; Debski, A. C.; Agarwal, G.; Reilly, M. A.; Gooch, K. J., Independent control of matrix adhesiveness and stiffness within a 3D self-assembling peptide hydrogel. *Acta biomaterialia* **2018**, 70, 110-119.
334. Tsutsumi, H.; Kawamura, M.; Mihara, H., Osteoblastic differentiation on hydrogels fabricated from Ca²⁺-responsive self-assembling peptides functionalized with bioactive peptides. *Bioorganic & Medicinal Chemistry* **2018**, 26 (12), 3126-3132.
335. Maclean, F. L.; Wang, Y.; Walker, R.; Horne, M. K.; Williams, R. J.; Nisbet, D. R., Reducing astrocytic scarring after traumatic brain injury with a multifaceted anti-inflammatory hydrogel system. *ACS Biomaterials Science & Engineering* **2017**, 3 (10), 2542-2549.
336. Chow, L. W.; Bitton, R.; Webber, M. J.; Carvajal, D.; Shull, K. R.; Sharma, A. K.; Stupp, S. I., A bioactive self-assembled membrane to promote angiogenesis. *Biomaterials* **2011**, 32 (6), 1574-1582.
337. Li, R.; Boyd-Moss, M.; Long, B.; Martel, A.; Parnell, A.; Dennison, A. J.; Barrow, C. J.; Nisbet, D. R.; Williams, R. J., Facile Control over the Supramolecular Ordering of Self-assembled Peptide Scaffolds by Simultaneous Assembly with a Polysaccharide. *Scientific reports* **2017**, 7 (1), 4797.
338. Wight, T. N., Versican: a versatile extracellular matrix proteoglycan in cell biology. *Current opinion in cell biology* **2002**, 14 (5), 617-623.
339. Rodriguez, A. L.; Wang, T.-Y.; Bruggeman, K. F.; Li, R.; Williams, R. J.; Parish, C. L.; Nisbet, D. R., Tailoring minimalist self-assembling peptides for localized viral vector gene delivery. *Nano Research* **2016**, 9 (3), 674-684.
340. Schöneich, C.; Dremina, E.; Galeva, N.; Sharov, V., Apoptosis in differentiating C2C12 muscle cells selectively targets Bcl-2-deficient myotubes. *Apoptosis* **2014**, 19 (1), 42-57.
341. Bellis, S. L., Advantages of RGD peptides for directing cell association with biomaterials. *Biomaterials* **2011**, 32 (18), 4205-4210.
342. Liu, X.; Holzwarth, J. M.; Ma, P. X., Functionalized synthetic biodegradable polymer scaffolds for tissue engineering. *Macromolecular bioscience* **2012**, 12 (7), 911-919.
343. Stabenfeldt, S. E.; García, A. J.; LaPlaca, M. C., Thermoreversible laminin-functionalized hydrogel for neural tissue engineering. *Journal of Biomedical Materials Research Part A: An Official Journal of The Society for Biomaterials, The Japanese Society for Biomaterials, and The Australian Society for Biomaterials and the Korean Society for Biomaterials* **2006**, 77 (4), 718-725.
344. Foulcer, S. J.; Nelson, C. M.; Quintero, M. V.; Kuberan, B.; Larkin, J.; Dours-Zimmermann, M. T.; Zimmermann, D. R.; Apte, S. S., Determinants of versican V1 processing by the metalloproteinase ADAMTS5. *Journal of Biological Chemistry* **2014**, jbc. M114. 573287.
345. Nandadasa, S.; Foulcer, S.; Apte, S. S., The multiple, complex roles of versican and its proteolytic turnover by ADAMTS proteases during embryogenesis. *Matrix Biology* **2014**, 35, 34-41.
346. Mears, L. L.; Draper, E. R.; Castilla, A. M.; Su, H.; Dietrich, B.; Nolan, M. C.; Smith, G. N.; Douth, J.; Rogers, S.; Akhtar, R., Drying affects the fiber network in low molecular weight hydrogels. *Biomacromolecules* **2017**, 18 (11), 3531-3540.
347. Pelton, J. T.; McLean, L. R., Spectroscopic methods for analysis of protein secondary structure. *Analytical biochemistry* **2000**, 277 (2), 167-176.

348. Kim, K.-J.; Lee, O.-H.; Lee, B.-Y., Low-molecular-weight fucoidan regulates myogenic differentiation through the mitogen-activated protein kinase pathway in C2C12 cells. *British journal of nutrition* **2011**, *106* (12), 1836-1844.
349. Velleman, S. G.; Sporer, K. R.; Ernst, C. W.; Reed, K. M.; Strasburg, G., Versican, matrix Gla protein, and death-associated protein expression affect muscle satellite cell proliferation and differentiation. *Poultry science* **2012**, *91* (8), 1964-1973.
350. Widhe, M.; Shalaly, N. D.; Hedhammar, M., A fibronectin mimetic motif improves integrin mediated cell biding to recombinant spider silk matrices. *Biomaterials* **2016**, *74*, 256-266.
351. Kim, W.; Kim, M.; Kim, G. H., 3D-Printed Biomimetic Scaffold Simulating Microfibril Muscle Structure. *Advanced Functional Materials* **2018**, 1800405.
352. Garcia, A. J.; Vega, M. D.; Boettiger, D., Modulation of cell proliferation and differentiation through substrate-dependent changes in fibronectin conformation. *Molecular biology of the cell* **1999**, *10* (3), 785-798.
353. Lan, M. A.; Gersbach, C. A.; Michael, K. E.; Keselowsky, B. G.; García, A. J., Myoblast proliferation and differentiation on fibronectin-coated self assembled monolayers presenting different surface chemistries. *Biomaterials* **2005**, *26* (22), 4523-4531.
354. Liu, J. M.; Bignon, J.; Haroun-Bouhedja, F.; Bittoun, P.; Vassy, J.; Fermandjian, S.; Wdzieczak-Bakala, J.; Boisson-Vidal, C., Inhibitory effect of fucoidan on the adhesion of adenocarcinoma cells to fibronectin. *Anticancer research* **2005**, *25* (3B), 2129-2133.
355. Evanko, S. P.; Potter-Perigo, S.; Bollyky, P. L.; Nepom, G. T.; Wight, T. N., Hyaluronan and versican in the control of human T-lymphocyte adhesion and migration. *Matrix Biology* **2012**, *31* (2), 90-100.
356. Suntornnond, R.; An, J.; Chua, C. K., Bioprinting of thermoresponsive hydrogels for next generation tissue engineering: a review. *Macromolecular Materials and Engineering* **2017**, *302* (1), 1600266.
357. Wisotzki, E. I.; Hennes, M.; Schuldt, C.; Engert, F.; Knolle, W.; Decker, U.; Käs, J. A.; Zink, M.; Mayr, S. G., Tailoring the material properties of gelatin hydrogels by high energy electron irradiation. *Journal of Materials Chemistry B* **2014**, *2* (27), 4297-4309.
358. Reddy, N.; Reddy, R.; Jiang, Q., Crosslinking biopolymers for biomedical applications. *Trends in biotechnology* **2015**, *33* (6), 362-369.
359. Kishan, A.; Nezarati, R.; Radzicki, C.; Renfro, A.; Robinson, J.; Whitely, M.; Cosgriff-Hernandez, E., In situ crosslinking of electrospun gelatin for improved fiber morphology retention and tunable degradation. *Journal of Materials Chemistry B* **2015**, *3* (40), 7930-7938.
360. Zhang, Y.; Venugopal, J.; Huang, Z.-M.; Lim, C.; Ramakrishna, S., Crosslinking of the electrospun gelatin nanofibers. *Polymer* **2006**, *47* (8), 2911-2917.
361. Liang, H. C.; Chang, W. H.; Liang, H. F.; Lee, M. H.; Sung, H. W., Crosslinking structures of gelatin hydrogels crosslinked with genipin or a water-soluble carbodiimide. *Journal of Applied Polymer Science* **2004**, *91* (6), 4017-4026.
362. Wisotzki, E. I.; Friedrich, R. P.; Weidt, A.; Alexiou, C.; Mayr, S. G.; Zink, M., Cellular Response to Reagent-Free Electron-Irradiated Gelatin Hydrogels. *Macromolecular bioscience* **2016**, *16* (6), 914-924.
363. Singh, R.; Singh, D.; Singh, A., Radiation sterilization of tissue allografts: A review. *World journal of radiology* **2016**, *8* (4), 355.
364. Van Den Bulcke, A. I.; Bogdanov, B.; De Rooze, N.; Schacht, E. H.; Cornelissen, M.; Berghmans, H., Structural and rheological properties of methacrylamide modified gelatin hydrogels. *Biomacromolecules* **2000**, *1* (1), 31-38.
365. Ying, G.; Jiang, N.; Yu, C.; Zhang, Y. S., Three-dimensional bioprinting of gelatin methacryloyl (GelMA). *Bio-Design and Manufacturing* **2018**, *1* (4), 215-224.
366. Yue, K.; Trujillo-de Santiago, G.; Alvarez, M. M.; Tamayol, A.; Annabi, N.; Khademhosseini, A., Synthesis, properties, and biomedical applications of gelatin methacryloyl (GelMA) hydrogels. *Biomaterials* **2015**, *73*, 254-271.
367. Chen, Y. C.; Lin, R. Z.; Qi, H.; Yang, Y.; Bae, H.; Melero-Martin, J. M.; Khademhosseini, A., Functional human vascular network generated in photocrosslinkable gelatin methacrylate hydrogels. *Advanced functional materials* **2012**, *22* (10), 2027-2039.

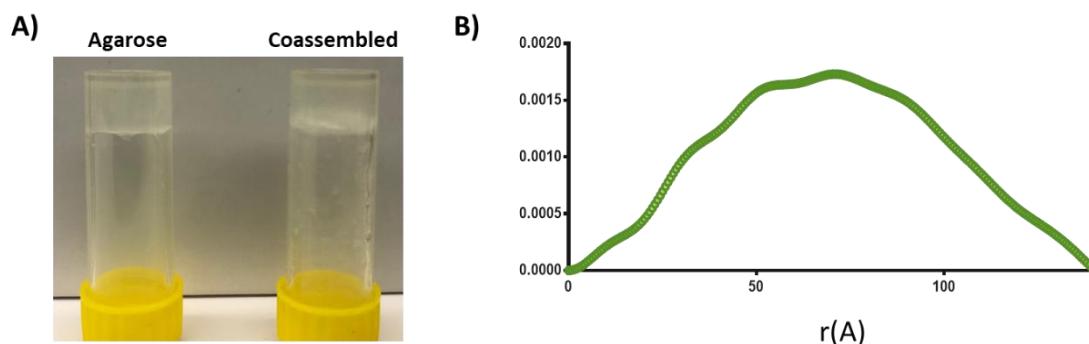
368. Nichol, J. W.; Koshy, S. T.; Bae, H.; Hwang, C. M.; Yamanlar, S.; Khademhosseini, A., Cell-laden microengineered gelatin methacrylate hydrogels. *Biomaterials* **2010**, *31* (21), 5536-5544.
369. Gu, Y.; Zhang, L.; Du, X.; Fan, Z.; Wang, L.; Sun, W.; Cheng, Y.; Zhu, Y.; Chen, C., Reversible physical crosslinking strategy with optimal temperature for 3D bioprinting of human chondrocyte-laden gelatin methacryloyl bioink. *Journal of biomaterials applications* **2018**, *33* (5), 609-618.
370. D O'Connell, C.; Onofrillo, C.; Duchi, S.; Li, X.; Zhang, Y.; Tian, P.; Lu, L.; Trengove, A.; Quigley, A.; Gambhir, S., Evaluation of sterilisation methods for bio-ink components: gelatin, gelatin methacryloyl, hyaluronic acid and hyaluronic acid methacryloyl. *Biofabrication* **2019**.
371. Bigi, A.; Cojazzi, G.; Panzavolta, S.; Rubini, K.; Roveri, N., Mechanical and thermal properties of gelatin films at different degrees of glutaraldehyde crosslinking. *Biomaterials* **2001**, *22* (8), 763-768.
372. Paar, A. Anton Paar technical document - Amplitude sweeps. <https://wiki.anton-paar.com/en/amplitude-sweeps/>.
373. Leijten, J.; Seo, J.; Yue, K.; Trujillo-de Santiago, G.; Tamayol, A.; Ruiz-Esparza, G. U.; Shin, S. R.; Sharifi, R.; Noshadi, I.; Álvarez, M. M., Spatially and temporally controlled hydrogels for tissue engineering. *Materials Science and Engineering: R: Reports* **2017**, *119*, 1-35.
374. Kesti, M.; Eberhardt, C.; Pagliccia, G.; Kenkel, D.; Grande, D.; Boss, A.; Zenobi-Wong, M., Bioprinting complex cartilaginous structures with clinically compliant biomaterials. *Advanced Functional Materials* **2015**, *25* (48), 7406-7417.
375. Campbell, P. G.; Miller, E. D.; Fisher, G. W.; Walker, L. M.; Weiss, L. E., Engineered spatial patterns of FGF-2 immobilized on fibrin direct cell organization. *Biomaterials* **2005**, *26* (33), 6762-6770.
376. Aldana, A. A.; Malatto, L.; Rehman, M. A. U.; Boccaccini, A. R.; Abraham, G. A., Fabrication of Gelatin Methacrylate (GelMA) Scaffolds with Nano-and Micro-Topographical and Morphological Features. *Nanomaterials* **2019**, *9* (1), 120.
377. Shao, Y.; Fu, J., Integrated micro/nanoengineered functional biomaterials for cell mechanics and mechanobiology: a materials perspective. *Advanced Materials* **2014**, *26* (10), 1494-1533.
378. Li, L.; Eyckmans, J.; Chen, C. S., Designer biomaterials for mechanobiology. *Nature materials* **2017**, *16* (12), 1164.
379. De Santis, E.; Ryadnov, M. G., Peptide self-assembly for nanomaterials: the old new kid on the block. *Chemical Society Reviews* **2015**, *44* (22), 8288-8300.
380. Rodriguez, A.; Bruggeman, K.; Wang, Y.; Wang, T.; Williams, R.; Parish, C.; Nisbet, D., Using minimalist self-assembling peptides as hierarchical scaffolds to stabilise growth factors and promote stem cell integration in the injured brain. *Journal of tissue engineering and regenerative medicine* **2018**, *12* (3), e1571-e1579.
381. Li, R.; McRae, N. L.; McCulloch, D. R.; Boyd-Moss, M.; Barrow, C. J.; Nisbet, D. R.; Stupka, N.; Williams, R. J., Large and small assembly: Combining functional macromolecules with small peptides to control the morphology of skeletal muscle progenitor cells. *Biomacromolecules* **2018**, *19* (3), 825-837.
382. Çelik, E.; Bayram, C.; Akçapınar, R.; Türk, M.; Denkbaş, E. B., The effect of calcium chloride concentration on alginate/Fmoc-diphenylalanine hydrogel networks. *Materials Science and Engineering: C* **2016**, *66*, 221-229.
383. Hule, R. A.; Nagarkar, R. P.; Altunbas, A.; Ramay, H. R.; Branco, M. C.; Schneider, J. P.; Pochan, D. J., Correlations between structure, material properties and bioproperties in self-assembled β -hairpin peptide hydrogels. *Faraday discussions* **2008**, *139*, 251-264.
384. Lindemann, B.; Schröder, U. P.; Oppermann, W., Influence of the cross-linker reactivity on the formation of inhomogeneities in hydrogels. *Macromolecules* **1997**, *30* (14), 4073-4077.
385. Nair, K.; Gandhi, M.; Khalil, S.; Yan, K. C.; Marcolongo, M.; Barbee, K.; Sun, W., Characterization of cell viability during bioprinting processes. *Biotechnology Journal: Healthcare Nutrition Technology* **2009**, *4* (8), 1168-1177.
386. Gao, T.; Gillispie, G. J.; Copus, J. S.; Seol, Y.-J.; Atala, A.; Yoo, J. J.; Lee, S. J., Optimization of gelatin-alginate composite bioink printability using rheological parameters: A systematic approach. *Biofabrication* **2018**, *10* (3), 034106.
387. Chan, K. H.; Lee, W. H.; Zhuo, S.; Ni, M., Harnessing supramolecular peptide nanotechnology in biomedical applications. *International journal of nanomedicine* **2017**, *12*, 1171.

388. Zhuang, P.; Sun, A. X.; An, J.; Chua, C. K.; Chew, S. Y., 3D neural tissue models: From spheroids to bioprinting. *Biomaterials* **2018**, *154*, 113-133.
389. Hsieh, F.-Y.; Lin, H.-H.; Hsu, S.-h., 3D bioprinting of neural stem cell-laden thermoresponsive biodegradable polyurethane hydrogel and potential in central nervous system repair. *Biomaterials* **2015**, *71*, 48-57.
390. Yoo, J.; Kim, H. S.; Hwang, D. Y., Stem cells as promising therapeutic options for neurological disorders. *Journal of cellular biochemistry* **2013**, *114* (4), 743-753.
391. Dawson, E.; Mapili, G.; Erickson, K.; Taqvi, S.; Roy, K., Biomaterials for stem cell differentiation. *Advanced drug delivery reviews* **2008**, *60* (2), 215-228.
392. Hsieh, F.-Y.; Hsu, S.-h., 3D bioprinting: a new insight into the therapeutic strategy of neural tissue regeneration. *Organogenesis* **2015**, *11* (4), 153-158.
393. Stratesteffen, H.; Köpf, M.; Kreimendahl, F.; Blaeser, A.; Jockenhoevel, S.; Fischer, H., GelMA-collagen blends enable drop-on-demand 3D printability and promote angiogenesis. *Biofabrication* **2017**, *9* (4), 045002.
394. Shao, L.; Gao, Q.; Zhao, H.; Xie, C.; Fu, J.; Liu, Z.; Xiang, M.; He, Y., Fiber-based mini tissue with morphology-controllable GelMA microfibers. *Small* **2018**, *14* (44), 1802187.
395. García-Lizarribar, A.; Fernández-Garibay, X.; Velasco-Mallorquí, F.; Castaño, A. G.; Samitier, J.; Ramon-Azcon, J., Composite Biomaterials as Long-Lasting Scaffolds for 3D Bioprinting of Highly Aligned Muscle Tissue. *Macromolecular bioscience* **2018**, *18* (10), 1800167.
396. Levato, R.; Webb, W. R.; Otto, I. A.; Mensinga, A.; Zhang, Y.; van Rijen, M.; van Weeren, R.; Khan, I. M.; Malda, J., The bio in the ink: cartilage regeneration with bioprintable hydrogels and articular cartilage-derived progenitor cells. *Acta biomaterialia* **2017**, *61*, 41-53.
397. Zhu, W.; Harris, B. T.; Zhang, L. G. In *Gelatin methacrylamide hydrogel with graphene nanoplatelets for neural cell-laden 3D bioprinting*, Engineering in Medicine and Biology Society (EMBC), 2016 IEEE 38th Annual International Conference of the, IEEE: 2016; pp 4185-4188.
398. Arab, W.; Rauf, S.; Al-Harbi, O.; Hauser, C. A., Novel ultrashort self-assembling peptide bioinks for 3D culture of muscle myoblast cells. *Int. J. Bioprint.* **2018**, *4*, 129.
399. Loo, Y.; Hauser, C. A., Bioprinting synthetic self-assembling peptide hydrogels for biomedical applications. *Biomedical Materials* **2015**, *11* (1), 014103.
400. Rutz, A. L.; Hyland, K. E.; Jakus, A. E.; Burghardt, W. R.; Shah, R. N., A multimaterial bioink method for 3D printing tunable, cell-compatible hydrogels. *Advanced Materials* **2015**, *27* (9), 1607-1614.
401. Knowlton, S.; Anand, S.; Shah, T.; Tasoglu, S., Bioprinting for neural tissue engineering. *Trends in neurosciences* **2018**, *41* (1), 31-46.

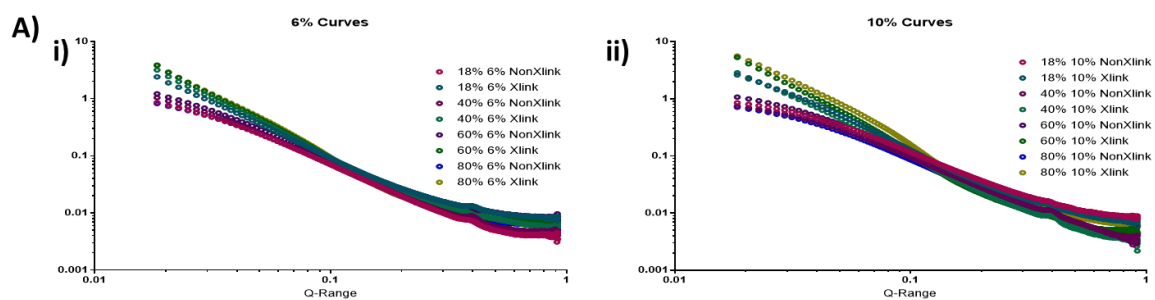
APPENDIX



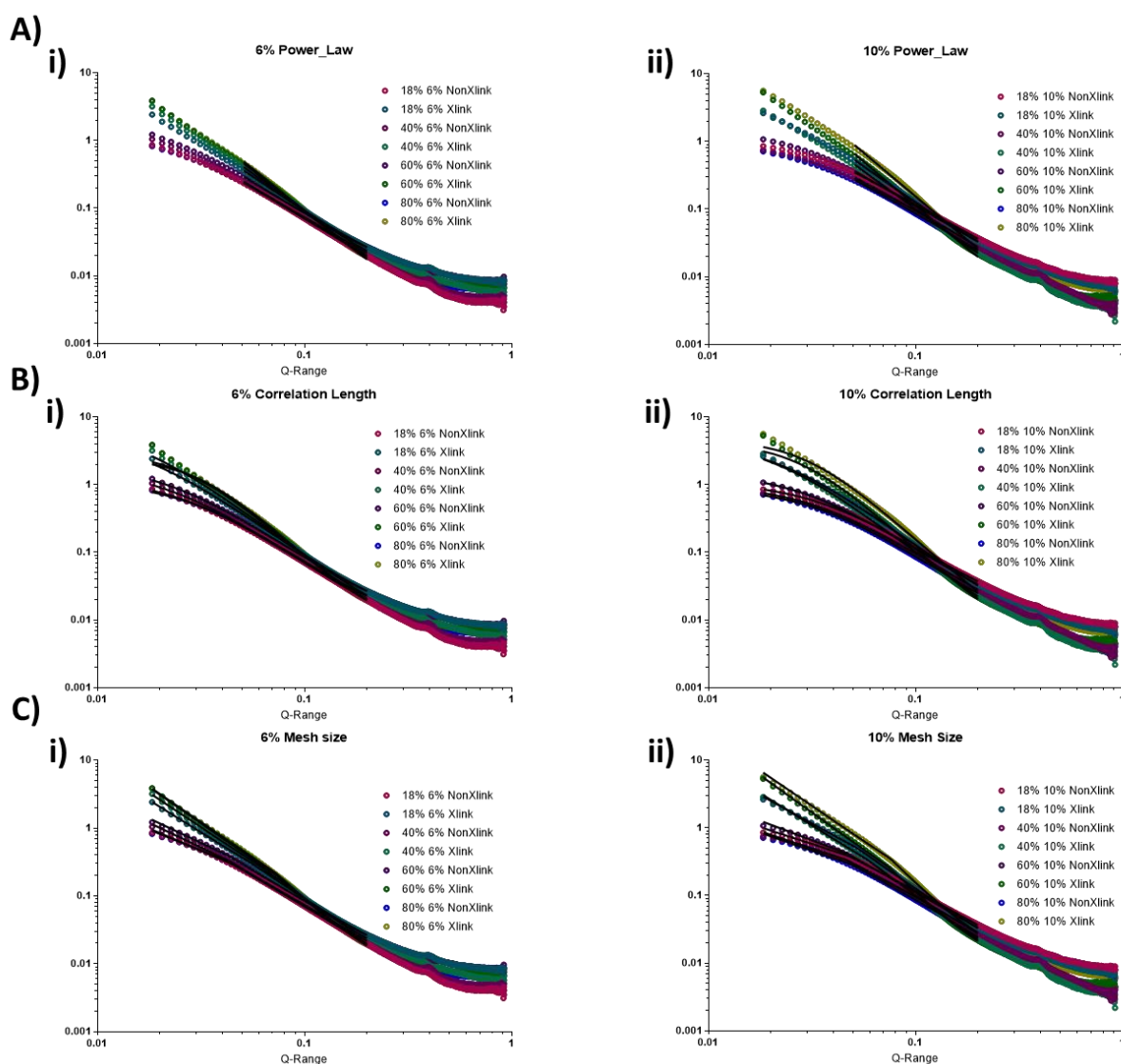
Supplementary Figure S - 1 – Structure of post-assembled Fmoc-FRGDF + fucoidan hydrogels. A) AFM of post-assembled Fmoc-FRGDF + fucoidan network showing lack of bundle formation and presence of aggregates. B) CD spectra for the control gel (fucoidan added post assembly) vs. Fmoc-FRGDF C) full fluorescence emission spectra for the samples D) Control vs Fmoc-FRGDF of the feature centred on 495 nm E) Frequency sweep analysis of a solution of 10 mg/mL fucoidan showing no significant elastic contribution to the system.



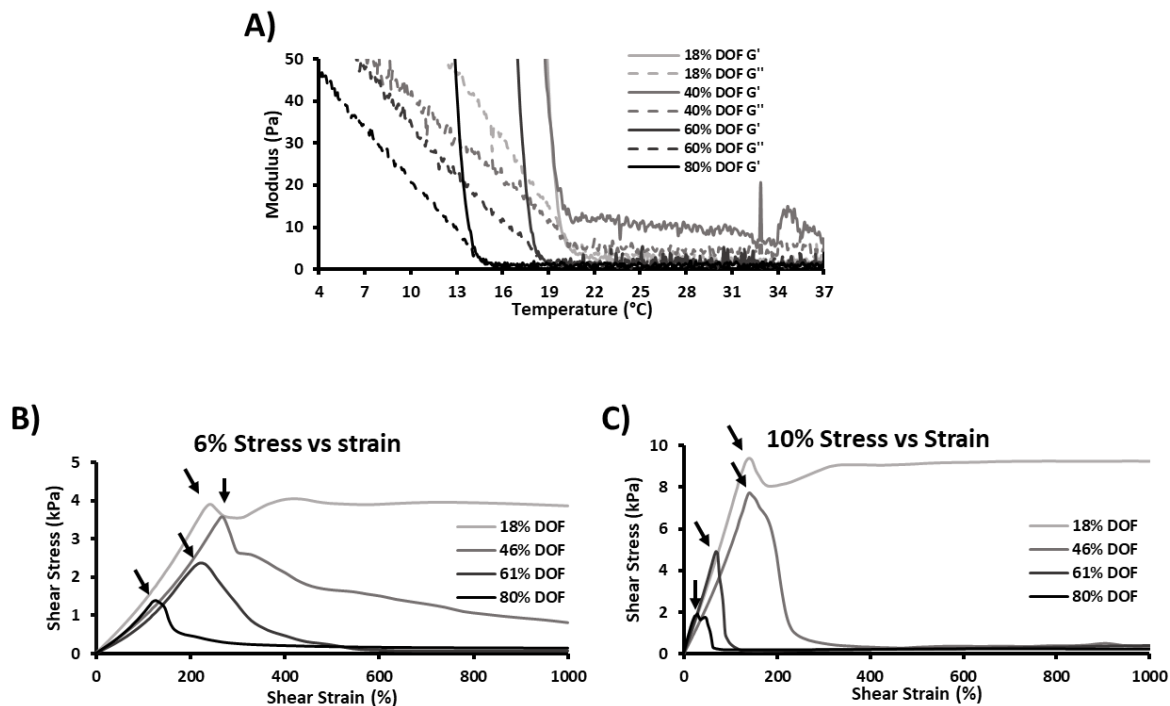
Supplementary Figure S - 2 – Structural properties of agarose and Fmoc-FRGDF/Fmoc-DIKVAV coassembled hydrogels. A) Inverted hydrogels showing structural stability, B) Resultant $P(r)$ curve from IFT $P(r)$ analysis of Fmoc-FRGDF/Fmoc-DIKVAV coassembled hydrogel SAXs Data.



Supplementary Figure S - 3 – Small-angle X-ray scattering curves. A) 6% GelMA Hydrogels, and B) 10% GelMA Hydrogels.



Supplementary Figure S - 4 – Fitting of small-angle X-ray scattering curves. A) Fitting for power-law model (mass fractal dimension) in i) 6% GelMA Hydrogels, and ii) 10% GelMA Hydrogels. B) Fitting for correlation length model in i) 6% GelMA Hydrogels, and ii) 10% GelMA Hydrogels. C) Fitting for two-power model (mesh size) in i) 6% GelMA Hydrogels, and ii) 10% GelMA Hydrogels.



Supplementary Figure S - 5 – Viscoelastic properties of GelMA with differing DoFs A) G' and G'' response to temperature change showing lack of traditional fluidic state of some DoF samples. B) Complex Stress response to strain in 6% GelMA samples showing effective yield point (arrows). C) Complex Stress response to strain in 10% GelMA samples showing effective yield point (arrows).

Supplementary Table S - 1 – Comparison of Loss tangent < 1 and Loss tangent < 0.1 in 6% GelMA hydrogels.

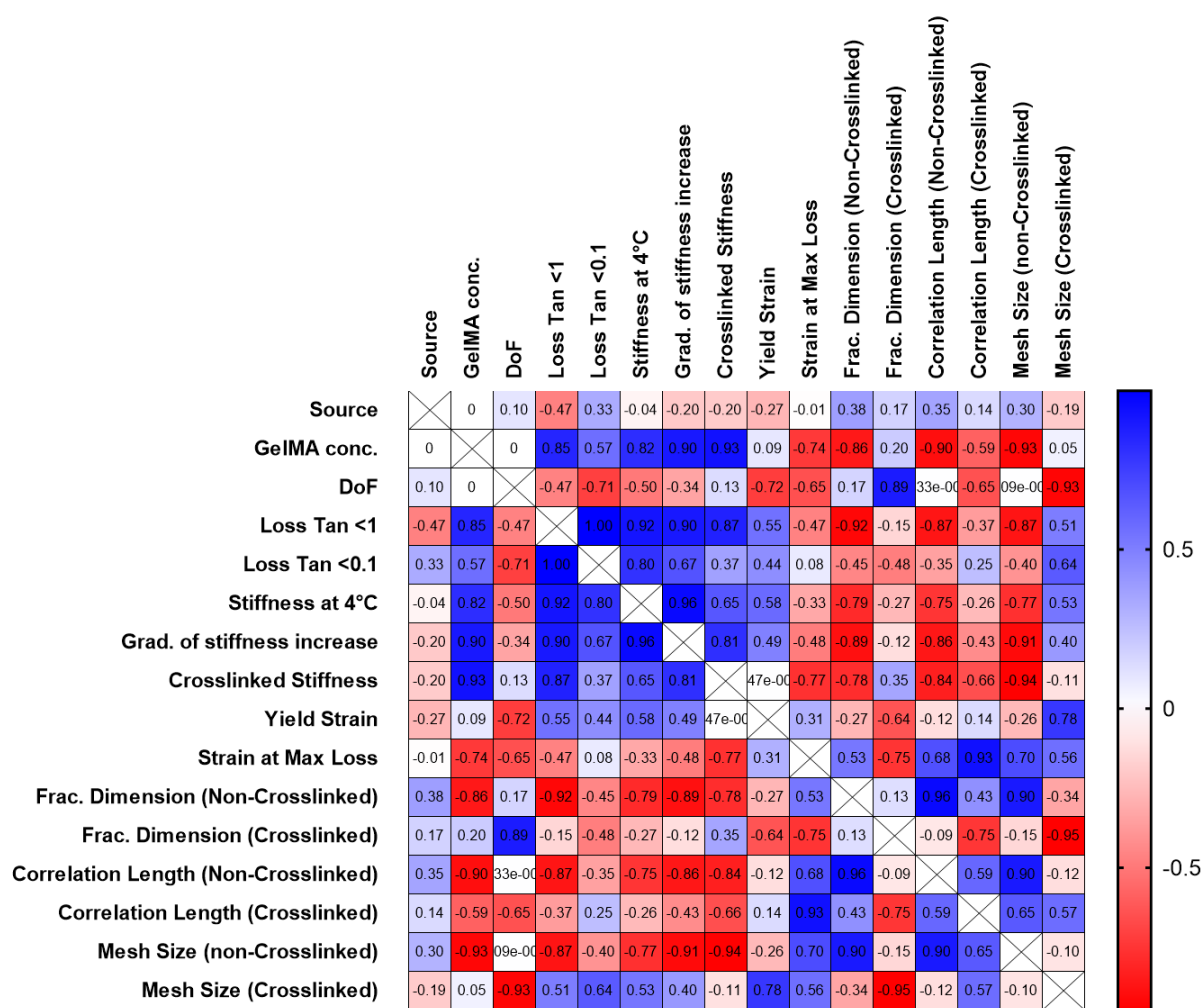
DoF	Loss tangent < 1	Loss tangent < 0.1
18	16.41666667	14.92667
46	16.41333333	14.76
61	13.68333333	12.11333
80	NA	8.066667

Supplementary Table S - 2 - Comparison of Loss tangent < 1 and Loss tangent < 0.1 in 10% GelMA hydrogels.

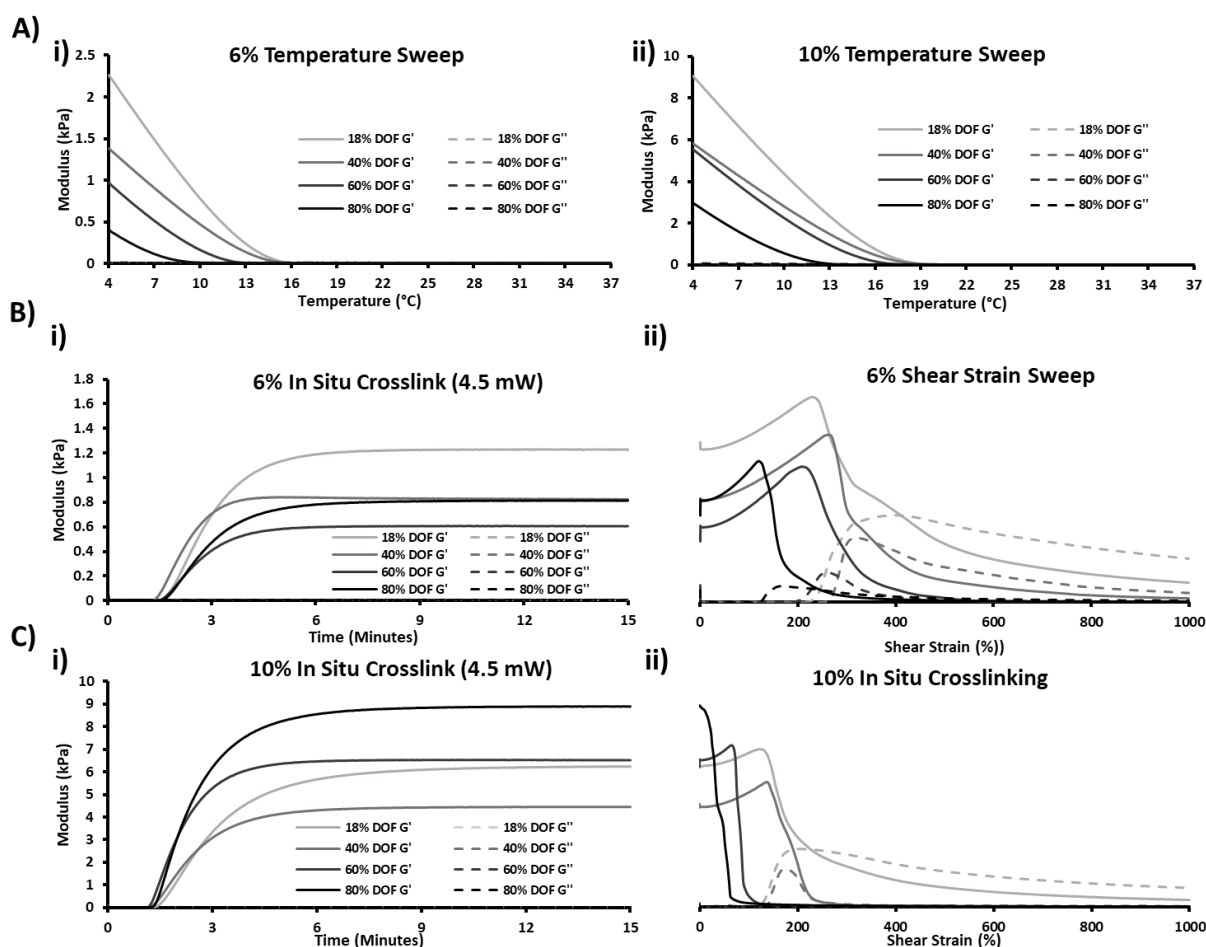
DoF	Loss tangent < 1	Loss tangent < 0.1
18	19.96333333	17.73333
46	NA	17.56667
61	18.39666667	16.41333
80	NA	12.12

Supplementary Table S - 3 – Molecular Weight and Number of 18% DoF and 80% DoF GelMA.

	18% DoF	80% DoF
Molecular Weight (Da)	107,464	62,688
Molecular Number	39,171	19,666
PDI (MW/MN)	2.743	3.188

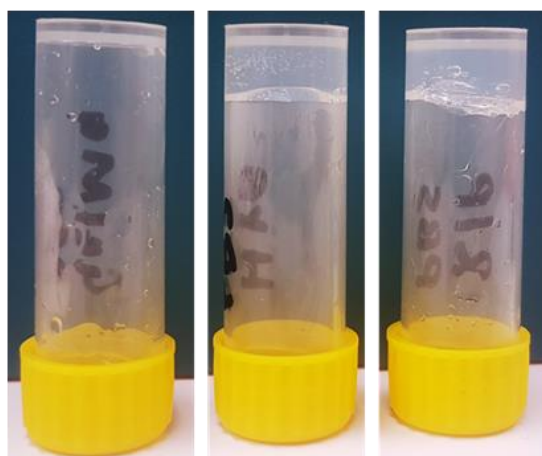


Supplementary Figure S - 6 – Heatmap showing Pearson r values as an indication of correlations between investigated variables as calculated through Pearson correlation test.

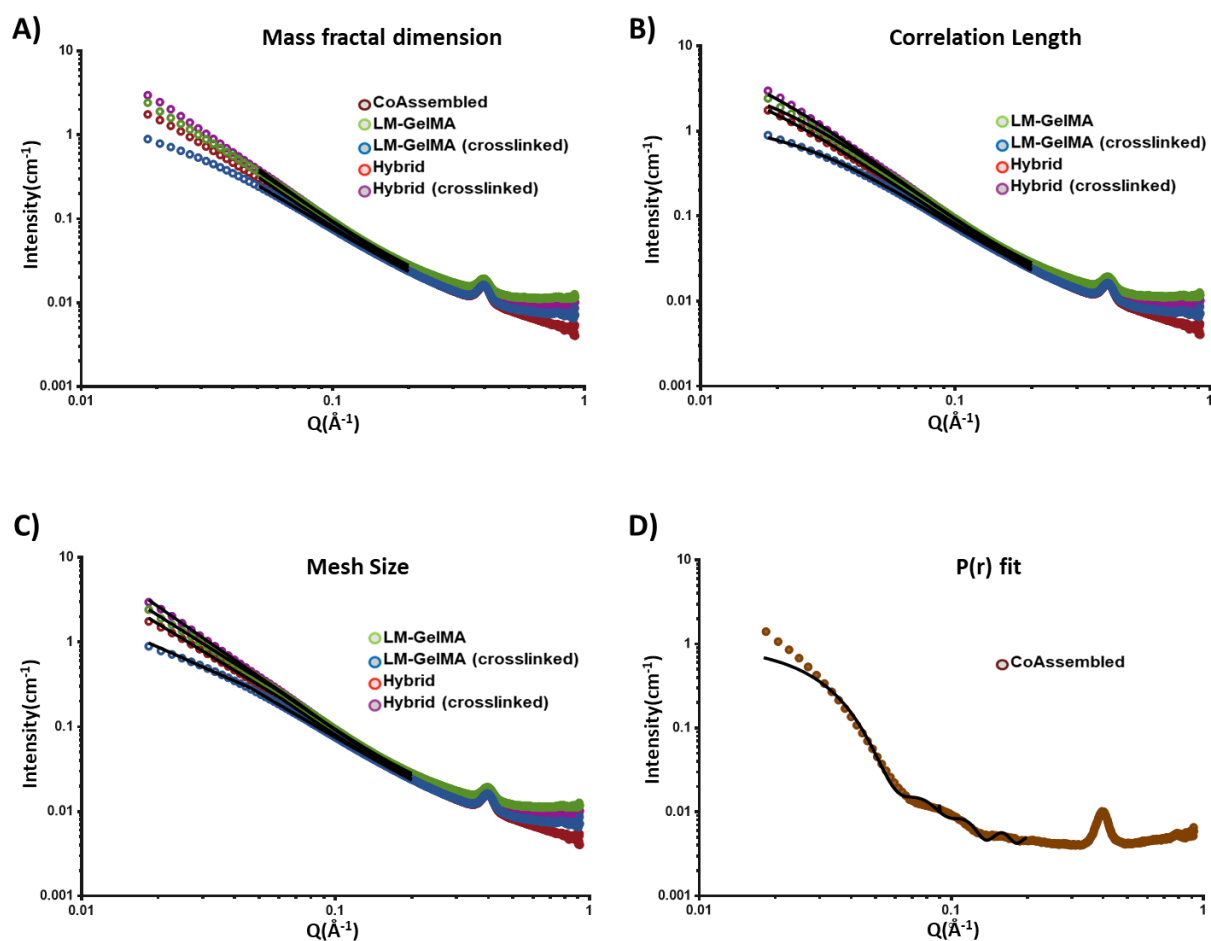


Supplementary Figure S - 7 – Viscoelastic Properties of GelMA hydrogels at different DoF and concentration. A) G' and G'' response to cooling in i) 6% GelMA and ii) 10% GelMA samples. B) G' and G'' response to i) crosslinking in 6% GelMA samples and ii) shear-strain in 6% GelMA samples. C) G' and G'' response to i) crosslinking in 10% GelMA samples and ii) shear-strain in 10% GelMA samples.

LM-GelMA Hybrid Coassembled



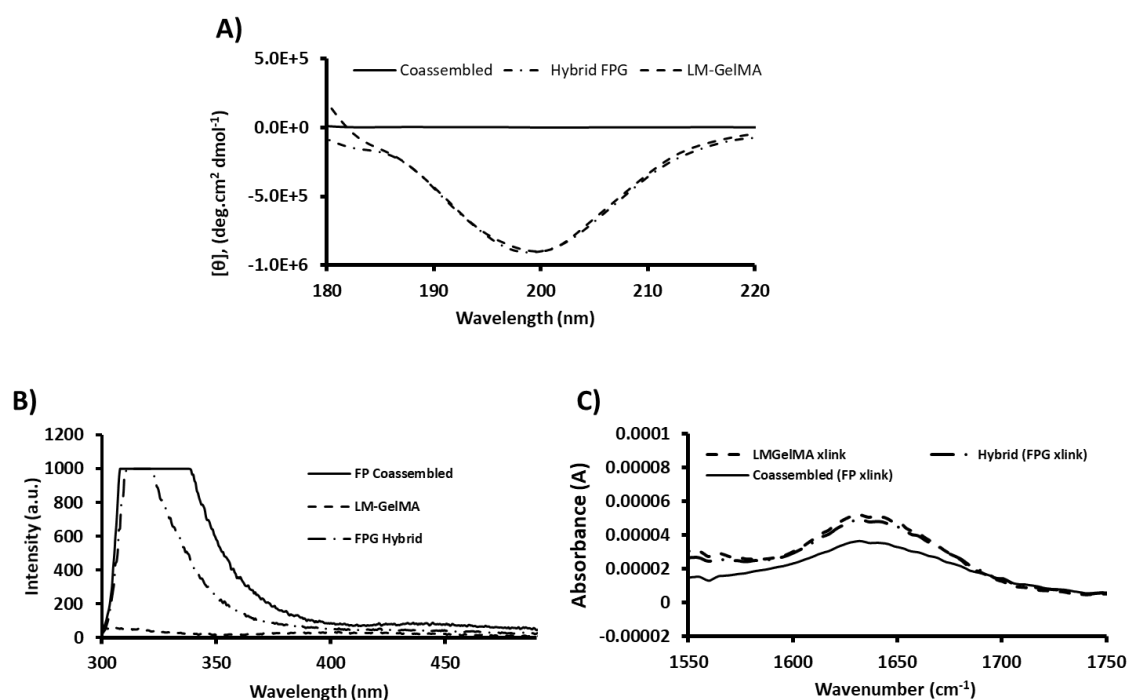
Supplementary Figure S - 8 – Inversion test showing stable gel formation in Fmoc-SAP containing hydrogels (Coassembled and Hybrid) at room temperature (23°C)



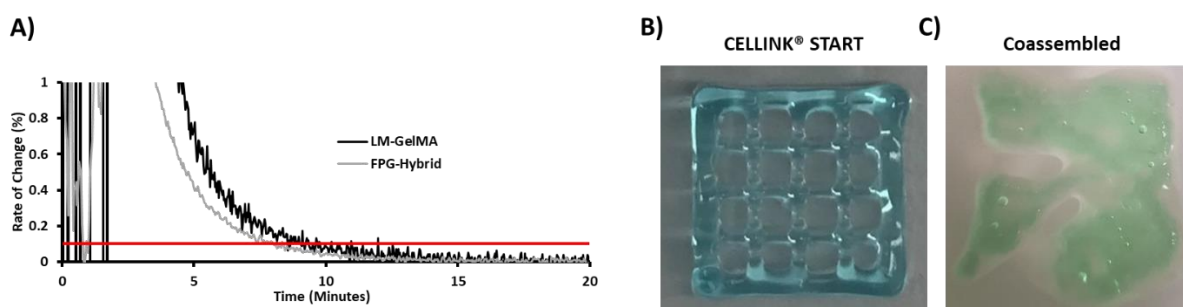
Supplementary Figure S - 9 - Fitting of small-angle X-ray scattering curves. A) Fitting for power-law model (mass fractal dimension) in coassembled (Fmoc-FRGDF/Fmoc-PHSRN), LM-GelMA. And FPG-Hybrid samples. B) Fitting for correlation length model in coassembled (Fmoc-FRGDF/Fmoc-PHSRN), LM-GelMA. And FPG-Hybrid samples. C) Fitting for two-power model (mesh size) in coassembled (Fmoc-FRGDF/Fmoc-PHSRN), LM-GelMA. And FPG-Hybrid samples. D) Fitting for $P(r)$ for coassembled (Fmoc-FRGDF/Fmoc-PHSRN) hydrogels

Supplementary Table S - 4 – Porod values for LM-GelMA and FPG-Hybrid samples as determined through fitting to the correlation length model.

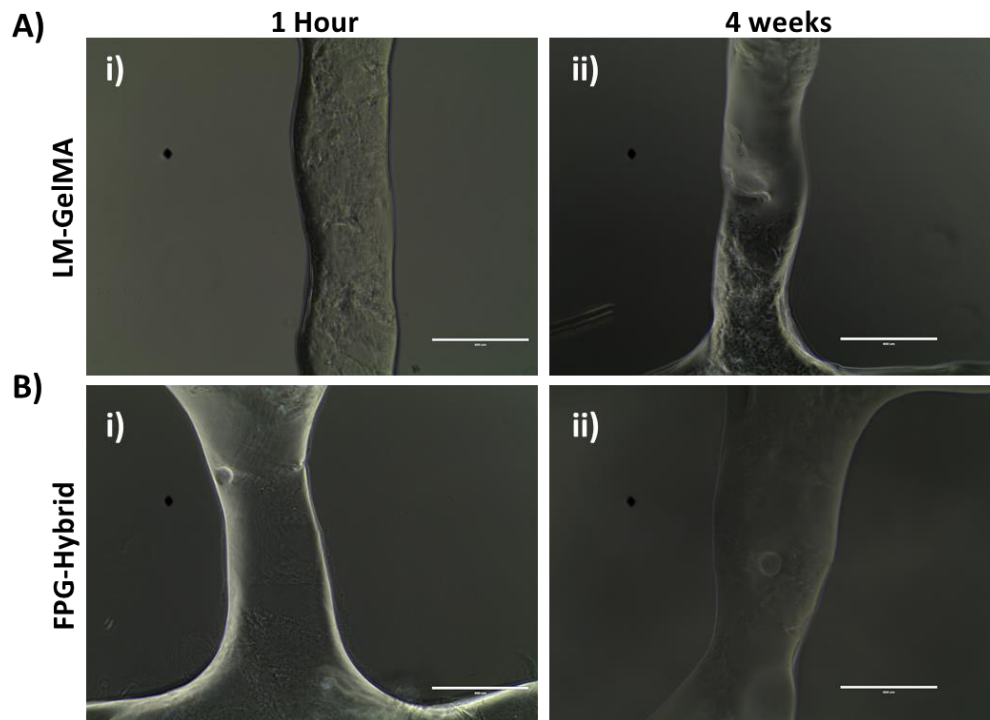
Sample	Noncrosslinked	Crosslinked
LM-GelMA	2.0536 ± 0.0030974	2.2176 ± 0.0025718
FPG-Hybrid	2.0409 ± 0.0025209	2.2808 ± 0.0025982



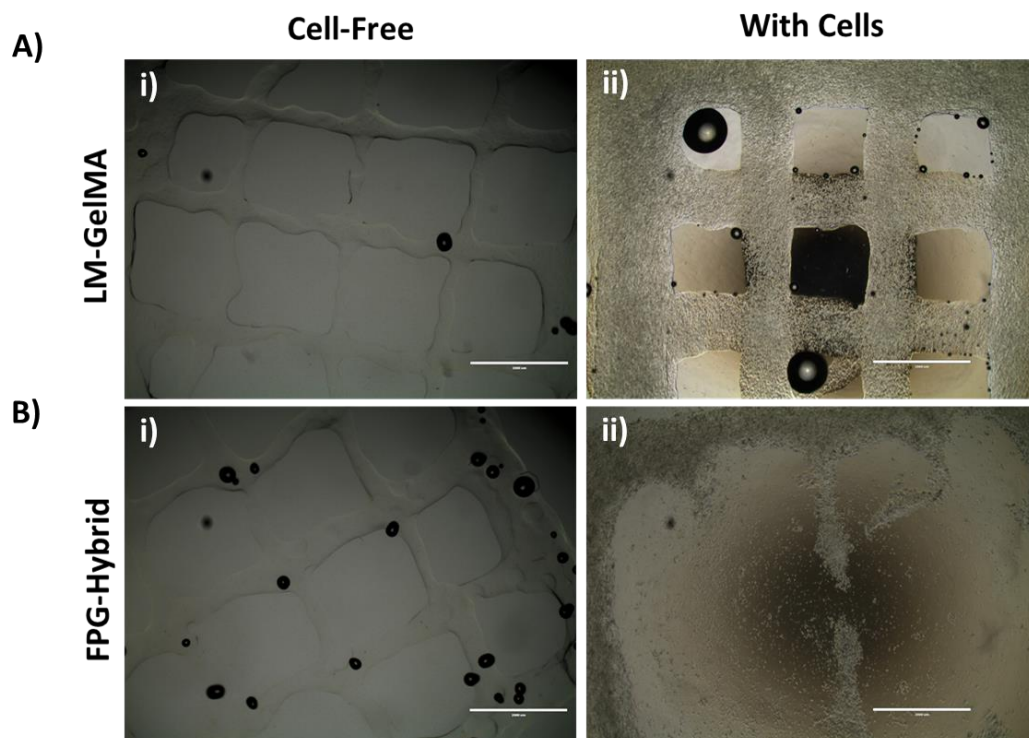
Supplementary Figure S - 10 – Spectroscopic analysis of coassembled (Fmoc-FRGDF/Fmoc-PHSRN), LM-GelMA, and FPG-Hybrid hydrogels showing GelMA dominance. A) Circular Dichroism analysis, B) Fluorescence spectroscopy, C) FT-IR Spectroscopy.



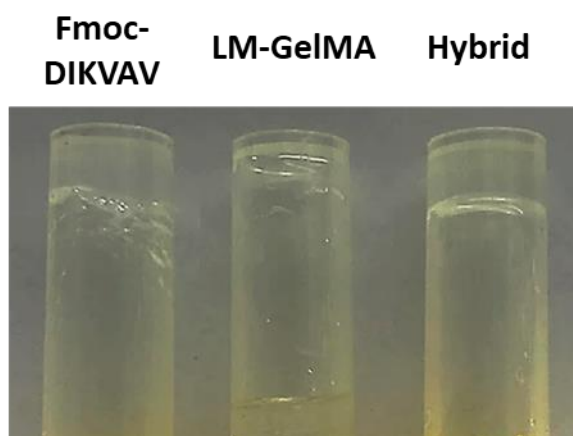
Supplementary Figure S - 11 - Bioink Properties A) Rate of change of LM-GelMA and FPG-Hybrid in response to crosslinking as calculated through analysis of in-situ crosslinking rheological data. Red line indicates defined level of effective crosslinking (0.1% s⁻¹) B) Demonstration of G-code print as printed using commercial, non-cytocompatible CELLINK® START. C) Coassembled (Fmoc-FRGDF/Fmoc-PHSRN) printed construct showing poor printability.



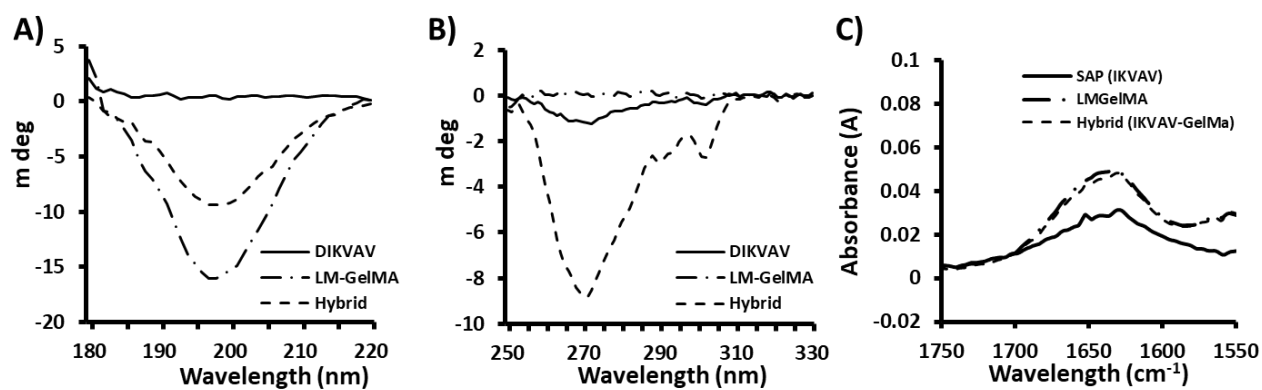
Supplementary Figure S - 12 – microscopic images showing material longevity past 4 weeks simulated culture ($1 \times \text{PBS}$, 37°C). A) LM-GelMA following i) 1 hour and ii) 4 weeks simulated culture. B) FPG-Hybrid following i) 1 hour and ii) 4 weeks simulated culture.



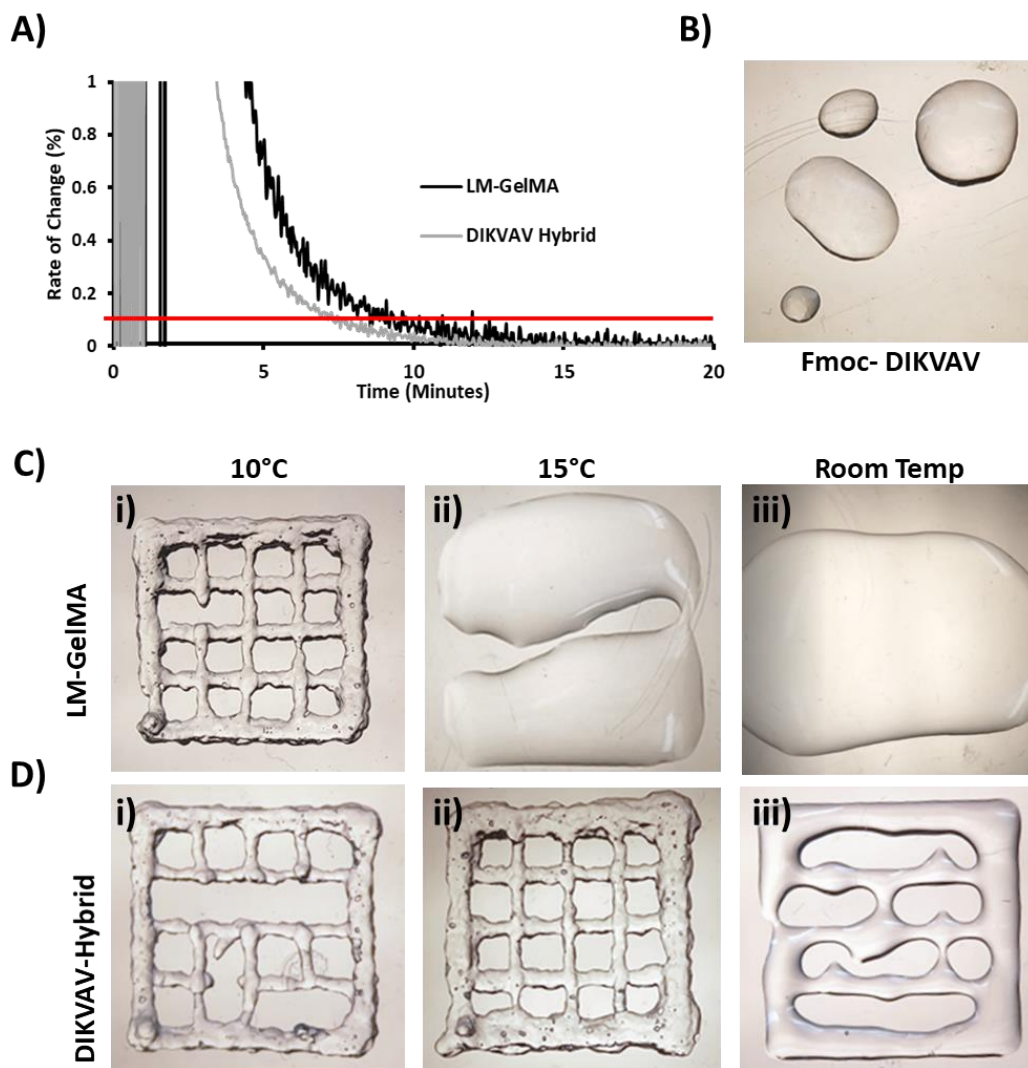
Supplementary Figure S - 13 – representative microscopic images showing material stability with and without primary myoblasts after 3h culture. A) LM-GelMA i) without cells and ii) with cells. B) FPG-Hybrid i) without cells and ii) with cells. FPG-Hybrid stability is substantially compromised following cell addition.



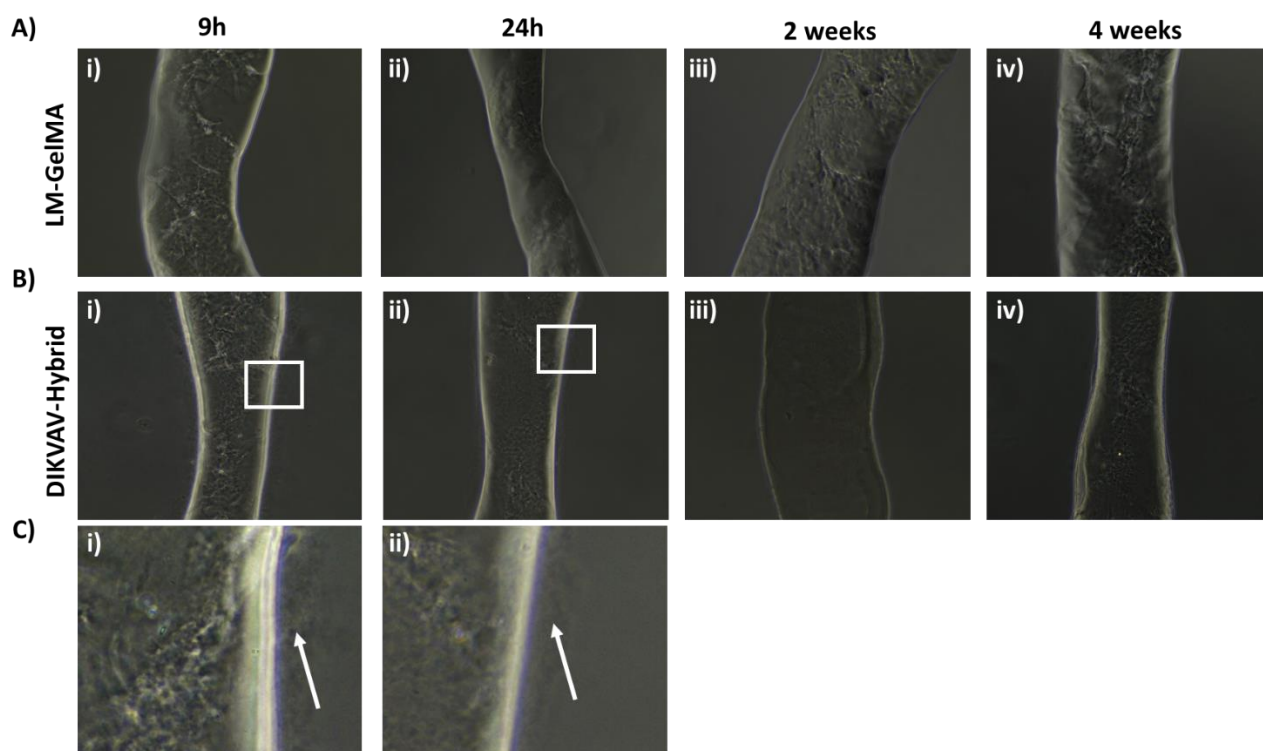
Supplementary Figure S - 14 – Inversion test showing stable gel formation in Fmoc-SAP containing hydrogels (Fmoc-DIKVAV and DIKVAV-Hybrid) at room temperature (23°C)



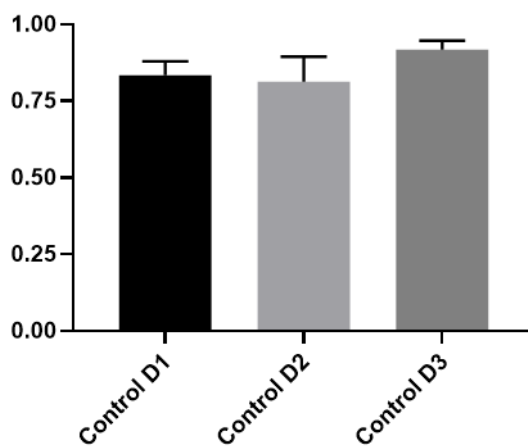
Supplementary Figure S - 15 - Spectroscopic analysis of Fmoc-DIKVAV, LM-GelMA, and DIKVAV-Hybrid hydrogels showing GelMA dominance. A, B) Circular Dichroism, C) FT-IR Spectroscopy



Supplementary Figure S - 16 – Bioink Printability and crosslinking properties. A) Rate of change of LM-GelMA and DIKVAV-Hybrid in response to crosslinking as calculated through analysis of in-situ crosslinking rheological data. Red line indicates defined level of effective crosslinking ($0.1\% \text{ s}^{-1}$). B) Fmoc-DIKVAV printed construct showing very poor printability. C) Printability of LM-GelMA at i) 10°C, ii) 15°C, and iii) room temperature (23°C). D) Printability of LM-GelMA at i) 10°C, ii) 15°C, and iii) room temperature (23°C). Printability assessed visually through ability to form grid structure.



Supplementary Figure S - 17 – Microscopic images showing longevity of material and feathered region over 4 weeks simulated culture (1 × PBS, 37°C). A) LM-GelMA following i) 9 hours, ii) 24 hours, iii) 2 weeks, and iv) 4 weeks simulated culture. B) FPG-Hybrid following i) 9 hours, ii) 24 hours, iii) 2 weeks, and iv) 4 weeks simulated culture. C) Feathered region following i) 9 hours and ii) 24 hours simulated culture.



Supplementary Figure S - 18 – Viability of 2D laminin control over 3-day culture.